博士論文

Nagaoka University of Technology
Graduate School of Engineering
Department of Materials Science and Technology

Synthesis and thermal properties of metal-oxide films with several porosities using flame spraying apparatus

フレーム溶射装置を使用した
異なる気孔率を持つ金属酸化物膜の合成及び熱特性

用火焰喷涂设备合成多种气孔率的金属氧化膜
及其热性能的测试与技术开发

YanXin Dan

August 2020

Table of Contents

Table of Contents

List of Publications

Chapter 2

[1] Densification of metal oxide films synthesized from metal complexes by flame spraying

Keiji Komatsu, Tomoyuki Shirai, Ayumu Toyama, Takao Iseki, D. Y. Xin (YanXin Dan), Takashi Costa, Atsushi Nakamura, Yu Li, Shigeo Ohshio, Hiroyuki Muramatsu, Hidetoshi Saitoh.

Surface & Coatings Technology 325 (2017) 89–97

Chapter 3

[2] Splat morphology and microstructure of chelate flame sprayed Er_2O_3 films

YanXin Dan, XiaoLong Zhou, Atsushi Nakamura, Keiji Komatsu, Hidetoshi Saitoh

Submitted to Journal of the Ceramic Society of Japan

Chapter 4

[3] Effect of parameters on metal-oxide splat morphology by chelate flame spray

YanXin Dan, Takashi Costa, Atsushi Nakamura, Keiji Komatsu, Hidetoshi Saitoh

Chapter 5

[4] Heat-shock properties in yttrium-oxide films synthesized from metal–ethylenediamine tetraacetic acid complex through flame-spray apparatus

D. Y. Xin (YanXin Dan), Keiji Komatsu Keita Abe, Takashi Costa, Yutaka Ikeda, Atsushi Nakamura, Shigeo Ohshio, Hidetoshi Saitoh

Appl. Phys. A (2017) 123:194

Chapter 6

[5] Synthesis of Y_2O_3 films on an aluminum alloy substrate using flame-spray apparatus with a H_2-O_2 flame

Keiji Komatsu, Takashi Costa, Yutaka Ikeda, Keita Abe, YanXin Dan, Tetsuro Kimura, Tomoyuki Shirai, Atsushi Nakamura, Hidetoshi Saitoh

International Journal of Applied Ceramic Technology, (2018) 1-10

Chapter 7

[6] Thermal barrier coatings formed by flame spray with metal-EDTA

YanXin Dan, Takashi Costa, ZhenYu Guo, Atsushi Nakamura, Keiji Komatsu, Hidetoshi Saitoh

Japanese Journal of Applied Physics DOI: https://doi.org/10.35848/1347-4065/ab9ef6

Chapter 8

[7] Microstructural design and thermal conductivity of the sprayed Er_2O_3 thermal barrier coating with coolant system

YanXin Dan, Atsushi Nakamura, Keiji Komatsu, Hidetoshi Saitoh

List of Meetings

National conferences

- **[1] Metal oxide films synthesized with diameter-controlled metal–EDTA complexes**

  T. Shirai, D. Y. Xin (Yanxin Dan), K. Komatsu, A. Nakamura, S. Ohshio, H. Saitoh, The 62st Spring Meeting of the Japan Society of Applied Physics, March 11th–14th at Tokai University, Kanagawa, Japan (2015).

- **[2] Synthesis of Y_2O_3 films with quick thermal cycling resistance with metal–EDTA complex**

  Toyama, T. Shirai, A.Satoh, D. Y. Xin (Yanxin Dan), K. Komatsu, A. Nakamura, I. Toda, S. Ohshio, H. Muramatsu, H. Saitoh, The 62st Spring Meeting of the Japan Society of Applied Physics, March 11th–14th at Tokai University, Kanagawa, Japan (2015).

- **[3] Microstructures on metal oxide films with Diameter-Controlled metal-EDTA complexes**

  Tomoyuki Shirai, D. Y. Xin (Yanxin Dan), Keiji Komatsu, Atsushi Nakamura, Shigeo Ohshio, Hidetoshi Saitoh, The 4th International GIGAKU Conference in Nagaoka, June19th-21th at Nagaoka, Japan (2015).

- **[4] Thermal shock resistance of Y_2O_3 films synthesized with metal-EDTA complexes**

  Yanxin Dan, Atsushi Nakamura, Keiji Komatsu, Hidetoshi Saitoh, The 76st Autumn Meeting of the Japan Society of Applied Physics, September 13th–16th at Nagoya Congress Center, Nagoya, Japan (2015).

- **[5] Cross-sectional observation of Y_2O_3 and Er_2O_3 films deposited by chelate flame method**

  Yanxin Dan, Atsushi Nakamura, Keiji Komatsu, Hidetoshi Saitoh, The 63th Spring

Meeting of the Japan Society of Applied Physics, March 19th–22th at Tokyo Institute of Technology (Ookayama campas), Tokyo, Japan (2016).

- **[6] Cross-sectional observation of Er_2O_3 films deposited on stainless steel and aluminum alloy by chelate flame method**

  Yanxin Dan, Atsushi Nakamura, Keiji Komatsu, Hidetoshi Saitoh, The 77th Autum Meeting of the Japan Society of Applied Physics, September 13th-16th at Toki Messe, Niigata, Japan (2016).

- **[7] Cross-sectional observation of Er_2O_3 films deposited on quartz glass by chelate flame method**

  Yanxin Dan, A. Nakamura, K. Komatsu, H. Saitoh, The Ceramic Society of Japan Annual Meeting 2017, March 17th–19th at Nihon University (Surugadai Campus), Tokyo, Japan (2017).

- **[8] Thermal insulating properties of stacked micro-hollow beads**

  Yanxin Dan, Atsushi Nakamura, Keiji Komatsu, Hidetoshi Saitoh, The 79st Autumn Meeting of the Japan Society of Applied Physics, September 18th–21th at Nagoya Congress Center, Nagoya, Japan (2018).

- **[9] Thermally insulating properties of oxide films on aluminum alloy by chelate flame method**

  Yanxin Dan, Atsushi Nakamura, Keiji Komatsu, Hidetoshi Saitoh, The 66st Spring Meeting of the Japan Society of Applied Physics, March 9th–12th at Tokyo Institute of Technology University, Tokyo, Japan (2019).

- **[10] Thermally insulating properties of oxide films with different porosities by chelate flame method**

  Y.X. Dan, A. Nakamura, K. Komatsu, H. Saitoh, The Ceramic Society of Japan Annual Meeting 2019, March 24th–26th at kogakuin University (shinjuku campus),

Tokyo, Japan (2019).

- **[11] Synthesis of iron oxide films with metal-EDTA complex solution using atmospheric reaction assisted by H_2–O_2 combustion gas**
  Yanxin Dan, Atsushi Nakamura, Keiji Komatsu, Hidetoshi Saitoh, The 80st Autumn Meeting of the Japan Society of Applied Physics, September 18th–21th at Hokkaido University, Hokkaido, Japan (2019).

International conferences

- **[1] Thermally insulating oxide films synthesized on aluminum alloy(A5052) by chelate flame method**
  Yanxin Dan, T. Costa[1], A. Nakamura, K. Komatsu, H. Saitoh, The International Fall Meeting of MATERIALS RESEARCH SOCIETY(MRS), November 25th–30th 2018 at Boston, United States of America(USA).

- **[2] Heat-shock properties on Y_2O_3 films synthesized with metal ethylenediamine tetraacetic acid complex**
  K. Komatsu, D. Y. Xin (Yanxin Dan), K. Abe, T. Costa, Y. Ikeda, A. Nakamura, S. Ohshio, H. Saitoh, International Thermal Spray Conference & Exposition (ITSC), May 10th-13th 2016 at Shanghai, China (CN).

List of Patents

- **[1]** Patent title**: [producing a composite material of Y_2O_3 films deposited on silicon oxide substrate];** Patent number**:2018-140913(P2018-140913A)**
- **[2]** Patent title**: [Metal film coating method and sealing material];** Patent number**:190100(provisional).**

List of Tables and Figures

Chapter 1 General introduction

Chapter 2 Synthesis of metal oxide films using chelate flame method with different carrier gas

Chapter 3 Analysis of cross-sectional structure of metal oxide films deposited using chelate flame method

Chapter 6 Heat resistance and adhesion properties of Y_2O_3 films on aluminum alloy substrate

Acknowledgments

This thesis has been carried out under the guidance of Prof. Hidetoshi Saitoh of the Department of Materials Science and Technology at Nagaoka University of Technology. The author wishes to express his sincere gratitude to his dissertation supervision, Prof. Hidetoshi Saitoh, for their innumerable advice, invaluable discussion, and constant guidance throughout this work.

I especially would like to thank the rest of my thesis committees: Vis. Prof. Dr. Atsushi Nakamura and Assoc. Prof. Dr. Haruhiko Ito, for their supports and guidance made my thesis work possible. They have been actively interested in my work and always been available to help and advise me.

Also, thanks, Mr. Shigeo Ohshio, Assist. Prof. Dr. Keiji Komatsu, and all staff in Optoelectronic Ceramics Laboratory for good advising supporting and helping in my research.

The author is indebted to present and past members of Optoelectronic Ceramics Laboratory for many discussions and suggestions. The author would like to thank Messrs. Syouta Nakamura, Takashi Costa, Taisuke Kobori, Keita Abe, Yutaka Ikeda, Motohiro Yamazaki, Ke Huang, Tetsurou Kimura, Youhei Nakamura, Zhenyu Guo, Shaoji Liang, Takuya Kudo, Atsuhiro Saito, Taito Kikuchi, Yunosuke Takatoku, Heng Li, Yukuen Fan, Ruohui Xu, Quang Hiep Nguyen, and, Mses. Katsuko Nagano, Yukino Kanma, Rui Okuda, and Mirai Yamamura for help with experiments and analyses related to this work.

Finally, the author extremely thanks his parents, his wife parents and sisters and all the members of my family for their continuing support and encouragement. He really appreciates his wife`s unlimited help in his graduate studies.

YanXin Dan

Nagaoka University of Technology

August 2020

Chapter 1

General Introduction

1.1 Overview

The thermal spraying method is a method of melting or semi-melting a metal or oxide as raw material and spraying the molten metal or metal oxide film on the surface of the material **[1]**. A coating applied by this method is called a thermal spray coating. The “thermal” of thermal spraying means melting the raw material, and the “spraying”(projection, spraying) corresponds to spraying the raw material. For example, in order to melt metal(wire) or ceramic(powder) as the thermal spray raw material, the heat source is performed by combustion of high temperature combustible of high-temperature combustible gas or electric discharge et al., and the melted particles are accelerated by the carrier gas and impact with the substrate, and the moment it solidifies to form the film(thickness of ˜20 μm) or coatings(thickness of 100˜μm), the process as shown in **Fig**.1-1. It is applied mainly for the purpose of improving the corrosion, abrasion resistance, heat resistance, or thermal barrier of the substrate.

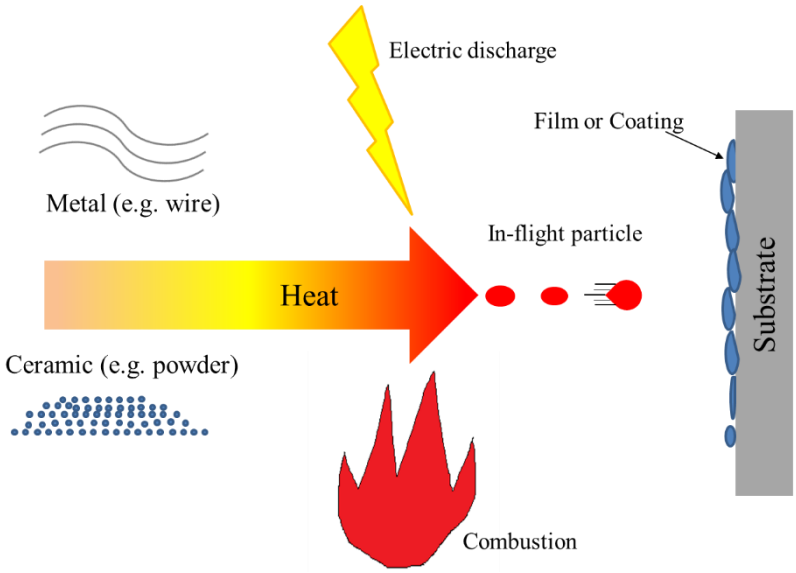

Figure 1-1 The process of thermal spray.

The number kind of thermal spraying methods has been developed greatly in the past years for the application of protecting the materials. Among them, the typical spraying methods include plasma spraying(PS), high-velocity oxygen fuel(HVOF), and flame spray(FS), et al. **[2-4]**. In general, the characteristics of these technologies are determined by the flame temperature and the velocity of inflight particles. Hence, the use of different techniques for depositing similar coatings may lead to various results in quality and cost terms. For example, some specific functional coatings such as thermal barrier coatings and oxidation resistant coatings, are more easily achieved using APS and HVOF technologies. Which can be attributed to the following factors: particle the high-temperature(PS:10000-15000 K) and high-velocity(550-800 m/s) of the inflight particles for completely melting the raw-materials and flattening the splats to synthesis the dense or porous structure which can enhance the performance(thermal insulation, oxidation, et al.) of the coating. However, other techniques, such as flame spraying(FS), are still recommended given their lower cost and high deposition rate. Therefore, it is a key with the choice of raw materials that are more easily melted at low temperatures to obtain similar or better performance of the coating. Hence, the precursor of ethylenediaminetetraacetic acid(EDTA) is suggested in this method as the metal-EDTA complex.

In this study, EDTA is the most famous chelating agent. As the characteristic, EDTA has achromic crystal powder, and a molecular weight of 292.25 and a decomposition point of 240 ℃. It was reported that the Y_2O_3:(Eu, B) phosphor powder was obtained by the thermal decomposition method of Y-EDTA, Eu-EDTA at firing conditions. From this study, it can be used the morphological and compositional design for metal oxide using metal-EDTA complex route**[5-7]**. In addition, it is possible to obtain thin film with complicated metallic composition by thermal decomposition of metal-EDTA complexe powders formed by the method. In the follow-up study, the Yttrium(Y^{3+}) ions were selected to form the metal-EDTA complexes, and the metal oxide films were deposited on stainless steel(SUS) substrate with an H_2-O_2 combustion flame. I called this spray method as the chelate flame spray(CFS). The deposition process of metal

oxide film involves two mechanisms, namely chemical reaction and physical collision. It begins with a chemical reaction in which the precursor material such as the metal-EDTA complex is decomposed and oxidized to form metal oxide particles. Finally, the physical collision of the molten metal oxide particles impact to the substrate with subsequent cooling and solidification processes and form metal oxide films. Hence, this process exhibits some advantages over plasma spray(PS) and HVOF even for high melting ceramic materials such as Y_2O_3 that melts at approximately 2430 ℃**[8]**. In addition, there are two interesting findings as follows: (1) The Y_2O_3 film synthesized using the rotation apparatus with cooling agents(such as compressed air, liquid nitrogen, and atomized purified water) exhibited porosity range of 22.8 % - 36.4%. (2) the Y_2O_3 cubic crystalline phase were confirmed in all films, synthesized with EDTA·Y·H. Thus, it means that the metal oxide films synthesized in this method exhibit the potential for stronger thermal insulation properties, due to the low thermal conductivity of 12.5 W/(m·K)(293 K) **[8]**, high porosity, and stable crystalline structure**[9]**. From the above described, the chelate flame method considered to synthesize ceramic coating at a low cost and rapidly. It also can be expected that with thermal insulation capability, and so-called the thermal barrier coating(TBC) for applications in the hot-section metallic components of gas turbines or aero engines, such as burners, turbine blades, vans, and et al. **[10,11]**.

1.2 Literature survey

1.2.1 Types of thermal spraying method

The thermal spraying technology developed by M.U.Schoop of Switzerland in 1909 has become an important basic technology in various industrial fields as a film deposition process. The basic theory of thermal spraying method is “a kind of surface modification technology in which the material particles are heated in molten or semi-molten using the combustion or electric energy, and are sprayed onto the substrate surface to synthesis the film.” Thermal spraying techniques have numerous advantages, including a high deposition rate and the ability to deposit coatings on large areas on an

industrial scale. **Fig.** 1-2 shows the relationship between the in-flight particles velocity and the flame temperature in various thermal spraying methods. Flame spraying(FS), wire flame spraying, arc spraying(AS), and plasma spraying(PS) are "temperature(melting)" oriented types that melt well and spray at low speed. On the other hand, explosive spraying with high-velocity oxy-fuel(HVOF) is "speed(spraying)" oriented types that spray semi-molten particles at high speed. In addition, the methods of AS and PS have a higher flame temperature and completely melt the raw material above the melting point of the raw materials. Thus, a certain level of energy is required to adhesion and deposition splats, but the characteristic of various thermal spraying methods are how the energy is balanced between the temperature(thermal energy) and velocity(Kinetic energy) of the flying particles. However, compared with other spraying methods, among of the flame spraying is not only low in flame temperature but also slow in particle velocity**[12]**.

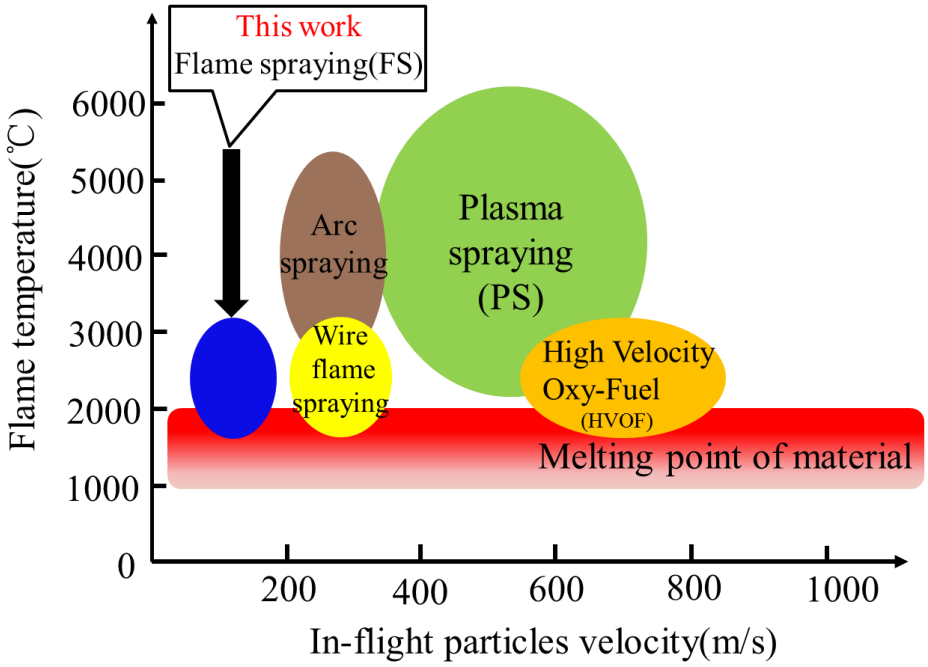

Figure 1-2 The classification of thermal spraying methods.

In addition, it is a process in which a protective coating is applied on a substrate by spraying on it, small size (from 10 to 100 μm) and high-velocity (above 100 m s^{-1}) molten particles of metals, alloys or ceramics which merge and solidify after impact producing to be dense and thin layers or lamellae, called splats, that conform and adhere

to the substrate surface**[12, 13]**. The deposition process of thermal spray, as shown in **Fig.** 1-3. The formation of the coating in the thermal spraying process is characterized by the subsequent impingement of a large number of more or less molten particles that are deposited on top of each other, and the layering of the individual splats determines the microstructure(such as deposited semi-molten splat, and formed the mechanical interlocking part) and eventually the properties of the coating**[14, 15]**. From the deposition process, thermal spray coatings are used to provide various properties to protect mechanical parts from corrosion, erosion, and heat**[16-18].** It is well known that coating defects such as porosity, microcracks, and un-melted particles are correlated with adhesion strength, the shape of these splats, and how they bond together to the substrate. From the above, it can be said that the choose spraying method is a key to synthesis the coating with excellent properties.

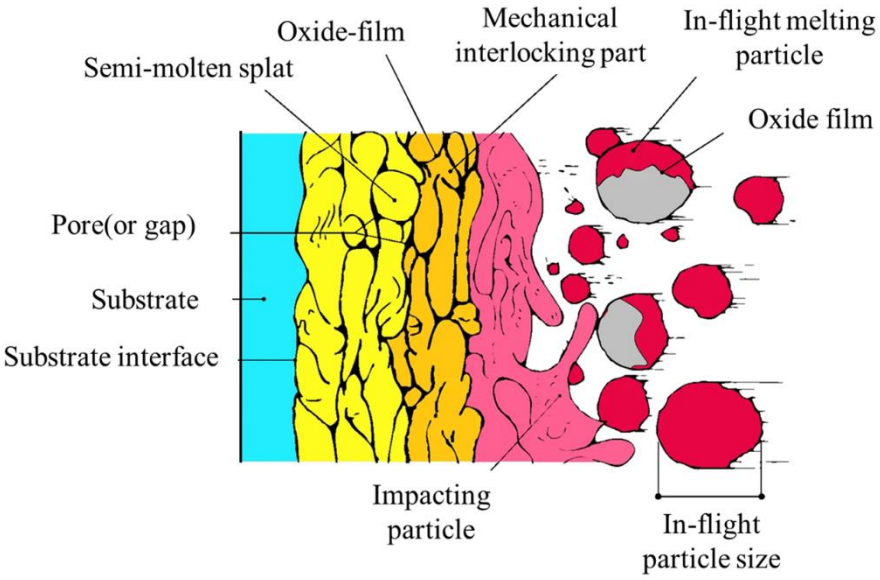

Figure 1-3 The deposition process of thermal spray.

1.2.2 Traditional raw materials of thermal spraying

Above the spray method tell us that use of different techniques for depositing similar coatings may lead to various results in quality and cost terms. Thermal spray coatings are frequently used as oxidation-resistant materials and thermal insulation coatings. From the above application of coatings, the raw materials(or powder) are selected with mainly divided into following two categories: (1) metal (MCrAlY alloys(where M:

metal stands for Co, Ni, or for both)) and (2) ceramic (yttria stabilized partially with zirconia(YSZ)), respectively**[19]**.

1.2.2.1 Sprayed coating with metal raw materials

The quality of coating produced by thermal spraying techniques depends on a very large number of parameters such as raw materials types, carrier gas types, and spray process. However, before optimization of such process parameters to obtain great coatings quality(protection performance), the first decision concerns the choice of the spray process and second choice of the raw material. In other words, it is not only important to choose the appropriate spraying technology to play a key role in the coating properties, but also to select the appropriate spraying material. Therefore, it means that the two factors to determine a better coating property of (1) raw material(or powder) itself and (2) spraying method(or spray parameters) **[20, 21]**. For example, the HVOF process belongs to the system of thermal spray techniques and are widely used in many industries to protect the components against wear and erosion**[22,23]**. In addition, the standards of the original equipment manufactures(OEMs) recommend MCrAlY alloys being deposited using HVOF, because of the higher velocity of the in-flight particles(550-800 m/s) **[24]**. Furthermore, the most reported that the wear behavior of HVOF sprayed coatings have low porosity of approximately 1 %, the SEM images are shown in **Fig.** 1-4**[25-29]**. As the result, it is now clearly proved that particle velocity is an important process variable that affects particle melting and ultimately, the density and adhesion of the deposited material(or coating) **[30]**.

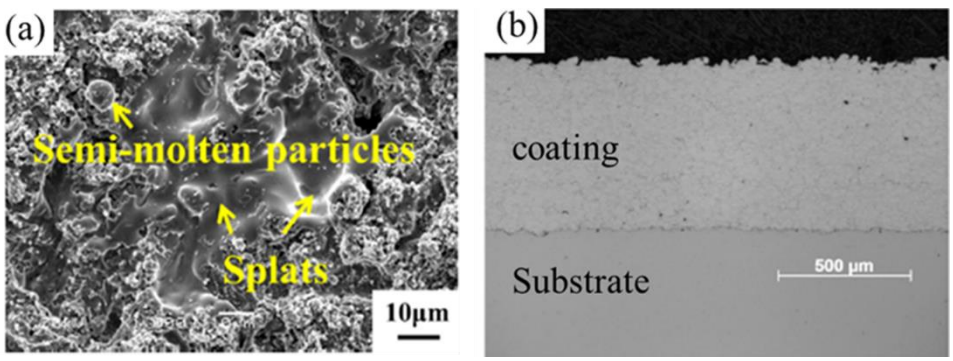

Figure 1-4 Images of the as-sprayed coatings by HVOF
(a) Surface, (b) Cross-sectional.

1.2.2.2 Sprayed coating with ceramic raw materials

On the other hand, it is also admitted that in-flight particle temperature is a critical parameter that influences coating thermal properties such as porosity and oxide level **[31]**. For example, Plasma-sprayed(PS) thermal barrier coating(TBC) with yttria stabilized zirconia(YSZ) systems has been developed in thermal insulating components. In PS, the feedstock powder is melted and accelerated towards the substrate where it flattens and rapidly solidifies. Generally, the shape of the powder is globular, and it is easier to melt in the flame. **Fig.** 1-5 (a), (b) shows the morphology of YSZ powder and cross-sectional of the as-sprayed coatings by PS method**[32]**. From the cross-sectional SEM images, coatings are made of a bond coat and a zirconia based ceramic topcoat. The topcoat of zirconia behaves as a thermal barrier layer**[33, 34]**, hence, it exhibits a microstructure containing pores, cracks, and inter-splats interfaces, with a porosity level of 10 - 30 %, which provides a reduced thermal conductivity even less than of ～ 1W/(m·K) and is essential to service durability during thermal cycling and thermo-mechanical loading**[35]**. Whereas bond coat provides protection against oxidation and corrosion to the substrate**[34, 36],** and it also helps to increase adhesion of ceramic topcoat to the metallic substrate**[37]**.

As the high-temperature(10000-15000K) process that the thermal interaction between the particles and the spray jet is modified and control the microstructure to improve the thermal insulation capability**[24]**. As a conclusion, these methods exhibit that the advantages of the equipment itself such as an increase of the velocity of the particle, result in an increase in the kinetic energy or rise in temperature for melting the high-melting-point(e.g., zirconia of 2943 K) of the particle. In addition, other techniques, such as flame spraying(FS), are still recommended given their lower cost. However, it cannot be widely developed in these fields, because of the lower particle velocity and flame temperature.

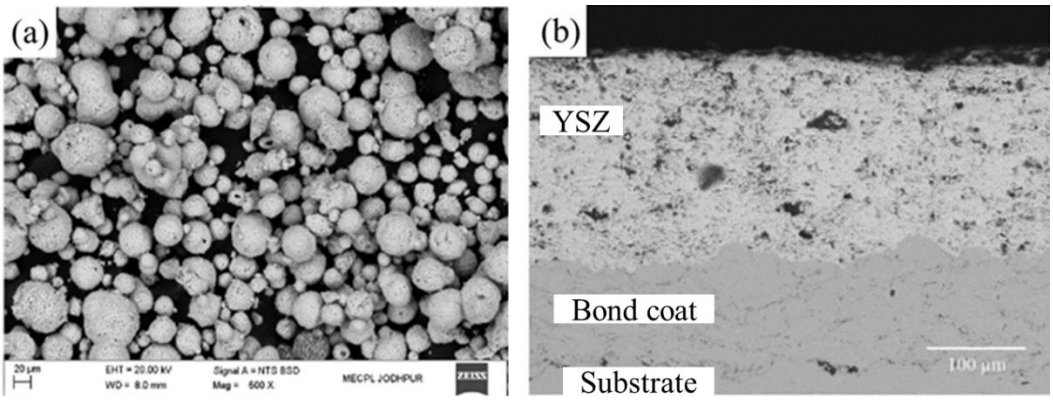

Figure 1-5 SEM images (a)YSZ powder
(b) Cross-sectional of the as-sprayed coatings by PS.

1.2.3 New raw materials of thermal spraying

1.2.3.1 Ethylenediaminetetraacetic acid (EDTA)

Generally, thermal-sprayed coating systems of the raw materials melts or softens in the flame. It can synthesis the coating of almost any material(metal, ceramic, plastic, composite material). As described in the previous section, a physical reaction process occurs in thermal spraying. Recently, a new type raw material(such as metal-EDTA complex) has been developed and used in the thermal spraying systems to synthesis the coating.

Ethylenediaminetetraacetic acid(EDTA) is the most famous chelating agent. EDTA is an artificial organic compound that has characteristic structure consisting of 6 ligands: 4 -COOH and 2 amines, as shown in **Fig**. 1-6. EDTA has achromic crystal powder, and a molecular weight of 292.25 and a decomposition point of 240 ℃**[38]**. In addition, EDTA has specific characteristics never seen at other organic compounds. It forms stable and water-soluble metal chelate with metal ion having two or more valences. And the ratio of metal ion chelated to the EDTA molecule is always 1:1. Metal-EDTA complex has several five-membered chelate rings that are in the most state, as shown in **Fig**.1-7. It is a so-called chelating effect**[39]**. Moreover, EDTA is widely used in

synthesize ceramics composed of (single or multi)-elements by taking advantage of these characteristics. For example, as described in the section of 1.1, metal oxide ceramic films were synthesized from metal-EDTA complexes using a flame spraying technique.

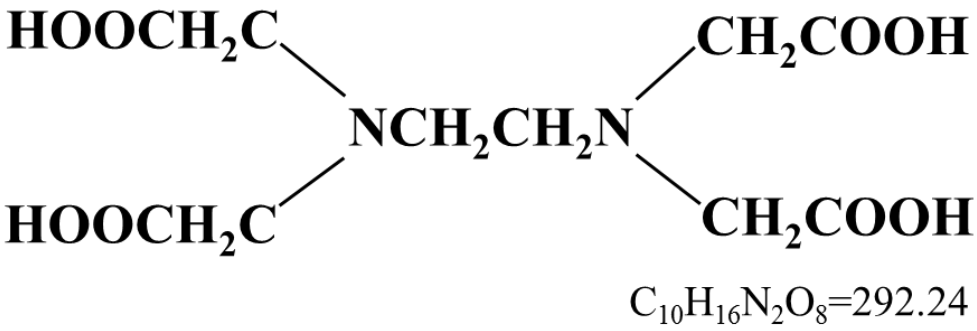

Figure 1-6 Structural formula of EDTA.

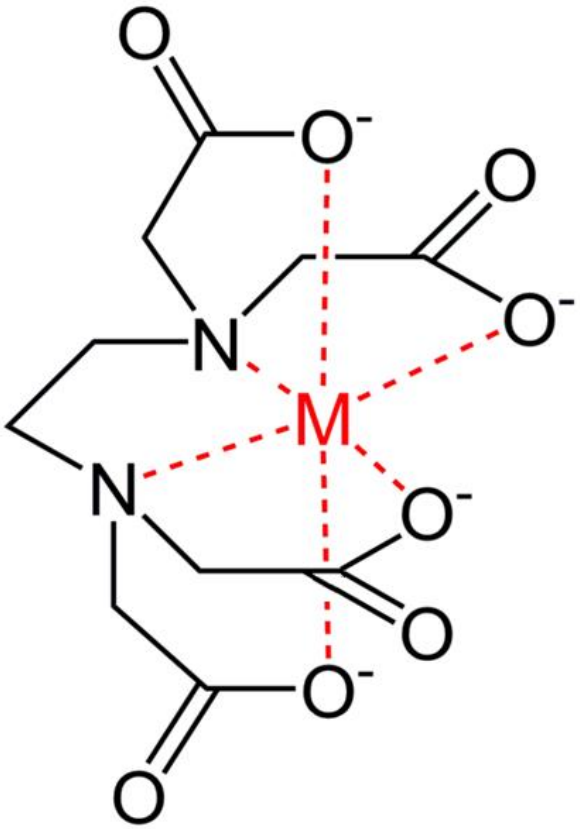

Figure 1-7 Structural formula of metal-EDTA.

1.2.3.2 Metal-EDTA complex

The PS and HVOF method, which are mainly used in thermal spraying method, can synthesize coating on the substrate suitable for a variety of working environments and improving the properties such as the durability and anticorrosion(chemical or thermal resistance) et al. because these can obtain a higher temperature and velocity of the sprayed particles than other thermal spraying methods, as shown in **Fig** 1-2. However, these methods have some weak points such as severe noise during operation and high-cost of the equipment. Hence, the lower cost spraying method was proposed such as flame spraying. However, this method has limitations in technical fields, such as high melting point materials cannot be melted and synthesized coating, and it is also difficult to synthesis a dense coating because of the lower flame temperature of 2300-2900 K and lower velocity of the in-flight particles of 100-200 m/s, respectively. Therefore, as the new synthesis method, a flame spraying apparatus using oxyhydrogen(H_2-O_2) flame as a heat source and a synthesis method using metal-EDTA complex as a spraying material were proposed by H. Saitoh et al. **[40]**. In this study, the metal-EDTA complex as a raw material is put into a flame, which is the heat source, and its thermal decomposition reaction and oxidation reaction of supported metal ions are used. This method exhibits some advantages over plasma spray(PS) and HVOF even for high melting oxide-metal materials, such as Y_2O_3 and Er_2O_3 synthesized by the metal(Y or Er)-EDTA complex that decompose at approximately 365 ℃（effect of the metal）. The EDTA·Er·H and EDTA ·Y·H complex have a structure, as shown in **Fig**.1-8 and 1-9. Based on **Fig**. 1-7, the Er^{3+} ion is coordinated to the central metal ion and has a structure in which “H” is bonded to one of the four carbonyl groups. EDTA ·Y·H same as the EDTA ·Er·H has a similar structure because of the Y^{3+} ion is also the central metal. A characteristic of this method is that the high-melting-point metal oxide coating can be synthesized at a relatively low temperature. Therefore, it shows a potential that the coating can be synthesized without the need to raise the synthesis temperature to the melting point of the target metal oxide (2000 ℃ or higher), such as thermal barrier coating(TBC).

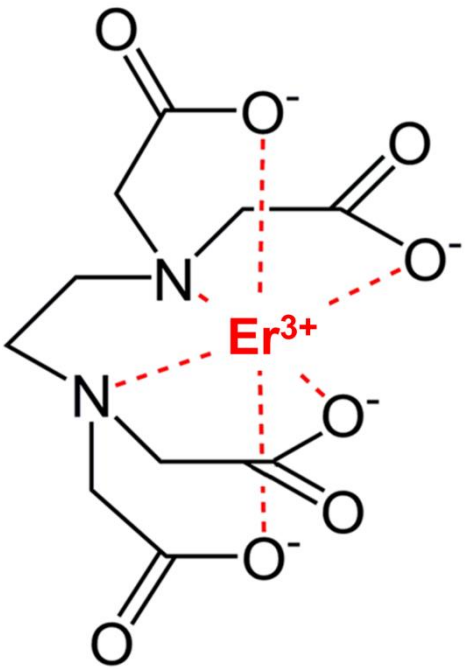

Figure 1-8 Structural formula of EDTA·Er·H of raw materials.

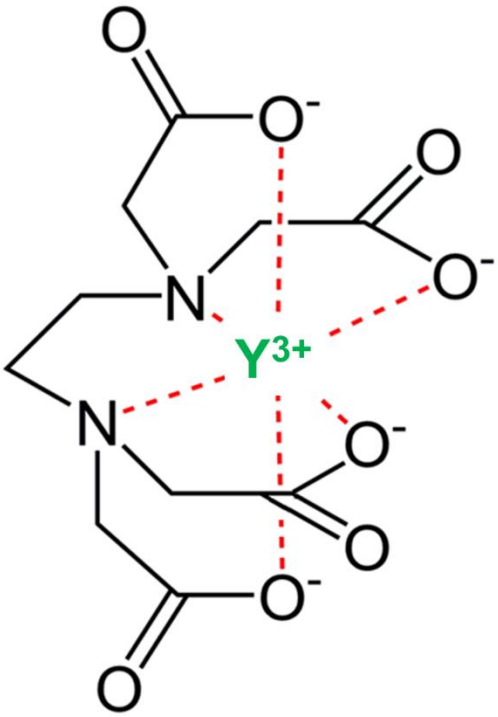

Figure 1-9 Structural formula of EDTA·Y·H of raw materials.

1.2.3.3 Research of new raw materials

At present, a new method to synthesize the metal-oxide ceramic coatings. Using the metal-ethylenediaminetetraacetic acid(EDTA) complex with the flame spraying(FS) apparatus has been developed**[41]**. In this method, the metal-EDTA complex was placed in a feed unit and transported by flowing N_2 gas to the spray gun. As this technique allows for high deposition rates, coatings with thicknesses of several tens of micrometers could be obtained. The cross-sectional porosities of these films were 6-15%. The highlight of the method is that the deposition process involves two processes (1) a chemical reaction and (2) physical collision. During the chemical reaction, the metal-EDTA complex decomposes and oxidizes to form metal oxide particles. In addition, the chemical reaction of EDTA·M·H(M: metal species) can be represented by equation (1-1).

$$2EDTA \cdot M \cdot H + 24O_2 \rightarrow M_2O_3 + 20CO_2 + 13H_2O + 4NO_2 \qquad 1\text{-}1$$

In Eq.(1-1), EDTA·M·H reacts with O_2 to form an M_2O_3 film. Moreover, it can be seen from the reaction equation that the products(gas of CO_2, H_2O, and NO_2) have no effect on the formation of metal oxides. In the second process, these molten particles impact with the substrate and form a thick metal oxide ceramic layer. During the spray process, the supply of oxygen atoms to the metal-EDTA complex is key for ensuring that the chemical reaction takes place, the spraying process model image is as shown in **Fig**. 1-10.

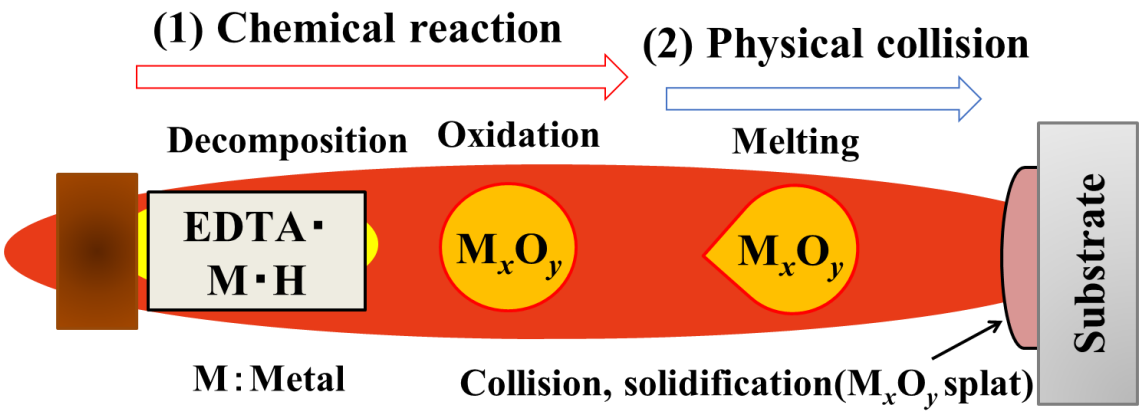

Figure 1-10 Spraying process of metal-EDTA complex.

In this spray process system, using the metal-EDTA complexes could be synthesized the various of the metal-oxide ceramic films such asY_2O_3, Eu_2O_3 and Er_2O_3, the cross-sectional SEM images of the films deposited on SUS substrate as shown in **Fig**.1-11. From this study, the presence of crystalline Y_2O_3, Eu_2O_3, and Er_2O_3 phases was confirmed, and the cross-sectional porosities, thicknesses in the obtained films were estimated as 6-15%, 9-22 μm, respectively**[42]**. These results mean that the true density of the metal oxide formed by the metal-EDTA reaction process plays an important role in the achievement of films with the desired microstructure using the flame spraying method. Therefore, this method exhibits the potential that using the lower flame temperature and in-flight particle velocity can be synthesized similar property coating at the low cost, compare with HVOF and PS.

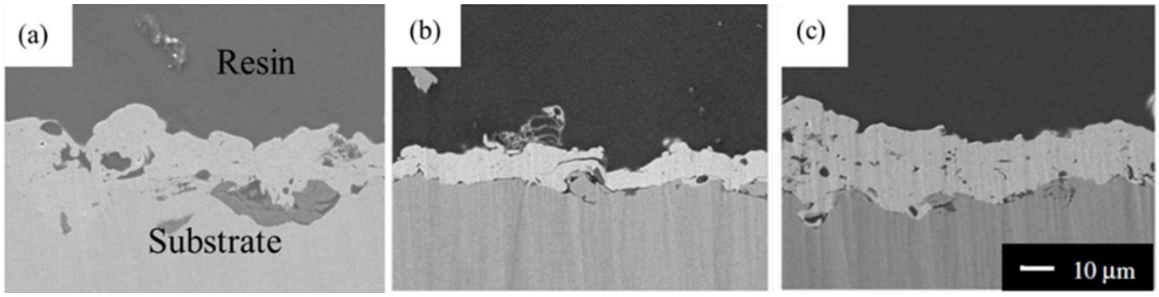

Figure 1-11 Cross-sectional SEM image of the as-synthesized films of (a) Y_2O_3, (b) Eu_2O_3, (c) Er_2O_3.

1.2.4 Application with thermal barrier coating (TBC)

The thermal barrier coatings were developed and utilized as early as the 1940s, and rapidly made them high performances. These have been the subject of vigorous research activities over the last decades, and a number of reviews are found in the recent literature on both aspects of materials and processes**[43-47]**. Thermal barrier coating(TBC) is a film that has the function of preventing necessary heat from being released or preventing heat from entering from outside**[48]**. Now day, it is widely used in thermal insulating components such as gas turbines blades in power plants, engines

in car and jet engines airplanes, etc.

1.2.4.1 TBC

As described in **1.2.2**, TBC is composed of a two-layer coating, the one of a bond-coat formed of a heat-resistant alloy and a top-coat formed of ceramics. The main purpose of this dual-layer system is to provide thermal insulation of the superalloy components, thus improving performance or lifetime**[49]**. The role of the bond coat has three points: (1) improve the bond between the substrate and the ceramic, (2) protect the substrate from high temperatures, and (3) relieve the thermal stress due to the difference in the thermal expansion coefficient between the substrate and the ceramic films. As a bond coat, an MCrAlY alloy (M: Ni, Co, etc.) having oxidation resistance is often used.

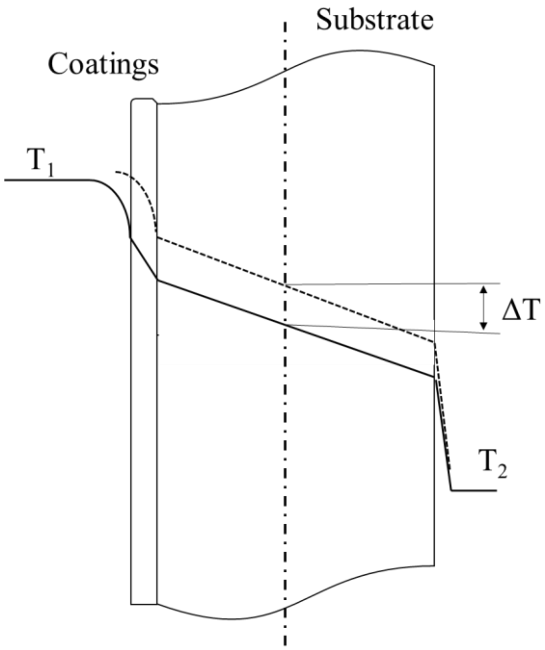

Figure 1-12 The theory of Thermal Barrier Coating (TBC).

Fig. 1-12 shows the theory of TBC. The temperature T_1 is on the high temperature side, and the temperature T_2 in on the low temperature side. In the steady state, if there

is TBC, the temperature drops significantly in the films as shown by the solid line. On the other hand, if there is no TBC that the temperature distribution is as shown by the dotted line. In Japanese Industrial Standard (JIS H7851), ΔT is defined as thermal insulating performance and is represented by a temperature difference between the front surface and the back surface of the top-coat.

The primary role of the top-coat is to protect the substrate and bond coat from high temperatures or thermal cycles. It is well known, the ability of a material to withstand a given temperature change depends on a complex combination of stable phase structure, thermal conductivity, and the overall geometry of that material. In the following, the authors will briefly introduce the influencing factors of thermal insulation capability.

A. Thermal conductivity

For the materials itself, thermal conductivity of standard plasma-sprayed 6 – 8 wt.% yttria partially stabilized zirconia coatings is typically 1.1- 1.4 W/(mK) **[35]**. Lowering this value, which is a key physical property of TBCs, could ensure further engine performance mainly by improving the combustion efficiency. In addition, the thermal conductivity of a porous ceramic coating depends on the intrinsic thermal conductivity of the bulk material related to its composition and structure, as well as on the architecture of the porous network. Therefore, to obtain low thermal conductivity films, it is much important to design the film structure, such as splat gap, porosity, and thickness, to improve the thermal transport time for thermal insulation capability.

B. Phase structure

As we all known, the phase structure of the coating determined its performance**[50]**. For example, D. Yan et al. reported that the monoclinic Er_2O_3 showed better radiation resistance**[51]**, and cubic phase Er_2O_3 exhibited higher hardness and elastic modulus than monoclinic and amorphous Er_2O_3**[52, 53]**. Furthermore, T.P. Wen et al. reported that the cubic Y_2O_3-MgO-ZrO_2 exhibited good thermal shock resistance than the monoclinic Y_2O_3-MgO-ZrO_2**[54]**. However, the effect of pure ZrO_2 resulted from phase transformation will reduce its thermal shock resistance, thus, it is necessary to use a stabilizer such as Y_2O_3 and MgO to stabilize ZrO_2. Therefore, it means that the effect

of improving the thermal performance(such as thermal insulation and thermal shock) can be achieved by the stabilized crystal structure.

Furthermore, from the above analysis that the temperature drops down in TBC with low thermal conductivity, as shown in **Fig.** 1-12. As mentioned above, if the thermal conductivity of TBC is even lower, the slope of the temperature drop with the increases, and effect of thermal insulation ΔT also increases. Therefore, it can be seen that the thermal insulation performance of TBC is affected by thermal conductivity. Simultaneously, based on the experimental and theoretical analysis, the empirical formula of the thermal conductivity k is as shown following Equation(1-2)

$$k \approx kc(1 - \beta P) \qquad 1\text{-}2$$

where kc is the thermal conductivity of the bulk material, β is the factors by means of the microstructure of substances and materials, P is the porosity. From this equation, it can be seen that as the porosity increases, the thermal conductivity decreases. In the following study, S. Sivakumar et al. synthesized $La_2Zr_2O_7$ films(porosity of 16% to 28 %) with different porosity using plasma spray and measured the thermal conductivity**[55]**. In the results, it was reported that the thermal conductivity decreased up to 25% when the porosity increased. As described above, it can be considered that the thermal conductivity of the TBC changes depending on the porosity.

1.2.4.2 Method of the sprayed TBC

Thermal spraying is a typical method for synthesizing TBC with top-coat **[56]**. In this system, the plasma spraying (PS) is often used for TBC**[57- 60]**. The origin of thermal spray coating is that molten or semi-molten particles impact with a base-material and flatten to be the disk-like shaped splats, which are formed by innumerable deposition. Therefore, based on the process that the kind of microstructure to form such as the pores, the cracks between splats and the gap between both splats are present in the coating. In general, it is said that air exists in the pores and the thermal conductivity is lower than that of a solid or density so that thermal insulation can be obtained. Furthermore, since thermal conduction is transmitted by phonons, it is also explained that thermal

insulation to be obtained by inhibiting the mean free path of phonons by pores. In the previous reports, we could observe the details of TBC with cross-sectional structures by thermal spray, as shown in **Fig.1-13**, as well as the result details listed in **Table 1-1**. It can be clearly seen that the reported TBC contains pores, the film thickness is about 150-400 μm, the porosity is about 7.0 – 20.0%, and ΔT 65 -133℃, respectively**[61-63]**. It can be considered that thermal insulation capability becomes good with increasing porosity. Those structural analyses of the TBCs which the pores have become the most important research project for understanding their properties.

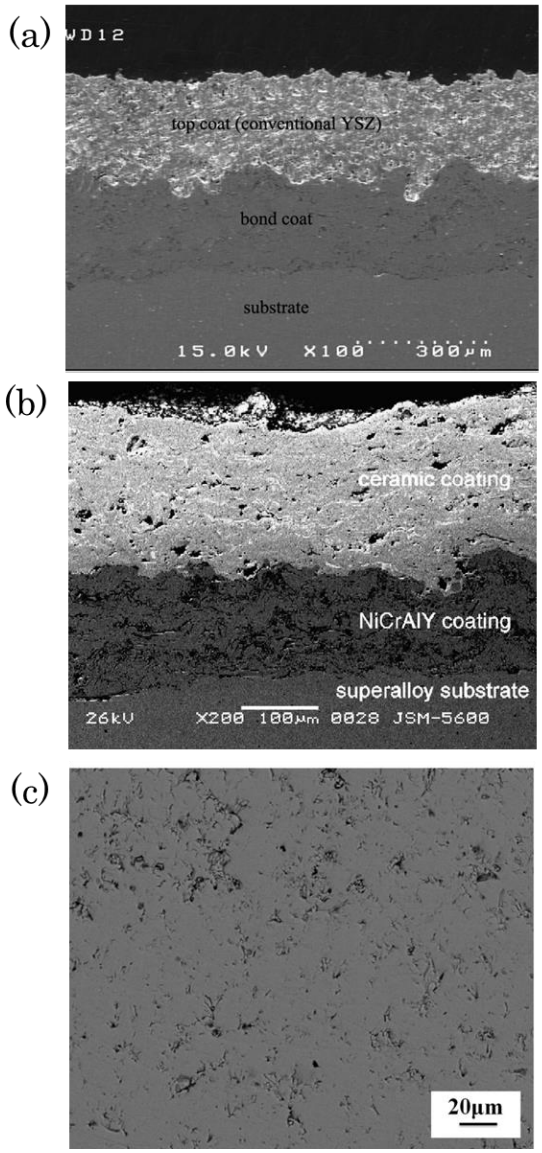

Figure 1-13 Cross-sectional structure of TBC deposited by thermal spraying method (a) The TBCs of the 7-8 wt % YSZ and bond-coat NiCrAlY, (b) The TBCs of the 8 wt % YSZ and bond-coat NiCrAlY, (c) 8 wt%YSZ.

Table 1-1 The values of TBCs by thermal spraying.

Spray method	Top-coat /Bond-coat / substrate	thickness(μm) / porosity(%)	ΔT(℃)
atmospheric plasma spray (APS)	7-8 wt%YSZ/ NiCrAlY / Ni	Approximately 430 / 20.37	133[61)]
APS	8 wt%YSZ / NiCrAlY / Ni	320 / 13.0	71[62)]
APS	8 wt%YSZ / Ni_3Al	150 / 6.83	65[63)]

The TBC made of YSZ/M(metal alloy) is formed by APS, however, the techniques are very expensive, due to the high powder output and large equipment. Therefore, a new method of spraying should be developed. Recently, yttrium oxide(Y_2O_3) films were synthesized from a metal-ethylenediaminetetraacetic(metal-EDTA) complex by the H_2-O_2 combustion flame. And it was also discussed the relationship between microstructures(porosity) of the metal-oxide film and the cooling agents, the various cross-section EDX images of films shown in **Fig.**1-14. In this study, the Y_2O_3 films synthesized using the rotation apparatus with cooling agents exhibited the high porosity of 22.8 - 36.4 %, respectively**[64]**. As conclusion, it means that the M-EDTA complex combined with the flame spray technique can be expected to synthesis the thermal barrier coating. However, a serious of research still need to investigate such as the microstructure evolution and the thermal performance (heat resistance, adhesion, thermal conductivity, and thermal insulation capability) of the coating in this method.

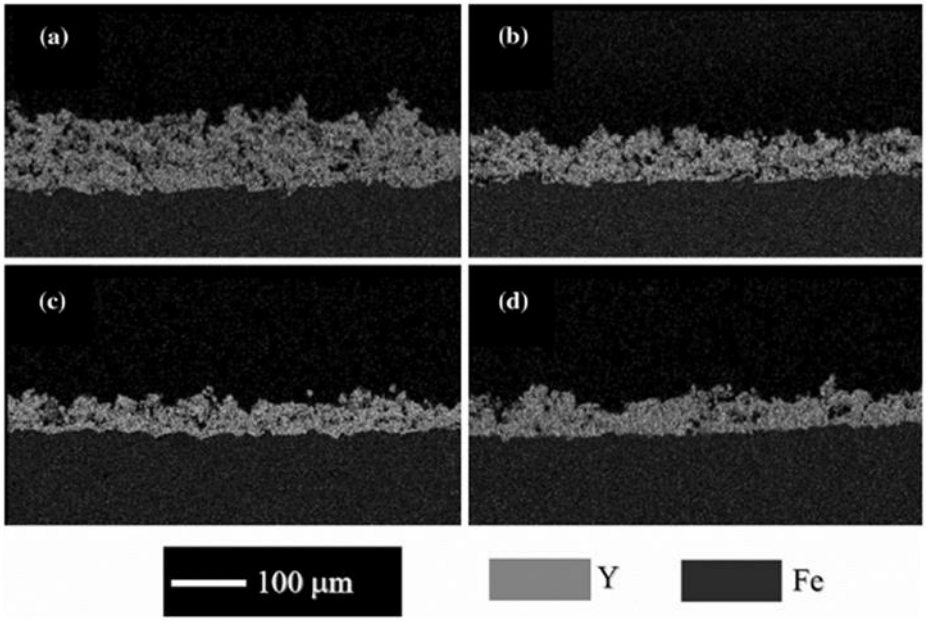

Figure 1-14 Deposited by flame spray in different conditions at rotation velocity of 45 rpm. (a) not cooling, (b) compressed air, (c) liquid nitrogen (d) purified water atomization.

1.3 Statement of problem

As described in **1.2.4**, the structure of thermal barrier coatings(TBCs) is a crucial way to understand the difference between properties and applications of these materials. In addition, Plasma-sprayed TBC systems are widely used in spray method. The coating is generally composed of the top layer and the bond layer, result in the necessary to multiple deposition processes. This system is a popular traditional approach to fabricate metallic coatings from melted metal particles **[65-69]**. However, the stable coating characteristic requires equivalent energy conversion, such as flame temperature, higher power conditions **[70,71]**. Therefore, development of another approach of spray technology with lower energy consumption, fast, and convenient is particularly important, such as chelate flame spray(CFS).

The CFS process exhibits some advantages over plasma spray and HVOF even for high melting oxide-ceramic such as metal-ethylenediaminetetraacetic acid(EDTA) that decomposes at approximately 673K**[72]**. This is the reason why the EDTA can be chosen as the raw materials precursor for flame spray system. Recently, metal oxides were synthesized from metal-EDTA complexes using a flame spraying technique**[73-75]**. This method is not only being successfully synthesized dense metal oxide films with a cross-sectional porosity of 3 % and thickness of 20 μm but also being synthesized porous structure metal oxide films with a cross-sectional porosity of 36 % and thickness of 36 μm by CFS method**[64, 72]**. Therefore, this method is suitable and qualified for the synthesis of the TBCs. However, the coating with thermal insulation capability must require sufficient porous structure with a large number of areas(or layers), so the resulting coating must require stable thickness such as 300 μm. Thus, to obtain stable thickness with porous coating, it is possible for this method to design composition precisely of the parameter in the spray process. In contrast, it is difficult to determine the appropriate morphology of splats. Therefore, we should accurately grasp the following points: (1) regulation of the speed of decomposition and oxidation of raw materials in flame. (2) condensation rate and morphology of each molten particle

deposited on the substrate. Both the (1) and (2) points are important to synthesize TBCs, which will focus on a discussion in this study.

On the other hand, the thermal insulation capability evaluation schemes of TBC are quite important during select them to use in some industrial fields, such as internal combustion engine wall, jet engines air-planes, etc. it has also undergone a development process, that from summing predecessors and summarizing data to performing thermal insulation capability test method and analysis standard. However, those methods are difficult to combine with the actual application conditions, and to get properties closer to the TBC. In order to overcome these limitations, the harsh test environment(high temperature thermal cycle) and tools to simulate the combustion chamber with the Flash theory will be discussed in the study.

1.4 Objectives of this study

The objective of this study is to realize synthesis of the film with the high porosity to provide thermal insulation capability on an Al alloy substrate by the chelate flame spray(CFS) method. In this method, to design TBC on the Al alloy substrate with a low melting point, to change each parameter and try to design the splat shape on the substrate in the state of the flying molten particles. Based on the above analysis, the condition with a small number of disk-like shaped splats is set, and the metal oxide thick coating with the various kind of porosity is deposited. Furthermore, the thermal insulation capability of the thick coating will be evaluated by the various test methods. This study is divided into four issues, as follows:

- To synthesize the metal-oxide film on the stainless steel substrates, and to investigate the relationship between the films and the carrier gas types(air, N_2, and O_2). Furthermore, to investigate the relationship between the films and the various kinds of the substrates (quartz glass, stainless steel, Al-Mg alloy), and to compare changes structural of the films.

- To change the parameters of the CFS method to design the splat shape on Al alloy substrate in the state of flying particles, and then, to evaluate the heat resistance and adhesion of the coating through the thermal cycling and the annealing test.
- To set spray conditions based on the splat morphology, and the metal oxide thick coating to synthesize on an Al alloy substrate, and to investigate the coating structure.
- To test and evaluate the thermal insulation capability and the thermal conductivity of the deposited metal oxide thick coating.

1.5 Outline of this thesis

This thesis is composed of nine chapters presenting the detail as follows:

Chapter 1 "*General Introduction*" describes the overview, literature survey the statement of problems and objectives of this research.

Chapter 2 "*Synthesis of metal oxide films using the chelate flame method with the different carrier gas*" describes the difference of the carrier gas plays an important role in determining the thickness and porosity of the metal oxide coating.

Chapter 3 "*cross-sectional structure of metal oxide films using the chelate flame method and the analysis*", to investigate the cross-sectional structures of the Er_2O_3 coatings, on substrates with different common materials, i.e., quartz glass, stainless steel (SUS304), and aluminum-magnesium alloy (A5052). The result shows the design of a ceramic film microstructure that reduces cracks in the ceramic film.

Chapter 4 "*Effect of deposition parameters on metal-oxide splat morphology in chelate flame spray process* ", using the chelate flame spraying method combined with multi-dimensional modes are proposed to control the morphology of splats.

Chapter 5 "*Heat-shock properties in Y_2O_3 films synthesized on the stainless-steel substrate*", through characterizing the film thickness, surface cracks, and microstructure, the results show that the Y_2O_3 films have high thermal-shock resistance with the cyclic thermal test, and are suitable for use as thermal barrier coatings

Chapter 6 "*Heat resistance and adhesion properties of Y_2O_3 films on an aluminum alloy substrate by atmospheric annealing test*", describes the Y_2O_3 coatings exhibits a strong adhesion with the aluminum alloy substrate, and it is provided that elemental diffusion in the joining was not observed from cross-sectional EDX analysis.

Chapter 7 "*Thermal insulation capability of Y_2O_3 and Er_2O_3 coatings on an aluminum alloy substrate*", describes the thermal insulation capacity of the Y_2O_3, Er2O3 coatings synthesized by the cooling substrate with liquid nitrogen method is improved.

Chapter 8"*A new method development for thermal analysis of metal-oxide coating*", Developed a new test method with thermal insulation capability and thermal conductivity of coating using the flame-spray experiment.

Finally, Chapter 9 "*General Conclusions*" describes conclusions of this work.

References

[1] Japan Thermal Spray Society(JTSS), *Thermal Spray Technology an introduction*, *chapter 1*, 1 (2006).

[2] J.A. Brogan, ‘‘Processing and Property Relationships of Thermally Sprayed Polymer Systems,’’ Ph.D. Thesis, State University of New York, 1996.

[3] Y. Bao, D.T. Gawne, D. Vesely, and M.J. Bevis, *Trans. Inst. Metal Finish.*, **72**(pt 3), 110-113 (1994).

[4] T. Twardowski, M. Reilly, and R. Knight, *ASM International*, Singapore, 369-373 (2001).

[5] A. Nakamura, N. Nambu, K. Kawahara, S. Ohshio and H. Saitoh, *Journal of the Ceramic Society of Japan*, **111**(2), 142-146 (2003).

[6] H. Saitoh, K. Kawahara, S. Ohshio, A. Nakamura, and N. Nambu, *Journal of the Ceramic Society of Japan*, **110**(9), 874-876 (2002).

[7] A. Nakamura, R. Satoh, S. Ohshio, N. Nambu, and H. Saitoh, *Japanese Journal of Applied Physics*, **41**, 3033-3038 (2002).

[8] J.H. Yang, S.L. Xiao, C. Yuyong, L.J. Xu, X.P. Wang, D.D. Zhang, M.G. Li, *Materials Science and Engineering: A*, **761**, 2019.

[9] J.F. Shackelford, Introduction to Materials Science for Engineers(Seventh Edition), 70-104.

[10] N.P. Padture, G. Maurice, E.H. Jordan, *Science*, **296**, 280-284 (2002).

[11] J.H. Perepezko, The hotter the engine, the better, *Science*, **326**,1068-1069(2009).

[12] J.R. Davis ed, “Handbook of Thermal Spray Technology”, *ASM Thermal Spray Society*, 3(2004).

[13] Handbook of Thermal Spraying. *Japan Thermal Spray Society*, 39 (2010).

[14] H. Herman, Plasma-sprayed coatings, *Sci. Am.*, **259** (3), 112-117 (1988).

[15] S. Sampath, et al., *Mater. Sci. Eng. A*, **272** (1), 181-188 (1999).

[16] R. Dhiman, A.G. McDonald, S. Chandra, Predicting splat morphology in a thermal spray process, *Surf. Coat. Technol.*, **201** (18), 7789–7801(2007).

[17] J.R. Davis, et al., Handbook of Thermal Spray Technology, *ASM Int.*, 2004.

[18] R.B. Heimann, *Plasma Spray Coating*, Wiley-VCH, 2008.

[19] A.B. Elshalakany, T.A. Osman, W. Hoziefa, A.V. Escuder, V.Amigó, *Journal of Materials Research and Technology*, **8**(5), 4253-4263 (2019).

[20] Kevin M. Hubbard, Brent F. Espinoza, *Thin Solid Films*, **366**(1-2), 175-180 (2000).

[21] Y. Tsukuda, *Japan Sci. and Tech. Agency*, **8**, 1106-1108(1979).

[22] S. Li, C. Langlade, S. Fayeulle, D. Treheux, *Surf. Coat. Technol.*, 100-101 (1998).

[23] J.M. Guilemany, J.M. Miguel, S.Vizcaino, C. Lorenzana, J. Deigado, J. Sanchez, *Surf. Coat. Technol.*, **152**, 207-213 (2002).

[24] M. Prystay, P. Gougeon, C. Moreau, *J. Therm. Spray Technol.*, **10**, 67–75 (2001).

[25] J.G. Legoux, B. Arsenault, L. Leblanc, V. Bouyer, and C. Moreau, JTTEE5 **11**, 86-94.

[26] X.C. Zhang, B.S. Xu, Y.X. Wu, F.Z. Xuan, S.T. Tu, *Applied Surface Science*, **254**, 3879–3889 (2008).

[27] W.C. Li, S.H. Yang, C.Y. Su, S.C. Huang, I.C. Hsu, M.S. Leu, *Surf. Coat. Technol.*, **133-134**, 54-60 (2000).

[28] Y.J. Wang, E.K. Hao, Y.L. An, G.L. Hou, X.Q. Zhao, H.D. Zhou, *Applied Surface Science*, **525** (2020).

[29] L.L. Silverira, A.G.M. Pukasiewicz, D.J.M. de Aguiar, A.J. Zara, S. Björklund, *Surf. Coat. Technol.*, **374**, 910-922 (2019).

[30] J. Fincke, W. Swank, R. Bewley, D. Haggard, M. Gevelber, D. Wroblewski *Surf. Coat. Technol.*, **146–147**, 537 (2001).

[31] S. Siegmann, M. Margadant, A. Zagorski, M. Arana-Antelo C. Moreau, B. Marple (Eds.), *ASM International*, OH, USA, 1591 (2003).

[32] S. Tailor, A. Modi, S.C. Modi, *Ceramic International*, **44,** 6762-6768(2018).

[33] H. Jamali, R. Mozafarinia, R. Shoja Razavi, R. Ahmadi-Pidani, M.R. Loghman-Estarki, *Curr. Nanosci.*, **8**, 402–409 (2012).

[34] X. Chen, Y. Zhao, L. Gu, B. Zou, Y. Wang, X. Cao, *Corr. Sci.*, **53**, 2335–2343 (2011).

[35] S. Tailor, R. Upadhyaya, S.Y. Manjunath, A.V. Dub, A. Modi, S.C. Modi, *Ceramics International*, **44**, 2691-2699 (2018).

[36] S.A. Tsipas, I.O. Golosnoy, *J. Eur. Ceram. Soc.*, **31**, 2923–2929 (2011).

[37] S. Das, S. Datta, D. Basu, G.C. Das, *Ceram. Int.*, **35**,1403–1406 (2009).

[38] A. Nakamura, N. Nambu, K. Kawahara, S. OhShio and H. Saitoh, *Journal of the Ceramic Society of Japan*, **111**(2), 142-146 (2003).

[39] G. Schwarzenbach, *Helv. Chim. Acta.*, **35**, 2344(1952).

[40] Komats K, Shirai T, Toyama A, Iseki T, Xin DY, Costa T, et al., *Surf. Coat. Technol.*, **325**, 89–97(2017).

[41] H. Akasaka, M. Ohto, Y. Hasebe, A. Nakamura, S. Ohshio, H. Saitoh, *Surf. Coat. Technol.*, **205**, 3877–3880 (2011).

[42] K. Komatsu, T. Sekiya, A. Toyama, Y. Hasebe, A. Nakamura, M. Noguchi, Y. Li, S. Ohshio, H. Akasaka, H. Muramatsu, H. Saitoh, *J. Therm. Spray Technol.*, **23**, 833–838(2014).

[43] M. Belmonte, *Adv. Eng. Mat.*,**8** (8), 693-703 (2006).

[44] D.R. Clarke, S.R. Phillpot, *Materials Today*, **8** (6), 22 (2005).

[45] D. Zhu, R.A. Miller, *Int. J. Appl. Ceram. Technol*., **1** (1), 86-94 (2004).

[46] C.G. Levi, Curr. Opin. *Solid State Mater. Sci.*, **8**, 77 (2004).

[47] U. Schulz, C. Leyens, K. Fritscher, M. Peters, B. Saruhan-Brings, O.Lavigne, J.-M. Dorvaux, M. Poulain, R. Mévrel, M. Caliez, Aerosp, *Sci. Technol.*, **7**, 73 (2003).

[48] M. Magome, Thermal Spraying Manual(JIS usage series), *Japanese Standards Association*, 170-173 (1998).

[49] F.O. Soechting, *J. Therm. Spray Technol.*, **8** (4), 505 (1999).

[50] Y.Y. Wu, D. He, S. Li, X.P. Liu, S.M. Wang, L.J. Jiang, *Int. J. Hydrog. Energy*, **39**, 20305-20312 (2014).

[51] M. Tang, P. Lu, J.A. Valdez, K.E. Sickafus, *J. Appl. Phys.*, **99**, Article 063514-1-7 (2006).

[52] X.L. Li, P. Wu, H. Qiu, S. Chen, B.B. Song, *Acta Phys. Sin.*, **60**, Article 036805-1-7 (2011).

[53] X.L. Li, P. Wu, H. Qiu, S. Chen, B.B. Song, *Thin Solid Films*, **520**, 2316-2320 (2012).

[54] T.P. Wen, L. Yuan, T. Liu, Q.Y. Sun, E.D. Jin, C. Tian, J.K. Yu, *Ceram. Int.*, 2020.

[55] S.Sivakumar et al., *Surf. Coat. Technol.*, **326**, 173-182 (2017).

[56] Y. Kobayashi et al., *Thermophysical properties*, **29**, 13-18 (2015).

[57] R. Srinivasan, J.M. Merrilea, *Surf. Coat. Technol.*, **160**, 187 (2002).

[58] A.G. Evans, D.R. Mumm, J.W. Hutchinson, G.H. Meier, F.S. Pettit, *Prog. Mater. Sci.*, **46**, 505 (2001).

[59] I. Gurrappa, *J. Mater. Sci. Lett.*, **17,** 1267 (1998).

[60] D. Schwingel, R. Taylor, T. Haubld, J. Wigren, C. Gualco, *Surf. Coat. Technol.*, **108–109**, 99 (1998).

[61] Reza Ghasemi et al., *Ceramics International*, **43**, 8556-8563 (2017).

[62] W.B. Gong et al., *Surf. Coat. Technol.*, **201**, 3109-3115 (2006).

[63] Dan Chen et al., *Ceramics International*, **43**, 4324-4329 (2017).

[64] K. Komatsu, A. Toyama, T. Sekiya, T. Shirai, A. Nakamura, I. Toda, S. Ohshio, H. Muramatsu, H. Saitoh, *J. Therm. Spray Technol.*, **26**, 195-202 (2017).

[65] L. Pawlowski, The Science and Engineering of Thermal Spray Coatings, *John Wiley & Sons*, 2008.

[66] B.J. Sparks, E.F. Hoff, L. Xiong, J.T. Goetz, D.L. Patton, *ACS Appl. Mater. Interfaces*, **5**, 1811–1817 (2013).

[67] X. Chen, Y. Gong, X. Suo, J. Huang, Y. Liu, H. Li, *Appl. Surf. Sci.,* **356**, 639–644 (2015).

[68] C. Zhang, Y. Wu, L. Liu, *Appl. Phys. Lett.*, **101**, 121603 (2012).

[69] X. Chen, Y. Gong, D. Li, H. Li, *Colloids Surf. A Physico. Chem. Eng. Asp.*, **492**, 19–25 (2016).

[70] H. Liao, E. Beche, F. Berger, and C. Coddet, On the microstructures of thermally sprayed ‘‘PEEK’’ polymer, Thermal Spray: Meeting the Challenges of

the 21st Century, C. Coddet Ed., May 25-29, ASM International, Nice, France, 25-30 (1998).

[71] G. Bolelli, B. Bonferroni, J. Laurila, L. Lusvarghi, A. Milanti, K. Niemi, P. Vuoristo, *Wear*, **276–277**, 29–47 (2012).

[72] K. Komatsu, T. Shirai, A. Toyama, T. Iseki, D.Y. Xin, T. Costa, A. Nakamura, Y. Li, S. Ohshio, H. Muramatsu, H. Saitoh, *Surf. Coat. Tech*., **325**, 89–97 (2017).

[73] H. Akasaka, M. Ohto, Y. Hasebe, A. Nakamura, S. Ohshio, H. Saitoh, *Surf. Coat. Technol.*, **205**, 3877–3880 (2011).

[74] K. Komatsu, T. Tsuchiya, Y. Hasebe, T. Sekiya, Y. Hasebe, A. Toyama, A. Nakamura, H. Akasaka, and H. Saitoh, *J. Therm. Spray Tech.*, **23**, 885-889 (2014).

[75] K. Komatsu, T. Sekiya, A. Toyama, A. Nakamura, I. Toda, S. Ohshio, H. Muramatsu, H. Saitoh, *Int. J. Chem. Nuc. Metal. Mater. Eng.*, **8**, 1322–1326 (2014).

Chapter 2

Synthesis of metal oxide films using chelate flame method with different carrier gas

Abstract

In this study, we synthesized dense metal oxide films from a metal ethylenediaminetetraacetic acid complex using a flame sprayer. Erbium oxide (Er_2O_3), Yttrium oxide (Y_2O_3) films were synthesized on stainless steel substrates using N_2, air (O_2 + N_2), or O_2 as the carrier gas and an H_2-O_2 mixture as the combustion gas. When O_2 was used as the carrier gas, 9.9–20.5 μ m thick oxide layers were deposited on the stainless steel substrate. The cross-sectional porosities of the films were 3–5%. In contrast, oxide layers with 8.1–15.8 μ m thickness were synthesized on stainless steel substrates when N_2 and air were used as carrier gases. The cross-sectional porosities of these films were 16.1–23.4%. These results indicated that the carrier gas plays an important role in determining the thickness and porosity of the resulting film.

2.1 Introduction

Thermal spraying is a surface-modification technique commonly used to deposit thermal barrier coatings, which are effective in improving the durability and anticorrosion (chemical resistance) and heat-shock properties of structural materials [1-3]. Thermal spraying techniques have numerous advantages, including a high deposition rate and the ability to deposit coatings on large areas on an industrial scale. For example, the chemical resistance of a material plays a critical role in determining the stability of the material in corrosive environments at temperatures lower than 550 °C [4]. Some of the commercial materials that exhibit high chemical resistances are zinc, aluminum, and zinc-aluminum alloys [5]. Four approaches are defined in the Japanese Industrial Standard H8250-1998 for fabricating films with high chemical resistances. These are (1) corrosion-prevention spraying to prevent the corrosion of the raw metal, (2) anti-rust spraying to prevent the formation of rust in steel, (3) corrosion-resistant spraying to protect high-resistance materials from corrosive environments, and (4) anti-high-temperature oxidation spraying to prevent the high-temperature oxidation of materials in severe environments. Ideally, the corrosion resistant films deposited on materials to be protected should not exhibit cracks. However, a few cracks are always formed on industrially coated films. In such cases, a sealing treatment must be performed on the films to fill these cracks [6,7]. Thus, corrosion-resistant films with higher densities are desirable.

The temperature and velocity of the in-flight particles are the key factors for obtaining films with a dense morphology. For examples, plasma spraying (PS) and high-velocity oxygen fuel (HVOF) coating techniques are suitable for synthesizing dense films by thermal spraying [8-10]. In the PS technique, the in-flight particles have temperatures of 10,000–15,000 K, and their velocity reaches 100–200 m/s. In contrast, for the HVOF coating technique, these parameters are 2300–2900 K and 550–800 m/s. The films synthesized by the HVOF coating technique are denser than

those obtained by the PS technique. Thus, it seems likely that the velocity of in-flight particles determines the density of the deposited films. Recently, metal oxides were synthesized from metal ethylenediaminetetraacetic acid (EDTA) complexes using a flame spraying technique [11-13]. The metal-EDTA complex was placed in a feed unit and transported by flowing N_2 gas to the spray gun. As this technique allows for high deposition rates, films with thicknesses of several tens of micrometers could be obtained. The cross-sectional porosities of these films were 6–15%. This deposition technique involves two processes: a chemical reaction and physical collisions. During the chemical reaction, the metal-EDTA complex decomposes and oxidizes to form metal oxide particles. In the second process, these particles collide with the substrate and form a thick metal oxide layer. During the synthesis process, the supply of oxygen atoms to the metal-EDTA complex is crucial for ensuring that the chemical reaction takes place.

In this study, dense Er_2O_3 and Y_2O_3 films were synthesized from EDTA·Er·H and EDTA·Y·H complexes through flame spraying; the process involved a chemical reaction of the complex. The Er_2O_3 and Y_2O_3 films were deposited on stainless steel substrates using various gases as the carrier gas and a mixture of H_2-O_2 as the combustion gas. The carrier gases used were nitrogen, commercial air (nitrogen and oxygen), and oxygen. First, we determined the effects of the carrier gas used on the decomposition of the complexes. Next, we examined the effects of the carrier gas on the microstructures of the deposited films. Furthermore, the effects of the carrier gas on the characteristics of the deposited films were also studied.

2.2 Materials and methods

As mentioned above, the EDTA complex powders, EDTA·Er·H and EDTA·Y·H (Chubu Chelest Co., Ltd.) were used for synthesizing the Er_2O_3 and Y_2O_3 films. A conventional flame-spraying apparatus consisting of a feed unit (5MPE, Sulzer Metco) and a spray gun (6P-II, Sulzer Metco) was used to perform the reactive spraying. This apparatus is used commercially for the deposition of metal or self-fluxing alloy films

with an acetylene or hydrogen flame. As has been stated above, we employed different carrier gases to determine the effects on the carrier gas on the properties of the deposited films. The EDTA·Er·H and EDTA·Y·H complexes were placed in the feed unit and transported by O_2, air (O_2 + N_2), or N_2 to the spray gun. The carrier-gas flow rate was set at 7.1 L/min. Next, we changed the flow rate of 14.2 L/min to investigate the effect of O_2 carrier gas composition for dense Er_2O_3 film. In addition, we changed the flow rates of powder of 10 g/min and 20 g/min to investigate the effect of particle temperature and velocity for structure of Er_2O_3 film. Furthermore, we employed the EDTA·Er·H complex with different diameters (or raw materials size). Including the unscreened cuboid EDTA·Er·H powder, five raw material particle sizes, i.e., unscreened, 75-μm-on, 53-μm-on (75-53 μm), 45-μm-on (53 – 45 μm), and 45-μm-pass, with average particle sizes of 67.89, 82.37, 63.37, 54.71, and 42.26 μm, respectively, were selected for the experiments. In this study, we selected hydrogen gas as the fuel. A mixture of H_2 and O_2, with the respective flow rates being 32.6 and 43.0 L/min, was used as the flame gas. The EDTA·Er·H and EDTA·Y·H powders were introduced to the flame and made to react with oxygen, which resulted in the thermal decomposition of EDTA. The particles of the resulting product were then sprayed onto the SUS304 stainless steel substrate(30 × 50 × 1 mm^3), which had been previously blasted with #60 alumina grit (purity of 99.7%, particle size of 212–250 μm, Fuji Manufacturing Co., Ltd.), resulting in the deposition of a metal oxide film. The distance between the spray gun and the substrate was 150 mm. The deposition duration was 4–10 s. The gun traverse rate was 50 mm/s. Next, the spray nozzle was moved in a longitudinal direction, and deposition was performed again for approximately 6 s for each area without preheating the substrate. The yield percentage (i.e., deposition efficiency) of this technique was approximately 60%, as determined by actual measurements.

The thermogravimetric (TG)/differential thermal analysis (DTA) profiles of the EDTA·Er·H complex in the O_2 + N_2 and N_2 atmospheres were obtained using a thermogravimetric analyzer (ThermoPlus 2, Rigaku). X-ray diffraction (XRD) analysis (M03XHF22, MAC Science) were performed using Cu *K*α radiation to observe the

crystal structures of the films. The remaining organic matter in the films was evaluated by Fourier transform infrared spectroscopy (FT-IR, IMPACT-410: Nicolet) by the attenuated total reflection method. The surface and cross-sectional morphologies of the films were observed using field-emission scanning electron microscopy (FE-SEM) (JSM-6700F, JEOL). The constituent elements in the films and their distributions were estimated through energy-dispersive X-ray spectroscopy (EDX) combined with FESEM. The thicknesses and porosities of the films were determined by analyzing SEM images of the films using the software Image J. First, the thickness is average thickness of 20 transverse sections in the whole image. The standard deviation of thickness was also estimated. Next, the porosity was estimated from area ratio of film in the image. The temperatures and velocities of the particles in the combustion gas were measured with an infrared camera (Accura Spray-G3: Tecnar). It working at the particles temperature of 900 ℃ or more, and velocities measured in 5 – 1200 m/s, then a signal is generated when the particle passes through the slit, and the velocity of the particle can be calculated form pass time and distance. First, a combustion flame was formed by mixing hydrogen and oxygen. Next, the camera was set vertically at a distance of 20 cm from the center of the flame plume. The temperature and velocity of the in-flight particles were measured at nozzle-substrate distances of 110, 130, 150, and 170 mm.

2.3 Results and discussion

We first investigated the thermal decomposition behaviors of the EDTA·Er·H complex in the different atmospheres. Exothermic peak means combustion and decomposition reaction processes in the EDTA complex. In contrast, endothermic peak means vaporization reaction process of the complex. The TG/DTA profile of the complex in air (O_2 + N_2) is shown in **Fig.** 2-1. An exothermic peak can be seen at approximately 365 °C. This peak indicated that the oxidative decomposition of the EDTA·Er·H complex occurred in the O_2 + N_2 atmosphere. The TG/ DTA profile of the complex in the N_2 is shown in **Fig.** 2-2. An endothermic peak can be

seen at approximately 400 °C. The peak indicated that had decomposition of EDTA·Er·H occurred in the N_2 atmosphere. These TG/DTA profiles were confirmed in the EDTA·Y·H complex [12]. Thus, the thermal pyrolysis behavior of EDTA·Er·H was depended on the reaction environment.

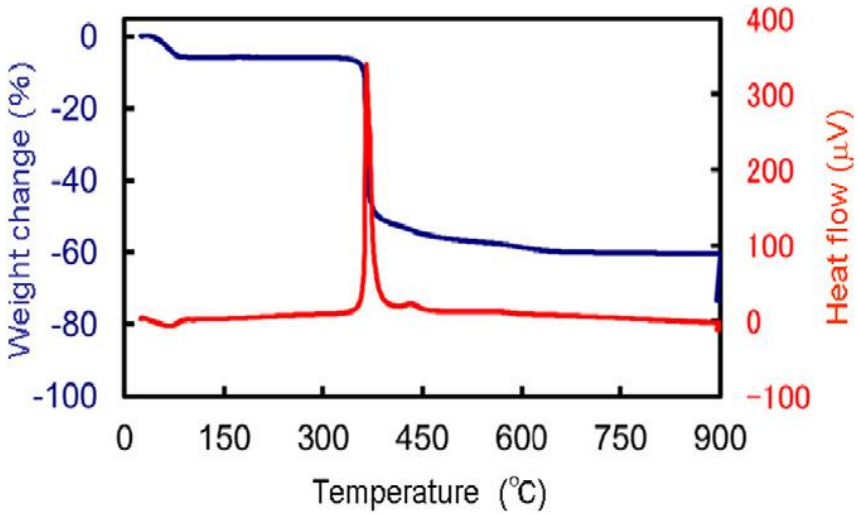

Figure 2-1 TG/DTA curves for the EDTA·Er·H complex with air (O_2 + N_2) as the carrier gas.

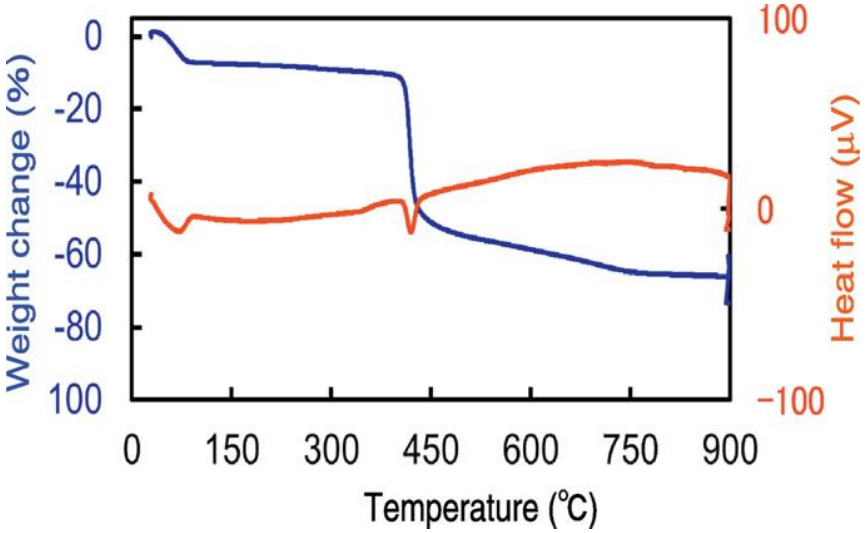

Figure 2-2 TG/DTA curves for the EDTA·Er·H complex with N_2 as the carrier gas.

Fig. 2-3 shows photographs of the experimental setup. The commercial flame-spraying apparatus and the H_2-O_2 flame can be seen. When O_2 was used as the

carrier gas, a brighter flame was obtained that when N_2 was used as the carrier gas. Photographs of the films deposited with the EDTA·Er·H using the different carrier gases are shown in **Fig.** 2-4. The color of the blasted SUS substrate was light gray. After the deposition, it changed to pink, which was also the color of Er_2O_3. This confirmed the presence of the films on the SUS substrates. Further, there was no difference in the colors of the films deposited using the different carrier gases. These phenomena were confirmed in with the EDTA·Y·H. The color of Y_2O_3 was white.

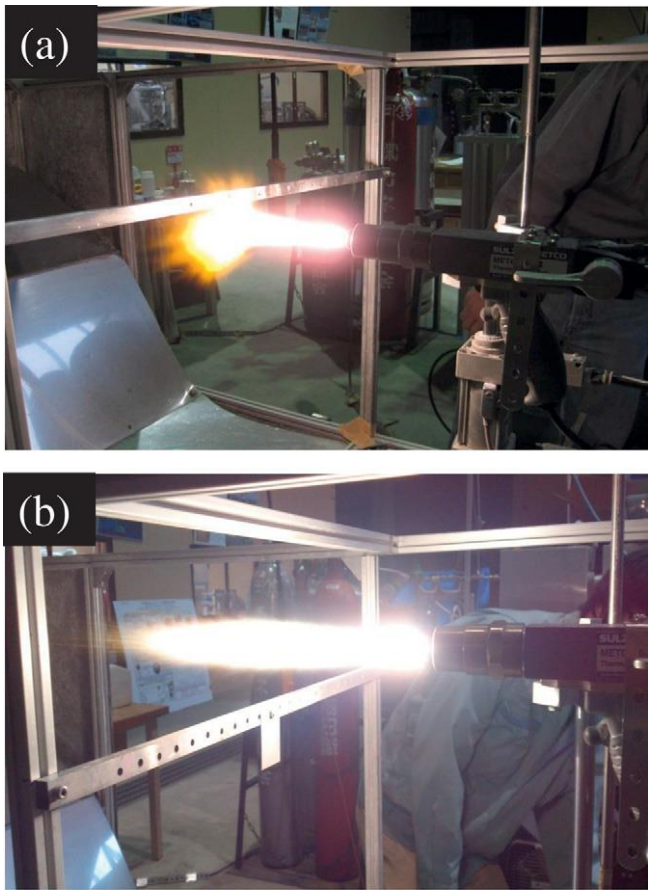

Figure 2-3 Photograph of the experimental setup, which included a commercial flame- spraying apparatus and an H_2-O_2 flame and used (a) O_2 as the carrier gas, and (b) N_2 as the carrier gas.

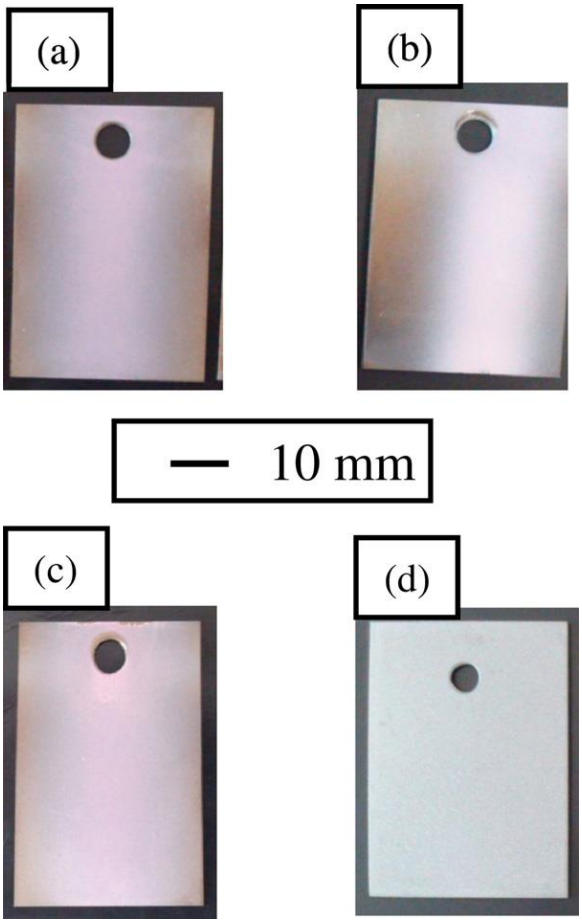

Figure 2-4 Photographs of the films synthesized with EDTA·Er·H on SUS304 substrates from the EDTA·Er·H complex using (a) O_2 as the carrier gas, (b) air (O_2 + N_2) as the carrier gas, and (c) N_2 as the carrier gas. The photograph in (d) is of a blasted SUS substrate.

To determine the crystalline structures of the deposited films, XRD analyses were performed. **Fig.** 2-5 shows the XRD profiles of the three films deposited on the SUS304 substrates. The peaks in their XRD profiles could be assigned using the International Centre for Diffraction Data (ICDD) cards as references. In **Fig.** 2-5 (1), all the films deposited using EDTA·Er·H exhibited cubic and monoclinic Er_2O_3 crystalline phases (ICDD Card Nos. 00-008-0050 and 01-077-6226, respectively).

Er_2O_3 exhibits three structural polymorphisms: cubic, monoclinic, and hexagonal, which are commonly known as C-, B-, and A-type structures, respectively [14]. In **Fig.** 2-5b, the cubic Y_2O_3 crystalline phase (ICDD Card No. 00-041-1105) were confirmed in all films with EDTA·Y·H. Thus, the choice of the carrier gas had no effect on the crystal structures of the deposited films.

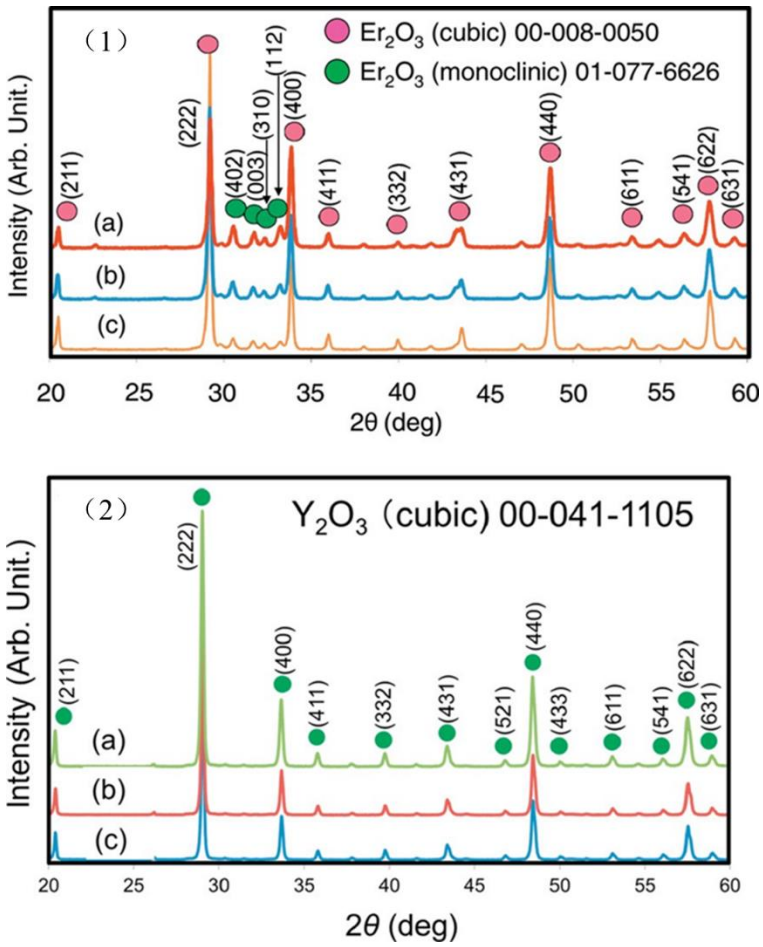

Figure 2-5 (1) XRD profiles for 2θ of 10–80° for the films synthesized with EDTA·Er·H using (a) O_2 as the carrier gas, (b) air (O_2 + N_2) as the carrier gas, and (c) N_2 as the carrier gas. (2) XRD profiles for 2θ of 10–80° for the films synthesized with EDTA·Y·H using (a) O_2 as the carrier gas, (b) air (O_2 + N_2) as the carrier gas, and (c) N_2 as the carrier gas.

The chemical compositions of the obtained films were assumed to be an indicator of

the degree of decomposition of the EDTA complex. The organic constituents were determined by FT-IR. **Fig.** 2-6 shows the FT-IR spectra of the Er_2O_3 films obtained using the different carrier gases. The FT-IR spectrum of the EDTA·Er·H complex is shown for comparison. The EDTA·Er·H complex exhibited peaks at 1440 and 1500– 1700 cm^{-1}, which could be assigned to the carbonyl group. Further, the broad peaks at 2900 and 3300 cm^{-1} in the FT-IR spectrum indicated the presence of carbon-hydrogen bonds and the hydroxyl group [11]. In contrast, the Er_2O_3 films did not exhibit any FT-IR peaks, confirming that they did not contain many organic constituents. These results were also confirmed in the FT-IR spectra of the Y_2O_3 films obtained using the different carrier gases. These results indicated that the decomposition and oxidation of the EDTA complex occurred in all the carrier gases.

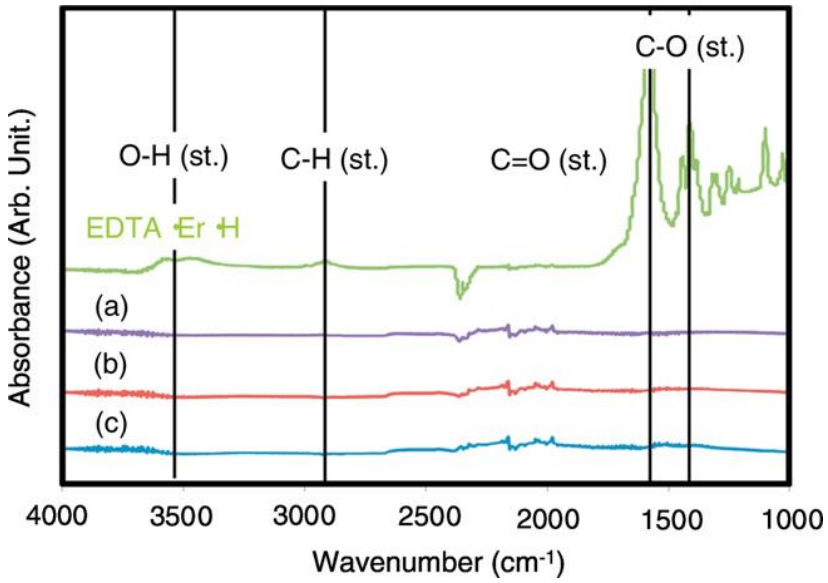

Figure 2-6 FT-IR spectra of the metal oxide films synthesized with EDTA·Er·H using (a) O_2 as the carrier gas, (b) air (O_2 + N_2) as the carrier gas, and (c) as the N_2 carrier gas.

Fig. 2-7 shows surface SEM images of the three Er_2O_3 films. When N_2 was used as the carrier gas, a number of spherical (i.e., not flattened) particles with sizes of approximately 5–10 μm was also observed. Further, even though large pores were present, flattened particles were also seen in the Er_2O_3 film synthesized using O_2 + N_2

as the carrier gas. Finally, a large number of flattened particles were seen in the Er_2O_3 film deposited using O_2 as the carrier gas. Particles with the highest degree of flatness (or splatting) were observed in the Er_2O_3 film obtained using O_2 as the carrier gas, for which flat Er_2O_3 particles were deposited (Fig. 2-7a). In contrast, when N_2 was used as the carrier gas, the degree of flatness was the lowest, with spherical particles also being observed (Fig. 2-7c). Thus, the choice of the carrier gas caused differences in the surface morphologies of the deposited Er_2O_3 films. In general, the microstructures of the films deposited by the PS and HVOF coating techniques vary with the combustion gas used and its composition [15,16]. This is because these parameters determine the flame's temperature and the density of the plasma in the reaction system. These, in turn, determine the temperature and velocity of the in-flight particles. **Fig.** 2-8 shows surface SEM images of the three Y_2O_3 films. The highest degree of flatness was observed in the Y_2O_3 with O_2 as the carrier gas. In contrast, the lowest degree of flatness was observed in the Y_2O_3 with N_2 as the carrier gas. Thus, the chemical reaction processes (decomposition and oxidation) of the EDTA complex can be varied by changing the carrier gas used.

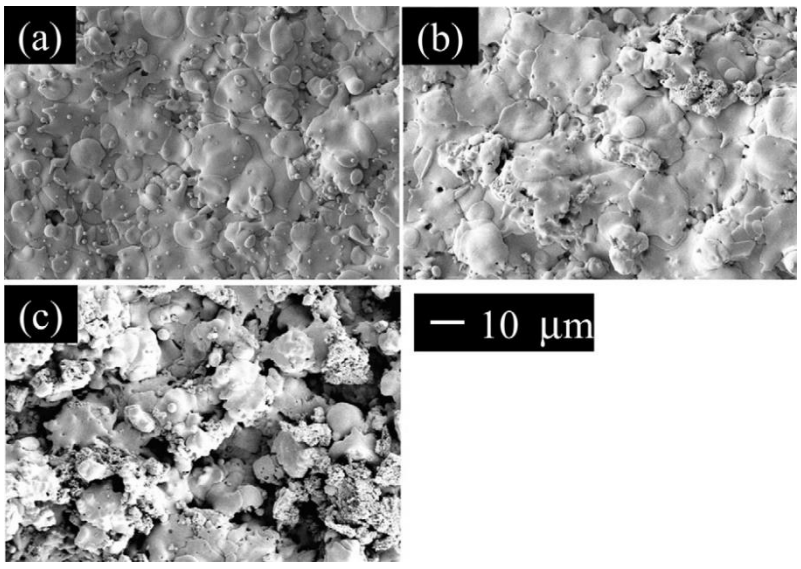

Figure 2-7 Surface SEM images of the films synthesized with EDTA·Er·H using (a) O_2 as the carrier gas, (b) air (O_2 + N_2) as the carrier gas, and (c) N_2 as the carrier gas.

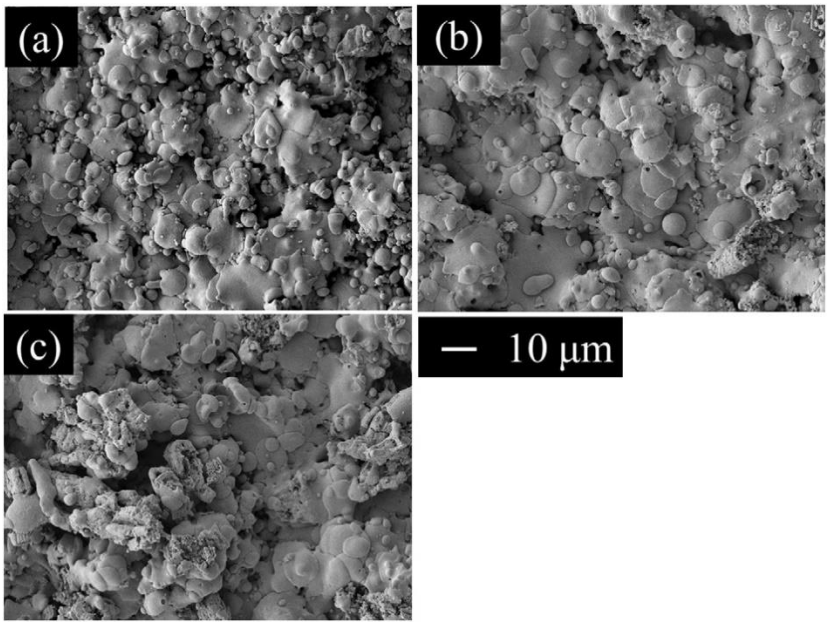

Figure 2-8 Surface SEM images of the films synthesized with EDTA·Y·H using (a) O_2 as the carrier gas, (b) air (O_2 + N_2) as the carrier gas, and (c) N_2 as the carrier gas.

Next, the cross-sectional morphologies and elemental distributions of the films were determined using SEM and EDX analyses. **Fig.** 2-9 shows cross-sectional SEM images for the Er_2O_3 films obtained using the various carrier gases. The films consisted of several Er_2O_3 layers with thicknesses on the micron scale. Large pores with diameters of approximately 2–5 μm were observed in the Er_2O_3 film deposited using N_2 as the carrier gas. Furthermore, it was found that the number of pores in the Er_2O_3 film synthesized using O_2 + N_2 as the carrier gas was lower. Finally, the film deposited using O_2 as the carrier gas had the fewest pore. **Table** 2-1 shows the thicknesses and cross-sectional porosities of the Er_2O_3 films; The porosities were determined by analyzing SEM images of the films. This analysis method can be used to determine the numbers of both open and closed pores [17]. The Er_2O_3 film obtained using N_2 as the carrier gas had an average thickness of 15.8 μm and a cross-sectional porosity of 23.4%. Next, in the case of O_2 + N_2 as the carrier gas, these values were 22.1 μm and 5.9%, respectively. When O_2 was

the carrier gas, the resulting film was the densest, having a porosity of 3.0% and an average thickness of 20.5 μm. In addition, we investigated the effect of O_2 carrier gas composition for dense Er_2O_3 film. **Fig.** 2-10 shows cross-sectional SEM images for the Er_2O_3 films obtained using different flow rates of powder. The Er_2O_3 film obtained using 10 g/min powder as the flow rates had a cross-sectional porosity of 8.3%. In contrast, in the case of 20 g/min powder as the flow rates, the value was 17.3%. The porosity values have variation, the Er_2O_3 film was densified by the flow rates of powder with 10g/min. **Fig.** 2-11 shows cross-sectional SEM images for the Er_2O_3 films obtained using different O_2 carrier gas composition. The Er_2O_3 film obtained using 14.2 L/min O_2 as the carrier gas had a cross-sectional porosity of 6.6%. In contrast, in the case of 7.1 L/min O_2 as the carrier gas, the value was 3.0%. Although the porosity values have variation, the Er_2O_3 film was densified by O_2 carrier gas. To further investigate the microstructures in Er_2O_3 films deposited on substrates with various sizes of EDTA·Er·H particles, cross-sectional SEM images, as shown in **Figs**.2-12 (a) to (e), were analyzed. The microstructures of the pores and gaps can be clearly seen in films. Large pores were observed in the Er_2O_3 film deposited using the raw material size unscreened with the porosity of 5.9 %. And in the case of 75 μm on as the raw materials, the value was 3.1%. Furthermore, it was found that the almost no change of pores in the Er_2O_3 films synthesized using the raw materials 75 – 53 μm and 53-45 μm/ 45 μm pass with the porosity of 4.6 %, 4.2%, 4.4 %, respectively. **Fig.** 2-13(a) shows cross-sectional SEM images for the Y_2O_3 films obtained using the various carrier gases. **Fig.**2-13(b) show cross-sectional EDX mapping images of the particles synthesized from the EDTA·Y·H complex. The areas of bright contrast indicate yttrium. Dense Y_2O_3 film layer was also observed in case of O_2 carrier gas. **Table** 2-2 shows the thicknesses and cross-sectional porosities of the Y_2O_3 films. From **Tables** 2-1 and 2-2, the Er_2O_3 films were thicker than the Y_2O_3 ones. The Er_2O_3 have a higher true density compared to Y_2O_3. The Er_2O_3 particle would have higher adhesion efficiency compared to that of Y_2O_3, because of higher collision energy of the in-flight particle. These results indicated that O_2 is the most suited

carrier gas for fabricating dense metal oxide layers.

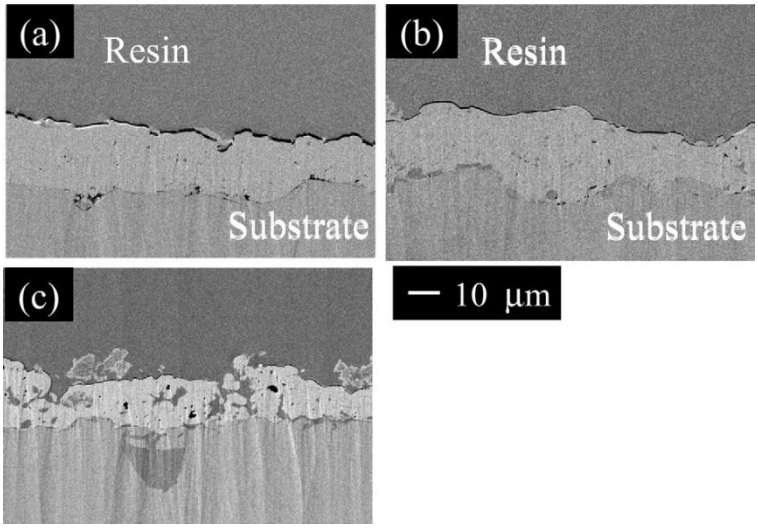

Figure 2-9 Cross-sectional SEM images of the films synthesized with EDTA·Er·H using (a) O_2 as the carrier gas, (b) air (O_2 + N_2) as the carrier gas, and (c) N_2 as the carrier gas.

Table 2-1 Thicknesses and cross-sectional porosities of the films synthesized on the SUS304 substrates with EDTA·Er·H complex using the different carrier gases. SD is standard deviation.

Carrier gas	Film thickness (SD) (μm)	Cross-sectional porosity (%)
N_2	8.1(4.2)	16.1
O_2 + N_2 (Air)	9.5(5.9)	12.0
O_2	9.9(3.1)	5.0

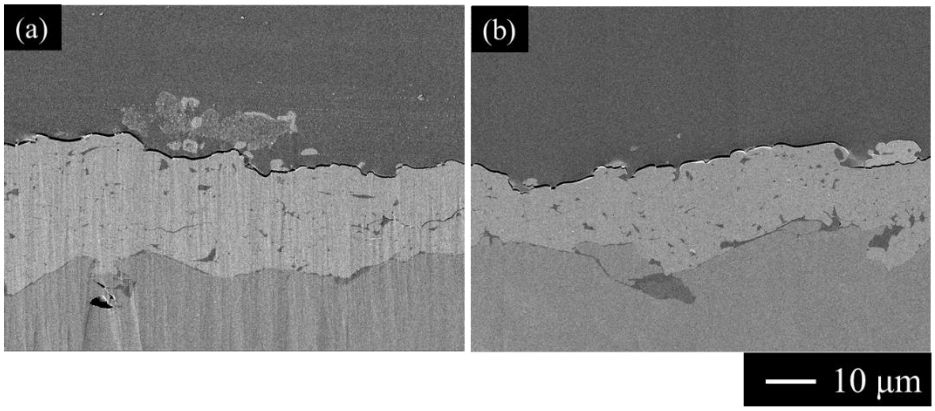

Figure 2-10 Cross-sectional SEM images of the films synthesized with EDTA·Er·H using different flow rates of powder. (a) 10 g/min (b) 20 g/min.

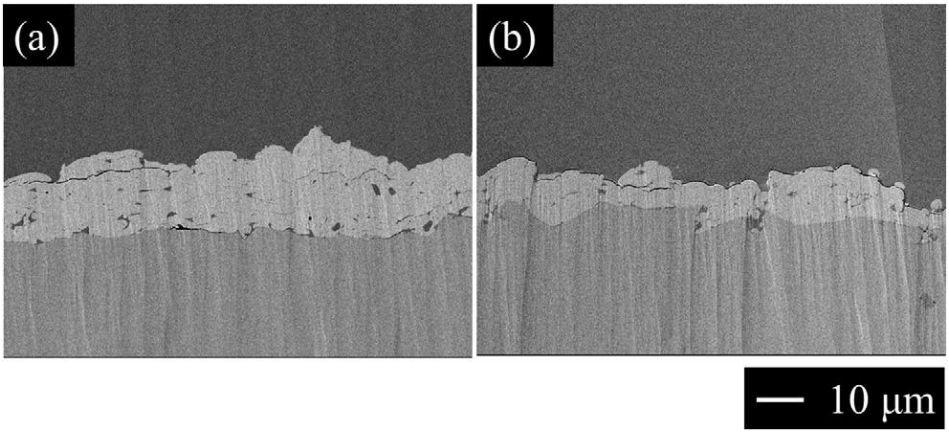

Figure 2-11 Cross-sectional SEM images of the films synthesized with EDTA·Er·H using different O_2 carrier gas composition. (a) 7.1 L/min (b) 14.2 L/min.

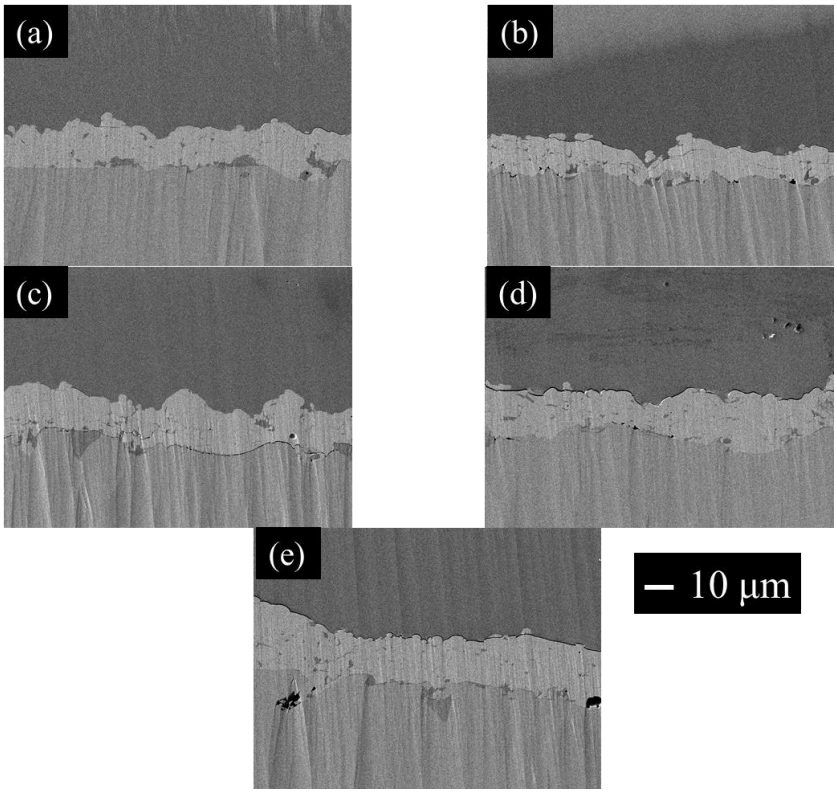

Figure 2-12 Cross-sectional SEM images of the films synthesized with EDTA·Er·H using different raw material size. (a) unscreened (b) 45 μm pass (c)53 – 45 μm (d) 75 – 53 μm (e) 75 μm on.

Table 2-2 Thicknesses and cross-sectional porosities of the films synthesized on the SUS304 substrates with EDTA·Y·H complex using the different carrier gases. SD is standard deviation.

Carrier gas	Film thickness(SD) (μm)	Cross-sectional porosity (%)
N_2	15.8(4.7)	23.4
$O_2 + N_2$ (Air)	22.1(6.0)	5.9
O_2	20.5(3.6)	3.0

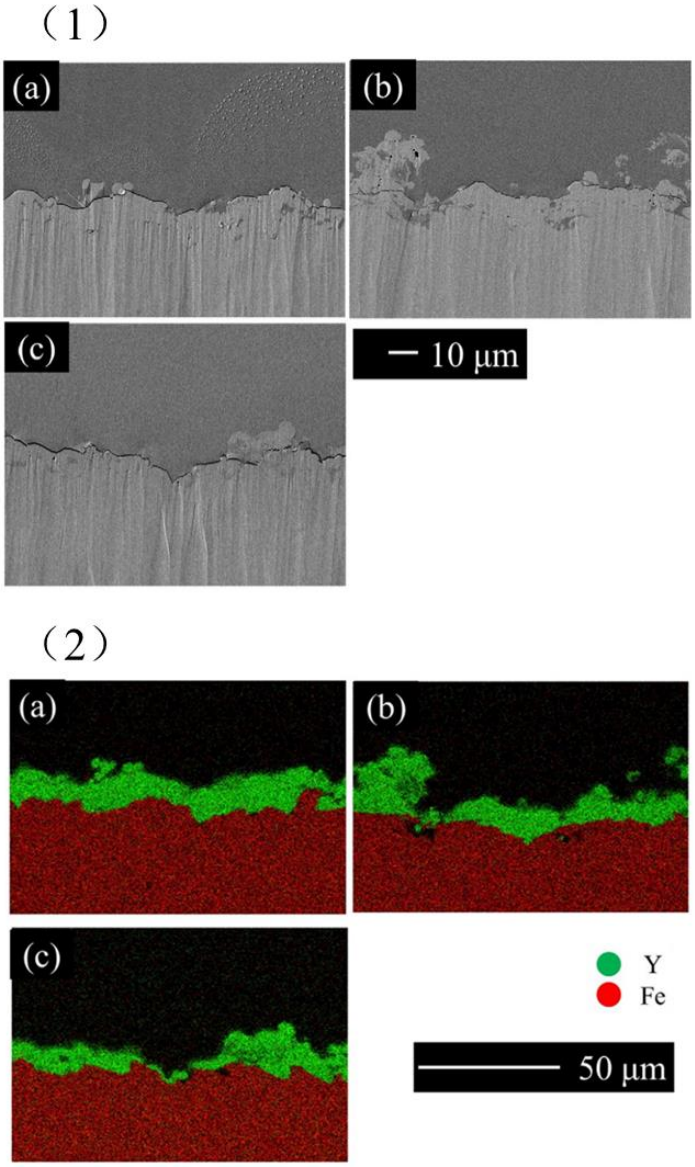

Figure 2-13 (1) Cross-sectional SEM images of the films synthesized with EDTA·Y·H using (a) O_2 as the carrier gas, (b) air (O_2 + N_2) as the carrier gas, and (c) N_2 as the carrier gas. (2) Cross-sectional EDX images of the films synthesized from the EDTA·Y·H using (a) O_2 as the carrier gas, (b) air (O_2 + N_2) as the carrier gas, and (c) N_2 as the carrier gas. The areas of bright contrast indicate yttrium.

With respect to thermal spraying, knowing the temperature and velocity of the in-flight particles is useful for determining their collision behavior, which affects the crystalline structure and morphology of the deposited film [18,19]. **Figs.** 2-14 and 2-15 show the temperature and velocity of the in-flight particles with EDTA·Er·H for each carrier gas as a function of the nozzle-substrate distance. At a nozzle-substrate distance of 150 mm, the temperatures were 2290 °C in N_2 gas, 2300 °C in $O_2 + N_2$, and 2400 °C in O_2 gas. Further, the velocities of the particles were 99 m/s in N_2 gas, 96 m/s in $O_2 + N_2$ gas, and 90 m/s in O_2 gas. The maximum temperature was in N_2 gas at a distance of 150 mm. However, when the distance was changed to 110 mm, the highest temperature was obtained in $O_2 + N_2$ and O_2 gas. The velocity in N_2 gas was the highest at a distance of 150 mm and decreased gradually as the distance was decreased. In contrast, the velocities in $O_2 + N_2$ and O_2 gas decreased with an increase in the nozzle-substrate distance. **Figs.** 2-16 and 2-17 show the temperature and velocity of the in-flight particles with EDTA·Y·H for each carrier gas as a function of the nozzle-substrate distance. At a nozzle-substrate distance of 150 mm, the temperatures were 2330 °C in N_2 gas, 2330 °C in $O_2 + N_2$, and 2570 °C in O_2 gas. Further, the velocities of the particles were 100 m/s in N_2 gas, 99 m/s in $O_2 + N_2$ gas, and 100 m/s in O_2 gas. The maximum temperature was in O_2 gas at a distance of 150 mm. The velocity in O_2 gas was the highest at a distance of 110 mm and decreased gradually as the distance was decreased. These phenomena were also observed in $O_2 + N_2$ gas, and in N_2 gas.

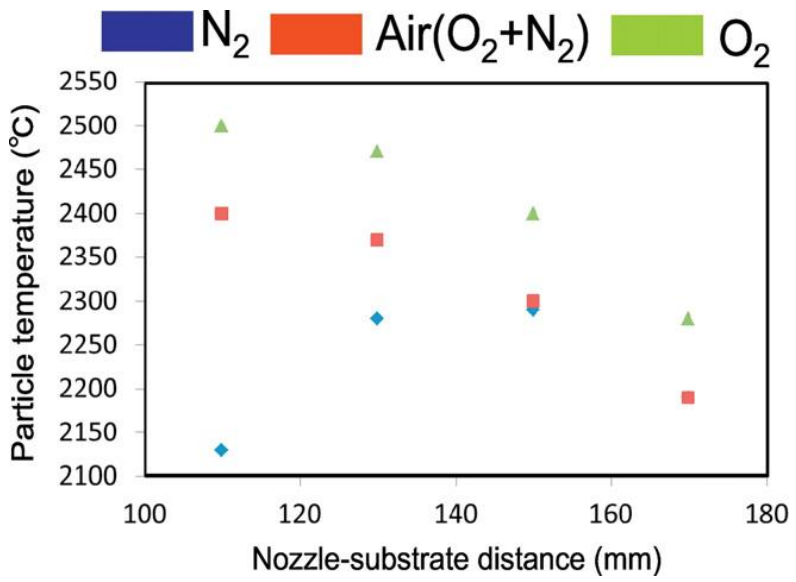

Figure 2-14 Temperatures of the in-flight particles with EDTA·Er·H propelled in the H_2-O_2 combustion gas mixture at different nozzle-substrate distances while using (a) O_2 as the carrier gas, (b) air (O_2 + N_2) as the carrier gas, and (c) N_2 as the carrier gas.

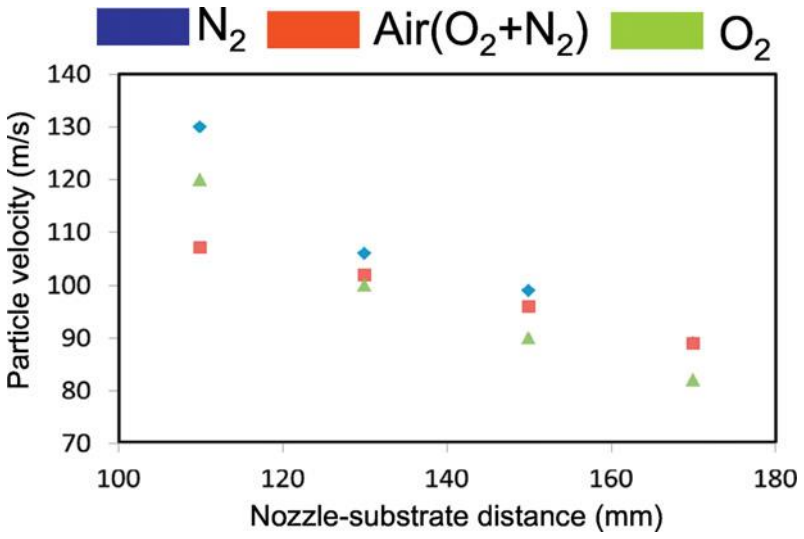

Figure 2-15 Velocities of the in-flight particles with EDTA·Er·H propelled in the H_2-O_2 combustion gas mixture at different nozzle-substrate distances while using (a) O_2 as the carrier gas, (b) air (O_2 + N_2) as the carrier gas, and (c) N_2 as the carrier gas.

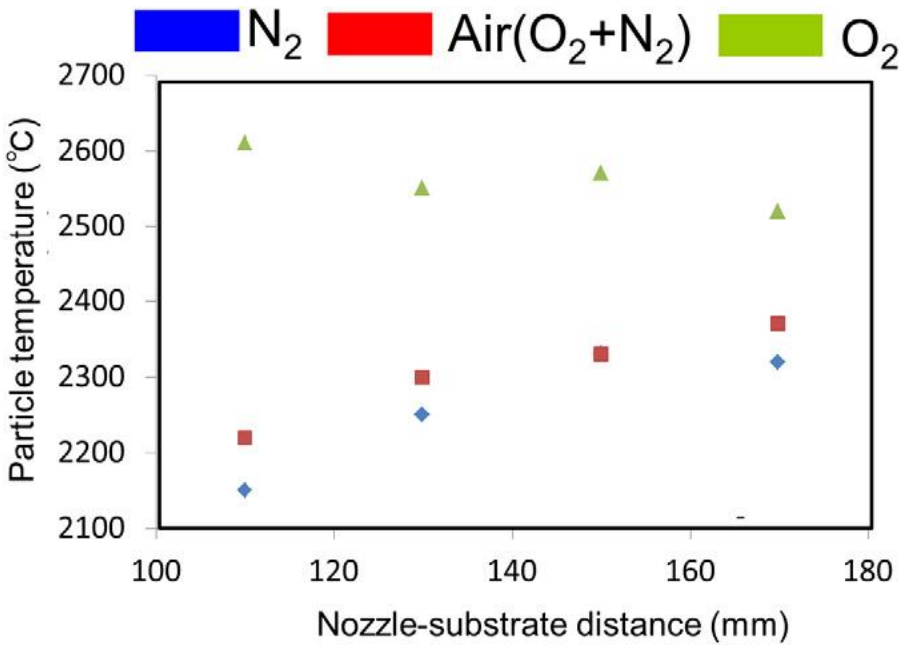

Figure 2-16 Temperatures of the in-flight particles with EDTA·Y·H propelled in the H_2-O_2 combustion gas mixture at different nozzle-substrate distances while using (a) O_2 as the carrier gas, (b) air (O_2 + N_2) as the carrier gas, and (c) N_2 as the carrier gas.

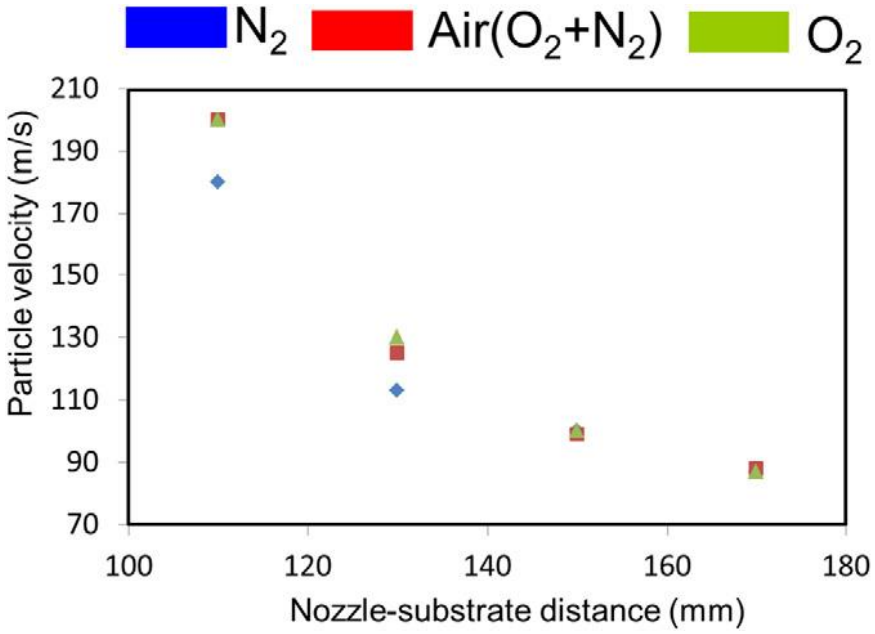

Figure 2-17 Velocities of the in-flight particles with EDTA·Y·H propelled in the H_2-O_2 combustion gas mixture at different nozzle-substrate distances while using (a) O_2 as the carrier gas, (b) air (O_2 + N_2) as the carrier gas, and (c) N_2 as the carrier gas.

On the basis of these results, the effects of the carrier gas on the properties of the deposited films are discussed below. The cross-sectional porosities of Er_2O_3 films were 23.4%, 5.9%, and 3.0% when carrier gas was N_2, O_2 + N_2, and O_2, respectively. The porosities of Y_2O_3 films were 16.1%, 12.0%, and 5.0% when carrier gas was N_2, O_2 + N_2, and O_2, respectively. These results indicated that the carrier gas used has an effect on the decomposition and oxidation of the complex. The chemical reaction of EDTA·M·H (M: metal species) can be represented by Eq. (1). In Eq. (1), For an instance, EDTA·Er·H reacts with O_2 to form a Er_2O_3 film.

$$2EDTA \cdot Er \cdot H + 24O_2 \rightarrow Er_2O_3 + 20CO_2 + 13H_2O + 4NO_2$$

Hence, Eq. (1) confirms that, by varying the carrier gas used, the properties of the deposited film can be changed. Denser metal oxide films can be formed by supplying higher amounts of thermal energy to the metal oxide particles. Bae et al. reported that a higher thermal energy resulted in films with lower porosities [20]. In this study, the temperature of the in-flight metal oxide particle obtained from the decomposition and oxidation of EDTA·Er·H complex were 2400 °C in O_2, 2300 °C in O_2 + N_2 and 2290 °C in N_2. The thermal energy of the particles can be calculated as shown below [21]:

$$Q = mcT$$

where Q is the thermal energy (J), m is the weight of sample (kg), c is the specific heat capacity of the material (kJ/(kg K)), and *T* is the temperature (K).

This equation suggests that higher the temperature, higher would be the thermal energy. **Table** 2-3, 2-4, 2-5 shows temperature and velocity of in-flight particles in each metal oxide film synthesis with EDTA·Er·H and EDTA·Y·H complexes, spray conditions with different flow rates and size of EDTA·Er·H powder, as well as the cross-sectional porosities of deposited films. Nozzle-substrate distance was 150 mm. Higher the temperature of in-flight particles, denser microstructure

was formed. The reaction process that takes place when the metal-EDTA complex is introduced into flame. First, the precursor melts and thermally decomposes, resulting in the production of the gases CO_2, H_2O, and NO_2. Then, metal ions are released from the chelating ligand. Next, the metal oxide particles are formed and undergo rapid cooling. These cooled particles then solidify rapidly [22,23]. Hence, the densest metal oxide film was obtained using O_2 as the carrier gas because the temperature of the in-flight particles was the highest in this case. The precursor melting rate in H_2-O_2 flame would be higher in O_2 than that of in N_2. The obtained TG/DTA profiles indicated that the choice of the carrier gas determined the decomposition temperature of EDTA·Er·H, which decreased to 365 °C in O_2 + N_2 from 420 °C in N_2. In addition, the TG/DTA profiles suggested that an exothermic reaction occurred in O_2 + N_2 while an endothermic reaction took place in the N_2 atmosphere. In the O_2 + N_2 atmosphere, the exothermic reaction involving EDTA·Er·H occurred owing to the oxygen present. In contrast, the endothermic peak indicated that a self-decomposition reaction occurred in the N_2 atmosphere. Hence, the use of O_2 as the carrier gas resulted in the synthesis of dense films with improved microstructures.

Table 2-3 Temperature and velocity of in-flight particles in each metal oxide film synthesis with EDTA·Er·H and EDTA·Y·H complexes, and cross-sectional porosities of deposited films. Nozzle-substrate distance was 150 mm.

Material	Carrier gas	In-flight particles temperature (℃)	In-flight particles velocity (m/s)	Porosity(%)
EDTA・Er・H	N_2	2290	99	23.4
	Air	2300	96	5.9
	O_2	2400	90	3.0
EDTA・Y・H	N_2	2330	100	16.1
	Air	2330	99	12.0
	O_2	2570	100	5.0

Table 2-4 Temperature and velocity of in-flight particles in each metal oxide film synthesis with different flow rates of EDTA·Er·H complexes in the carrier gas O_2, and cross-sectional porosities of deposited films. Nozzle-substrate distance was 150 mm.

Conditions		Particle temperature(℃)	Particle velocity(m/s)	Porosity(%)
Flow rates of powder	10 g/min	2610	115	8.3
	20 g/min	2400	86	17.3

Table 2-5 Temperature and velocity of in-flight particles in each metal oxide film synthesis with various size of EDTA·Er·H complexes in the carrier gas O_2, and cross-sectional porosities of deposited films. Nozzle-substrate distance was 150 mm.

Conditions		Particle temperature (℃)	Particle Velocity (m/s)	Porosity (%)
Raw material size	Unscreened	2530	87	5.9
	45 μm pass	2660	104	4.4
	53 ～ 45 μm	2660	97	4.2
	75 ～ 53 μm	2580	94	4.6
	75 μm on	2590	90	3.1

2.4 Conclusions

Dense metal oxide films with a cross-sectional porosity of 3% were synthesized from a metal-EDTA complex using a commercial flame spraying apparatus. O_2, air (O_2 + N_2), and N_2 were used as the carrier gases, in order to investigate the effects of the carrier gas on the properties of the deposited films. By varying the carrier gas, the cross-sectional porosity of the deposited metal oxide films could be varied from 3.0% to 23.4%. It was found that O_2 was the better carrier gas for fabricating dense metal oxide films at low costs by the synthesis.

References

[1] C. Zhou, Q. Zhang, Y. Li, Thermal shock behavior of nanostructured and microstructured thermal barrier coatings on a Fe-based alloy, *Surf. Coat. Technol.,* **163**, 51–59 (2010).

[2] H. Pokhmurska, B. Wielage, T. Lampke, T. Grund, M. Student, N. Chervinska, Post-treatment of thermal spray coatings on magnesium, *Surf. Coat. Technol.,* **202**, 4515–4524 (2008).

[3] R.S. Lima, B.R. Marple, Nanostructured YSZ thermal barrier coatings engineered to counteract sintering effects, *Mater. Sci. Eng. A,* **485**, 182–193 (2008).

[4] D. Toma, W. Brandl, G. Marginean, Wear and corrosion behaviour of thermally sprayed cermet coatings, *Surf. Coat. Technol.,* **138**, 149–158 (2001).

[5] A. Pardo, P. Casajus, M. Mohedano, A.E. Coy, F. Viejo, B. Torres, E. Matykina, Corrosion protection of Mg/Al alloys by thermal sprayed aluminum coatings, *Appl. Surf. Sci.,* **255**, 6968–6977 (2009).

[6] S. Liscano, L. Gil, M.H. Staia, Effect of sealing treatment on the corrosion resistance of thermal-sprayed ceramic coatings, *Surf. Coat. Technol.,* **188–189**, 135–139 (2004).

[7] S. Ahmaniemi, P. Vuoristo, T. Mantyla, Improved sealing treatments for thick thermal barrier coatings, *Surf. Coat. Technol.,* **151–152**, 412–417 (2002).

[8] J.-G. Legoux, B. Arsenault, L. Leblanc, V. Bouyer, C. Moreau, Evaluation of four high velocity thermal spray guns using WC-10% Co-4% Cr cermets, *J. Therm. Spray Technol.,* **11**, 86–94 (2002).

[9] M. Prystay, P. Gougeon, C. Moreau, Structure of plasma-sprayed zirconia coatings tailored by controlling the temperature and velocity of the sprayed particles, *J. Therm. Spray Technol.,* **10**, 67–75 (2001).

[10] M.P. Planche, H. Liao, B. Normand, C. Codde, Relationships between NiCrBSi particle characteristics and corresponding coating properties using

different thermal spraying processes, *Surf. Coat. Technol.,* **200**, 2465–2473 (2005).

[11] H. Akasaka, M. Ohto, Y. Hasebe, A. Nakamura, S. Ohshio, H. Saitoh, Yttria coating synthesized by reactive flame spray process using Y-EDTA complex, *Surf. Coat. Technol.,* **205**, 3877–3880 (2011).

[12] K. Komatsu, T. Sekiya, A. Toyama, Y. Hasebe, A. Nakamura, M. Noguchi, Y. Li, S. Ohshio, H. Akasaka, H. Muramatsu, H. Saitoh, Deposition of metal oxide films from metal–EDTA complexes by flame spray technique, *J. Therm. Spray Technol.,* **23**, 833–838 (2014).

[13] K. Komatsu, T. Sekiya, A. Toyama, A. Nakamura, I. Toda, S. Ohshio, H. Muramatsu, H. Saitoh, Synthesis of Y2O3 films by spray coating with milled EDTA·Y·H complexes, *Int. J. Chem. Nuc. Metal. Mater. Eng.,* **8**, 1322–1326 (2014).

[14] P.P. Bose, M.K. Gupta, R. Mittal, S. Rols, S.N. Achary, A.K. Tyagi, S.L. Chaplot, Phase transitions and thermodynamic properties of yttria, Y2O3: inelastic neutron scatter- ing shell model and first-principles calculations, *Phys. Rev. B,* **84**, 094301 (2011).

[15] E. Lugscheider, C. Herbst, L. Zhao, Parameter studies on high-velocity oxy-fuel spraying of MCrAlY coatings, *Surf. Coat. Technol.,* **108–109**, 16–23 (1998).

[16] B. Pateyron, M.-F. Eichinger, G. Delluc, P. Fauchais, Thermodynamic and transport properties of Ar-H~ and Ar-He plasma gases used for spraying at atmospheric pressure: properties of the mixtures, *Plasma Chem. Plasma Process.,* **12**, 421–448 (1992).

[17] S. Deshpande, A. Kulkarni, S. Sampath, H. Herman, Application of image analysis for characterization of porosity in thermal spray coatings and correlation with small angle neutron scattering, *Surf. Coat. Technol.,* **187**, 6–16 (2004).

[18] F. Tarasi, M. Medraj, A. Dolatabadi, J. Oberste-Berghaus, C. Moreau, Effective parameters in axial injection suspension plasma spray process of

alumina-zirconia ceramics, *J. Therm. Spray Technol.,* **19**,787–795 (2010).

[19] A. Aguero, F. Camon, J. Garcıa de Blas, J.C. del Hoyo, R. Muelas, A. Santaballa, S. Ulargui, P. Valles, Phase formation and transformation in alumina/YSZ nanocomposite coating deposited by suspension plasma spray process, *J. Therm. Spray Technol.,* **20**, 1292–1309 (2011).

[20] G. Bae, S. Kumar, S. Yoon, K. Kang, H. Na, H.-J. Kim, C. Lee, General aspects of interface bonding in kinetic sprayed coatings, *Acta Mater.,* **57**, 5654–5666 (2009).

[21] K. Taheria, R. Gadow, A. Killinger, Exergy analysis as a developed concept of energy efficiency optimized processes: the case of thermal spray processes, *Proc.,* **CIRP 00**, 000 (2014).

[22] K. Komatsu, Y. Hasebe, T. Sekiya, A. Nakamura, S. Ohshio, H. Akasaka, I. Toda, H. Saitoh, Structural analysis of TiO_2 particles synthesized from Ti-EDTA·NH4 complex, transactions on GIGAKU, **2**, 02002-1–02002-6 (2014).

[23] K. Komatsu, T. Tsuchiya, Y. Hasebe, T. Sekiya, A. Toyama, A. Nakamura, H. Akasaka, H. Saitoh, Synthesis of metal oxide particles using reaction route from rare-earth metal-EDTA complexes, *J. Therm. Spray Technol.,* **23**, 885–889 (2014).

Chapter 3

Analysis of cross-sectional structure of metal oxide films deposited using chelate flame method

Abstract

The chelate flame spray (CFS) method is an inexpensive flame spray technique with low energy consumption used to deposit rare earth erbium oxide (Er_2O_3) films with Er-ethylenediaminetetraacetic acid (EDTA·Er·H) complexes of various particle sizes as the raw material. To investigate the cross-sectional structures of the Er_2O_3 films, substrates of different common materials, i.e., quartz glass, stainless steel (304), and aluminum-magnesium alloy (A5052), were selected. We found that in the CFS deposition process, EDTA·Er·H was decomposed, oxidized, and melted in the flame to form molten Er_2O_3 particles, and Er_2O_3 films with an average thickness of 9.7-13.5 μm, cross-sectional porosity of 1.6-4.9%, and crack numbers of 29-51 were deposited on quartz glass. Oxide films with 7.6-14.3 μm thickness were synthesized on an aluminum-magnesium alloy (A5052) substrate. The cross-sectional porosity and microcrack numbers of these films were 5.2-6.9% and 10-20, respectively. In addition, to observe the Er_2O_3 film stacking structure more clearly, we screened the powder raw materials

to make them uniform. The results of this study enable the design of a ceramic film microstructure that reduces cracks in the ceramic film, thereby increasing the application potential.

3.1 Introduction

The microstructures and properties of thermally sprayed ceramic coatings have been extensively investigated due to their potential benefits in broad thermal barrier coating applications and sliding wear applications [1–4]. Atmospheric plasma spraying (APS) and high-velocity oxi-fuel (HVOF) spraying are commonly thermal spray methods that due to the high-temperature (15000-20000 K) and high speed of spray particles [5]. However, high energy consumption and large-scale installation requirements limit the further application of these methods [5–7]. Thus, there is a pressing need for spraying techniques with low energy consumption to be developed. Recently, metal-ethylenediaminetetraacetic acid (EDTA) complexes have been used to synthesize metal oxide coatings using a new flame spray method [8-10] called the chelate flame-spray (CFS) technique. In the CFS process, the raw materials of metal-EDTA complexes are placed into a feed unit and transported by flowing carrier gas (N_2 or O_2) to the spray gun. Then, the gas-solid mixture is introduced into a C_2H_2-O_2 or H_2-O_2 flame and reacted with oxygen after the thermal decomposition of EDTA. Thereafter, the melting particles are sprayed onto a substrate at high speed to deposit ceramic oxide films [9]. In a previous study, we discussed the effect of the starting material state (molecularly or mechanically mixed) and carrier gases (N_2, air, and O_2) on the oxide films by CFS

process [10,11]. After the porosity of the metal oxide coating was effectively controlled, a preliminary investigation of thermal shock properties was reported [8]. In the follow-up study, we successfully synthesized the Y_2O_3 films on an aluminum alloy(A5052), and the joining showed strong adhesion without delaminations [9].

Cracks in microstructures are key to determining the mechanical behavior and thermal shock resistance of coatings [8,12,13]. In thermal spray processing, after the raw materials are melted using a high-temperature flame, they are deposited onto the substrate and instantaneously transferred from the molten state to the solid state. During this process, stress is generated on the other side, which causes cracks in the solidified particles [14]. Coatings, such as thermal barrier coatings (TBCs) (1273-3273 K), which are one of the most important coating types [15,16], are applied in extreme environments. Under these conditions, Valarezo et al. made thick yttria-stabilized zirconia (YSZ) films via APS with rapid deposition [13]. They evaluated the effect of the inter splat and the inter pass interface stress on the microstructure of the ceramic film. Other research has reported the strain tolerance behavior of APS-YSZ coatings [15-19]. The results suggest that an effective reduction in the stress of the molten metal oxide during the solidification process will effectively reduce the occurrence of cracks. Unfortunately, in Valarezo's research, the results of substrates with different types for ceramic film structures were not systematically tested.

In this work, two series of experiments were performed to study the cross-sectional structure of Er_2O_3 coatings deposited by a CFS method. Scanning electron microscopy (SEM) and image analysis software (ImageJ, SmileView) were used to analyze the

crack formation mechanism of Er_2O_3 coatings. First, Er_2O_3 coatings were sprayed on substrates with different materials, i.e., quartz glass, stainless steel (304), and aluminum alloy (A5052). The Er_2O_3 coating particle state and influence of the substrate thermal conductivity on the coatings were evaluated. Er_2O_3 coatings were prepared with various particle sizes of the EDTA·Er·H raw material, and the effect of the raw material size on the cross-sectional structure of these coatings was investigated.

3.2 Experimental details

As mentioned above, the EDTA precursor powder is complexed that was decomposed at approximately 673K [10], the structure of the EDTA metal complex is shown in **Fig.**3-1. The EDTA complex powders, EDTA·Er·H (Chubu Chelest Co., Ltd) was used for synthesizing the Er_2O_3 films in the chelate flame spray (CFS) process. To obtain various sizes of the raw material, sieves (Kansai Wire Netting Co., Ltd.) with mesh sizes of 75 μm, 53 μm, and 45 μm were vertically stacked, and the unscreened raw material was passed from the top, as shown in **Fig.** 3-1a. Including the unscreened cuboid EDTA·Er·H powder, five raw material particle sizes, i.e., unscreened (Fig. 3-1b), 75-μm-on (Fig. 3-1c), 53-μm-on (Fig. 3-1d), 45-μm-on (Fig. 3-1e), and 45-μm-pass (Fig. 3-1f), with the average particle size of 67.89, 82.37, 63.37, 54.71, and 42.26 μm, respectively, were selected for the experiments. For the substrates, quartz glass, stainless steel (304), and aluminum alloy(A5052), with thermal conductivities of 1.38, 16.7, and 137 W/(mK) at room temperature [20,21], respectively, were selected because they are commonly used and ideal substrate materials. Except for quartz glass (DAICO

MFG Co., Ltd.), which was directly purchased in a disc shape of $\pi \times (25)^2 \times 5$ mm^3, the substrates were simply processed into areas of 30 × 50 × 1 mm^3 for the rectangular shape stainless steel substrate (304 Ni-Cr-Mn-Si-C) and 100 × 100 × 10 mm^3 for the square shape aluminum alloy substrate (A5052 Al-Mg, Fuji Manufacturing Co., Ltd.), as shown in **Table 3-1**. All substrates were blasted with #60 alumina grit (purity of 99.7%, particle size of 212–250 μm, Fuji Manufacturing Co., Ltd.) for 1 min at a pressure of 0.6 MPa and then ultrasonically precleaned with acetone for 5 min twice before each deposition process

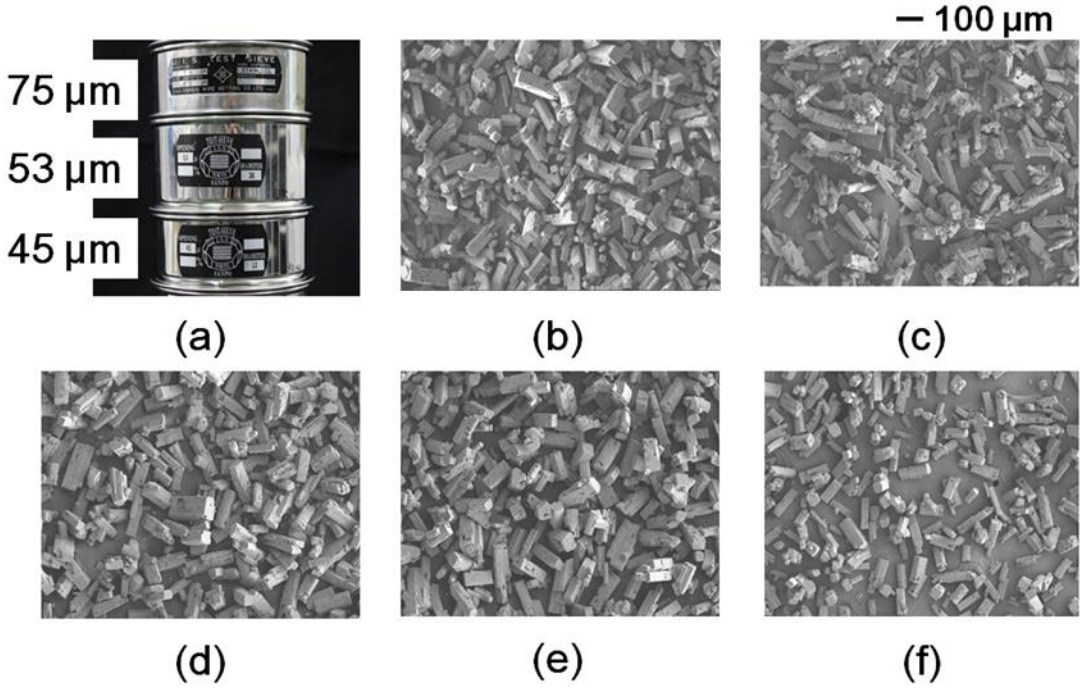

Figure 3-1 The powder state of raw material EDTA·Er·H, (a) the stacking state of sieves; SEM images of the raw materials (b) unscreened, (c) residual on the 75-μm sieve, (d) residual on the 53-μm sieve, (e) residual on the 45-μm sieve, and (f) passed through the 45-μm sieve. Their average particle size values were 67.89, 82.37, 63.37, 54.71, and 42.26 μm, respectively.

Table 3-1 substrate properties used in the thermal spraying.

Substrate	Size (mm^2)	Thickness (mm)	Coefficient of thermal expansion (10^{-6}/k@ 273K)	Thermal conductivity (W/(mK))
Quartz glass	$\pi \times (25)^2$	5	0.5	1.38
Stainless steel (304)	30×50	1	17.6	16.7
Aluminum alloy (A5052)	50×50	10	23.8	138

A flame-spraying apparatus consisting of a feed unit (5MPE, Sulzer Metco) and a spray gun (6P-II, Sulzer Metco) was used to perform each spraying. EDTA·Er·H was placed in the feed unit and transported by a carrier gas O_2 with a measured powder feed rate of approximately 5 g/min to the spray gun. The carrier gas flow rate was set at 7.1 L/min. The flow rates of the combustion gases, H_2 and O_2, were set to 32.6 and 43.0 L/min, respectively. The distance between the spray gun and the substrate (nozzle substrate distance) was set at 150 mm. The gun traverse rate was 50 mm/s; thus, the spray nozzle was moved in a longitudinal direction, next each pass of the flame moving over the whole substrate was within 1–2 s, as shown in **Fig.** 3-2 During the spraying process, the temperature of the flame was approximately 2773–3273 K, resulting in a substrate temperature over 493 K [22]. Thus, after 2 scans, the sample was allowed to cool for 5 min. An infrared camera (Accura Spray-G3: Tecnar) was used to measure the velocities and temperatures of the particles during and after the deposition process. All samples were subjected to 4 scans with a cooling interval of 5 min after 2 scans.

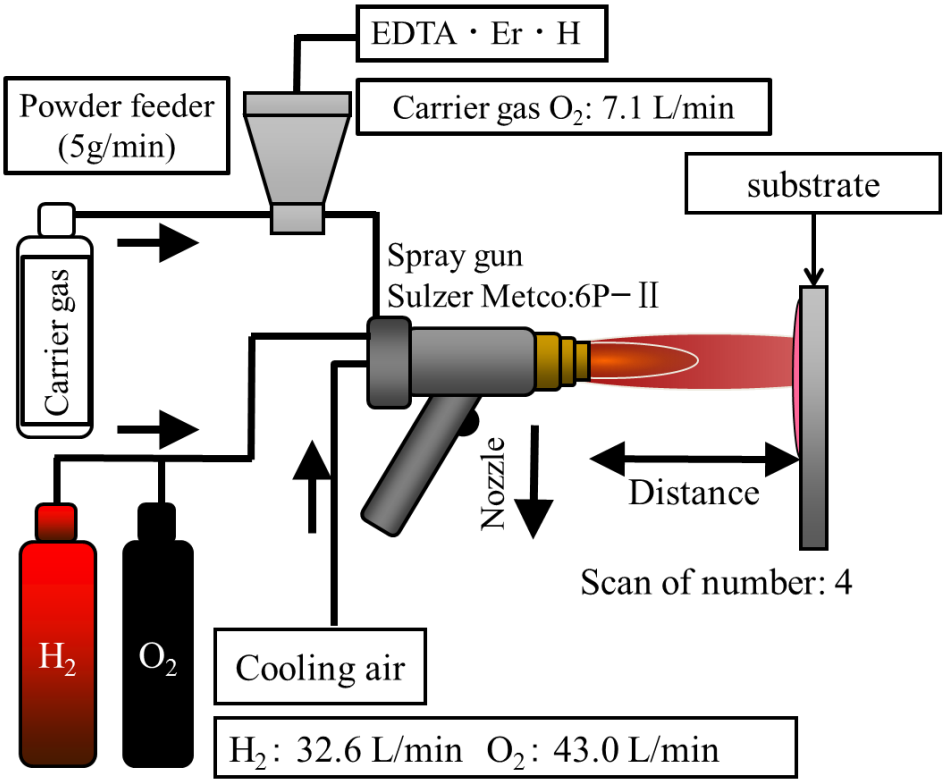

Figure 3-2 Schematic of the film deposition setup for EDTA·Er·H complexes on various substrates.

X-ray diffraction (XRD) analysis was performed to observe the crystal structures of the deposited films. The XRD measurements (M03XHF22, MAC Science) were taken on an instrument with a Cu *Kα* X-ray source and wavelength of 1.54 Å operated at 40 kV × 40 mA in the scan range of 2θ=10–80° with a step size of 0.02°. The surface and cross-sectional morphologies of the samples were observed using field-emission scanning electron microscopy (FE-SEM) (JSM-6700F, JEOL) under an acceleration voltage and irradiation current of 5 kV × 8 μA and 12 kV × 20 μA, respectively. Secondary electron and backscattered electron(compositional) images of the deposited films were acquired. The porosity was measured by digitizing the obtained SEM images

using commercial software (ImageJ). Next, the thickness is average thickness of 20 transverse section in the whole image and repeat 3 times. And then, the porosity was estimated from area ratio of film in the image [23]. The Er_2O_3 film's microstructure of the deposited on different substrates were analyzed as follows. Firstly, each obtained COMPO image was digitized using ImageJ. Secondly, the number of cracks, crack lengths, and crack areas were measured from the digitized (Black-White) image. Furthermore, number of cracks per unit area was estimated using the following equation (1):

$$\text{Number of cracks per unit area}\left(\frac{\text{number}}{\text{pixels}}\right) = \frac{\text{Number of cracks in the deposited film}}{\text{Area of the deposited films excluding pore voids}}$$

(number/μm^2). (1)

3.3 Results and discussion

3.3.1 Characterization of Er_2O_3 coatings on different substrates

Fig. 3-3 shows the XRD patterns of the Er_2O_3 coatings deposited on the three substrates. The peaks in the XRD profiles were assigned using the International Centre for Diffraction Data (ICDD) cards as references. In **Fig.** 3-3a–c, the unscreened EDTA·Er·H films deposited on quartz glass, stainless steel (304), and aluminum alloy (A5052) exhibited cubic and monoclinic Er_2O_3 crystalline phases. Er_2O_3 exhibits three structural polymorphisms: cubic, monoclinic, and hexagonal, which are commonly known as C-, B-, and A-type structures, respectively [11]. Hence, the substrate has no effect on the crystal structure of the deposited coatings.

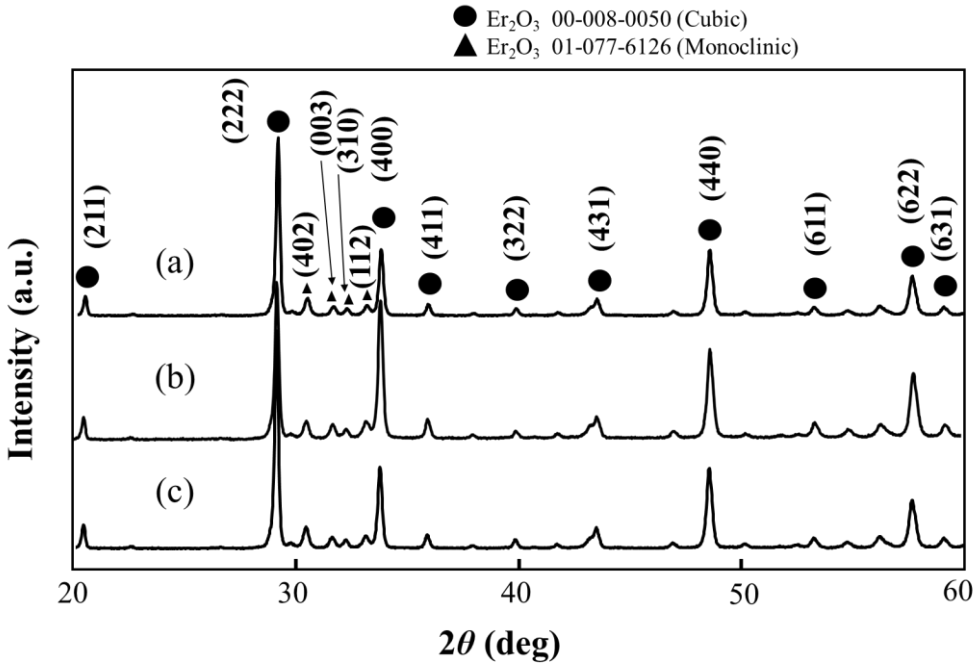

Figure 3-3 XRD patterns of coatings deposited from unscreened EDTA·Er·H onto blasted substrates of (a) quartz glass, (b) stainless steel (304), and (c) aluminum alloy (A5052).

Fig. 3-4 shows surface SEM images of Er_2O_3 coatings deposited from unscreened EDTA·Er·H onto the three blasted substrates. Flattened and spherical particles approximately 1–20 μm in diameter were observed in all sprayed coatings. The coatings deposited on the quartz glass, a number of spherical (i.e., not flattened) particles, disc particles and pores were also observed. Further, even though small spherical particles with sizes of approximately 1 μm was also seen in the Er_2O_3 film synthesized on stainless steel (304) substrate. Finally, a large number of flattened and small-particles size spherical were seen in the Er_2O_3 film deposited on aluminum alloy(A5052). When

quartz glass was used as the substrate, the degree of flatness was the lowest, with spherical particles also being observed, as shown in **Fig.** 3-4a. In contrast, Particles with the highest degree of flatness (or splatting) were observed in the Er_2O_3 film obtained on the aluminum alloy(A5052), for which flat Er_2O_3 particles were deposited, as shown in **Fig.** 3-4c. Additionally, cracks were clearly observed in the coatings deposited on the quartz glass, as shown in the area highlighted by the arrow line in **Fig.** 3-4a_1, while the other coatings showed no significant cracks in the surface SEM images. Thus, the choice of the substrate causes difference in the surface morphologies of the deposited Er_2O_3 films. Perhaps due to temperature sensitivity of the films deposited on the different materials, such as aluminum alloy metal, the resulting deposited coatings appear significantly different.

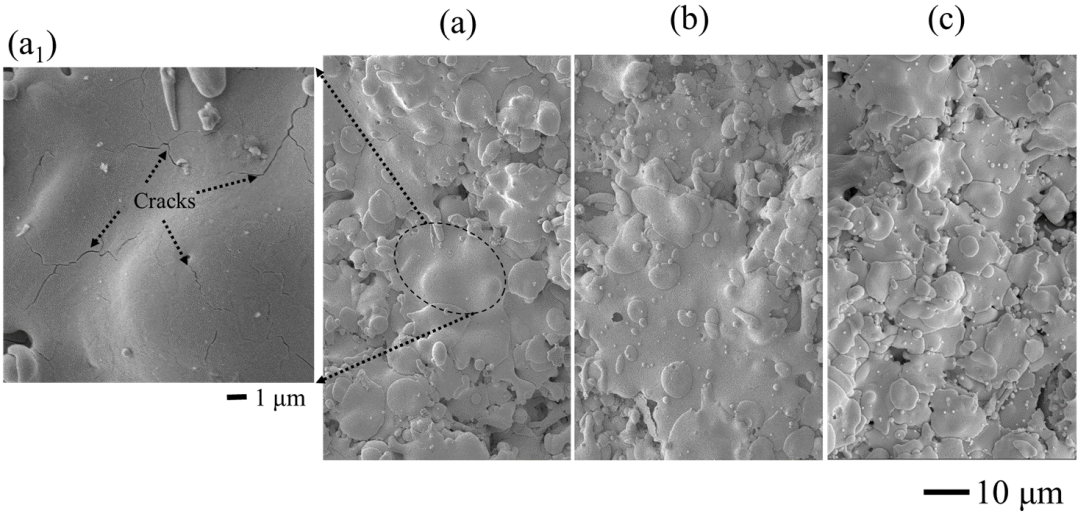

Figure 3-4 SEM images of the surface of the coating deposited from unscreened EDTA·Er·H onto blasted substrates of (a) quartz glass and (a_1) magnification image, (b) stainless steel (304), and (c) aluminum alloy (A5052). Cracks were clearly observed in the area of the dotted line.

To further investigate the differences in the Er_2O_3 coatings deposited on different substrates, we analyzed cross-sectional SEM and digitized (Black-White) images of these coatings, as shown in **Fig.** 3-5. The images clearly show the deposited state of the splattered particles and can be used to accurately estimate the cracks in the Er_2O_3 coatings. Numerous cracks were found in the coatings deposited on the quartz glass substrate. The number of cracks in the coatings deposited on the stainless steel (304) substrate was less than that on the quartz glass substrate, the film deposited on the aluminum alloy (A5052) substrate had the least the number of cracks. An extensive flat coating structure was observed. **Table** 3-2 shows the values estimated from the digitized (Black-White) images of the average thickness, porosity, number of cracks, average crack length, and number of cracks per unit area for the Er_2O_3 coatings. Through a comparison of these results, we found that the number of cracks, average crack length, and number of cracks per unit area was the lowest for the coatings deposited on the aluminum alloy (A5052) substrate, although its coating deposition rate was the highest of the three substrates. Additionally, the coatings on the aluminum alloy (A5052) substrate showed a lamellar structure, but the coatings deposited on the quartz glass and stainless steel (304) substrates were quite different, showing a dense structure. The difference in structure may be the reason why the porosity of the coatings on the aluminum alloy (A5052) substrate was highest.

As mentioned above, during thermal spray processing, after the raw materials are melted by a high-temperature flame, they are deposited onto the substrate, where they instantaneously transition from the molten state to the solid state, generating stress on

the other side and causing cracks in the solidified particles [24,25]. Additionally, we found that the number of cracks and average crack length of the coatings will be reduced as the thermal conductivity increases, and the solidification time of molten particles on the substrate decreases [26]. Due to the increase in stress relaxation and the decrease in coating thickness, the particles will be flatter.

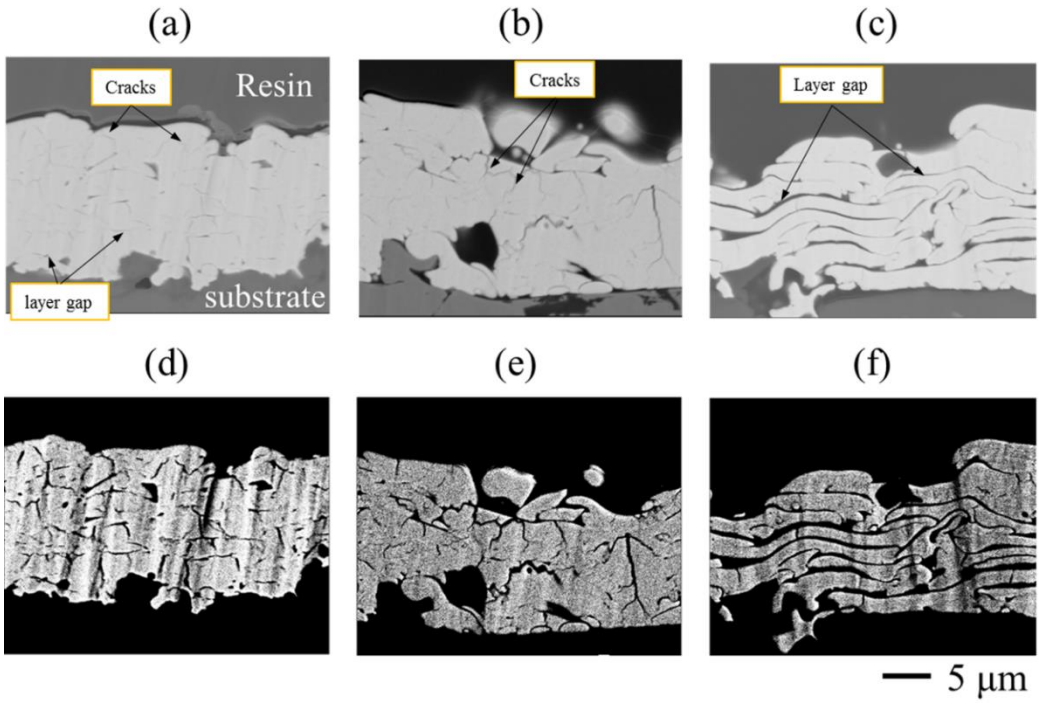

Figure 3-5 Cross-sectional SEM (a, b, and c) and digitized(Black-White)images (d, e, and f) of coatings deposited from unscreened EDTA·Er·H onto blasted substrates of quartz glass (a and d), stainless steel (304) (b and e), and aluminum alloy (A5052) (c and f).

Table 3-2 Values of estimated average thickness, porosity, number of cracks, average crack length, and number of cracks per unit area in Er_2O_3 coatings deposited from unscreened EDTA·Er·H onto blasted substrates of quartz glass, stainless steel (304), and aluminum alloy (A5052).

Substrate	Average thickness (μm)	Cross-sectional porosity (%)	Number of cracks	Average crack length (μm)	Number of cracks per unit area $\times 10^{-5}$ (number/μm^2)
Quartz glass	13.5	2.0	39	1.2	5.9
Stainless steel (304)	12.7	3.7	20	1.3	3.1
Aluminum alloy (A5052)	14.3	6.9	13	1.0	2.0

3.3.2 Characterization of Er_2O_3 coatings with various size of raw materials

Fig. 3-3 showed the XRD patterns of Er_2O_3 coatings deposited on the quartz glass and aluminum alloy (A5052) substrates. The samples can be identified using ICDD card Nos. 00-008-0050 (cubic Er_2O_3 phase) and 01-077-6226 (monoclinic Er_2O_3 phase) without any significant differences. The raw material particle size had no obvious effect on the phase structure of the Er_2O_3 coatings.

Figs. 3-6 and 3-7 show the coating surface, with **Fig.** 3-6 showing SEM images of the Er_2O_3 film coatings deposited on the quartz glass and the **Fig.** 3-7 showing the coatings on aluminum alloy (A5052). Each top column shows a different powder size. The Er_2O_3 coatings deposited on quartz glass had flattened spherical particles. A number of spherical (or lowest degree of flatness) particles were observed for particle size 75-μm-on, and cracks occurred on the coating surface, as shown in the arrow line in **Fig.** 3-6(b). The coatings deposited from the raw material with a particle size of 53-μm-on still had cracks that can be discerned in the surface SEM image, but as the

particle size of the raw material decreased, the area of the flattened particles also decreased, and no obvious cracks were present in their surface SEM images(Fig. 3-6(c) to (e)). In addition, spherical particles approximately 1-4 μm in diameter were observed in surface images Fig. 3-6(b) to (d)). We found that for the same raw material particle size, the extent of the flattened particles in the Er_2O_3 coating deposited on aluminum alloy (A5052) was greater than that on the quartz glass substrate, especially for 75-μm-on particles, as shown in **Fig.** 3-7(g). Additionally, the coating with unscreened and a raw material size of 75-μm-on had a crack in its surface SEM images. Further, more small-particles spherical with a size of below 0.1 μm in diameter were also seen on the coating surface, as shown in the area highlighted by the dotted line in **Fig.**3−7(f), (i), (j). In contrast, the presence of small-particles size spherical in surface images (Fig.3-7(g),(h)) after screening was not significant. Thus, the comparison of the SEM images of the Er_2O_3 coating surfaces indicated that significant differences in the size of the spherical particles. In general, the reason why the solidification speed of the molten droplets on substrate (or different substrates) is different, resulting in different degrees of spattering of the accelerated droplets.

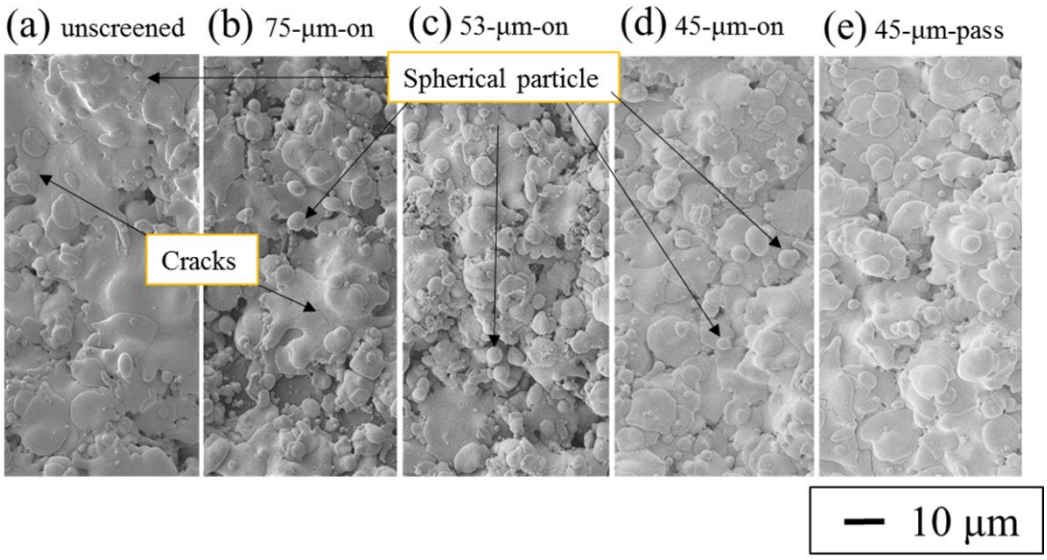

Figure 3-6 Surface SEM images of coatings deposited from unscreened (a), 75-μm-on (b), 53-μm-on (c), 45-μm-on (d), and 45-μm-pass (e) EDTA·Er·H onto blasted substrates of quartz glass. Cracks were observed in the area of the dotted line.

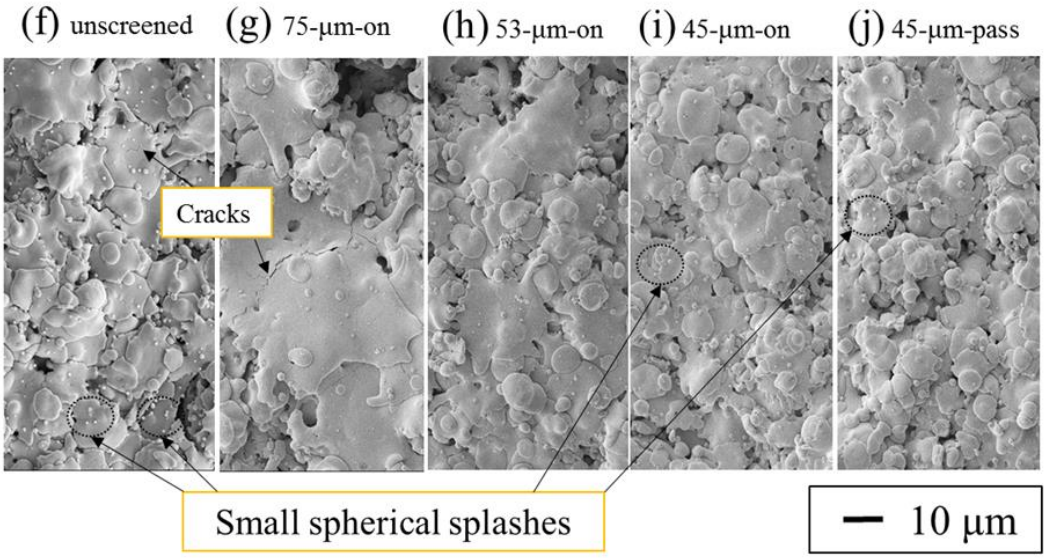

Figure 3-7 Surface SEM images of coatings deposited from unscreened (f), 75-μm-on (g), 53-μm-on (h), 45-μm-on (i), and 45-μm-pass (j) EDTA·Er·H onto blasted substrates of aluminum alloy (A5052). Cracks were observed in the area of the dotted line.

To further investigate the microstructural in Er_2O_3 coatings deposited on different substrates with various sizes of EDTA·Er·H particles, the cross-sectional SEM and digitized (Black-White) images, as shown in **Figs.** 3-8 and 3-9, were analyzed. **Fig.** 3-8(a) to (b) show the cross-sectional SEM, digitized (Black-White), and particle shape images of Er_2O_3 coatings deposited on a quartz glass substrate with various sizes of EDTA·Er·H particles. Several micron-ordered Er_2O_3 layers were confirmed on the quartz glass substrate. It can be clearly seen in **Fig.**3-8(digitized images) that the microstructures of the cracks, pores (layer gap), and columns gap. The large pores and lone cracks were observed in the Er_2O_3 film deposited using the raw material size of 75-μm-on. Furthermore, it was found that the number of pores in the Er_2O_3 films synthesized using the raw material of unscreened, screened(53-μm-on, 45-μm-on/pass) were lower, and the crack length to shorter. **Table** 3-3 shows the thicknesses, porosity, number of cracks, average crack length, and number of cracks per unit area of the films. The porosities were determined by analyzing SEM images of the films. This analysis method can be used to determine the numbers of both open and closed pores [10]. The Er_2O_3 film obtained using raw material of unscreened had an average thickness of 13.5 μm, porosity of 2.0%, and number of cracks of 39. Next, in the case of raw material to screened with 75-μm-on, 53-μm-on and 45-μm-on/pass that the thickness to changes in 9.7-14.2 μm, porosity to changes in 1.6-4.9 %, and number of cracks in 29-51. The Er_2O_3 film was densified and fewer cracks by screened raw material of 45-μm-pass when using the quartz glass substrate.

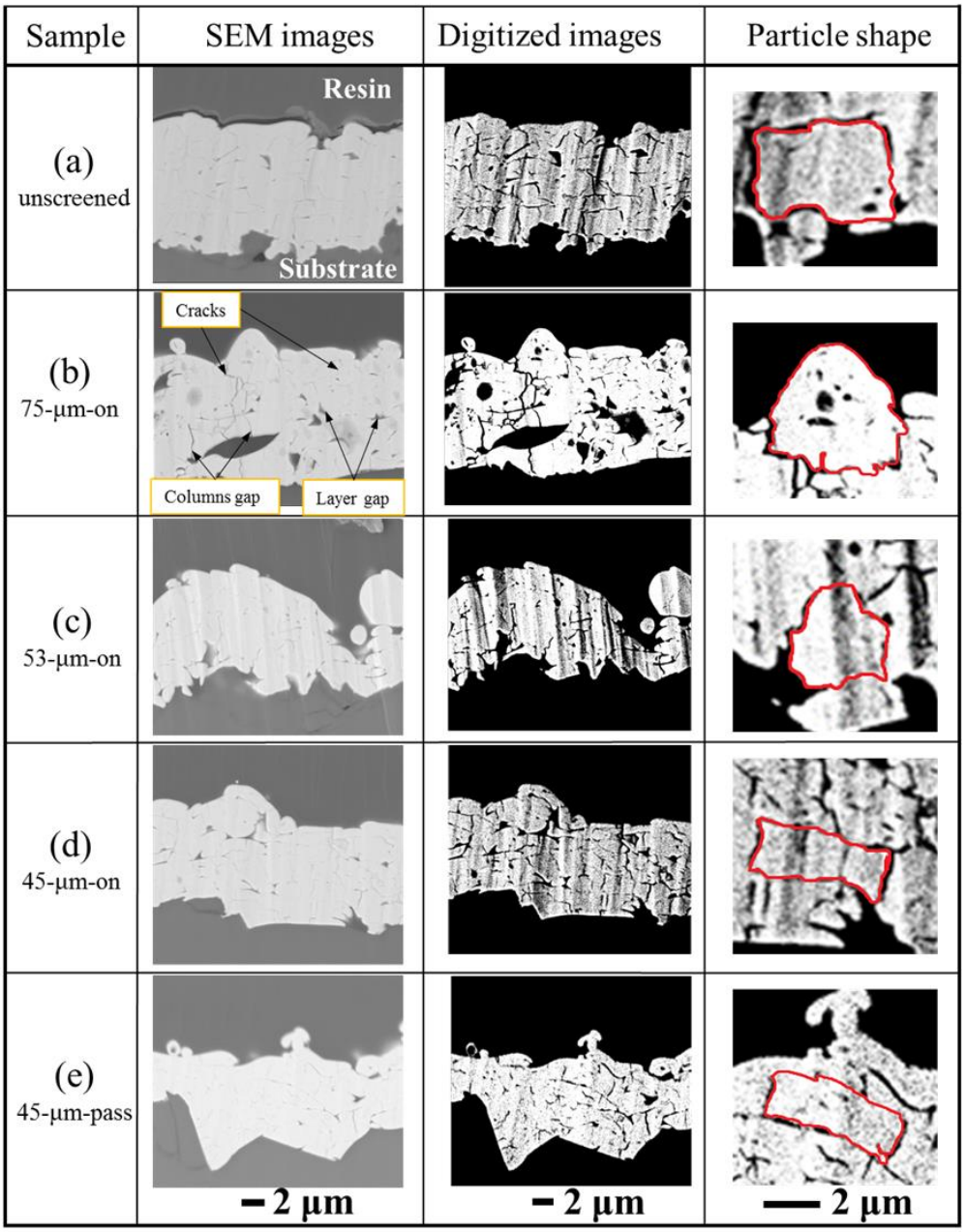

Figure 3-8 Cross-sectional SEM, digitized(Black-White) and particle shape images of coatings deposited from EDTA·Er·H onto blasted substrates of quartz glass(a-e). In each row from top to bottom are the coatings deposited from unscreened, 75-μm-on, 53-μm-on, 45-μm-on, and 45-μm-pass EDTA·Er·H raw materials.

Figure 3-9 (f) to (j) show the cross-sectional SEM, digitized (Black-White) and particle shape images of Er_2O_3 coatings deposited on aluminum alloy(A5052) substrate with various sizes of EDTA·Er·H particles. It can be clearly seen in **Fig**.3-9 to compare with **Fig.**3-8 that the films deposited on quartz glass and aluminum alloy(A5052) substrate are significantly different. The Er_2O_3 films (all samples) reveal a lamellar structure deposited on aluminum alloy(A5052) substrate. The Er_2O_3 films reveal typical microstructural such as layers, layer gap, and variety of pores, as indicated in **Fig.**3-9. **Table** 3-4 shows the thicknesses, cross-sectional porosities, and number of cracks of the Er_2O_3 films synthesized on the A5052 substrate. From **Tables** 3-3 and 3-4, the Er_2O_3 films deposited on aluminum alloy compared to quartz glass were more porous and fewer cracks. Furthermore, the built-up structure can be clearly observed, such as flattened strip with sizes of approximately 3-8 μm. In addition, the inner layer and outer layer particles are almost identical in shape, as shown in **Fig.**3-9(f) to (j).

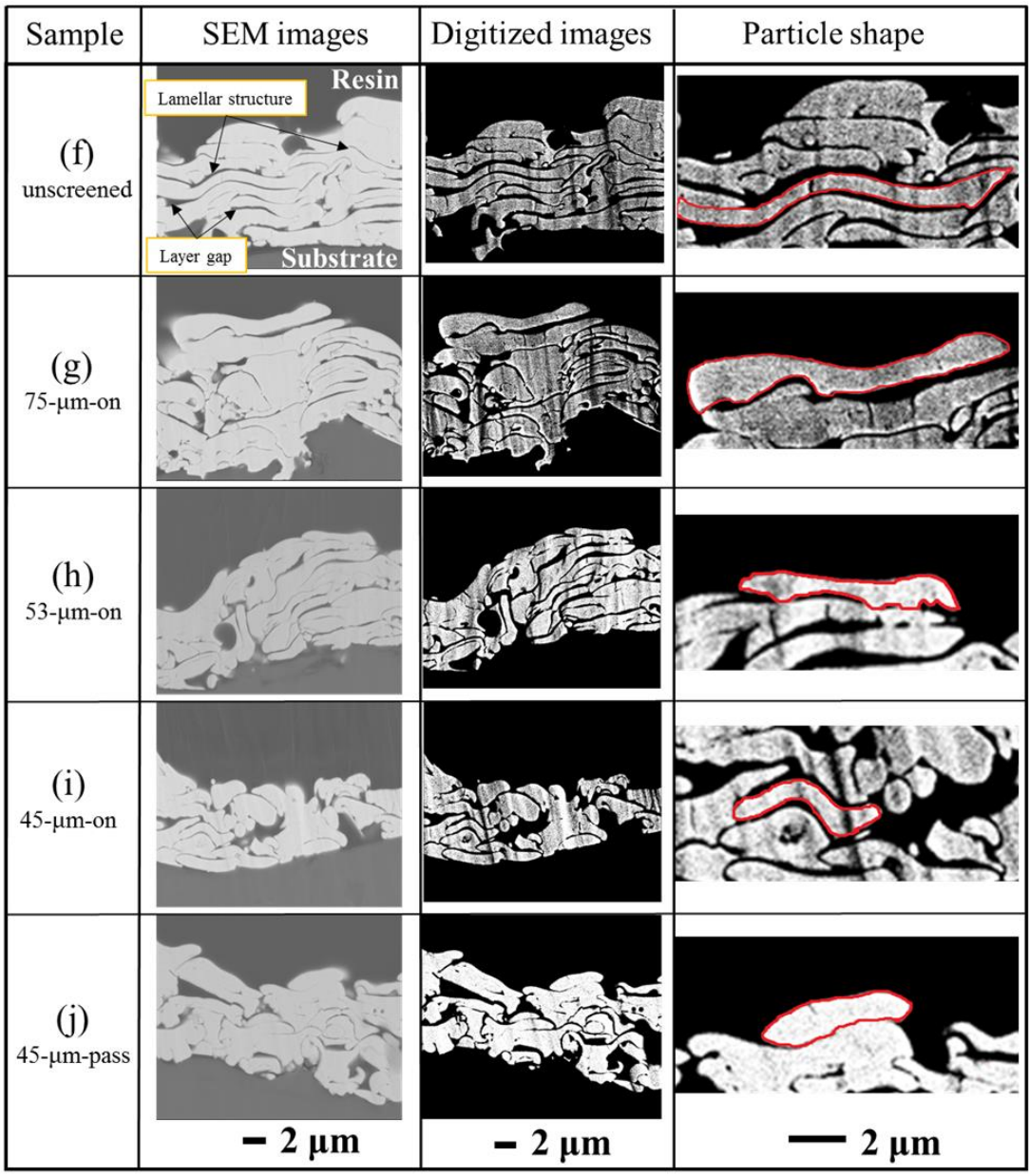

Figure 3-9 Cross-sectional SEM, digitized(Black-White), and particle shape images of coatings deposited from EDTA·Er·H onto blasted substrates of aluminum alloy (A5052)(f-j). (The particle size order is the same as Fig.3-8)

Table 3-3 Values of estimated average thickness, number of cracks, average crack length, and number of cracks per unit area in Er_2O_3 coatings deposited on quartz glass substrate with various raw material sizes.

Raw material size state	Average thickness (μm)	Cross-sectional porosity (%)	Number of cracks	Average crack length (μm)	Number of cracks per unit area $\times 10^{-5}$ (number/μm^2)
unscreened	13.5	2.0	39	1.2	5.9
75-μm-on	14.2	4.9	51	1.3	14.5
53-μm-on	10.5	2.0	34	1.2	5.2
45-μm-on	9.7	2.1	31	1.1	4.8
45-μm-pass	10.3	1.6	29	1.0	4.6

Table 3-4 Values of estimated average thickness, number of cracks, average crack length, and number of cracks per unit area in Er_2O_3 coatings deposited on aluminum alloy (A5052) with various raw material sizes.

Raw material size state	Average thickness (μm)	Cross-sectional porosity (%)	Number of cracks	Average crack length (μm)	Number of cracks per unit area $\times 10^{-5}$ (number/μm^2)
unscreened	14.3	6.9	13	1.0	2.0
75-μm-on	13.9	6.2	20	1.0	3.5
53-μm-on	11.3	5.2	16	1.0	2.9
45-μm-on	7.6	6.4	12	1.0	3.3
45-μm-pass	8.4	6.2	10	0.7	2.8

3.3.3 Discussion

In section 4.4.1, we deposited Er_2O_3 coatings on quartz glass, stainless steel (304), and aluminum alloy (A5052) substrates by the CFS method and analyzed XRD patterns, and surface/cross-sectional SEM and digitized (Black-White) images. On the basis of these results, the effects of the substrate on the properties of the deposited films are discussed below. First, the CFS deposition process, the chemical reaction of EDTA·M·H (M: metal species) can be represented by Eq. (1) [22,27]. In Eq. (2), for an instance, EDTA·Er·H reacts with O_2 to form a Er_2O_3 film.

$$2EDTA{\cdot}Er{\cdot}H + 24\,O_2 \rightarrow Er_2O_3 + 20CO_2\uparrow + 13H_2O\uparrow + NO_2\uparrow \quad (2)$$

Through the Eq. (1), the H_2-O_2 flame and reacts with O_2, and the precursor melts and thermally decomposes that the production of the gases CO_2, H_2O, and NO_2. Resulting in the formation of molten liquid Er_2O_3 particles that are sprayed onto substrates whose instantaneous surface temperatures reached approximately 2973 K [6].

Then, the cross-sectional porosities and number of cracks of Er_2O_3 films were 2.0%, 3.7%, 6.9% and 39, 20, 13 when substrates were quartz glass, stainless steel, and aluminum alloy, respectively. These results indicated that the substrate used has an effect on the solidification speed and shape of the molten droplet, which explains why different substrates result in Er_2O_3 coatings with completely different forms such as likely rectangle, elliptical and strip. To explain this phenomenon, the following two point could have happened during the deposition processes. First, a heat transfer effect due to the thermal conductivity of the aluminum alloy substrate. The solidification is linked to the heat transfer between the splat impact and the substrate [28]. Then, the solidification speed affects the degree of flattening because splat cooling depends on

the heat transfer rate through the initial solidification layer between the wetting range of both critical lines. However, the inner layer (substrate contact layer) may be affected by the wettability of the substrate. Furthermore, in the case of uniform particle size, the effect of the substrate on the top layer and inner layer of the structure of the Er_2O_3 film are discussed below.

In section 4.4.2, Er_2O_3 coatings with various raw material particle sizes were deposited on quartz glass and aluminum alloy (A5052) substrates. Through analyses of the surface, cross-sectional SEM, and digitized (Black-White) images, we found that except for the flatten degree, the spherical particle size is also different in surface images when substrates were quartz glass and aluminum alloy, respectively. Furthermore, from **Fig.**3-8 and **Fig.**3-9, we can observe that the shape of the particles deposited in the films are significantly different on quartz glass and aluminum alloy (A5052) substrates and shape such as likely mountain, rectangle, and strip, respectively. According to the structure, two effects could have happened during the deposition processes. First, with respect to thermal spraying, knowing the temperature and velocity of the in-flight particles is useful for determining their impact behavior, which affects the particle shape and morphology of the deposited films [29,30]. **Table** 3-5 shows the average diameters of raw material particles and the in-flight particle velocities and temperatures during the CFS deposition process when the nozzle-substrate distance was 150mm. the velocities of the unscreened particles were 87.1m/s, the in-flight particle temperature was 2803 K, as the particle size decreased, the velocity and temperature of the particles are 90.3-104.1 m/s and 2863-2933 K, respectively. The thermal energy of

the particle can be calculated as shown below **Eq** (3)[31]:

$$Q = mcT \quad (3)$$

Where Q is the thermal energy(J), m is the weight of sample (kg), c is the specific heat capacity of the material, and T is the temperature(K).

This equation suggests that higher the temperature, higher would be the thermal energy. Therefore, when the molten droplet impact the substrate, on the one hand, it instantly solidifies (or cooling) to form spherical particles. On the other hand, the solidification time becomes long, that the droplet splash forms a large number of small particles. Finally, in cross-sectional images, we can clearly observe that the top, middle and inner layer have the same particle shape with the strip when the film deposited on aluminum alloy substrate. On the other hand, when the Er_2O_3 film deposited on quartz glass, the particle shape become a polygon with the particle thickness of approximately 3, 4, 3.2, 1.9 and 1.8 μm by raw materials of size degree are unscreened and screened with 75-μm-on, 53-μm-on and 45-μm-on/pass, respectively. As described in the experimental result section, the number of cracks are the highest when the films deposited on the quartz glass substrate. The reason why the fast solidification speed. Thus, in the CFS process, the thermal conductivity of the substrate can affect the structure of the film, and the Er_2O_3 film deposited on quartz glass is the densest.

Table 3-5 Values of estimated raw material particle average diameters, in-flight particle velocities, and temperature in the CFS deposition process with a nozzle-substrate distance of 150 mm.

Raw material size state	Raw material average diameter (μm)	In-flight particle velocity (m/s)	In-flight particle temperature (K)
unscreened	67.9	87.1	2803
75-μm-on	82.7	90.3	2863
53-μm-on	63.4	94.2	2853
45-μm-on	54.7	97.0	2933
45-μm-pass	42.3	104.1	2933

3.4 Conclusions

To investigate the effect of substrate type and raw material particle size on the cross-sectional structure of Er_2O_3 coatings deposited by the CFS method, three common structural materials with very different thermal conductivities were selected as substrates, and EDTA·Er·H powder was used as the raw material. Analyses of photographs, XRD patterns, and surface, cross-sectional SEM, and digitized (Black-White) images suggested that the coatings contained cubic and monoclinic crystalline phases of Er_2O_3 films deposited from fully reacted liquid erbia particles. The coatings deposited on the aluminum alloy (A5052) substrate showed typical lamellar structures with few cracks. The densest coatings were obtained on quartz glass. Small, uniform raw material particles resulted in dense coatings. The CFS method, a new type of flame spray technique, has great potential for rapidly and inexpensively coating a variety of engineering materials.

References

[1] E. Lugscheider, Present overview of thermal spraying technology, *Schweissen & Schneiden.*, **54**, 64-67 (2002).

[2] G.E. Kim, Thermal sprayed nano-structured coatings: applications and developments, *Nanostruct Mater.*, 91-118 (2007).

[3] K.A. Habib, J.J. Saura, C. Ferrer, M.S. Damra, E. Giménez, L. Cabedo L, Comparison of flame sprayed Al_2O_3/TiO_2 coatings: their microstructure, mechanical properties and tribology behavior, *Surf. Coat. Technol.*, **201**,1436-1443 (2006).

[4] X.L. Li, Q. Yang, X. Huang, Z.L. Tang, Isothermal oxidation behavior of vc and columnar structured thermal barrier coatings deposited by suspension plasma spray technology, *J. Therm. Spray Technol.*, **24(6)**,1060-1070 (2015).

[5] J.-G. Legoux, B. Arsenault, L. Leblanc, V. Bouyer, C. Moreau, Evaluation of four high velocity thermal spray guns using WC-10% Co-4% Cr cermets, *J. Therm. Spray Technol*., **11**, 86–94 (2002).

[6] M. Prystay, P. Gougeon, C. Moreau, Structure of plasma-sprayed zirconia coatings tailored by controlling the temperature and velocity of the sprayed particles, *J. Therm. Spray Technol*., **10**, 67–75 (2001).

[7] M.P. Planche, H. Liao, B. Normand, C. Codde, Relationships between NiCrBSi particle characteristics and corresponding coating properties using different thermal spraying processes, *Surf. Coat. Technol*., **200**, 2465–2473 (2005).

[8] D.Y. Xin, K. Komatsu, K. Abe, T. Kosta, Y. Ikeda, A. Nakamura, S. Ohshio, H.

Saitoh, Heat-shock properties in yttrium-oxide films synthesized from metal-ethylenediamine tetraacetic acid complex through flame-spray apparatus, *Appl. Phys. A*, **123**(3), 194 (2017).

[9] K. Komatsu, T. Costa, Y. Ikeda, K. Abe, Y.X. Dan, T. Kimura, A. Nakamura, T. Shirai, H. Saitoh, Synthesis of Y_2O_3 films on an aluminum alloy substrate using flame-spray apparatus with a H_2-O_2 flame, *Int. J. Appl. Ceram. Tech*., **00**, 1-10 (2018).

[10] K. Komatsu, T. Shirai, A. Toyama, T. Iseki, D.Y. Xin, T. Costa, A. Nakamura, Y. Li, S. Ohshio, H. Muramatsu, H. Saitoh, Densification of metal oxide films synthesized from metal complexes by flame spraying, *Surf. Coat. Tech*., **325** 89–97 (2017).

[11] K. Komatsu, T. Sekiya, A. Toyama, T. Shirai, A. Nakamura, S. Oshio, H. Saitoh, Synthesis of $(Y, Er)_2O_3$ films from multiple-nuclei EDTA·(Y, Er) ·H complexes by frame spray method, *Mater. Trans.*, **57**(1), 70–74 (2016).

[12] P. Gehre, C.G. Aneziris, EBSD-and CT-analyses for phase evolution and crack investigations of thermal shocked flame sprayed alumina and alumina-rich structures, *Ceram. Int.*, 1731-1737 (2011).

[13] A. Valarezo, G. Dwivedi, S. Sampath, R. Musalek, J, Matejicek, Elastic and anelastic behavior of TBCs sprayed at high-deposition rates, *J. Therm. Spray Technol.*, 160-167 (2015).

[14] N. Espallargas, Future development of thermal spray coatings, *Elsevier*, 2015, DOI: 10.1016/C2013-0-16360-X.

[15] S. Gong, K. VenEvery, H. Wang, R.W. Trice, Microstructure and thermal properties of inflight rare-earth doped thermal barriers prepared by suspension plasma spray, *J. Eur. Ceram. Soc.*, **34**(5), 1243–1253 (2014).

[16] Z. Xu, L. He, X. Chen, Y. Zhao, X. Cao, Thermal barrier coatings of rare-earth materials deposited by electron beam-physical vapor deposition, *J. Alloy. Compd.*, **508**(1), 94–98 (2010).

[17] S. Sato, R. Takahashi, M. Kobune, H. Gotoh, Basic properties of rare-earth oxides, *Appl. Catal. A.*, **356**, 57–63 (2009).

[18] M. Li, Y. Cheng, L. Guo, Y. Zhang, C. Zhang, S. He, W. Sun, F. Ye, Preparation of nanostructured $Gd_2Zr_2O_7$-$LaPO_4$ thermal barrier coatings and their calcium-magnesium-alumina-silicate (CMAS) resistance, *J. Eur. Ceram. Soc.*, **37**(10), 3425–3434 (2017).

[19] M.G. Gok, G. Goller, Microstructural characterization of GZ/CYSZ thermal barrier coatings after thermal shock and CMAS+hot corrosion test, *J. Eur. Ceram. Soc.*, **37**(6), 2501–2508 (2017).

[20] P. Liu, M. Zhu, Z. Zhang, Y.K. Leong, Y. Zhang, D. Zhang, Rheological behavior and stability characteristics of biochar-water slurry fuels: Effect of biochar particle size and size distribution, *Fuel Process. Technol.*, **156**, 27–32 (2017).

[21] C. Kittel, Interpretation of the thermal conductivity of glasses, *Phys. Rev.*, **75**(6), 972–974 (1949).

[22] Y.S. Touloukian, Thermal conductivity: metallic elements and alloys, *Thermophysical Properties of Matter*, **1**, 1307-1309 (1970).

[23] H. Akasaka, M. Ohto, Y. Hasebe, A. Nakamura, S. Ohshio, H. Saitoh, Yttria coating synthesized by reactive flame spray process using Y-EDTA complex, *Surf. Coat. Technol.*, **205**(13-14), 3877–3880 (2011).

[24] G. Adachi, N. Imanaka, The binary rare-earth oxides, *Chem. Rew.*, **98**(4), 1479–514 (1998).

[25] Y. Yinuyi, S. Sodeoka, K. Wueno, Y. Takatani, S. Oki, T. Tomita, Y. Sugie, Flame Spray of Ceramic, *Thermal Spray Technology an Introduction*, 1st ed., S.Oki., *Japan Thermal Spray Society*, 181-183 (2006).

[26] S. Kuroda, Thermal Spray Technology - A short Review on the Coating Formation and Structure-property Relationship, *NIMS.*, **305**, 0047 (2009).

[27] X. Ren, X. Yan, Z. Yu, W. Li, L. Wang, Photoluminescence and phase transition in Er_2O_3 under high pressure, *J. Alloy. Compd.*, **725**, 941–945 (2017).

[28] P. Fauchais, M. Fukumoto, A. Vardelle, M. Fukumoto, Knowledge concerning splat formation: an invited review. *J. Therm. Spray Technol.*, **13**, 337-60 (2004).

[29] F. Tarasi, M. Medraj, A. Dolatabadi, J. Oberste-Berghaus, C. Moreau, Effective parameters in axial injection suspension plasma spray process of alumina-zirconia ceramics. *J. Therm. Spray Technol.,* **19**, 787–795 (2010).

[30] Ulargui, P. Valles, Phase formation and transformation in alumina/YSZ nanocomposite coating deposited by suspension plasma spray process. *J. Therm. Spray Technol.,* **20**, 1292–1309 (2011).

[31] K. Taheria, R. Gadow, A. Killinger, Exergy analysis as a developed concept of energy efficiency optimized processes: the case of thermal spray processes. *Proc*.,

CIRP 00, 000 (2014).

Chapter 4

Effect of deposition parameters on splat morphology in chelate flame spray process

Abstract

Splat morphology and its microstructure are of significance to affect the comprehensive capability of new technology with chelate flame sprayed (CFS) coatings, the study deals with the quantitative characterization of spreading morphologies of flame sprayed Er_2O_3 splats directly deposited on mirror polished aluminum alloy substrate with different spray conditions. The influence of in-flight particle temperature and velocity, substrate temperature, carrier gas types, and carrier gas ratio on the solidification mechanism of molten droplets were investigated. In addition, using the rotation apparatus with 12-hedron, combine the rotation speed to reduce the substrate temperature. The image analysis methods were employed to identify single splat from the field emission scanning electron microscope (FE-SEM) morphology. The results show that the substrate temperature, carrier gas types(N_2) and carrier gas ratio has a significant effect on the flattening and oxidizing behavior of molten droplets. A spraying method combined with multi-dimensional modes is proposed to control the morphology of splats.

4.1 Introduction

Flame spraying, a versatile deposition technology, has now been widely used to prepare coatings, which is applied on mechanical parts to protect the substrate [1-4]. The protects capability of the coatings depends dramatically on the design of the structure, such as pores, inter-lamellar cracks, and gap etc. [5,6]. From the microscopically, the flame spray process to synthesis films is built-up by the amount of flying molten or semi-molten particles which combine and condensation after impact synthesizing dense or porous and thin layers or lamellae, it is called splats, that conform and adhere to the substrate surface. Therefore, the achieved films with desired thickness and capability are generally deposited by lamellar layers with the number of splats. The splat shape depends on factors firstly by the raw material of the powder with size [7-9], and finally, by the flying molten particle conditions such as velocity, temperature, and spray distance with the substrate [10-12]. For example, partial melting and irregular depositing of splats generally lead to such blemish as voids and microcracks as the inter-splat boundaries, which allow poor adhesion between the contiguous splats and easier splat loosening, results in the deteriorating the mechanical, thermal and chemical properties of the sprayed coatings [13,14]. Thus, an in-depth studying of splat formation, its morphology selection, and microstructure development are of the key to design the comprehensive properties of the sprayed coating.

As we all known, plasma spray(PS) and high velocity oxygen fuel(HVOF) spray methods are widely used the synthesizes various types of coating, and these spray method have that the in-flight particles have higher temperatures(10000-15000 K) and velocity (550-800 m/s) in the spray process [15,16]. Therefore, it is difficult to take advantage of these techniques for rapid coating on widely used low melting point metal substrate, such as aluminum series. Recently, a new spray technique using a metal-ethylenediaminetetraacetic acid (EDTA) complex has been developed [17]. We call to "chelate flame spray (CFS)" method in this work. In this CFS process, the metal-EDTA complexes were placed into a feed unit and transported by flowing carrier gas (N_2 or O_2) to the spray gun. The metal-EDTA powder was mixed with the C_2H_2-O_2 or H_2-O_2

flame and reacted with oxygen after the thermal decomposition of EDTA. The reacted particles were sprayed onto a substrate in a quite-high speed and deposited a micrometer thickness of metal oxide coating [17]. In the previous study, we have discussed the effect of starting material states (molecular or mechanically mixed) [18] and carrier gases (N_2, air, and O_2) [19] on the porosity of Yttria-Erbia (Y_2O_3-Er_2O_3), (Y, Er)$_2O_3$, Y_2O_3, and Er_2O_3, respectively. Thus, it is of great significance to systematically study the morphology of the coating on the low melting point substrate such as aluminum alloys by the chelate flame spray method.

In this study, scare works are available on developments of splat morphology and microstructure of chelate flame spraying by the process parameters of the system. And Er_2O_3 splats were synthesized on an aluminum alloy substrate using a flame-spray apparatus with H_2-O_2 flame. An extensive experimental analysis of the effect of deposition parameters including raw materials size, powder feed rate, substrate temperature, carrier gas flow, carrier gas types, and spray-gun to substrate standoff distance, and then, the results such as circularity, disk-like ratio, and splat particles size were investigated to reveal the microstructure evolution and splat shape formation mechanism in chelate flame spray process.

4.2 Experimental

4.2.1 Prepare of raw materials and spray conditions of splat

Fig.4-1 shows the flame-spray equipment for film deposition on the aluminum alloy (A5052, 50×50×5 mm^3, surface was polished) substrate with the complex of EDTA(ethylene-diamine-tetra-acetic), EDTA·Er·H (Chubu Chelest Co., Ltd) for a photograph of the test with fixed. In addition, the substrate surface was cleaned with acetone for twice and dried in air. A traditional hydrogen-oxygen fuel thermal spray system consisting of a feed unit (5MPE, Sulzer Metco, Westbury,NY) and flame-spray gun (6-P Ⅱ,Sulzer Metco) was used to execute splat spraying. A mixture of H_2 and O_2 was applied as the flame gas, with flow rates of 70 and 90 SCFH, respectively. To obtain raw material of the sizes about 45 μm, sieves (Kansai Wire Netting Co., Ltd.) with 75 μm, 53 μm, and 45 μm, mesh sizes were vertically stacked, and the unscreened raw

material was passed from the top. We using the size of 45-μm-on and unscreened EDTA·Er·H powder to do the splat tests.

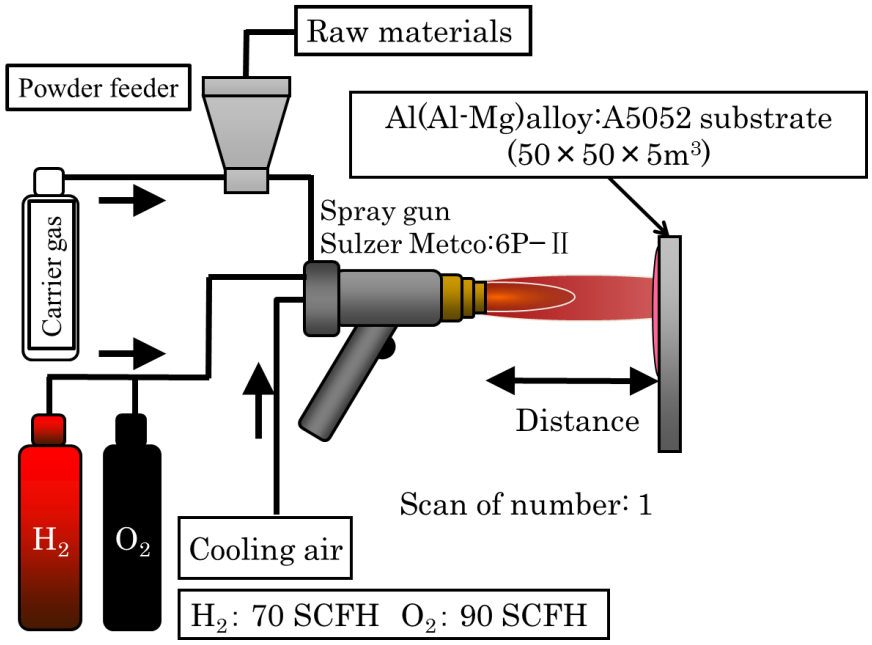

Figure 4-1 Schematic of the films deposited setup for splat morphologies.

In addition, for the purpose of study the relationship between substrate temperature and splat morphology, we used the flame-spray apparatus and a 12-side rotation apparatus that substrate is fixed on it, and the substrate temperature is lowered by rotation. Then, dig a groove on the reverse side of the substrate and inserted the K-type thermocouple to measure the temperature at different rotation speeds of the substrate during the experiment. The thermocouple was combined with a data logger (EL-USB-TC-LCD, MK Scientific) to receive data of substrate temperature every second interval. Temperature profiles were obtained in each experiment using analysis software.

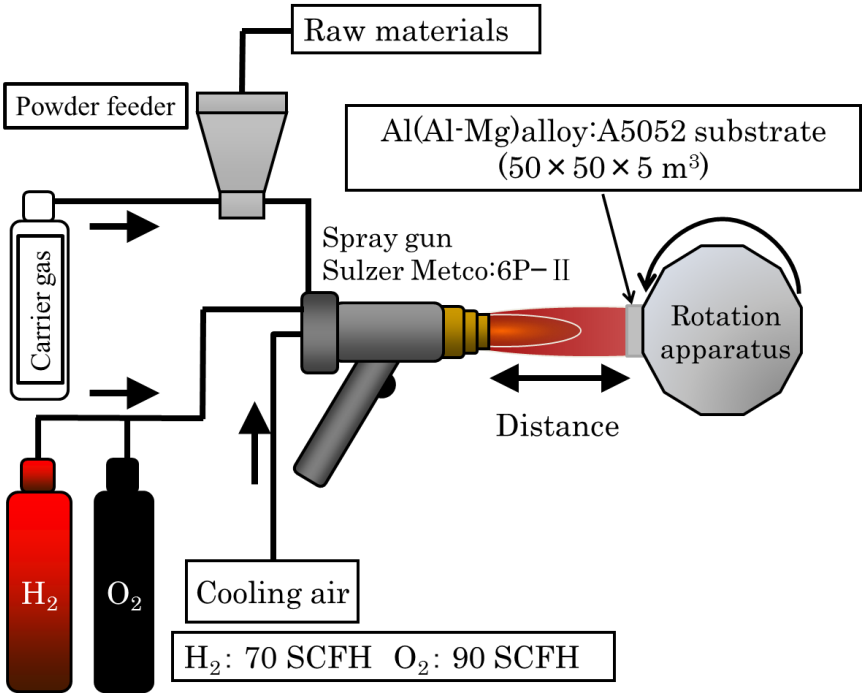

Figure 4-2 Schematic of the films deposited setup for splat morphologies.

Table 4-1 to 4-4 lists the carrier gas O_2 and N_2 used to deposited Er_2O_3 particles morphology with changed the parameters (flow rates of powder, flow rates of carrying gas, distance, rolling velocity, and scan of numbers.) by 45-μm-on and unscreened of raw material EDTA·Er·H powder.

Table 4-1 Experimental conditions of splat morphologies deposited by EDTA・Er・H with change of flow rates of carrying gas. Carrier gas O_2 with sample No. (1) - (4), carrier gas N_2 with sample No. (15) - (18).

No.	Method	Raw material	Flow rates of powder (g/min)	Flow rates of carrying gas (L/min)	Distance (mm)	Scan of numbers	Carrier gas
1 / 15	fixed	45 μm on	0.2	2.4	150	1	O_2 / N_2
2 / 16				4.7			
3 / 17				7.1			
4 / 18				9.5			

Table 4-2 Experimental conditions of splat morphologies deposited by EDTA・Er ・H with change the distance. Carrier gas O_2 with sample No. (5) - (7), carrier gas N_2 with sample No. (19) - (21).

No.	Method	Raw material	Flow rates of powder (g/min)	Flow rates of carrying gas (L/min)	Distance (mm)	Scan of numbers	Carrier gas
5 / 19					100		
6 / 20	fixed	45 μm on	0.2	7.1	130	1	O_2 / N_2
7 / 21					160		

Table 4-3 Experimental conditions of splat morphologies deposited by EDTA・Er H with change of flow rates of powder. Carrier gas O_2 with sample No. (8) - (11), carrier gas N_2 with sample No. (22) - (25).

No.	Method	Raw material	Flow rates of powder (g/min)	Flow rates of carrying gas (L/min)	Distance (mm)	Scan of numbers	Carrier gas
8 / 22			5.0				
9 / 23	fixed	unscreened	10.0	7.1	150	1	O_2 / N_2
10 / 24			15.0				
11 / 25			20.0				

Table 4-4 Experimental conditions of splat morphologies deposited by EDTA・Er・H with change of rolling velocity. Carrier gas O_2 with sample No. (12) - (14), carrier gas N_2 with sample No. (26) - (28).

No.	Method	Raw material	Flow rates of powder (g/min)	Flow rates of carrying gas (L/min)	Distance (mm)	Rolling velocity (rpm)	Scan of numbers	Carrier gas
12 / 26						30		
13 / 27	roll	45 μm on	0.2	7.1	150	75	10	O_2 / N_2
14 / 28						90		

4.2.2 Splat morphology

The splat morphology, microstructure, and composition of the deposited splat were observed using field-emission scanning electron microscopy (FE-SEM, JSM-6700F, JEOL, Japan) equipped with an energy dispersive X-ray spectroscopy (EDX, JED-2201-F, Japan).

The observed surface SEM images were binarized into black and white using ImageJ, the A5052 substrate was white, and the splat was black. Furthermore, the watershed algorithm was used for binarized surface SEM images to separate the splat overlap. Afterward, from the surface images, the circularity of the splat, the ratio of the disk-like splat having a circularity of 0.6 or more, and the splat particle size (area equivalent circle diameter) were calculated [20]. The average circularity of splat, the ratio of the disk-like splat, and splat particle size of the depositing were estimated by over 3 pixels randomly selected from the surface images. That the standard deviation (SD) of each value was calculated. The circularity is shown in Eq. (1).

$$C(\text{Circularity}) = \frac{4\pi A}{p2} \quad (1)$$

where A is the area of the splat, P is the perimeter of the splat. Then, the boundary tracking algorithm is used to determine the boundary determine the boundary from the image contour obtained by binarizing P with the software ImageJ, and the pixel length is added. In addition, when the shape of the splat is close to a disk shape, the circularity approaches one, and the splat that is distorted like the splash has a low circularity.

4.3 Results and discussion

4.3.1 State change of splat with types and flow rates of carrying gas

4.3.1.1 Carry gas types

The parameters expected to affect splat features are in-flight particle temperature. We measured the surface temperature of the particles that were found to be 2400 and 2290 ℃ with carrier gases O_2 and N_2 in the previous series of experiments[17]. Surface SEM and binary images of Er_2O_3 splats deposited on A5052 substrate by

changing carrier gas types, as shown in Fig.4-3. It was confirmed that the splat size deposited with O_2 as a carrier gas was small. By contrast, the splat size was large as well as many splash-like shaped and porous splats present on surface in N_2 gas, as shown in **Fig.**4-3 (a_1) and (c_1). In addition, through the image processing techniques to process the **Fig.**4-3(a) and (b) that are employed to lessen the noise effects and to improve the contrast and the results as shown in **Fig.**4-3 (b) and (d). Thus, the splat circularity, disk-like ratio, splat particle size, and standard deviation (SD) were calculated from the surface SEM images, as shown in **Table** 4-5. Furthermore, the circularity and splat particle size were shown in the column chart of the **Fig.**4-4 (a) and (b). From those conditions, in the case of the O_2 as a carrier gas, the circularity and the ratio of the disk-like shape were higher than those of N_2. In addition, have a large number of splat particle size were less than 15 μm using the O_2 as the carrier gas, and the average value was found to be about half of that using the carrier gas of N_2. Furthermore, the splat particle size has a wide distribution in column chart of the Fig.4-4 (b) using the N_2.

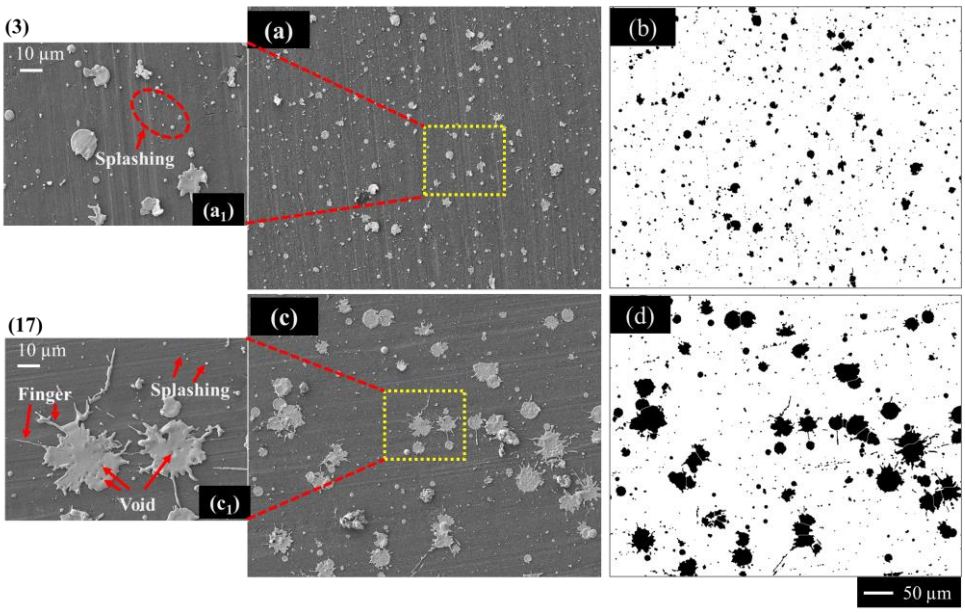

Figure 4-3 Surface SEM images of Er_2O_3 splats deposited on A5052 substrate by changing carrier gas. O_2: Sample (3), N_2: Sample (17). (a), (c) SEM images, (a_1), (c_1) enlarge images, (b), (d) binary images.

Table 4-5 Results of Er_2O_3 splats deposited on A5052 substrates with different carrier gas flow rates.

Carrier gas	Circularity / SD (-)	Disk-like ratio / SD (%)	Splat particles size / SD (μm)
O_2	0.70 / 0.02	72.7 / 7.2	10.6 / 0.3
N_2	0.64 / 0.01	47.0 / 9.4	18.1 / 0.7

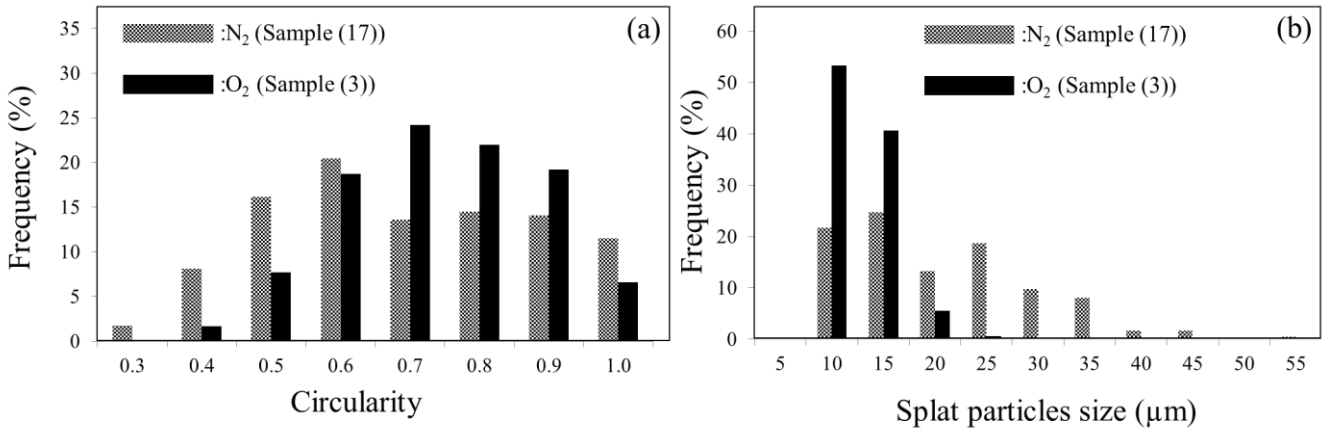

Figure 4-4 Results of Er_2O_3 splats deposited on A5052 substrate by various carrier gases (O_2, N_2): (a) Splats circularity (b) Splats particle size.

Compared to carrier gas of O_2, the ratio of disk-like shape decreased and the splat particle size increased in N_2. The reason is thermal decomposition and oxidation reaction of the EDTA metal complex used as a raw material. For instance, EDTA· M· H(M: metal species) reacts with O_2 to form the metal oxide film by Eq.(2).

$$2EDTA\cdot M\cdot H+24O_2 \rightarrow M_2O_3+20CO_2+13H_2O+4NO_2 \quad (2)$$

Therefore, it is considered that when the carrier gas is changed from O_2 to N_2, the reaction process is inhibited, the thermal energy of flying particles decreases, and the particle temperature decreases. On the other hand, it has been reported that the splat shape is affected by the thermal conductivity of the substrate. From this research, the thermal conductivity of the substrate is high, it(depositing splat) freezes quickly before the splats are formed, and resulting in a splash-like shape [21]. It's worth noting that

the splats are deposited on metals with high thermal conductivity (138 W/mK), such as aluminum alloy, the cooling rate of the particles increases. Thus, it means that the in-flight particle temperature is low, the solidification is semi-solidified at the time of impacting due to its cooling rate and scatters to form splats having a poor shape such as a splash. In previous research, it is known that the EDTA metal complexes are decomposed by endothermic reactions in a nitrogen atmosphere and exothermic reactions in the air atmosphere to form metal oxides. This may be the reason for the size of the splat, the carrier gas of O_2 can be shown the main disk-like shape and the N_2 can be deposited the many splashes shape. Thus, it is considered that N_2 is likely to increase the porosity in coatings because of lower flame temperature.

4.3.1.2 Flow rates of carrying gas

Fig.4-5 (1), (2), (4) and (15), (16), (18) shows the surface SEM images of Er_2O_3 splats deposited on A5052 substrate with different carrier gas flow rates of O_2 and N_2, respectively. In the case of O_2, splats with a flow rate of 4.7 L/min were found to be slightly larger, and the same as N_2. In addition, when the flow rate drops to 2.4 L/min of N_2, the number of splats decreases. In especially, it was seen that the splats to be slightly smaller as the flow rate reaches to 9.5 L/min. In N_2, deposited the splats size were larger in all conditions of flow rates compared those with O_2, as shown in surface images. Next, the circularity, disk-like ratio and splat particle size of these splats with SEM images were quantified, and the results were listed in **Table** 4-6. In carrier gas of O_2 with different flow rates, the effect on circularity and disk-like ratio are small. However, it is easier to change the splat particle size in varying degrees, for example, the splat particles size is 13.2 μm at flow rate of 4.7 L/min, that is reduced 10.6 μm at 7.1 L/min and it also to prove why is density films of Er_2O_3 in this conditions [17]. Comparing the N_2 with different flow rates, it was found that as the flow rate increased, the circularity and the ratio of disk-like shape increased. However, the splat particle size is reduced. Describes the effect of carrier gas on flying particles and flame, as shown below Eq.(3) [22]:

$$M_F = \frac{M_{Powder}}{M_{\text{jet stream}}} \quad (3)$$

Where M_F is the powder-to-jet mass flow ratio parameter, $M_{\text{jet stream}}$ is the mass flow of the gases composing the jet stream (g/min), and M_{powder} is the powder feed rate (g/min).

This equation suggests that if the value of M_F is large, the load applied to the flame is large, so that the particle temperature and the particle velocity decrease. In addition, it is generally considered that if the flow rate of the carrier gas is reduced with the same raw material feed rate, the M_F increases. This reduces the initial velocity and thermal energy of the flying particles, thus, resulting in a change in particle morphology of deposition. Furthermore, as mentioned above, the temperature and velocity of the in-flight particles were measured at nozzle-substrate distances of different parameters [17]. Same as that method, the temperature and velocity of the in-flight particles with EDTA・Er・H for each carrier gas and flow rate as a function of the nozzle-substrate distance, as shown in **Tables** 4-7 and 4-8. At the nozzle-substrate distance of 150 mm, the temperatures and velocity were 2620 ℃ and 102 m/s at the flow rate of 4.7 L/min, and those were that 2600 ℃ and 90 m/s at the flow rate of 9.5 L/min. Thus, same as the nozzle-distance (150 mm), there is a tendency for the particle velocity to increase as the flow rate decreases. It is considered to be because the M_F of the Eq. (3) decreases with an increase in the flow rate of the carrier gas O_2, but the mass flux of the flame decreases due to the increased flow rate. As we all known, since 80% of air is N_2, it is considered that the particle velocity shows the same tendency when it is used as the carrier gas. The particle temperatures are also found to be lower than carrier gas of O_2 and air from previous research [17].

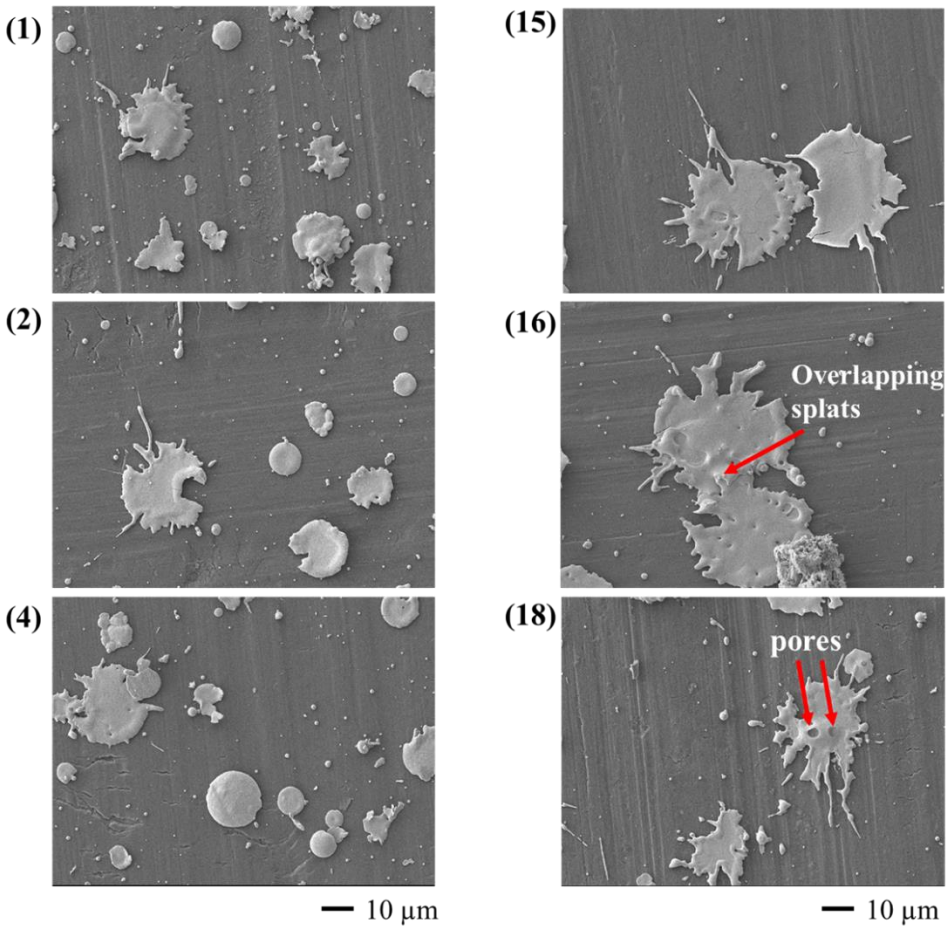

Figure 4-5 Surface SEM images of Er_2O_3 splats deposited on A5052 substrate with different carrier gas flow rates. O_2(1) / N_2(15): 2.4 L/min, O_2(2) / N_2(16): 4.7 L/min, O_2(4) / N_2(18): 9.5 L/min.

Table 4-6 Results of samples in which Er_2O_3 splats were deposited on A5052 substrate by changing the flow rate of carrier gas.

No. / carrier gas	Flow rates of carrying gas (L/min)	Circularity / SD (-)	Disk-like ratio / SD (%)	Splat particles size / SD (μm)
(1) / O_2	2.4	0.69 / 0.02	69.4 / 2.9	11.9 / 0.6
(2) / O_2	4.7	0.70 / 0.02	72.3 / 3.4	13.2 / 1.0
(3) / O_2	7.1	0.70 / 0.02	72.7 / 7.2	10.6 / 0.3
(4) / O_2	9.5	0.68 / 0.01	69.6 / 3.0	11.0 / 0.3
(15) / N_2	2.4	0.53 / 0.00	31.7 / 8.6	22.5 / 0.7
(16) / N_2	4.7	0.56 / 0.01	38.1 / 3.3	23.4 / 0.5
(17) / N_2	7.1	0.64 / 0.01	47.0 / 9.4	18.1 / 0.7
(18) / N_2	9.5	0.61 / 0.01	52.0 / 1.0	15.5 / 0.6

Table 4-7 Temperatures of the in-flight particles with EDTA・Er・H propelled in the H_2-O_2 combustion gas mixture at different nozzle-substrate distances and carrier-gas flow rates while using O_2 as the carrier gas.

Nozzle-substrate distance(mm)	In-flight particle	4.7 L/min	9.5 L/min
110	Temperature(°C)	2280	2330
	Velocity(m/s)	129	114
130	Temperature(°C)	2450	2500
	Velocity(m/s)	111	109
150	Temperature(°C)	2490	2500
	Velocity(m/s)	102	93
170	Temperature(°C)	2430	2470
	Velocity(m/s)	90	83

Table 4-8 Temperatures of the in-flight particles with EDTA・Er・H propelled in the H_2-O_2 combustion gas mixture at different nozzle-substrate distances and carrier-gas flow rates while using Air as the carrier gas.

Nozzle-substrate distance(mm)	In-flight particle	4.7 L/min	9.5 L/min
110	Temperature(°C)	2700	2730
	Velocity(m/s)	140	108
130	Temperature(°C)	2650	2660
	Velocity(m/s)	123	100
150	Temperature(°C)	2620	2600
	Velocity(m/s)	102	90
170	Temperature(°C)	2510	-
	Velocity(m/s)	84	-

It is clearly seen that the effect of carrier gas flow rate on splats circularity, disk-like ratio, and splat particle size in **Fig.**4-6. In this case of O_2, the circularity and flow rate change are almost linear (**Fig.**4-6(a)), that the changes have no significant effect on the results. An interesting finding is that the ratio is closer to use the N_2 at 7.1 L/min. In addition, when using the O_2 as a carrier gas, the follow rate at maximum (9.5 L/min) and minimum (2.4 L/min), more smaller size splat on the surface images to increase, however, more the larger-size splat at 4.7 L/min. The difference is that when N_2 as the carrier gas, the splat particle size becomes smaller as the flow rate increases with the exception of the 4.7 L/min (same as O_2), as shown in **Fig.**4-6 (c). Furthermore, the effect can be appreciated by comparing results circularity and splat particle size in histograms **Fig.**4-7 and 4-8. When the gas flow rate decreased, the frequency of which the 0.7(0.61 to 0.69) and 0.8(0.71 to 0.79) decreased, as well as the splat of 0.6(0.51 to 0.59) tended to increase, in O_2. When the N_2 as the carrier gas, which the flow rate 9.5 to 2.4 L/min, the splats with circularity of 0.4(0.31 to 0.39) and 0.6(0.51 to 0.59) to increase. In addition, as the flow rate increased, the number of smaller splats increased, and the distribution of the splat particle-sized tended to narrow.

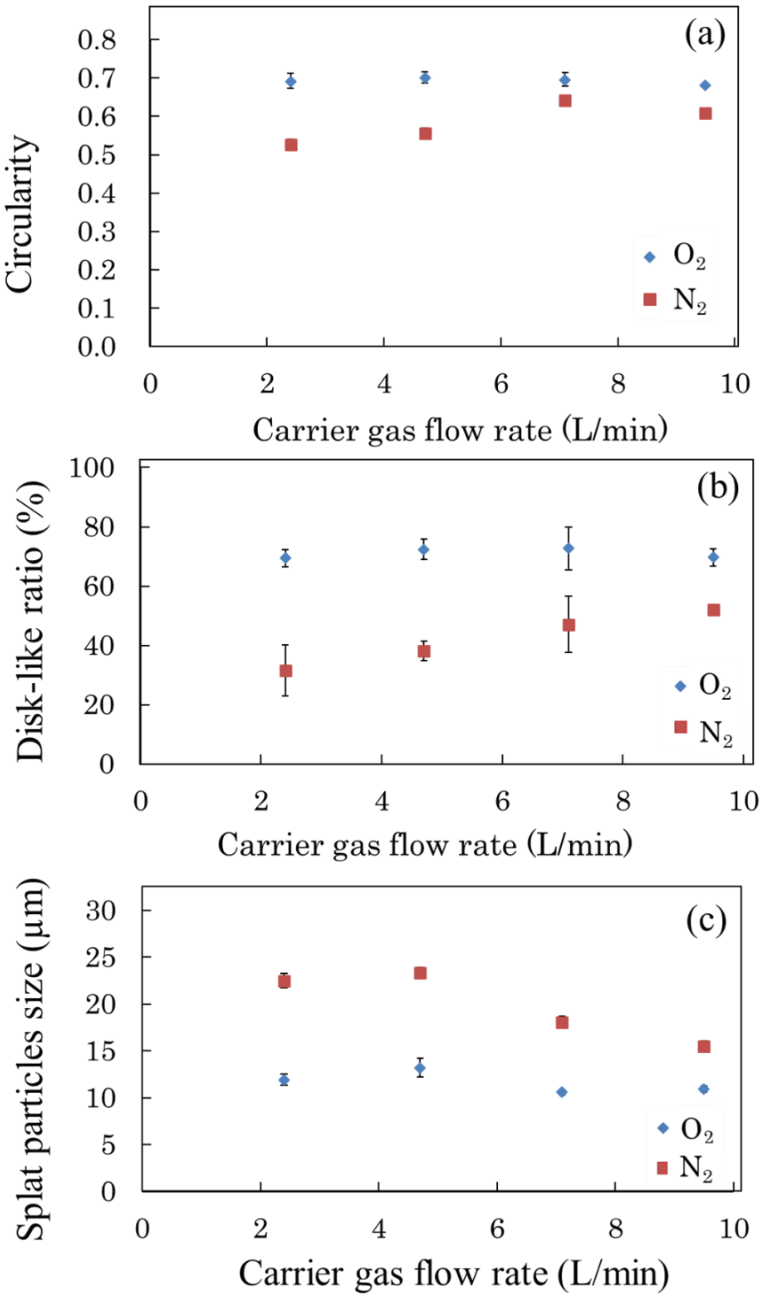

Figure 4-6 Results of Er_2O_3 splats deposited on A5052 substrates with different carrier gas flow rates. (a) Splats circularity (b) Disk-like ratio (c) Splats particle size.

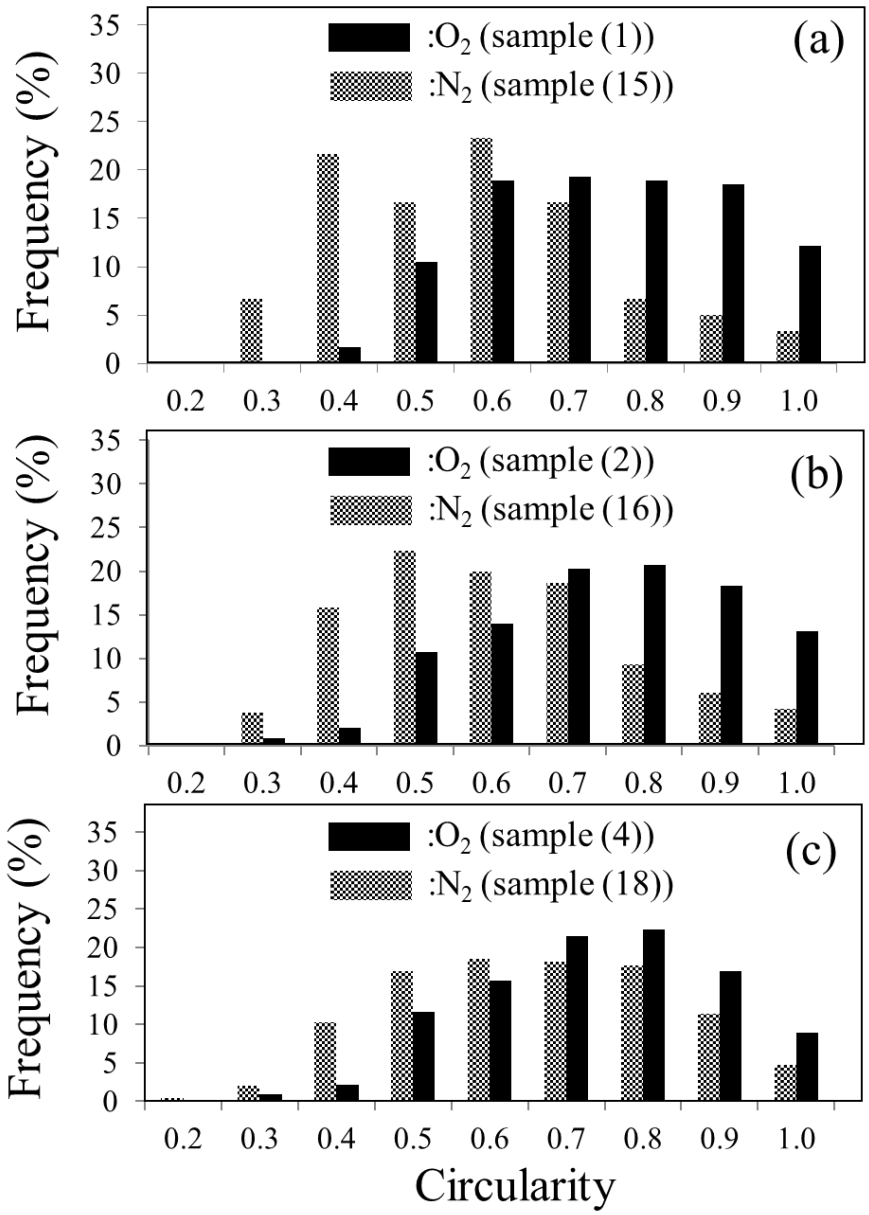

Figure 4-7 Circularity of Er_2O_3 splats deposited on A5052 substrates with different carrier gas flow rates. (a) 2.4 L/min (b) 4.7 L/min (c) 9.5 L/min.

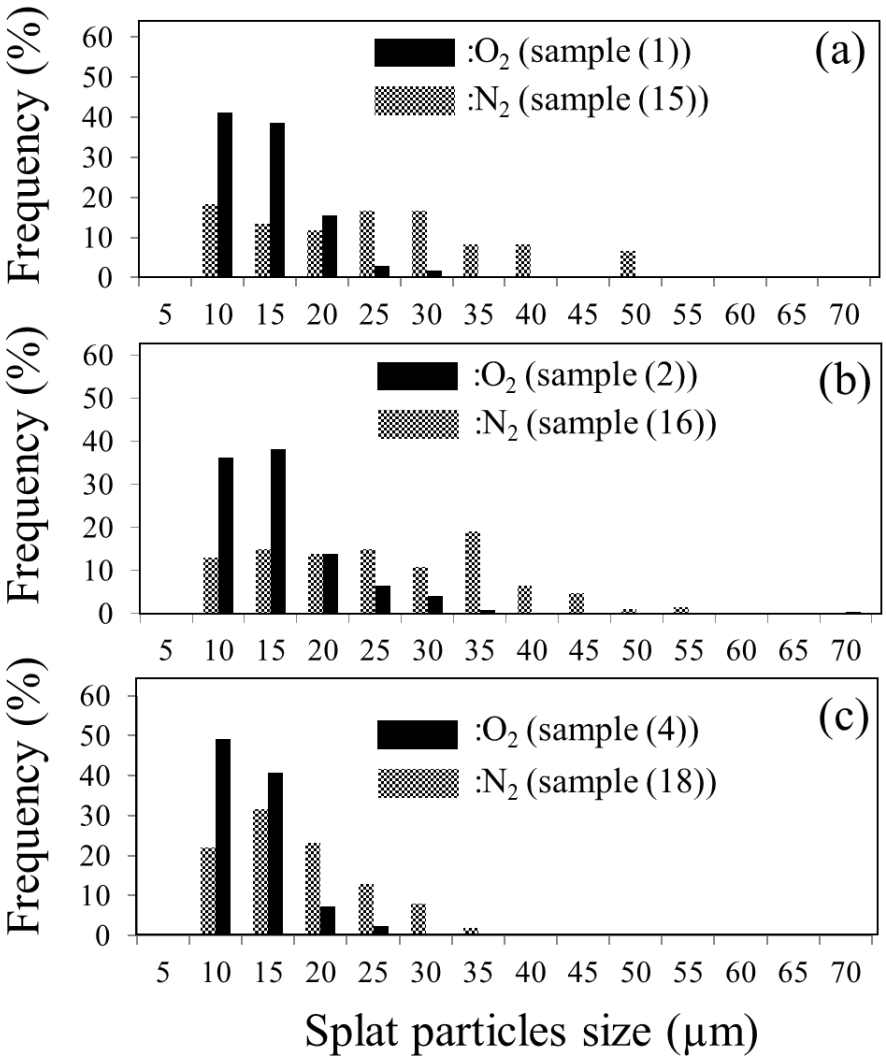

Figure 4-8 Particle size of Er_2O_3 splats deposited on A5052 substrates with different carrier gas flow rates. (a) 2.4 L/min, (b) 4.7 L/min, (c) 9.5 L/min.

For this fact, it is considered that the splats with low circularity increased because the particle velocity increased at the same temperature and the molten droplets scattered during the impact. And the same result was also reported in the plasma spray system [21,23]. This indicates that CFS method can be expected to have the same potential for synthesizing coatings.

4.3.2 State change of splat with nozzle-distance

The surface SEM images of the samples in which Er_2O_3 splats are deposited on the

A5052 substrate while changing the distance between the spray-gun and substrate, with the carrier gas O_2 and N_2, as shown in **Fig.**4-9 (5-7), (19-21). Those were found that the closer the distance from to substrate (distances of 100-160 mm), the more splats, and the smaller size the splats with both carrier gas O_2 and N_2. Compared to O_2, there were bigger size splats deposited on the substrate. In addition, it turns out that there were many porous splats with carrier gas O_2, at distance was 100 mm. However, same as the distance with O_2, one of the basic splat types was observed, which the closely ideal disk-shaped splat with very small irregularities and a high microcrack density by carrier gas N_2, as shown in **Fig.**4-9(19). They were also classified into the four basic splat types documented in previous research [24]. Furthermore, the interesting phenomenon can be observed that is the porous morphology on splat, as shown in **Fig.** 4-9 (21). This is the reason why as the spraying distance becomes longer, the hang time of flying particles increases, resulting in the decrease in particle temperature and the tendency to form the porous morphology.

Based on the SEM images (Fig.4-9), the splat circularity, disk-like shaped ratio, and average of splat particle size were calculated, the results listed in **Table** 4-9(sample (3) as the comparison value). In the case of O_2, the percentage of disk-like decreased from 77.3 % to 58.9 %, as the distance to change with 100 mm to 130 mm, and at 160 mm, the percentage increased to 81.5 %. Except for the spray distance of 130 mm, the increase of the spraying distance did not significantly change the circularity of the splats by evaluation results. However, as the spraying distance increases (150 and 160 mm), the splat particle size becomes significantly smaller (10.6 and 10.7 μm). Firstly, particle velocity and particle temperature in flying decrease with the distance between the substrate, and then, since the splat particle size becomes smaller as the distance between the spray-gun and the substrate to longer, it can be considered that the molten particle diameter(or size) of the flying becomes smaller with the standoff distance [25]. Moreover, the circularity and the ratio of disk-like splats increased at standoff distance of 100 mm. One reason is that it can confirm splat with convex in the SEM images(Fig.4-9 (5)), and it may be because the spraying distance is short, resulting in un-melted splats on the substrate. Finally, in this method, EDTA as the precursor and

complex with metal to synthesis splat. Thus, it decomposes and oxidizes in the flame, so there are points where flying particle size is rapidly reduced. It is considered that small size flying molten particles increase as close to the boundary point (or decomposition point). Therefore, the amount of smaller size splats can be observed on the substrate at a standoff distance of 100 mm. From this fact, those could be explained that the flying molten particle of after decomposed also causes the circularity and the ratio of the disk-like shape to decrease at standoff distance 130 and 150 mm. On the other hand, when the N_2 as a carrier gas, it is seen that un-melted splats increase in SEM images, the circularity and ratio of disk-like shape splat with a decrease to compared with O_2. Based on the results, the circularity increases at 150 mm, and decreases at 160 mm. The ratio of the disk-like shape tends to decrease with the standoff distance, but the splat size tends to become smaller at the standoff distance of 150 mm. In addition, the splat size increased at standoff distance of 130 mm, the reason why is that the flying particle size is large that carrier gas O_2, result in the particle velocity may be faster. Hence, it melted moderately at 130 mm to deposit the large splash splat on the Al alloy substrate. Furthermore, it is clearly seen that the number of porous present in splats are confirmed with marking line (**Fig.**4-9 (19, 21)). Therefore, when the carrier gas N_2 is used, it can be said that the porosity can be greatly increased with distance.

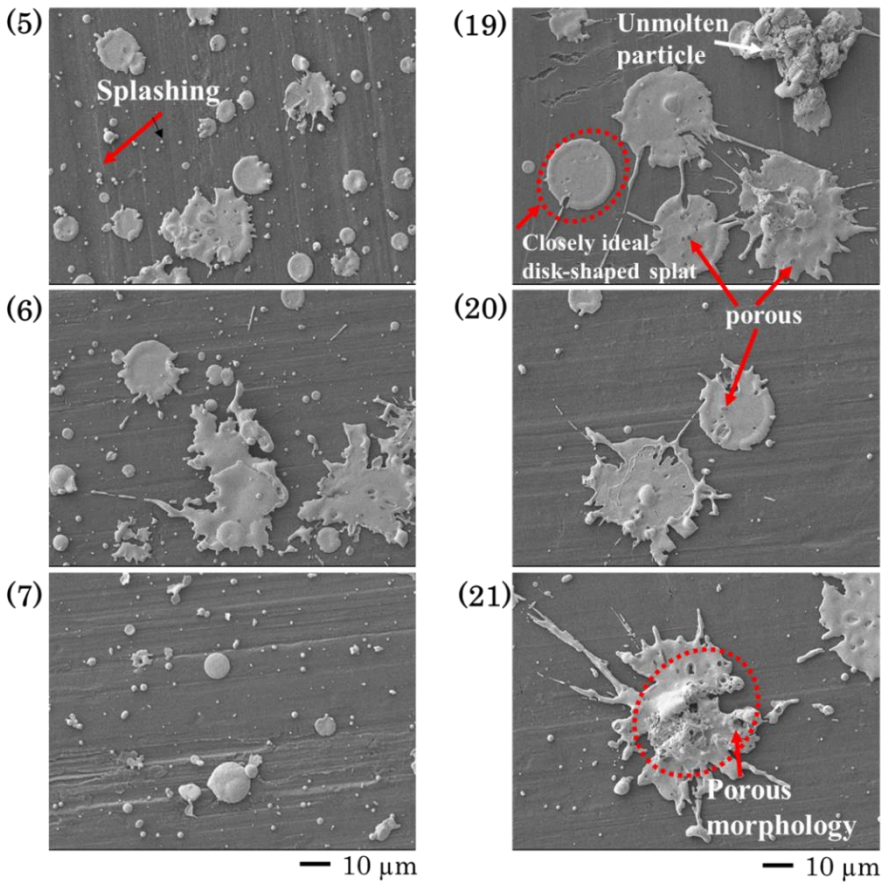

Figure 4-9 Surface SEM images of Er_2O_3 splats deposited on A5052 substrate with different nozzle-substrate distance. O_2(5) / N_2(19): 100 mm, O_2(6) / N_2(20): 130 mm, O_2(7) / N_2(21): 160 mm.

Table 4-9 Results of samples in which Er_2O_3 splats were deposited on A5052 substrate by changing the nozzle-substrate distance.

No. / carrier gas	Nozzle-substrate distance (mm)	Circularity / SD (-)	Disk-like ratio / SD (%)	Splat particles size / SD (μm)
(5) / O_2	100	0.72 / 0.02	77.3 / 5.2	13.3 / 0.2
(6) / O_2	130	0.65 / 0.02	58.9 / 5.8	13.1 / 0.1
(3) / O_2	150	0.70 / 0.02	72.7 / 7.2	10.6 / 0.3
(7) / O_2	160	0.71 / 0.02	81.5 / 5.3	10.7 / 0.2
(19) / N_2	100	0.63 / 0.02	56.3 / 5.5	20.4 / 0.6
(20) / N_2	130	0.60 / 0.02	52.0 / 7.2	23.0 / 1.2
(17) / N_2	150	0.64 / 0.01	47.0 / 9.4	18.0 / 0.7
(21) / N_2	160	0.59 / 0.03	45.7 / 8.2	16.0 / 2.3

4.3.3 State change of splat with flow rates of powder

Using the carrier gas of O_2, **Fig.** 4-10(8-11) shows the typical morphologies of Er_2O_3 splats obtained on different powder feed rates at 5 g/min, 10 g/min, 15 g/min, and 20 g/min, respectively. Macro, there was no significant change in splat morphology. In the case of the N_2 as a carrier gas, it was observed that the number of splats decreased and the splat size to be smaller as a consistent raise in powder feed rate, as shown in Fig.4-10 (22-25). Both contrast, the use of different gases with O_2 and N_2, there are significant differences in the morphology of particles and the number of the splats. **Table** 4-10 shows the temperatures of the in-flight particles at different powder feed rate with 10 g/min and 20 g/min by using the carrier gas O_2, respectively. It can be seen that the powder feed rate raises from 10 g/min to 20 g/min, the particle temperature and particle velocity of the flying particles tend to lower. In other words, this can be explained by Eq (3) shown by F. Fanicchia et al. as the powder feed rate increases with M_{powder}, result in the loading effect to increase. This is the reason why the velocity and the temperature of particle decreased in this method. Furthermore, the effect of in-flight particle parameters on particle melting, the equations are as follows [22, 26]:

$$\int_0^{\tau} Q_{int} \cdot dt > Q_M \quad (4)$$

$$\tau = \frac{SOD}{V_p} \quad (5)$$

$$Q_{int} = h\left(\pi {d_p}^2\right)\left(T_\infty - T_p\right) - \left(\pi {d_p}^2\right)\epsilon\sigma_s\left({T_p}^4 - {T_\alpha}^4\right)\,[W] \quad (6)$$

$$Q_M = \frac{4}{3}\pi\rho_p {d_p}^3\left(C_p(T_m - T_0) + L_m\right)\,[J\,] \quad (7)$$

Where Q_{int} is the heat transferred to the particles during the flight, Q_M is the heat required to melt the particle, τ is the particle in-flight dwell time, SOD is the standoff distance, V_p is the particle velocity, d_p, ρ_p, and C_p are the particle diameter, density and specific heat, respectively, h is the convective heat transfer coefficient, T_∞ is the flame temperature at the particle surface, ε is the particle emissivity, σ_s is the Stefan Boltzmann constant, T_p and T_α are the temperatures of the particle and surroundings, and T_m, T_0 and L_m are the particle melting and initial temperature and latent heat of fusion, respectively. In those equations, assumed, neglecting thermal conduction within the particle and oxidative phenomena. Thus, when Q_{int} is higher than Q_M , the particles

in the flame are melted. Those equations suggest that as the powder feed rate increased, it result in raise the loading effect, next to lower the temperature and velocity of the in-flight particle, resulting in a drop the heat transferred (Q_{int}) and the particle velocity, which had a negative on splat melting and diffusion. In other words, it can be concluded that with the powder feed rate increases, the temperature and velocity of the particle to be lower, as well as the diffusion during splat formation deteriorate. On the other hand, through the rapid solidifying of the splat according to the thermal conductivity of the A5052 substrate, it can be expected that the ratio of the splash-like and un-melted particles or the re-solidified splats will increase because of the deterioration to be worse. Furthermore, the circularity, ratio of the disk-like, and the splat particle size calculated from the surface SEM images (Fig. 4-10), as listed in **Table** 4-11. The results of using the carrier gas of N_2 showed that the circularity and ratio of the disk-like tended to increase with the raise the powder feed rate. Based on the obvious analysis, it is reasonable to understand that M_{powder} and Q_{int} values of the flying particles increase, result in the each of the temperature to drop, which is not enough to all of the in-flight particles reach the melting point and decomposition of EDTA·Er·H, it can be considered that the adhesion rate to lower at the powder feed rate of 20 g/min. Therefore, it is reasonable to hypothesize that the effect of the powder feed rate and carrier gas type to EDTA·Er·H in this study would design the porous or dense splat, and which can be expected to improve the mechanical properties by the chelate flame spray method.

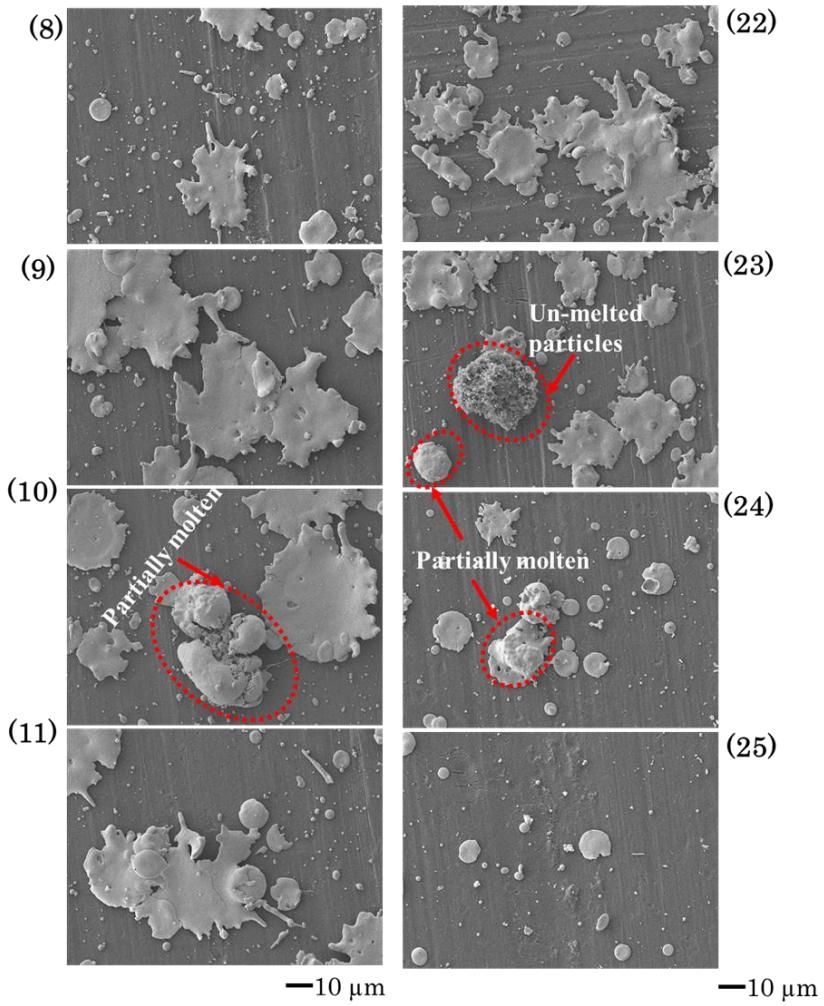

Figure 4-10 Surface SEM images of Er_2O_3 splats deposited on A5052 substrate with different flow rates of powder. O_2(8) / N_2(22): 5 g/min, O_2(9) / N_2(23): 10 g/min, O_2(10) / N_2(24): 15 g/min, O_2(11) / N_2(25): 20 g/min.

Table 4-10 Temperatures of the in-flight particles with EDTA・Er・H propelled in the H_2-O_2 combustion gas mixture at different nozzle-substrate distances and powder feed rate while using O_2 as the carrier gas.

Nozzle-substrate distance(mm)	In-flight particle	10 g/min	20 g/min
110	Temperature(°C)	2600	2200
	Velocity(m/s)	230	92
130	Temperature(°C)	2640	2300
	Velocity(m/s)	170	90
150	Temperature(°C)	2610	2400
	Velocity(m/s)	115	86
170	Temperature(°C)	2550	2420
	Velocity(m/s)	85	80

Table 4-11 Results of samples in which Er_2O_3 splats were deposited on A5052 substrate by changing the flow rates of powder.

No. / carrier gas	Flow rates of powder (g/min)	Circularity / SD (-)	Disk-like ratio / SD (%)	Splat particles size / SD (μm)
(8) / O_2	5.0	0.66 / 0.02	65.8 / 4.6	15.4 / 1.1
(9) / O_2	10.0	0.67 / 0.01	66.8 / 3.6	16.4 / 0.4
(10) / O_2	15.0	0.70 / 0.01	71.6 / 2.1	17.3 / 0.9
(11) / O_2	20.0	0.67 / 0.01	65.8 / 3.0	16.8 / 0.8
(22) / N_2	5.0	0.66 / 0.01	63.6 / 2.5	15.4 / 0.4
(23) / N_2	10.0	0.70 / 0.02	75.0 / 2.5	13.6 / 0.6
(24) / N_2	15.0	0.79 / 0.01	88.5 / 1.1	11.6 / 0.4
(25) / N_2	20.0	0.80 / 0.04	87.9 / 4.8	10.2 / 0.2

4.3.4 State change of splat with rotation velocity

Fig.4-11 shows SEM surface images of the obtained sprayed on A5052 substrate with carrier gas O_2 (sample 12, 13, 14) and N_2 (sample 26, 27, 28) condition. In the previous study, we used the contact thermometer to measure the temperature of the substrate

after spraying at 579, 454, 441 K for each rotation speed (30, 75, 90 rpm) [27].

In SEM image analysis, the splat types of the deposited differ significantly (fingering, splashing, void, microcrack, partially molten, and malformed splats). For carrier gas O_2, a larger flower-shaped depositing pattern and splashing of the particle posterior to impact that can be observed at rolling velocity is 30 rpm, in **Fig.**4-11 (12). In addition, it was found that the particle from flower-shaped to disc splat formed as the rotation velocity increased with 75 rpm to 90 rpm, as shown in **Fig.**4-11 (13), (14). On the other hand, the splat microstructure of the carrier gas N_2, which the deposited disc-splat size is relatively uniform. In addition to the same as carrier gas O_2, the deposited size becomes smaller as the rotation speed increases. It is clearly to be observed that the overlapping and microcrack in **Fig.**4-11 (26). In the case of rotation velocity is 75 rpm, produced the partially molten in the splats, as shown in **Fig.**4-11 (27). The long finger of the splats are clearly observed at higher rotation velocity (90 rpm) are determined from SEM photos in **Fig.**4-11(28). The formation could be caused by molten particles impact in high-speed rotation of the substrate that results in a rotational force for the deposited splats [28]. On the other hand, splats resulting from freezing-induced splashing are different in appearance from those that fragmented during impact (Fig. 4-11(13) and (28)). Thus, molten particles impact the lower temperature substrate and instant coagulation, and then the occurrence of the irregular periphery is increasing. For the above phenomenon, the deposited splat size of the carrier gas N_2 was found to be greater than the O_2.

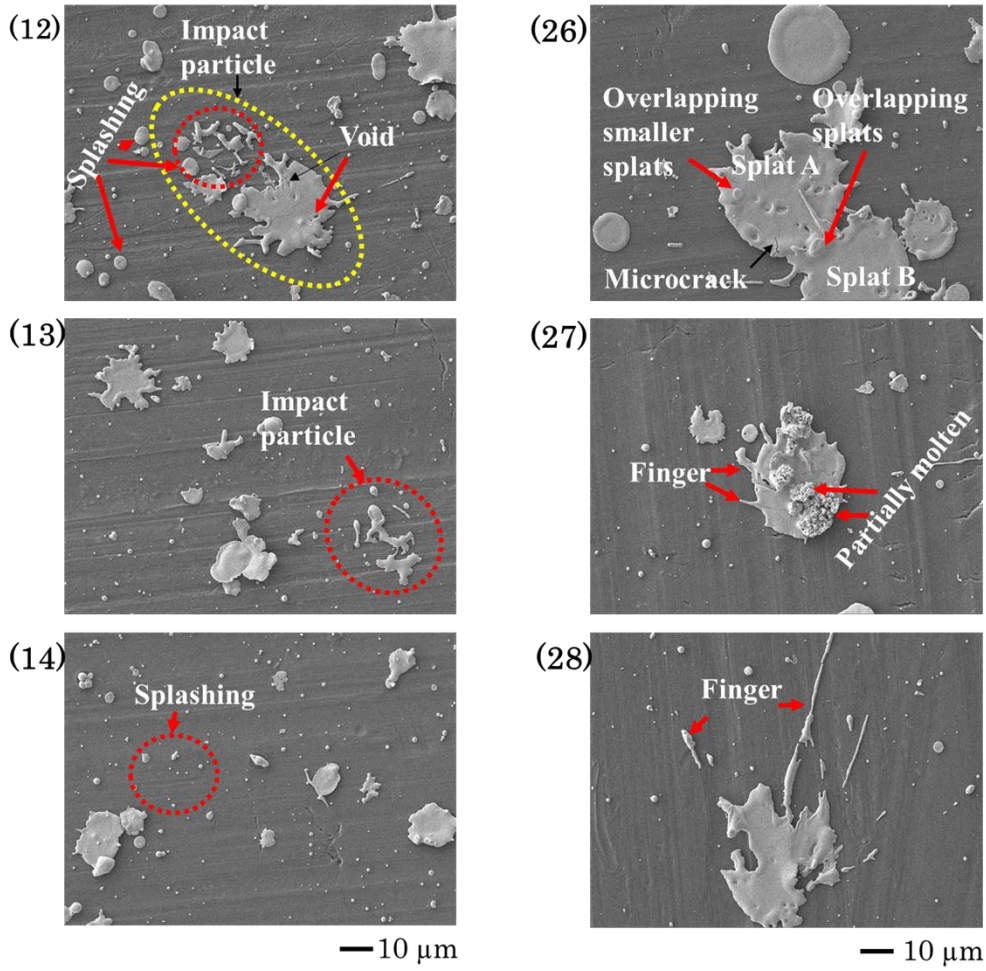

Figure 4-11 Surface SEM images of Er_2O_3 splats deposited on A5052 substrate with different rolling velocity. O_2(12) / N_2(26): 30 rpm, O_2(13) / N_2(27): 75 rpm, O_2(14) / N_2(28): 90 rpm.

In addition, through the surface images which the degree of circularity, the disk-ration, and the splat size of the deposited particles under the respective rotation velocity conditions in the case of carrier gas O_2 and N_2 were calculated (Eq.1), as shown the **Table** 4-12. From the results of calculated, both carrier gas of O_2 and N_2 showed a decrease in circularity and disk-like ration which the 75 rpm rotation condition. In the case of 90 rpm which these values are increasing. Comparing two carrier gases, it was found that O_2 had a higher degree of circularity and disk-shaped while the smaller splat particle. In addition, both of the gases which as the number of rotations increased, the

splat size tended to decrease and its concentration in 10 - 15 μm, as shown in **Fig**.4-12. The column chart of the **Fig**.4-13 shows the circularity of Er_2O_3 splats deposited on A5052 substrates with different rolling velocity. In the case of O_2, the splats with the circularity of 0.8(0.7 to 0.79) increased as the rotation velocity increased. It is clearly seen that the splats having a circularity of 0.9(0.8 to 0.89) increased at rotation velocities of 30 rpm and 90 rpm. Furthermore, it was obvious found that the splats with the circularity of 0.6(0.5 to 0.59), 0.7(0.6 to 0.69), 0.9(0.8 to 0.89) increased as the rotation velocity increased when the N_2 as a carrier gas. Finally, carrier gas as the O_2 had more splats with higher circularity and ratio of small splats, comparting with N_2. Furthermore, the distribution of O_2 splat particle size was found to be narrow.

Table 4-12 Results of samples in which Er_2O_3 splats were deposited on A5052 substrate by changing the rolling velocity.

No. / Carrier gas	Rolling velocity (rpm)	Circularity / SD (-)	Disk-like ratio / SD (%)	Splat particles size / SD (μm)
(12) / O_2	30	0.72 / 0.01	77.7 / 4.0	12.0 / 0.5
(13) / O_2	75	0.70 / 0.00	74.3 / 3.5	10.4 / 0.4
(14) / O_2	90	0.74 / 0.02	84.1 / 7.2	10.2 / 0.5
(26) / N_2	30	0.70 / 0.02	69.7 / 6.4	17.3 / 0.7
(27) / N_2	75	0.66 / 0.00	61.8 / 5.3	14.4 / 0.4
(28) / N_2	90	0.70 / 0.01	73.1 / 1.11	13.8 / 1.8

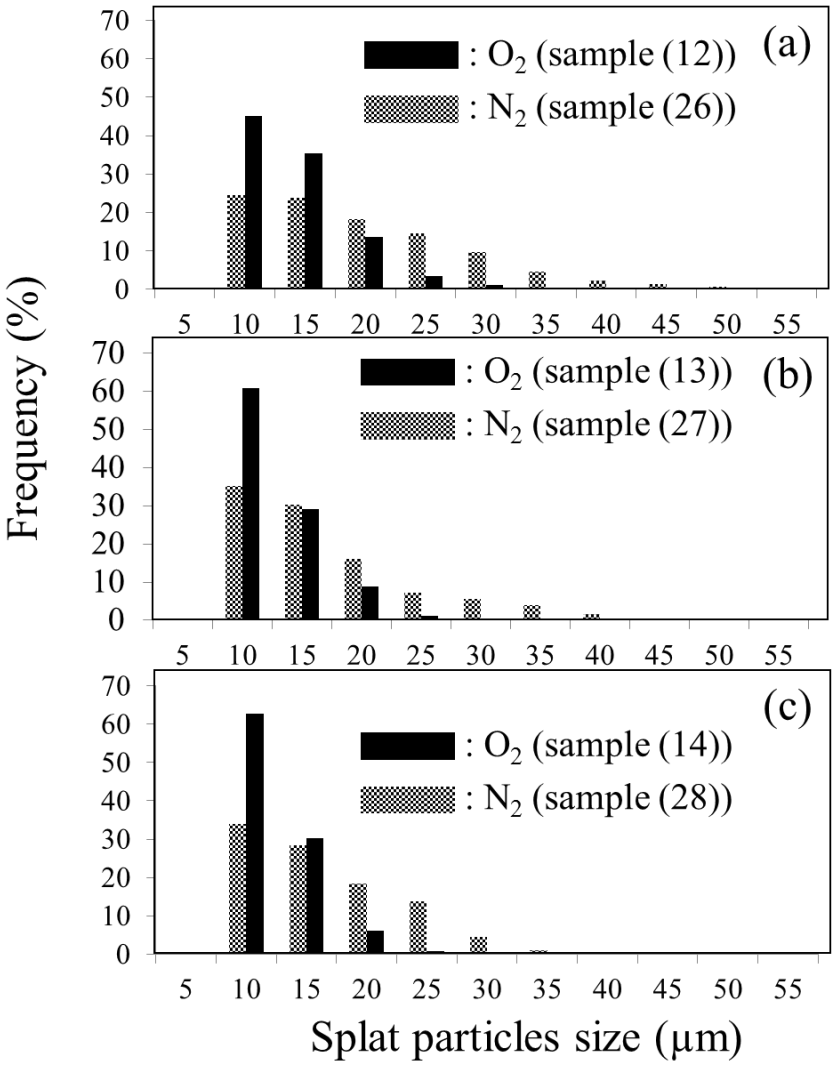

Figure 4-12 Particle size of Er_2O_3 splats deposited on A5052 substrates with different rolling velocity. (a) 30 rpm, (b) 75 rpm, (c) 90 rpm

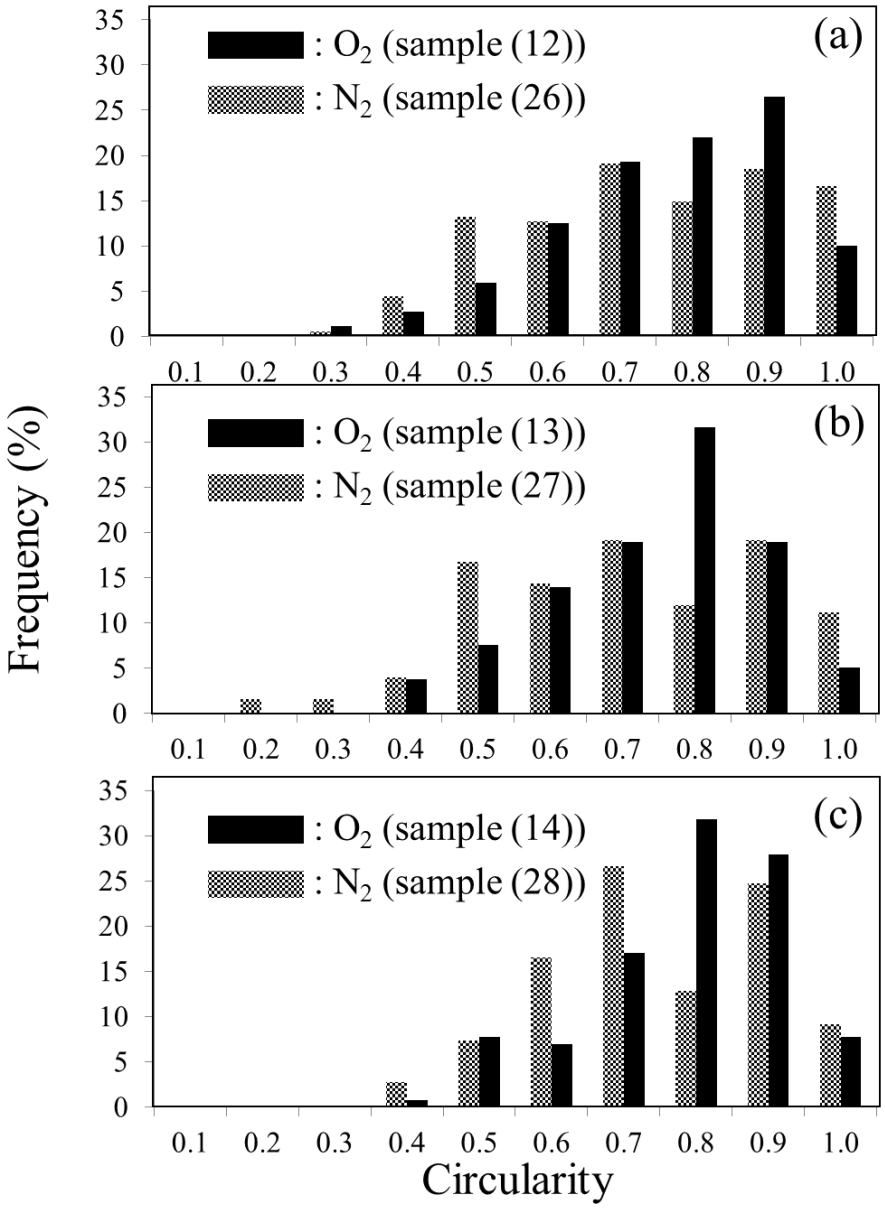

Figure 4-13 Circularity of Er_2O_3 splats deposited on A5052 substrates with different rolling velocity. (a) 30 rpm, (b) 75 rpm, (c) 90 rpm.

The effect of rolling velocity(rpm) with circularity, disk-like ratio and splat particle size shown in **Fig.**4-14. The circularity, disk-like ratio decreased with rolling velocity is 75 rpm, in contrast, it is increased at 90 rpm, as carrier gases with O_2 and N_2. In addition, it was clearly seen that the splat particle size tended to decrease with the rolling velocity, as shown in **Fig.**4-14 (c). The reason why is that can be seen from the above-mentioned, as the rolling velocity increases with the substrate temperature decreases. It is also considered that the substrate when the rolling velocity is increased to reduce the scan time corresponding to the flame, and the substrate temperature during deposition is also decreased. When the substrate temperature is low that the temperature gradient between the splat and the substrate increases to effect of the cooling rate increases. Therefore, when the flying particles impact with the substrate, they solidify or partially molten before flattening, so that the number of splashing or splats that cannot be flattened increases. From the above conditions, it is considered that the splash-like shape increased. As a result, the circularity and the disk-like ration were reduced at the rotation velocity was 75 rpm. In addition, since the splat particle size has decrease and it is considered that the re-solidified particle has also increased. At the 90 rpm, the splat particle size further decreased, and the number of re-solidified particles and non-flat splats increased as well as the circularity was increased on the surface. Thus, the circularity and the disk-like ratio also increased. Depending on the rotation velocity, this might be beneficial for the increased porosity of the coatings.

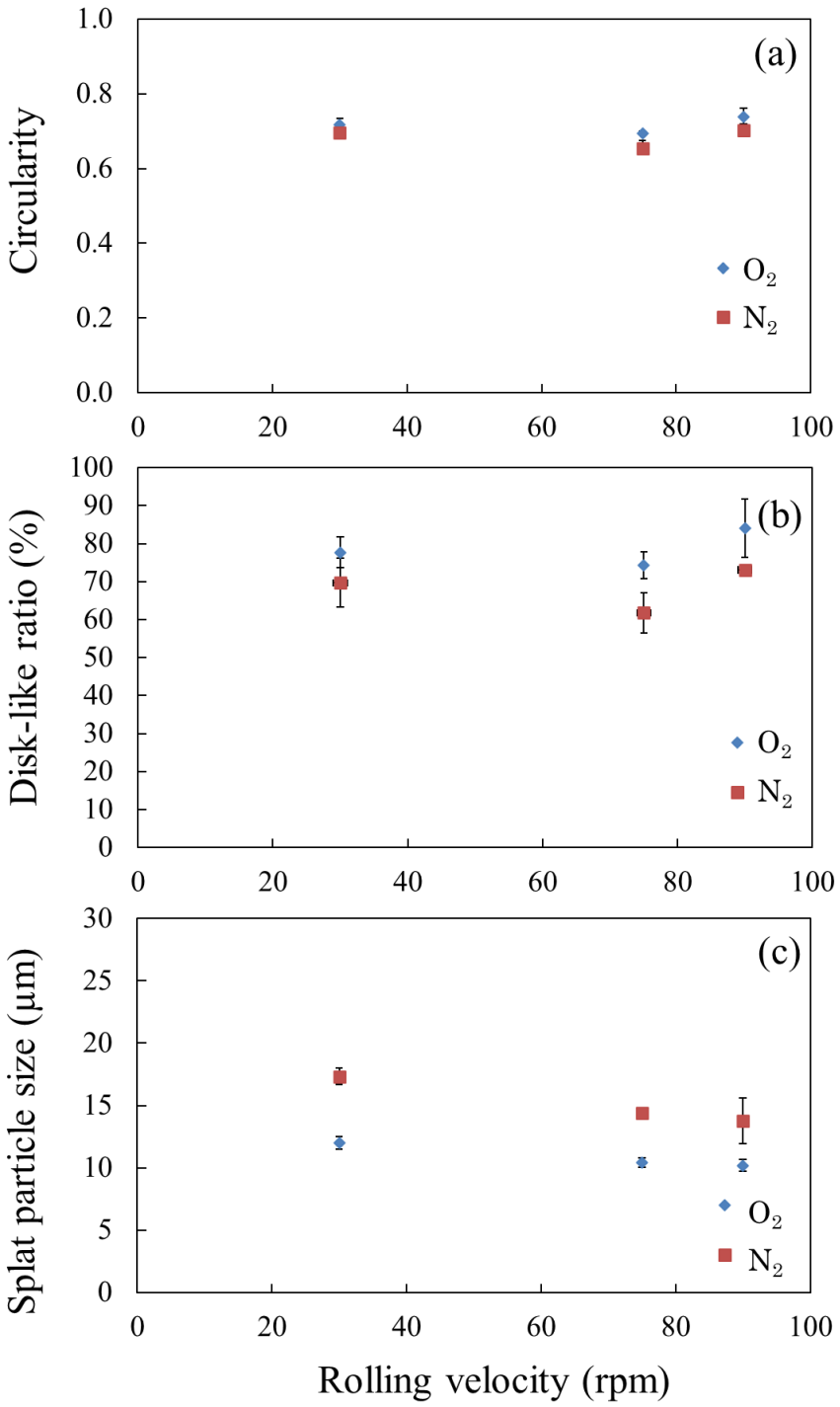

Figure 4-14 Results of Er_2O_3 splats deposited on A5052 substrates with different rolling velocity. (a) Splats circularity, (b) Disk-like ratio, (c) Splats particle size.

4.4 Conclusions

In summary, flame spray with chelate raw materials of EDTA·Er·H to sprayed Er_2O_3 single splats was deposited on the polished Al alloy substrate(A5052) at the various conditions(powder size, carrier gas types, velocity and temperature of in-flight particle and substrate temperature), the effect of those on splat morphology selection and its microstructure evolution were investigated. Results showed that the EDTA reactivity, temperature and velocity of the in-flight particle to be changed the splat morphology (porous, partially molten, splash with long finger, splat size), which is likely due to the fact that the process of decomposition, oxidation and melting in EDTA·Er·H to limit droplet spreading after being impacted on the substrate. In addition, compared to the plasma spray method, the theoretical calculation and experimental observations presented a good agreement with the chelate flame spray method. Thus, due to considerable equipment simplicity of the latter technique as compared to the former, and it can be expected that a new economically viable route combined with the possibility to designs the various type coatings (porous, dense) in narrow environments.

Reference

[1] R. Dhiman, A.G. McDonald, S. Chandra, Predicting splat morphology in a thermal spray process, *Surf. Coat. Technol.*, **201** (18), 7789–7801 (2007).

[2] J.R. Davis, et al., Handbook of Thermal Spray Technology, ASM Int., 2004

[3] R.B. Heimann, *Plasma Spray Coating*, Wiley-VCH, 2008.

[4] L. Pawlowski, *The Science and Engineering of Thermal Spray Coatings*, Wiley, 2008.

[5] L. Zhao, Y. Bai, J.J. Tang, K. Liu, C.H. Ding, J.F. Yang, Han. F Z.H, Effect of particle in-flight behavior on the composition of thermal barrier coatings, *Appl. Surf. Sci.*, **286**, 184–191 (2013).

[6] J.J. Tian, S.W. Yao, X.T. Luo, C. X. Li, C. J. Li, An effective approach for creating metallurgical self-bonding in plasma-spraying of NiCr-Mo coating by designing shell-core structured powders, *Acta Mater.*, **110**, 19–30 (2016).

[7] J. Houben, Ph.D. thesis Technische Universiteit Eindhoven, 1988.

[8] A. Syed, A. Denoirjean, B. Hannoyer, P. Fauchais, P. Denoirjean, A. Khan, J. Labbe, *Surf. Coat. Technol.*, **200** (7), 2317–2331 (2005).

[9] Z. Yin, S. Tao, X. Zhou, C. Ding, J. Eur. Ceram. Soc., **28** (6), 1143–1148 (2008).

[10] V. Pershin, M. Lufitha, S. Chandra, J. Mostaghimi, *J. Therm. Spray Technol.*, **12** (3), 370–376 (2003).

[11] M. Fukumoto, Y. Huang, *J. Therm. Spray Technol.*, **8** (3), 427–432 (1999).

[12] A. McDonald, C. Moreau, S. Chandra, *Int. J. Heat Mass Transf.*, **50** (9–10), 1737–1749 (2007).

[13] A. Ohmori, C.J. Li, Quantitative characterization of the structure of plasma-sprayed Al_2O3 coating by using copper electroplating, *Thin Solid Films*, **201**, 241–252 (1991),

[14] Y. Chen, S.R. Bakshi, A. Agarwal, Inter-splat friction force and splat sliding in plasma sprayed aluminum alloy coating during nanoindentation and micro indentation, *ACS Appl. Mater. Interfaces*, **1**, 235–238 (2009).

[15] J. G. Legoux, B. Arsenault, L. Leblanc, V. Bouyer, C. Moreau, Evaluation of four high velocity thermal spray guns using WC-10% Co-4% Cr cermets, *J. Therm.*

Spray Technol., **11**, 86–94 (2002).

[16] M. Prystay, P. Gougeon, C. Moreau, Structure of plasma-sprayed zirconia coatings tailored by controlling the temperature and velocity of the sprayed particles, *J. Therm. Spray Technol.*, **10**, 67–75 (2001).

[17] K. Komatsu, T. Shirai, A. Toyama, T. Iseki, D. Y. Xin, T. Costa, et al., Densification of metal oxide films synthesized from metal complexes by flame spraying, *Surf. Coat. Technol.*, **325**, 89–97 (2017).

[18] K. Komatsu, T. Sekiya, A. Toyama, T. Shirai, A. Nakamura, S. Ohshio, I. Toda, H. Muramatsu, H. Saitoh, Synthesis of $(Y,Er)_2O_3$ films frpm multiple-nuclei EDTA·(Y, Er) ·H complexes by frame spray method, *Mater. Trans.*, **57**(1), 70–74 (2016).

[19] K. Komatsu, A. Toyama, T. Sekiya, T. Shirai, A. Nakamura, I. Toda, S. Ohshio, H. Muramatsu, H. Saitoh, Flame-sprayed Y_2O_3 films with metal-EDTA complex using various cooling agents, *J. Therm. Spray Tech.*, **26**, 195–202 (2017).

[20] M.A. Mulero, J. Zapata, R. Vilar, V. Martínez, R. Gadow, Automated image inspection system to quantify thermal spray splat morphology, *Surf. Coat. Technol.*, **278**, 1-11 (2015).

[21] X. Wei, J. Wang, B. Christopher C., Analysis of EMAA Splats on Glass and Mild Steel Substrates, *J. Therm. Spray Technol.*, **23**(3), 317-324 (2014).

[22] F. Fanicchia et al., *Surf. Coat. Technol.*, **315**, 546-557 (2017).

[23] Guoliang Hou et al., *Ceramics International*, **44**, 3173-3182 (2018).

[24] MarkusMutter et al., *Surf. Coat. Technol.*, **318**, 157-169 (2017).

[25] Y.N. Tanaka, M.H. Fukumoto, Effect of Spray Distance on Velocity, Temperature and Flattening Behavior of Sprayed Ceramic Particles, *Japan Welding Society*, **19** (3), 440-445 (2001).

[26] F. Savkar, P. Siemers, Some recent developments in rapid solidification plasma deposition technology, in: M. Boulos (Ed.), *Workshop Applications*, 80–89 (1989).

[27] Y.X. Dan, T. K. Costa, Z. Y. Guo, A. Nakamura, K. Komatsu, H. Saitoh, Thermal barrier coatings formed by flame spray with metal-EDTA, *J. J. Appl. Phys*, DOI: https://doi.org/10.35848/1347-4065/ab9ef6.

[28] C.W. Kang, H.W. Ng, Splat morphology and spreading behavior due to oblique impact of droplets onto substrates in plasma spray coating process, *Surf. Coat. Technol.*, **200**, 5462-5477 (2006).

Chapter 5

Heat-shock properties in Y_2O_3 films synthesized on stainless-steel substrate

Abstract

Recently, a new deposition technique using metal–ethylenediaminetetraacetic acid (EDTA) complex has been developed. In this study, the heat-shock properties of metal-oxide films synthesized from a metal–EDTA complex were investigated. Y_2O_3 films were synthesized on stainless-steel (SUS) substrate from EDTA·Y·H through the combustion of H_2–O_2 gas. A cyclic heat-shock test was conducted on the fabricated Y_2O_3 films through exposure to the H_2-O_2 flame. The existence of Y_2O_3 crystals was confirmed. Surface cracks or damages were not observed in the samples after the cyclic thermal test. Although the number of cross-sectional cracks, crack lengths, and cracks per unit area were increased by the heat shock, delaminations were not observed in the Y_2O_3 films. The results show that the prepared Y_2O_3 films have high thermal shock resistance and are suitable for use as thermal barrier coatings.

5.1 Introduction

Recently, the level of desired properties in thermal barrier coatings (TBCs) for extreme environmental applications has increased [1, 2]. Ceramic coating techniques, which are applied in aircraft technology, have been selected for coating on top of TBCs. Jet engines in aircraft often operate under extreme thermal-shock environments at a temperature of approximately 1400 °C. Thermal shocks produce many issues; for instance, cracks are produced by thermal stress in ceramic films. Thermal stress occurs at grain boundaries with different diameters [3]. Such cracks lead to deformations and delaminations. Therefore, the accurate control of the microstructure of a ceramic film is required in TBC techniques. In the thermal-spraying deposition process, melted or semisolid in-flight particles collide with the substrate or are deposited in the ceramics layer and splatted. Subsequently, the splatted particles solidify. Consequently, pores are produced in the region between particles. Pores can be open or closed [4]. Pores penetrating the deposited layer are open pores. The relaxation of rapid thermal stress in a deposited film is accomplished by controlling the pores in the film's microstructure [5].

Recently, a new deposition technique using a metal–ethylenediaminetetraacetic acid (EDTA) complex was developed [6–8]. In this technique, metal–EDTA complex powders are introduced in a commercial flame-spraying apparatus. These complex powders are decomposed in the flame and forms metal-oxide particles, which are subsequently deposited on the substrate. Micron-order-thickness metal-oxide films with 6–15% cross-sectional porosities were deposited on stainless-steel (SUS) substrates in several seconds [7]. This technique is considered inferior to established thermal-spraying techniques, such as plasma spraying. Dense metal-oxide films can be deposited using the plasma-spraying technique. However, the established thermal-spraying techniques require high costs and large equipment, in contrast to the meta–EDTA deposition technique. Metal-oxide films obtained through metal–EDTA deposition are expected to have high thermal shock because of their dense microstructure. Therefore, the metal–EDTA deposition holds potential as a TBC

technique in extreme environments.

In this study, the heat-shock properties of yttrium-oxide (Y_2O_3) films synthesized using a metal–EDTA complex with flame-spray apparatus were investigated. Y_2O_3 was selected as it shows high plasma resistance [9]. The crystal structure and microstructure (surface and cross-sectional) were analyzed for the deposited films. A cyclic thermal-shock test [10, 11] was conducted to investigate the thermal-shock properties of the deposited films. The deposited films were exposed to an H_2–O_2 flame and the deposited film's microstructures were analyzed. Furthermore, the existence of cracks, deformation, and delamination in the deposited films was analyzed through the thermal-shock test.

5.2 Experimental

The EDTA complex, EDTA·Y·H (Chubu Chelest Co., Ltd.), was prepared for Y_2O_3 film syntheses [6]. A conventional flame-spray apparatus consisting of a feed unit (5MPE, Sulzer Metco) and spray gun (6P-II, Sulzer Metco) was used to perform reactive spraying. The EDTA·Y·H was then placed into a feed unit and transported through O_2 gas flow to the spray gun. The carrier gas flow rate was 7.1 L/min. In this study, hydrogen gas was selected as the fuel. A mixture of H_2 and O_2 was used as the flame gas. The flow rates were 32.6 and 43.0 L/min, respectively. The EDTA·Y·H powder was mixed with the flame and reacted with oxygen after the thermal decomposition of EDTA. The reacted particles were then sprayed onto a stainless-steel substrate (SUS304, 30 × 50 × 1 mm) that was previously blasted by #60 alumina grit (99.7% purity, 212–250 μm particle size, Fuji Manufacturing Co., Ltd.), resulting in the deposition of a metal-oxide film. The stand-off distance between the spray gun and the substrate was 150 mm. The deposition duration was 4–10 s. The traverse rate of the gun was 50 mm/s. Subsequently, the spray nozzle was moved in a longitudinal direction, and deposition was performed at each area for approximately 6 s without pre-heating the substrate. For reference, the yield percentage (deposition efficiency) of this

technique was measured to be approximately 60%.

Fig. 5-1 shows the setup of the thermal-shock test for films deposited from EDTA·Y·H on the SUS substrate with a photograph of the experiment. The rotation apparatus, which has the capability to deposit twelve samples at a time, was fabricated in-house. The mortar was used in the apparatus for rolling. The rolling velocity of the apparatus was kept within the range of 45–90 rpm by controlling the applied voltage of a variable autotransformer. To investigate the effects of thermal shock, the rotation apparatus was constant at only 45 rpm. To define the parameters for the thermal-shock test, the number of times the sample passed through the flame (number of scans) was counted. The numbers of scans used were 100, 300, and 500. Furthermore, the substrate temperature in situ using a *K*-type thermocouple was measured. First, the thermocouple was combined with a data logger (EL-USB-TC-LCD, MK Scientific). Next, the thermocouple was inserted in a hole bored into the substrate and fixed to the substrate using a bolt to measure the in-situ substrate temperature. Temperature profiles were obtained in each experiment using analysis software. The maximum substrate temperatures during thermal-shock tests were measured.

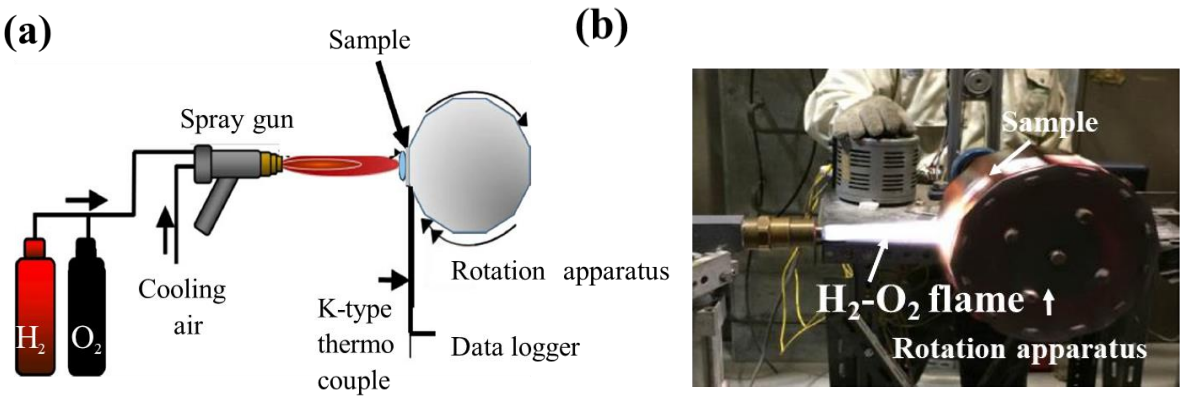

Figure 5-1 Thermal-shock test for films deposited from EDTA·Y·H complex on SUS substrate. (**a)** Schematic diagram of the experiment. (**b)** Photograph of the experiment.

X-ray diffractometry (M03XHF22, MAC Science) with Cu *Kα* radiation was used to observe the crystal structure. The surface and cross-sectional morphologies of the films were observed using field-emission scanning electron microscopy (FE-SEM, JSM-6700F, JEOL). Secondary-electron and backscattered-electron (COMPO) images of the deposited films were acquired. The elements contained in the sample and their distributions were estimated using energy-dispersive X-ray (EDX) spectroscopy combined with FE-SEM. The porosity was measured by digitizing the obtained SEM images using commercial software (Image J).

The heat-shock properties of the deposited films were analyzed as follows. First, each obtained COMPO image was digitized using commercial software (Image J). Next, the number of cracks, crack lengths, and crack areas were measured from the digitized image. Furthermore, the number of cracks per unit area(N) was estimated from the number of cracks in the deposited film (a) and area of the deposited film excluding pore voids (A) using the following equation(1) [12]:

$$N\ (\text{number}/\mu\text{m}^2) = a\ (\text{number})/A\ (\mu\text{m}^2). \quad (1)$$

5.3 Results and discussion

A photograph of the deposited samples is shown in **Fig.** 5-2. All samples deposited on the SUS304 substrates appear white [7]. The existence of cracks or delaminations was not observed. The thermal history during the thermal-shock test using the H_2–O_2 flame was measured. The maximum temperatures on the SUS substrates were increased by increasing the scan time. The maximum temperatures were 450.5, 625.5, and 728.5 °C at 100, 300, and 500 scans, respectively. The theoretical combustion-gas temperature of the H_2–O_2 flame was 2700 °C [13], which is greater than the melting point of the Y_2O_3 crystal of 2425 °C [14]. A difference in thermal expansion coefficients existed between the SUS substrate and the deposited material. Therefore, volume expansion stresses can lead to cracks in the coating upon cooling and may cause coating failure. Harsher conditions in the thermal-cycling test induce higher thermal stress in

the entire sample. Consequently, many cracks were produced in the deposited films [15].

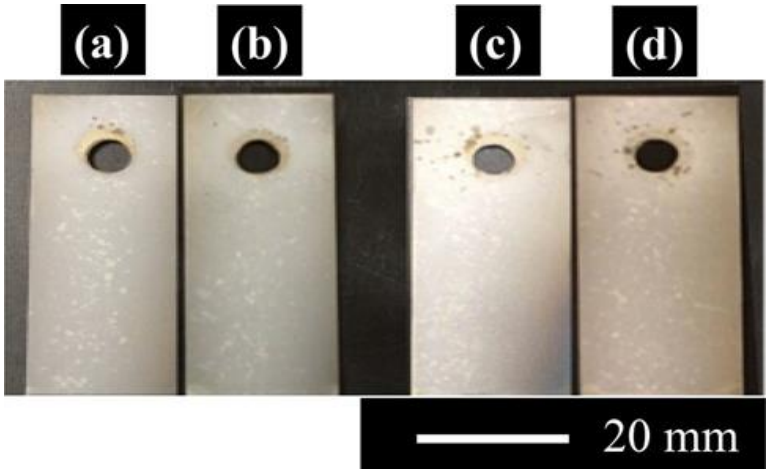

Figure 5-2 Photographs of films deposited using H_2–O_2 flame with EDTA·Y·H complex. (**a)** As-synthesized, (**b)** after 100 scans, (**c)** after 300 scans, and (**d)** after 500 scans

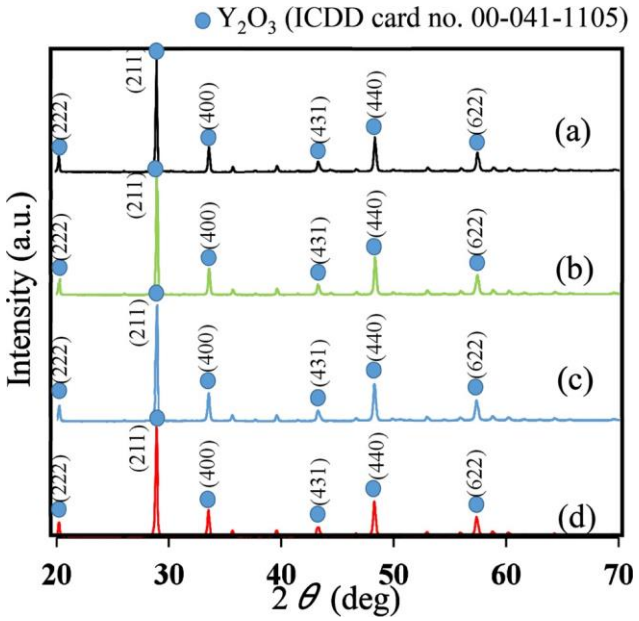

Figure 5-3 XRD profiles at 2θ = 20°–70° for films synthesized from EDTA·Y·H on SUS304 substrates using flame-spray apparatus.

Fig. 5-3 shows XRD profiles of the films deposited on SUS substrates. Crystal identification was conducted according to the International Centre for Diffraction Data (ICDD) card revealed that all deposited samples were composed of Y_2O_3 crystals with a cubic structure (ICCD card no. 00-041-1105). The crystal phase in the deposited films

was not changed by the cyclic thermal-shock test.

Surface SEM images of the deposited films are shown in **Fig.** 5-4. The surface morphologies of the deposited films were uneven. Splatted particles and spherical particles approximately 1–10 μm in diameter were observed. Cracks or damages were not observed in the samples after the cyclic thermal test. In previous reports, networks of cracks in deposited films have been expanded by increasing the number of thermal cycles. The cracks are thought to be produced by in-plane tensile stresses in surface layers [16–18].

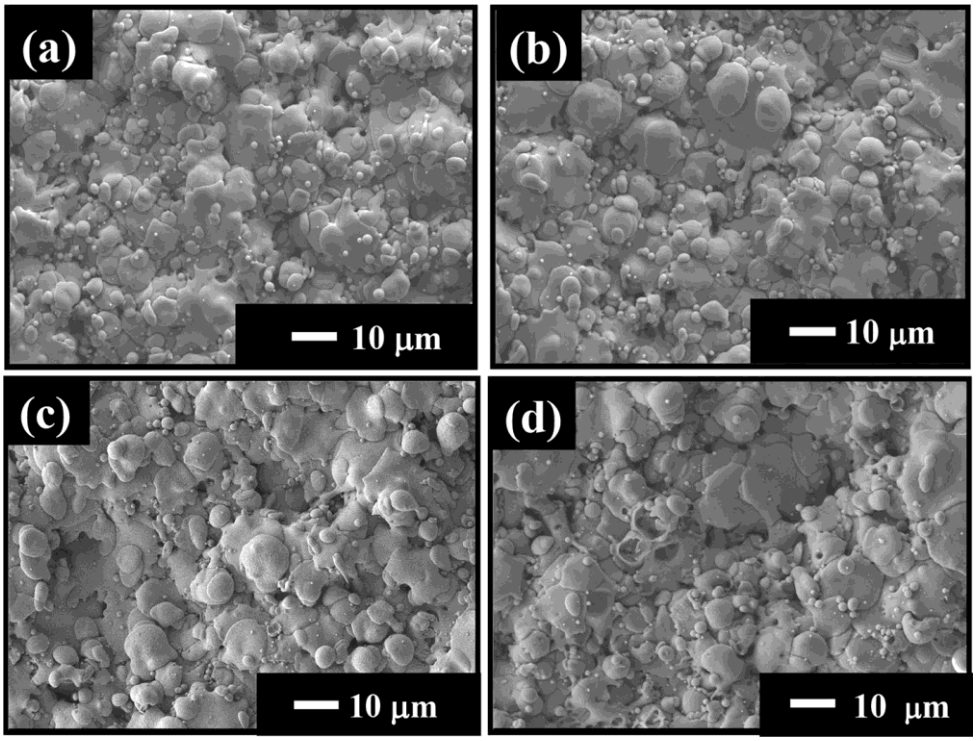

Figure 5-4 Surface SEM images of films synthesized on SUS304 substrates using the flame- spraying apparatus. (**a)** As-synthesized, (**b)** after heat-shock test (100 scans), (**c)** after heat-shock test (300 scans), (**d)** after heat- shock test (500 scans)

Y_2O_3 has high thermal stability. Many researchers have investigated the thermal conduction behaviors of Y_2O_3 for application as interlayers [19–21]. Cross-sectional microstructures were changed by the cyclic test. Cross-sectional SEM and EDX images of the deposited films are shown in **Figs.** 5-5 and 5-6, respectively. Metal-oxide layers with dense microstructure were observed on the SUS304 substrate. The SUS substrate

was also observed for any damages. **Table** 5-1 lists the average thicknesses and 2D porosities of the deposited films. The thicknesses of the deposited films were in the range of 8.8–13.5 μm. The 2D porosities were in the range of 5.1–7.2 %. In addition, the elemental distributions of the Y_2O_3 films were observed using the EDX measurement. A uniform elemental distribution was observed in the Y_2O_3 films. In addition, any elemental differences caused by the cyclic thermal test were observed.

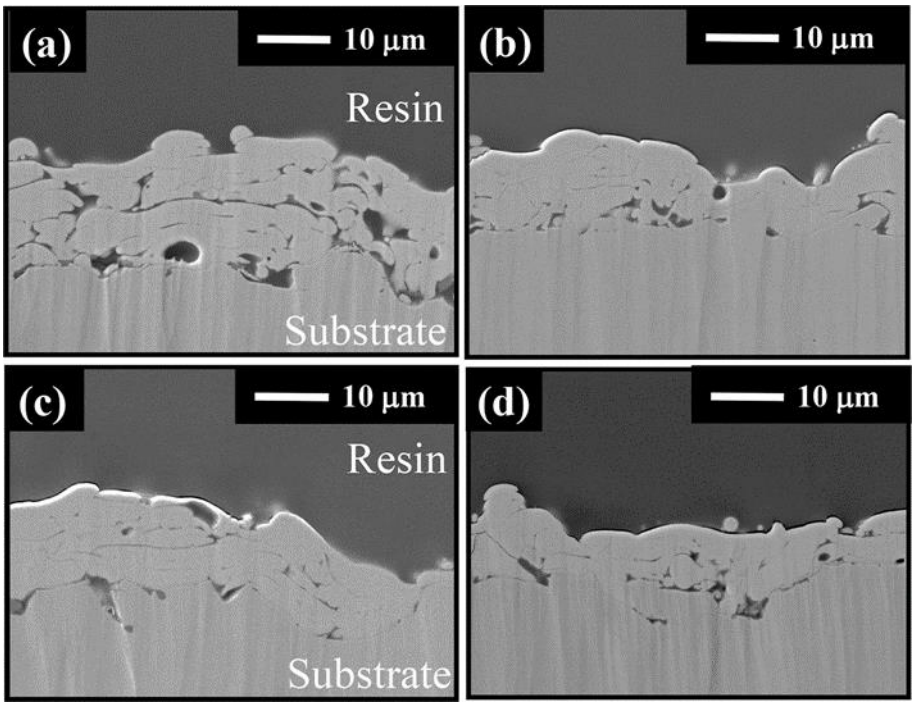

Figure 5-5 Cross-sectional SEM images of films synthesized on SUS304 substrates using flame- spraying apparatus. (**a)** As-synthesized, (**b)** after heat-shock test (100 scans), (**c)** after heat-shock test (300 scans), (**d)** after heat- shock test (500 scans)

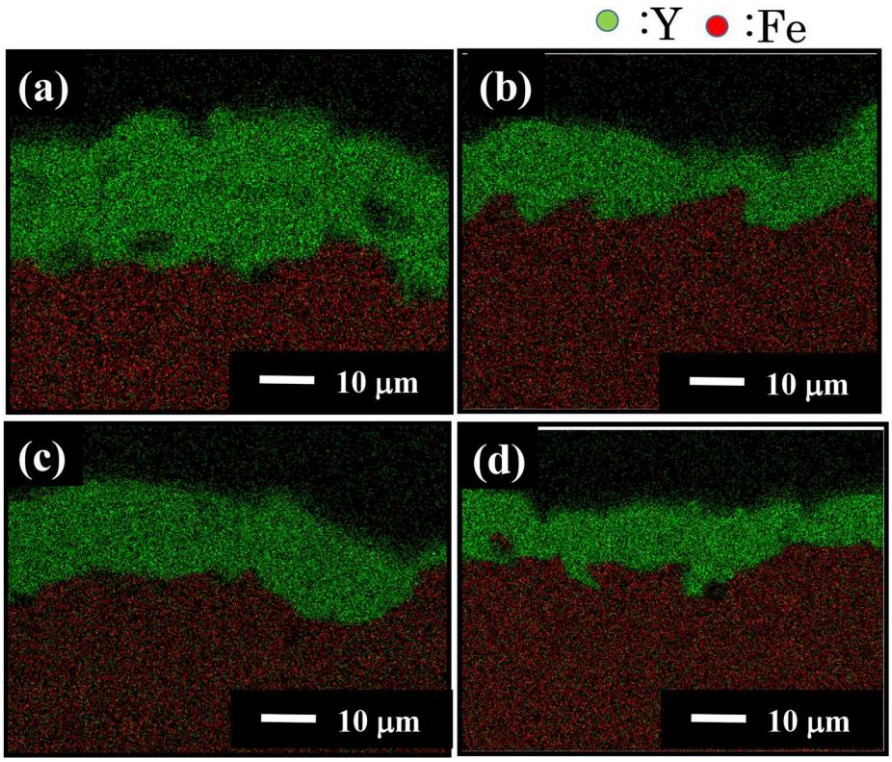

Figure 5-6 Cross-sectional elemental EDX images of films synthesized on SUS304 substrates using flame-spraying apparatus. (**a)** As-synthesized, (**b)** after heat- shock test (100 scans), (**c)** after heat-shock test (300 scans), (**d)** after heat-shock test (500 scans)

Table 5-1 Values of estimated film thickness and cross-sectional porosity of films synthesized on SUS304 substrates.

Sample	Average thickness (μm)	Maximum thickness (μm)	Minimum thickness (μm)	2D porosity (%)
As-synthesized	13.5	17.2	11.4	7.2
After the 100 scans	10.0	15.8	5.3	6.2
After the 300 scans	10.2	14.8	2.6	6.5
After the 500 scans	8.8	13.7	5.3	5.1

A distinct elemental boundary between the Y and Fe atoms was observed. Thermal elemental diffusion was not observed after the cyclic thermal test.

Microstructure behavior during thermal cycling of TBC coatings such as yttria-stabilized zirconia (YSZ) has been investigated [22–24]. In the present study, we attempted to observe the detailed microstructure of the deposited Y_2O_3 films through cyclic thermal tests. **Fig.** 5-7 shows cross-sectional COMPO images of the deposited Y_2O_3 films used for analyzing the detailed microstructure. The deposited Y_2O_3 films had various defects, such as micro-cracks, inter-splat voids, and open pores. Small structural cracks were observed in all Y_2O_3 films. For instance, the existence of many small structural cracks was confirmed from **Fig.** 5-6c. Particularly, vertical segmentation cracks were observed in the films (Fig. 5-7a). Furthermore, some coarse cracks horizontal to Y_2O_3 layers (Fig. 5-7b) were formed at splat–splat boundaries and inside the layers. These increase the stress between the Y_2O_3 layer and SUS substrate during thermal cycles, which causes the initiation and propagation of cracks at the splat–splat boundaries, the Y_2O_3 inside, and the Y_2O_3 layer/SUS substrate interface. Although crack structures were observed, through-thickness cracks were not observed in the Y_2O_3 films synthesized with the EDTA·Y·H complex (see Fig. 5-8).

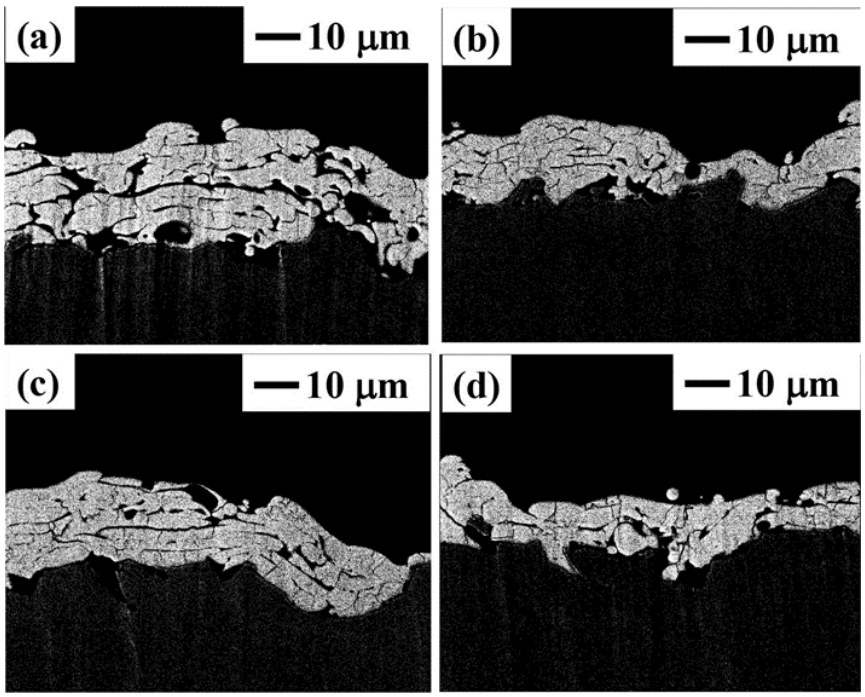

Figure 5-7 Cross-sectional BSE (COMPO) images of films synthesized on SUS304 substrates using flame-spraying apparatus. (**a)** As-synthesized, (**b)** after heat- shock test (100 scans), (**c)** after heat-shock test (300 scans), (**d)** after heat-shock test (500 scans)

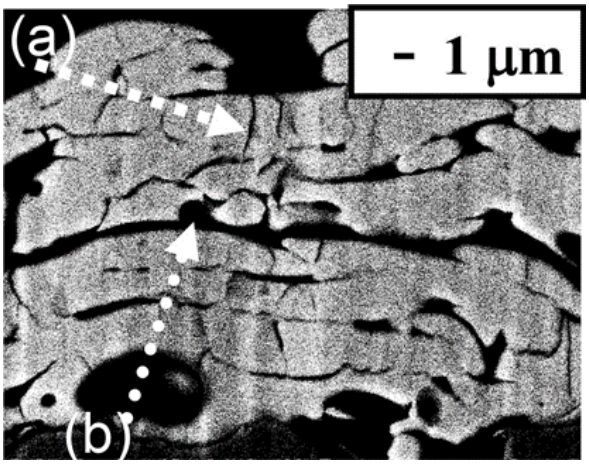

Figure 5-8 Examples of cracks in the deposited film. (**a)** Vertical segmentation crack, (**b)** horizontal crack. The COMPO image of the as-synthesized sample was used

The applicability of the Y_2O_3 films obtained from the EDTA·Y·H complex as TBCs was discussed. The Y_2O_3 films were formed by the decomposition of the EDTA·Y·H complex and oxidation. Subsequently, the Y_2O_3 particles were splatted on the SUS substrate, forming Y_2O_3 layers. Thermal-stress concentration occurs on

the grain boundary of Y_2O_3 films during the deposition process. As proof of these phenomena, many exploded Y_2O_3 particles were observed in **Fig.** 5-4d. The stresses produced many small cracks in the vertical direction, as shown in **Fig.** 5-6. The small cracks in the vertical direction occurred in all Y_2O_3 films. A decrease in sample thickness was also observed with increasing number of scans. This phenomenon is explained by delamination and deformation caused by the local thermal stress on the Y_2O_3 films. As mentioned above, the Y_2O_3 films formed from EDTA·Y·H have small cracks in the surface layers. Therefore, thermal stresses are focused on these small cracks. Stressed Y_2O_3 layers are eventually delaminated or deformed. The heat capacity of the Y_2O_3 films decreased with damage, and the temperature of the SUS substrate increased with damage. Finally, we attempt to analyze the Y_2O_3 films formed from the EDTA·Y·H complex quantitatively. Quantitative estimation was performed using cross-sectional COMPO images of the deposited samples. **Table** 5-2 lists values of the estimated crack numbers, sizes, and squares per unit area in the films synthesized on SUS substrates. These values increased after the thermal-shock test, and the increase was not commensurate with the number of scans. Although damage on the microstructure of the Y_2O_3 films was observed after the thermal-shock test, the degree of damage was low. The cracks did not progress or form a crack network. The damage causes viscoplastic deformations and delaminations in the deposited films. In a previous work, the stress at the tip of a crack located on the surface was higher than that at a crack located on the deposited layer, as revealed through simulations [25]. In addition, the presence of quenching stresses and thermal stresses during the cool down that follows the deposition process was simulated using a finite element method (FEM) analysis [26]. In the present study, cracks produced in the deposition process were progressed by thermal stress between the Y_2O_3 film and the SUS substrate. Hence, the heat-shock properties of the Y_2O_3 films synthesized with the metal–EDTA complex using flame- spray apparatus are high. Therefore, the deposited films are expected to be candidates for next-generation TBCs.

Table 5-2 Values of estimated crack numbers, sizes, and squares per unit area in films synthesized on SUS substrates.

Sample	Numbers of crack	Crack's average length (μm)	Numbers of crack per unit area × 10^{-4} (number/μm)
As-synthesized	25	1.6	1.27
After the 100 scans	33	1.7	2.77
After the 300 scans	29	1.6	1.86
After the 500 scans	26	1.5	1.84

5.4 Conclusion

Y_2O_3 films with high thermal-shock resistance were synthesized on SUS substrates with a metal–EDTA complex as the starting material. The EDTA·Y·H complex and commercial flame-spraying apparatus were used for the deposition of Y_2O_3 films. A cyclic thermal shock test was conducted using rotation apparatus and H_2–O_2 combustion gas. Y_2O_3 films with 13.5 μm thickness and 7.2% porosity were synthesized. The maximum temperature during the thermal shock test was in the range of 450–728 °C. Increases in the number of cracks, crack lengths, and number of cracks per unit area were confirmed in the thermal-shock test. The delamination of Y_2O_3 films was not observed.

References

[1] A. Feuerstein, J. Knapp, T. Taylor, A. Ashary, A. Bolcavage, N. Hitchman, *J. Therm. Spray Tech.*, **17**(2), 199 (2008).

[2] S. Matthews, B. James, *J. Therm. Spray Tech.*, **19**(6), 1267 (2010).

[3] A. Gilbert, K. Kokini, S. Sankarasubramanian, *Surf. Coat. Tech.*, **203**, 91 (2008).

[4] H. Guo, S. Kuroda, H. Murakami, *J. Am. Ceram. Soc.*, **89**(4), 1432 (2006).

[5] A. Scrivani, G. Rizzi, U. Bardi, C. Giolli, M. Muniz Miranda, S. Ciattini, A. Fossati, F. Borgioli, *J. Therm. Spray Tech.*, **16**(5–6), 816 (2007).

[6] H. Akasaka, M. Ohto, Y. Hasebe, A. Nakamura, S. Ohshio, H. Saitoh, *Surf. Coat. Tech.*, **205**, 3877 (2011).

[7] K. Komatsu, T. Sekiya, A. Toyama, Y. Hasebe, A. Nakamura, M. Noguchi, Y. Li, S. Ohshio, H. Akasaka, H. Muramatsu, H. Saitoh, *J. Therm. Spray Tech.*, **23**, 833 (2014).

[8] K. Komatsu, T. Sekiya, A. Toyama, A. Nakamura, I. Toda, S. Ohshio, H. Muramatsu, H. Saitoh, *Int. J. Chem. Nucl. Metall. Mater. Eng.*, **8**(12), 1322 (2014).

[9] J. Iwasawa, R. Nishimizu, M. Tokita, M. Kiyohara, K. Uematsu, *J. Am. Ceram. Soc.*, **90**(8), 2327 (2007).

[10] A. Keyvani, M. Saremi, M.H. Sohi, Z. Valefi, *J. Alloys Compd.*, **541**, 488 (2012).

[11] L. Sun, L.L. Zhang, D. Zhao, *J. Rare Earth*, **28**, 198 (2010).

[12] I. Ogata, K. Mizutani, K. Makino, Y. Kobayashi, *DENSO Tech. Rev.*, **13**, 112 (2008).

[13] M. Suga, Y. Kitamura, Kaenn-to-bakuhatu, *Sankyo publishing Co., Ltd.*, 64.

[14] K. Daijiten 3 (in Japanese), Kyoritsu Shuppan Co., Ltd., 895.

[15] G. Di Girolamo, F. Marra, C. Blasi, E. Serra, T. Valente, *Ceram. Inter.*, **37**, 2711 (2011).

[16] H. Jamalin, R. Mozafarinia, R. S. Razavi, R. A. Pidani, *Ceram. Inter.*, **38**,

6705 (2012).

[17] Y. Bai, Z. H. Han, H. Q. Li, C. Xu, Y. L. Xu, C. H. Ding, J. F. Yang, *Surf. Coat. Tech.*, **205**, 3833 (2011).

[18] A. Nusair Khan, J. Lu, *Surf. Coat. Tech.*, **166**, 37 (2003).

[19] N.C. Shukla, H.-H. Liao, J.T. Abiade, F. Liu, P.K. Liaw, S.T. Huxtable, *Appl. Phys. Lett.*, **94**, 081912 (2009).

[20] H.-S. Yang, J. W. Kim, G. H. Park, C. S. Kim, K. Kyhm, S. R. Kim, K. C. Kim, K. S. Hong, *Thermochim. Acta.*, **455**, 50 (2007).

[21] C. Durand, C. Valle´ e, V. Loup, O. Salicio, C. Dubourdieu, S. Blonkowski, M. Bonvalot, P. Holliger, O. Joubert, *J. Vac. Sci. Technol.*, A **22**, 655 (2004).

[22] H. B. Guo, R. Vaßen, D. Sto¨ver, *Surf. Coat. Tech.*, **192**, 48 (2005).

[23] S. Ahmaniemi, P. Vuoristo, T. Ma¨ntyla¨, C. Gualco, A. Bonadei, R. Di Maggio, *Surf. Coat. Tech.*, **190**, 378 (2005).

[24] Y. Bai, L. Zhao, J. J. Tang, S. Q. Ma, C. H. Ding, J. F. Yang, L. Yu, Z. H. Han, *Ceram. Inter.*, **39**, 4437 (2013).

[25] L. Wang, Y. Wang, W.Q. Zhang, X.G. Sun, J.Q. He, Z.Y. Pan, C.H. Wang, *Appl. Surf. Sci.*, **258**, 3540 (2012).

[26] P. Michlik, C. Berndt, *Surf. Coat. Tech.*, **201** 2369 (2006).

Chapter 6

Heat resistance and adhesion properties of Y_2O_3 films on aluminum alloy substrate

Abstract

Y_2O_3 films were synthesized on an aluminum alloy (A5052) substrate directly using a flame-spray apparatus with an H_2-O_2 flame. The Y_2O_3/A5052 joining was also annealed under atmospheric conditions. Although the joining was annealed close to the melting point of the A5052 substrate, the joining showed strong adhesion without delaminations. The resultant Y_2O_3 coating exhibits a strong adhesion with the aluminum alloy substrate. Elemental diffusion in the joining was not observed from cross-sectional EDX analysis. Directly ceramic film deposition method by a reactive spraying process was proposed.

6.1 Introduction

Aluminum alloys have wide applications in automotive and electronic fields [1,2]. They are lightweight materials and display electrical and thermal conductivity, as well as excellent specific strength, corrosion resistance, and machinability. However, their low abrasion and heat resistance limits the application of aluminum alloys. Applications of the alloys in technical parts subject to harsh conditions, such as friction and high temperatures, are accomplished with the use of surface coatings and modifications. Anodic oxidation [3], chemical vapor deposition (CVD) [4], physical vapor deposition (PVD) [5], plating [6], and thermal spraying [7] are the commonly used coating techniques. Interlayers are applied in ceramic coatings on aluminum alloys (ceramic-aluminum joining). These interlayers react at high temperatures, forming impurity phases, which can weaken properties such as the adhesion of the joining. Hence, the design of the ceramic-aluminum joining interface is important.

A new deposition technique using a metal–ethylenediaminetetraacetic acid (EDTA) complex has been developed [8-12]. In this technique, the metal–EDTA complex powders are introduced using a commercial flame spraying apparatus. These complex powders decompose in the flame, forming metal oxide particles, which are subsequently deposited on the substrate. Micron-order-thickness metal oxide films with 3%-24% cross-sectional porosities were deposited on stainless steel (SUS) substrates in several seconds [8-10]. The metal oxide films were synthesized on stainless steel (SUS) substrate from EDTA•M•H ($M=Y^{3+}$, Er^{3+}, Eu^{3+}) complexes through the combustion of H_2-O_2 gas. Recently, it has been found that the carrier gas plays an important role in determining the thickness and porosity of the resulting films. O_2 was found to be the better carrier gas for the fabrication of dense metal oxide films in past studies.[11] In addition, the cooling effects of the substrate, studied using various cooling units for solidification, were shown to be dominated by the heat of vaporization, not by these temperatures [12]. Hence, it is expected that dense metal oxide films will be synthesized on substrates that have high thermal conductivities and low melting points, such as aluminum alloys.

In this study, Y_2O_3 films were synthesized on an aluminum alloy substrate using a flame spray apparatus with an H_2-O_2 flame. The crystal structures and microstructures of the deposited films were investigated. In addition, annealing tests were conducted to prove that direct deposition of the metal oxide film on the aluminum alloys had occurred.

6.2 Experimental

The EDTA complex, EDTA•Y•H (Chubu Chelest, Mie, Japan), was prepared for the Y_2O_3 film syntheses [8]. **Fig.** 6-1 shows the experimental setup for film deposition from the EDTA•Y•H complex onto the aluminum alloy (aluminum-magnesium alloy, A5052) substrate with a photograph of the experiment. A conventional flame spray apparatus consisting of a feed unit (5MPE, Sulzer Metco, Westbury, NY) and spray gun (6P-II, Sulzer Metco) was used to perform reactive spraying. EDTA•Y•H was placed into the feed unit and transported through an O_2 gas flow to the spray gun. The carrier gas flow rate was 7.1 L/min. A mixture of H_2 and $O_2$was used as the flame gas, with flow rates of 32.6 and 43.0 L/min, respectively. EDTA•Y•H powder was mixed with the flame and reacted with oxygen after the thermal decomposition of EDTA. The reacted particles were then sprayed onto an aluminum alloy substrate (A5052, 100×100×10 mm^3) that had been previously blasted by #60 alumina grit (99.7% purity, 212-250 μm particle size, Fuji Manufacturing, Fujioka, Japan), resulting in the deposition of a metal oxide film. The stand-off distance between the spray gun and the substrate was 150 mm, the deposition duration was 4-10 seconds, and the traverse rate of the gun was 50 mm/s. Subsequently, the spray nozzle was moved in a longitudinal direction, and deposition was performed on each area for approximately 6 seconds without preheating of the substrate. For reference, the yield percentage (deposition efficiency) of this technique was measured to be approximately 60%. The blast pressure was varied at 0.2, 0.6, and 0.8 MPa.

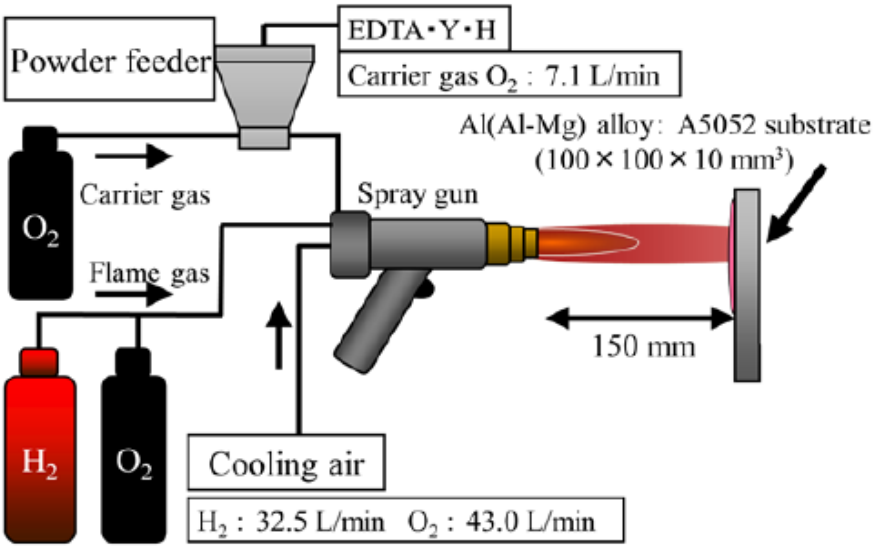

Figure 6-1 Schematic of the experiment for films deposited from EDTA•Y•H complexes on an A5052 substrate.

Atmospheric annealing was conducted for the deposited film using the following protocol. The deposited film was cut into four test pieces (30×30×10 mm^3). Each test piece was then annealed at 400, 500, and 600°C for 1 hour in atmosphere.

X-ray diffractometry (XRD, M03XHF22, Mac Science, Kanagawa, Japan) with Cu Kα radiation was used to observe the crystal structure. The surface and cross-sectional morphologies of the films were observed using field-emission scanning electron microscopy (FE-SEM, JSM-6700F, JEOL, Japan). Secondary electron and backscattered electron (compositional) images of the deposited films were acquired. The elements contained in the sample and their distributions were estimated using energy-dispersive X-ray (EDX) spectroscopy combined with FE-SEM. The porosity was measured by digitizing the obtained SEM images using commercial software (ImageJ). First, the thickness is average thickness of 20 transverse sections in the whole image. The standard deviation of thickness was also estimated. Next, the porosity was estimated from the area ratio of the film in the image. The heat-shock properties of the deposited films were analyzed as follows. First, each obtained COMPO image was

digitized using Image J. Next, the number of cracks, crack lengths, and crack areas were measured from the digitized image. Furthermore, number of cracks per unit area was estimated using the following equation: Number of cracks per unit area (number/pixels) = Number of cracks in the deposited film/Area of the deposited film excluding pore voids (μm^2). In addition, EDX line profiles were taken for the deposited films synthesized on aluminum alloy substrates.

Fig. 6-2 shows the setup used for the cyclic thermal tests for the films deposited from EDTA•Y•H on the A5052 substrate. The rotation apparatus, which can deposit twelve samples at a time, was fabricated in-house. The mortar was used for rolling, and the rolling velocity of the apparatus was kept at 45 rpm by controlling the applied voltage of a variable autotransformer. To define the parameters for the thermal shock test, the number of times the sample passed through the flame (i.e., the number of scans) was counted. The number of scans was 800, and after every 200 scans, the deposited films were brought back to room temperature. The rotation apparatus, at 45 rpm, was dipped into a hand-made SUS container (350×240×240 mm^3) filled with liquid nitrogen. The substrate temperature was also measured in situ using a K-type thermocouple. The thermocouple was combined with a data logger (EL-USB-TC-LCD, MK Scientific) and then inserted into a hole bored into the substrate and fixed to the substrate using a bolt to measure the in-situ substrate temperature. Temperature profiles were obtained in each experiment using analysis software.

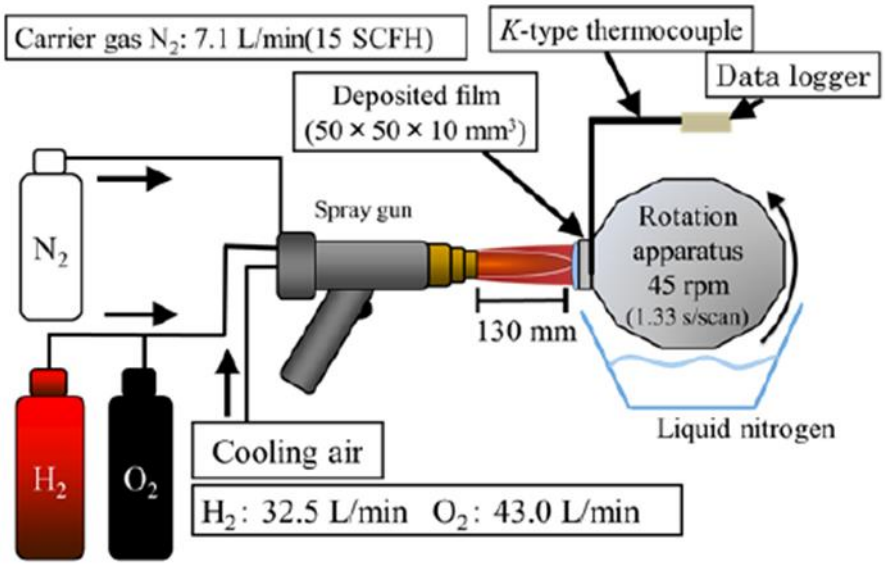

Figure 6-2 Schematic for the cyclic thermal test for films deposited from EDTA・Y・H complexes on an A5052 substrate.

6.3 Results and Discussion

Photographs of the films deposited using the EDTA•Y•H with commercial flame spraying are shown in **Fig.** 6-3. The color of the blasted aluminum alloy substrate was light gray. This changed to white after the deposition, which is also the color of Y_2O_3, confirming the presence of the films on the aluminum substrate. Photographs of the films after annealing in atmospheric conditions are also shown in **Fig.** 6-3. After annealing, the color of the deposited films was not changed, indicating that the Y_2O_3 films were deposited on the aluminum substrates directly, not in interlayers.

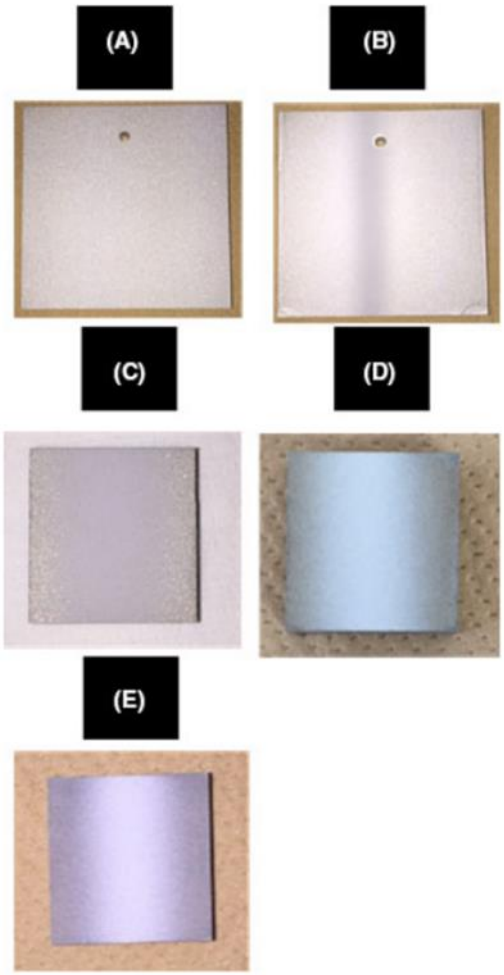

Figure 6-3 Photographs of films deposited using a H_2-O_2 flame with EDTA•Y•H complexes. (A) before deposition; (B) as-synthesized, (C) after annealing at 400 °Cfor 1 h, (D) after annealing at 500 °C for 1 h, (E) after annealing at 600 °C for 1 h.

To determine the crystalline structures of the deposited films and annealed films, XRD analyses were performed. **Figs.** 6-4 and 6-5 show the XRD profiles of the three films deposited on the aluminum substrates. The peaks in the XRD profiles were assigned using the International Center for Diffraction Data (ICDD) cards as references. The presence of a cubic Y_2O_3 crystalline phase (ICDD Card No.00-041-1105) was confirmed in the films formed from EDTA•Y•H. The existence of a Y_2O_3 crystalline phase was also confirmed in the annealed films. In the Y_2O_3-Al_2O_3 system, $Y_4Al_2O_9$

and $YAlO_3$ crystals are known to form at 1200-2000°C [13]. The existence of $Y_4Al_2O_9$ and $YAlO_3$ crystalline phases was not confirmed in the films. Further-more, Y_2O_3/MgO solid solutions are known to be formed. At over 1500°C (until 2000°C) in Y_2O_3-MgO systems [14]. The presence of MgO crystalline phases was not confirmed in the films. These results indicate that the Y_2O_3 films formed from EDTA•Y•H were deposited on the aluminum substrate successfully.

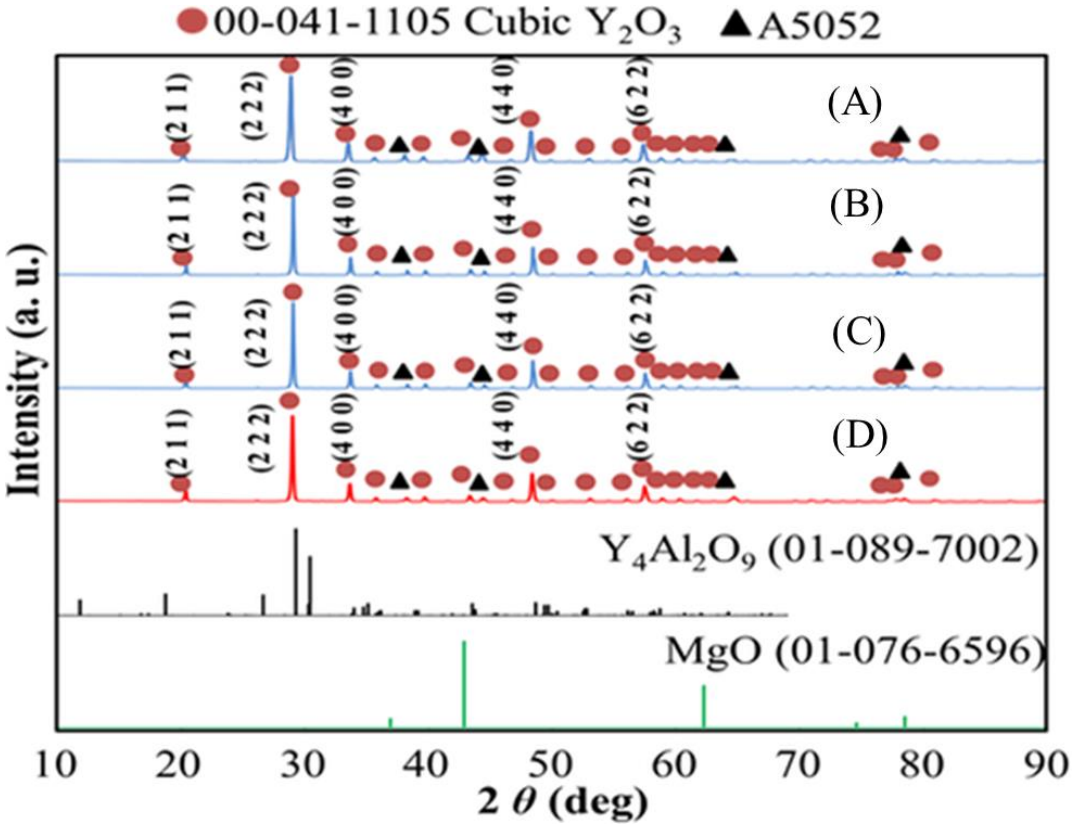

Figure 6-4 XRD profiles for 2θ values of 10-90°for the films synthesized on the A5052 substrate compared with ICDD cards for $Y_4Al_2O_9$ and MgO crystals, (A) after annealing at 600°C for 1 h, (B)after annealing at 500°C for 1 h, (C) after annealing at 400°C for1 h, (D) as synthesized.

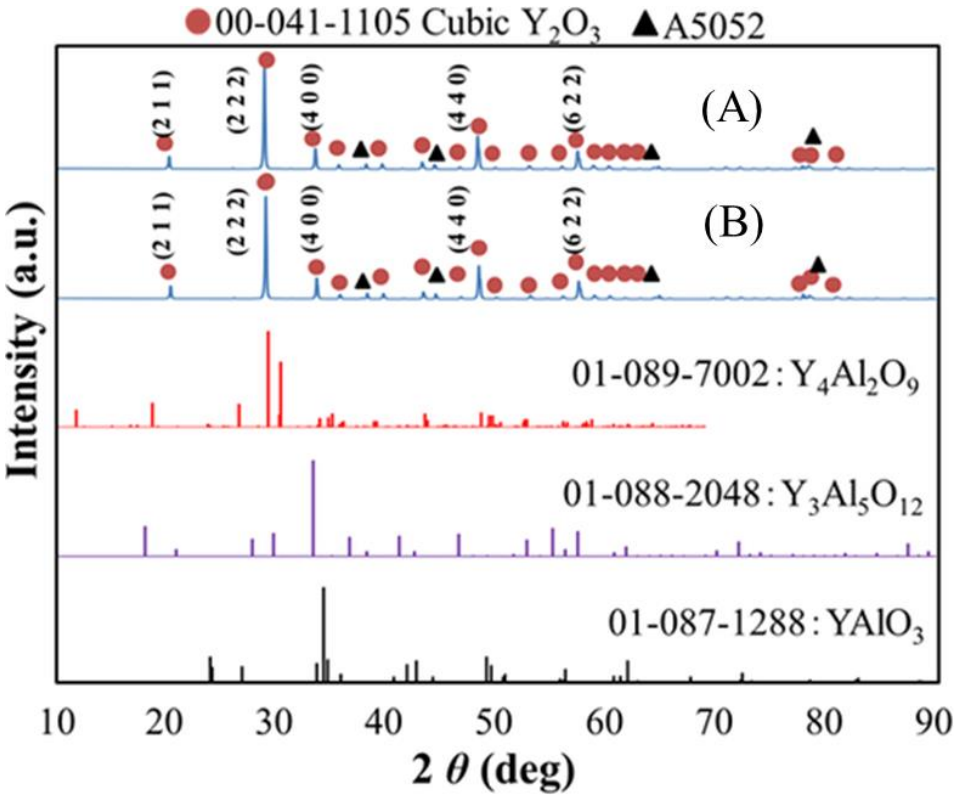

Figure 6-5 XRD profiles for 2θ values of 10-90° for the films synthesized on the A5052 substrate compared with ICDD cards for $Y_4Al_2O_9$, $Y_3Al_5O_{12}$, $YAlO_3$ crystals, (A) after annealing at 600°C for1 h, (B) after annealing at 500°C for 1 h.

The cross-sectional morphologies and elemental distributions of the films were then determined using SEM and EDX analyses. The elemental diffusion in the interface of the Y_2O_3/aluminum alloy was investigated in detail. **Figs.** 6-6 and 6-7 show the cross-sectional SEM and EDX images for the Y_2O_3 films deposited on the aluminum substrates. Several micron-ordered Y_2O_3 layers were confirmed on the substrates. **Table** 6-1 gives the thicknesses and cross-sectional porosities of the Y_2O_3 films; the porosities were determined by analyzing SEM images of the films. This analysis method can be used to determine the numbers of both open and closed pores. The as-synthesized Y_2O_3filmwas found to have an average thickness of 11.0 μ m and across-sectional porosity of 8.5%. Microstructural changes because of annealing (such as delamination or deformation) were not observed. From EDX analysis, elemental diffusion of Y, Al, and Mg atoms in the films was not detected, as shown in **Fig.** 6-7 After annealing, segregation of Mg atoms was confirmed at the interface between Y_2O_3 and the

aluminum substrates. In addition, elemental Y atom diffusion to the A5052 substrate was observed at 600°C. Furthermore, the EDX line profiles at the Y_2O_3/A5052interfaces were measured to investigate elemental diffusion by annealing. **Fig.** 6-8 shows the EDX line profile of the Y_2O_3 films. Elemental Y atom diffusion was observed after annealing at 600°C for 1 hour. In contrast, this diffusion was not observed in the as-synthesized and annealed films at 400 and 500°C for 1 hour. The melting point of A5052 is 607-649 °C [15]. These results indicate that the synthesized Y_2O_3 films improve the heat resistance of A5052.

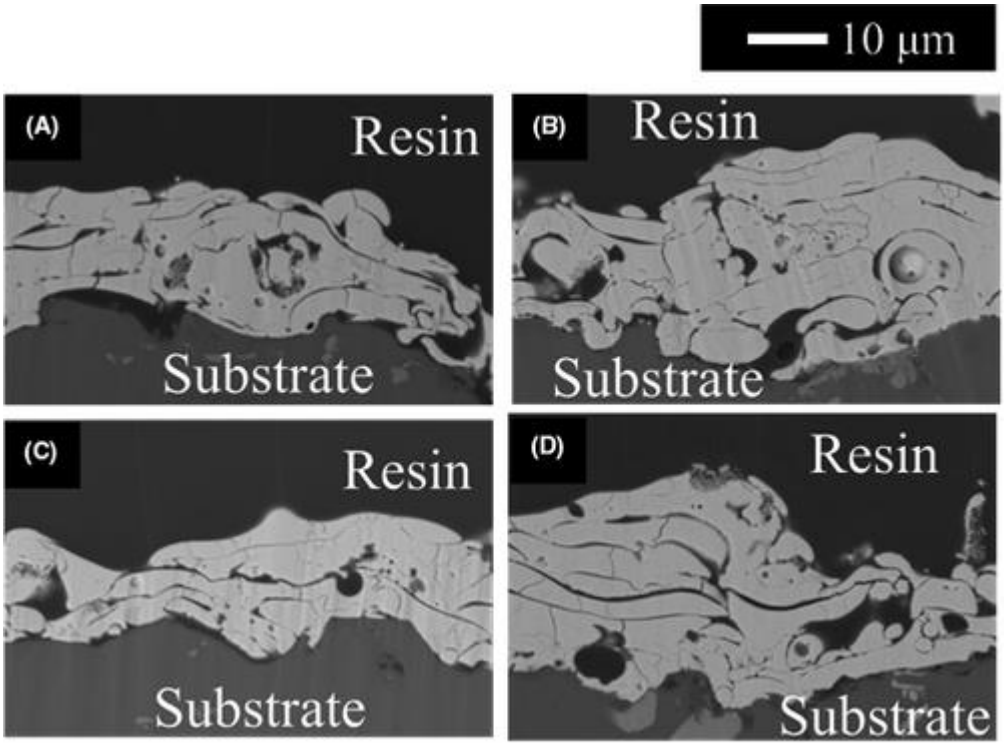

Figure 6-6 Cross-sectional SEM images of the films synthesized on the A5052 substrates, (A) as-synthesized, (B) after annealing at 400°Cfor 1 h, (C) after annealing at 500°C for 1 h, (D) after annealing at 600°C for 1 h.

Table 6-1 Thickness and cross-sectional porosities of the deposited film.

Sample	Film thickness (SD) (μm)	Cross-sectional porosity (%)
Before annealing (as-synthesized)	11.0 (3.4)	8.5
Annealed at 400 °C for 1 h	16.6 (3.7)	8.0
Annealed at 500 °C for 1 h	14.1 (3.9)	8.3
Annealed at 600 °C for 1 h	16.9 (5.0)	8.4

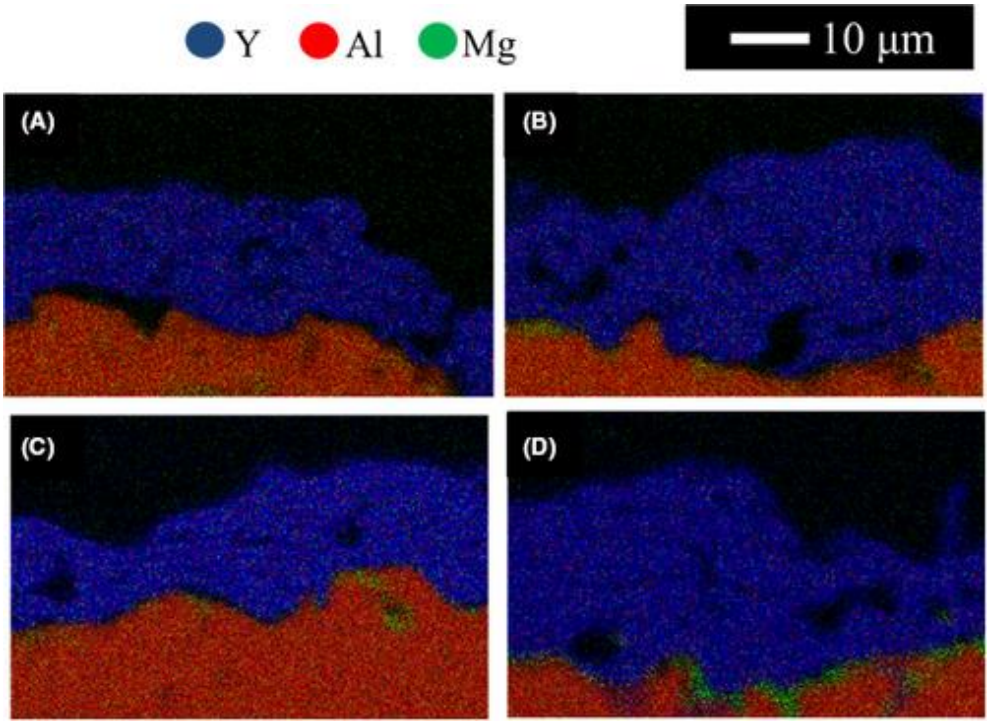

Figure 6-7 Cross-sectional EDX images of the films synthesized on the A5052 substrates, (A) as-synthesized, (B) after annealing at 400°Cfor 1 h, (C) after annealing at 500°C for 1 h, (D) after annealing at 600°C for 1 h.

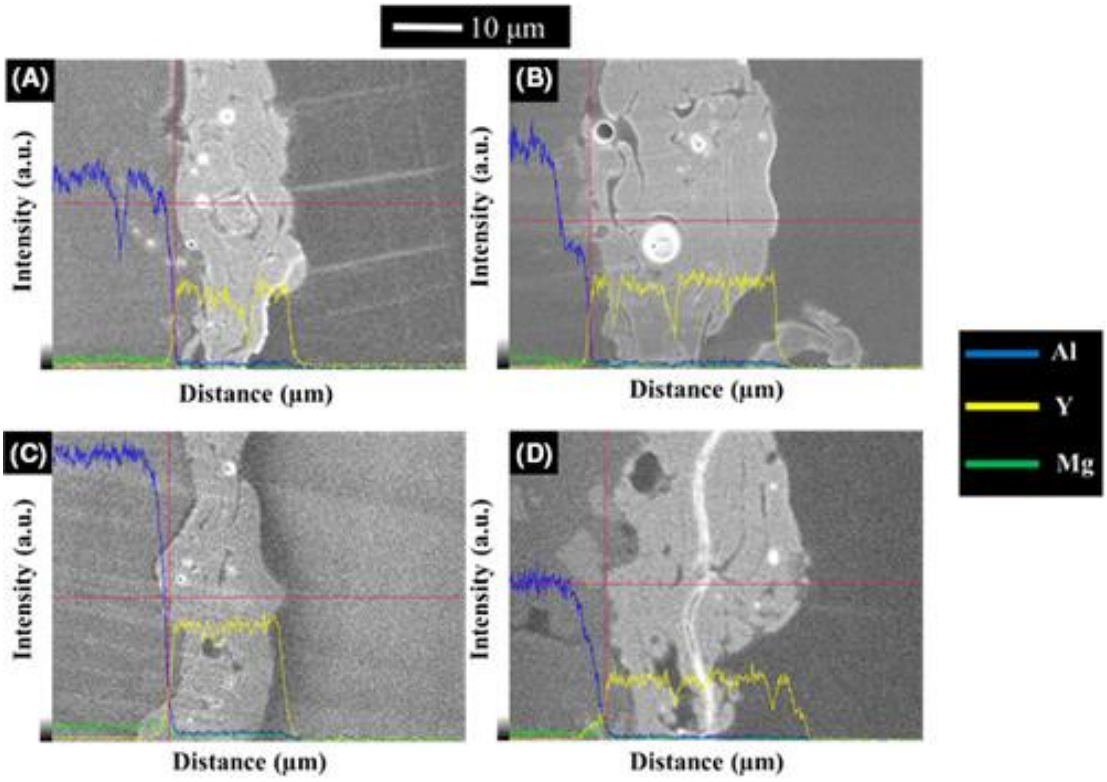

Figure 6-8 Cross-sectional EDX line profiles of the films synthesized on the A5052 substrates, (A) as-synthesized, (B)after annealing at 400°C for 1 h, (C) after annealing at 500°C for 1 h, (D) after annealing at 600°C for 1 h.

To investigate the adhesion of the interface between Y_2O_3 and the aluminum substrates, scratch tests were performed. **Fig.** 6-9 shows the scratch test results for the Y_2O_3 films synthesized on aluminum alloy substrates. These measured profiles were divided into three regions, and the breaking and delamination points for the as-synthesized and annealed Y_2O_3 films were estimated, given in **Table** 6-2 The measured profiles, and the loads were almost unchanged, showing that atmospheric annealing did not affect the adhesion of the Y_2O_3 films on the aluminum alloy substrates. These results indicate that Y_2O_3 films have strong adhesion.

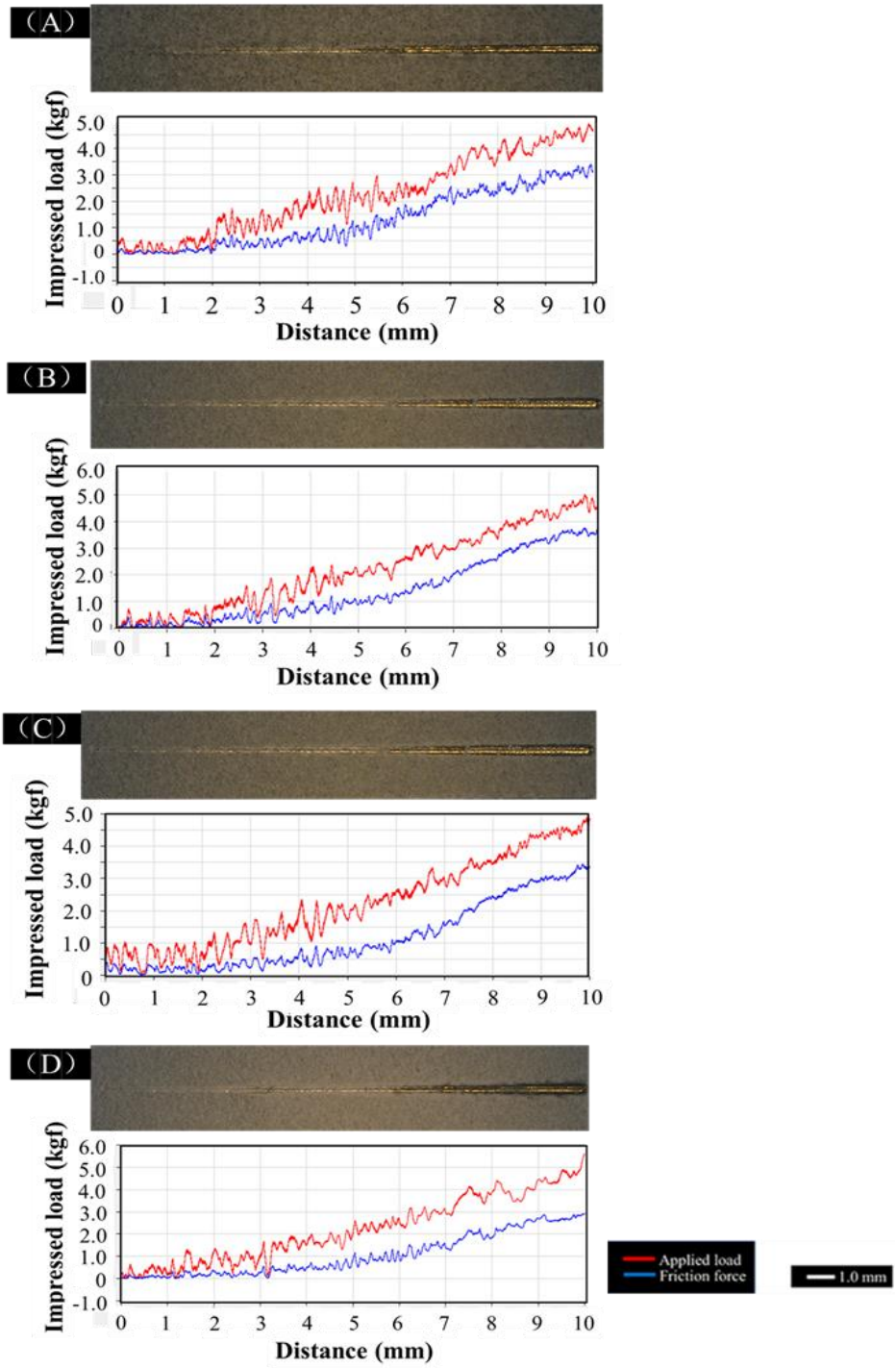

Figure 6-9 Scratch test results of the films synthesized on the A5052 substrates, (A) as-synthesized, (B) after annealing at 400°C for 1 h, (C) after annealing at 500°Cfor 1 h, (D) after annealing at 600°C 1h.

Table 6-2 Estimated breaking and delamination points for deposited films.

Sample	Breaking load (kgf)	Delamination load (kgf)
Before annealing (as-synthesized)	1.5	2.5
Annealed at 400°C for lh	0.9	2.7
Annealed at 500°C for lh	1.0	2.6
Annealed at 600°C for lh	1.0	2.9

The direct formation of Y_2O_3 layers with strong adhesion properties on the A5052 substrate was confirmed, as seen from the above results. In this study, we also attempted to verify the physical joining, which is equivalent to the anchor effect of the blasted substrate [16]. The adhesion property of the joining can be increased by increasing the roughness of the substrate. Cyclic thermal tests were conducted for the Y_2O_3 films synthesized on the blasted A5052 substrates with different surface roughness values.

Fig. 6-10 shows the surface roughness of A5052 with various blast pressures. By increasing the pressure, the roughness could be increased. The R_α values were changed to 4.681 from 1.795μm by increasing the blast pressures. In contrast, the R_α for the non-blasted (as-synthesized, prepared) A5052 was 0.166 μm. XRD measurements indicate that cubic Y_2O_3 crystalline phases were confirmed in all the deposited films, independent of the pressure. All films deposited on the A5052 substrates appeared to be white, and these appearances were not changed after the cyclic thermal tests. The presence of cracks or delaminations was not observed. The thermal history was measured during the cyclic thermal tests using the H_2-O_2 flame. **Fig.** 6-11 shows the substrate temperature profiles for the deposited films during the cyclic thermal tests. The maximum temperature was varied between 522, 473, and 488°C by increasing the blast pressure. The theoretical combustion temperature of the H_2-O_2 flame is 2700°C [17], which is greater than the melting point of the Y_2O_3 crystal at 2425°C [18]. These results indicate that the thermal histories of the deposited films are not changed by the blast pressure.

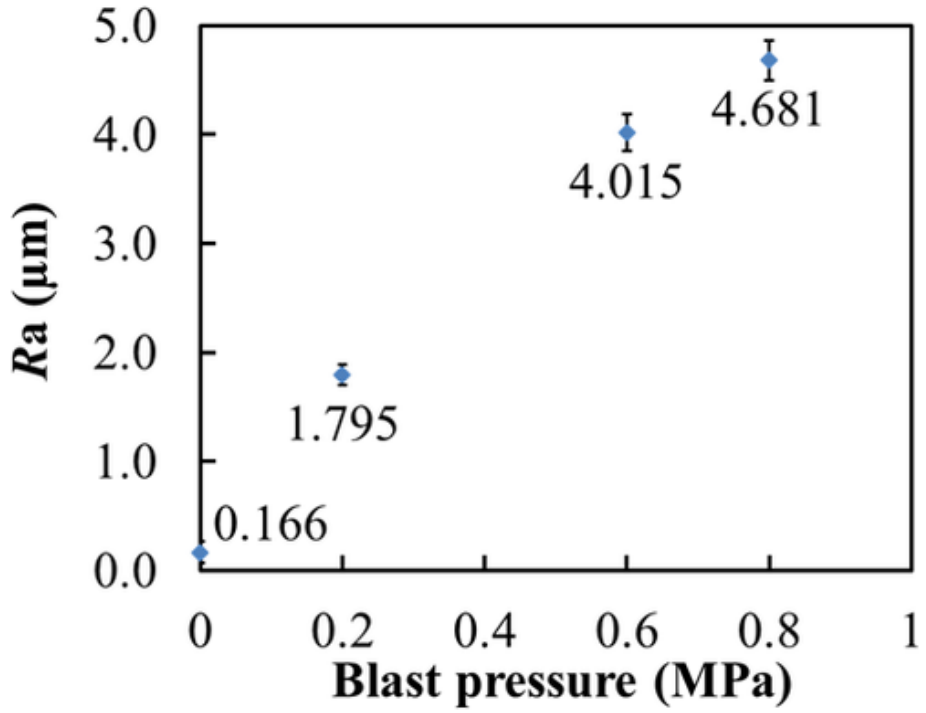

Figure 6-10 The surface roughness of the A5052 substrates with various blast pressures.

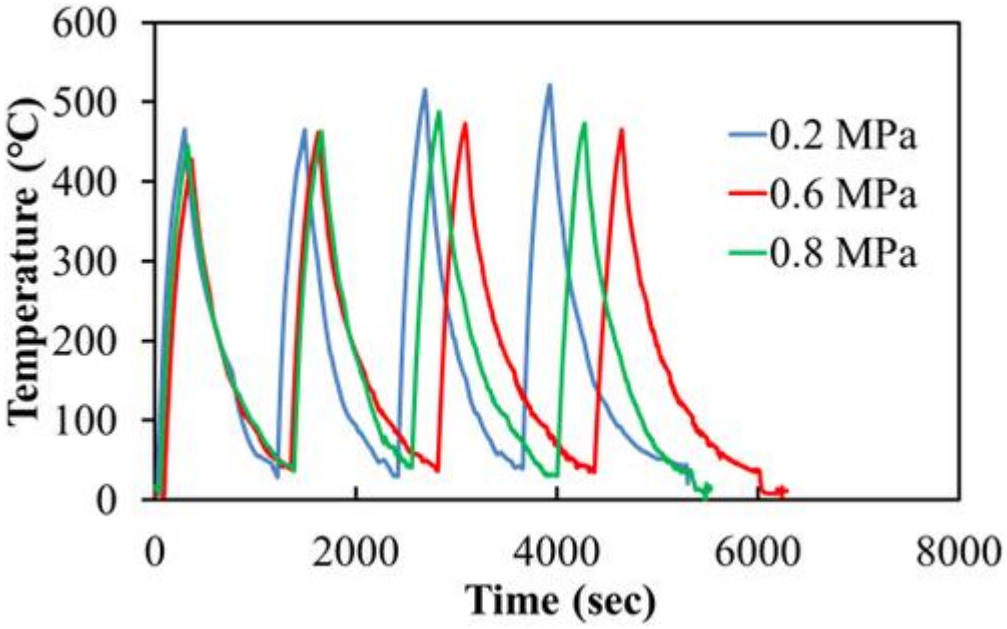

Figure 6-11 Temperature profiles of the films during the cyclic thermal shock tests.

Fig. 6-12 displays the XRD profiles of the films deposited on the blasted A5052 substrates at various blast pressures. The existence of Y_2O_3 crystals with a cubic system was confirmed. The crystalline phase was unchanged during the cyclic thermal tests at all blast pressures. The same phenomena were observed on Y_2O_3 films synthesized on stainless steel substrates [10]. The existence of $Y_4Al_2O_9$ and $YAlO_3$ crystalline phases was not confirmed in the films. Furthermore, Y_2O_3/MgO solid solutions were not present after the cyclic thermal tests. These results suggest that the thermal history during deposition had little effect on the film crystallinity. Thermal elemental diffusion phenomenon would be happened during the cyclic thermal tests. Next, we conducted the qualitatively elemental analysis by EDX mapping. **Figs.** 6-13 and 6-14 show cross-sectional SEM and EDX images for the films synthesized on the blasted A5052 substrates at various blast pressures. Metal oxide layers with dense microstructures were observed on the A5052 substrates. Delamination and deformation of the deposited films were not observed. The A5052 substrate was also analyzed for damages**. Table** 6-3 lists the average thicknesses, 2D porosities, and number of cracks per unit area of the films. The number of cracks and number of cracks per unit area was increased because of the cyclic thermal tests. In addition, the elemental distributions of the Y_2O_3 films were observed using the EDX measurements. A uniform elemental distribution was observed in the Y_2O_3 films. In addition, macroscopic elemental differences caused by the cyclic thermal tests were observed; a distinct, macroscopic elemental boundary between the Y, Al, and Mg atoms was seen. According to previous reports, inter-metallic compounds of Al and Mg atoms were formed at the interlayer of the enamel film on aluminum-magnesium substrates by preheating at 410°C [19]. The existence of such compounds results in low adhesion. In contrast, thermal elemental diffusion in our films was not observed after the cyclic thermal tests. Although the maximum temperatures of the cyclic thermal tests were 488-522°C, the Y_2O_3 films synthesized on aluminum-magnesium alloys were not delaminated or deformed.

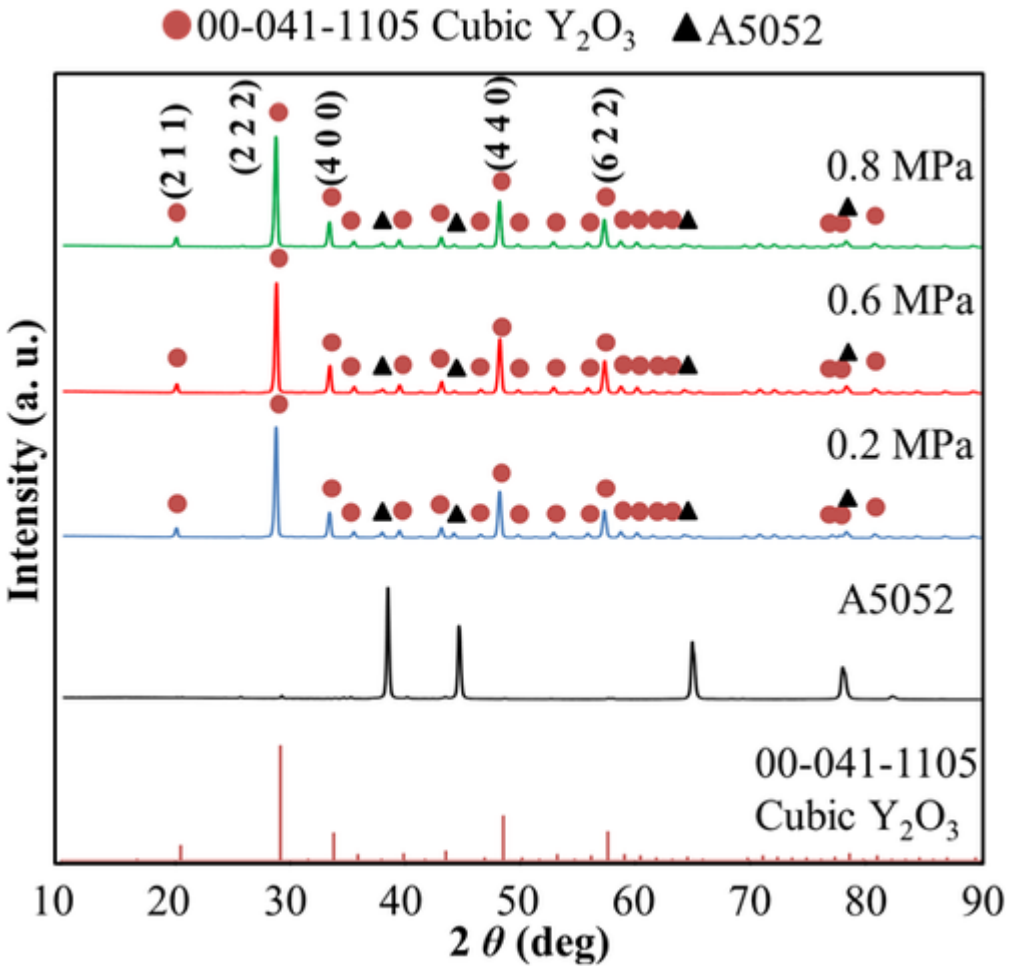

Figure 6-12 XRD profiles for 2θ values of 10-90°for the films synthesized on the blasted A5052 substrates at various blast pressures compared with ICDD cards for Y_2O_3 crystals.

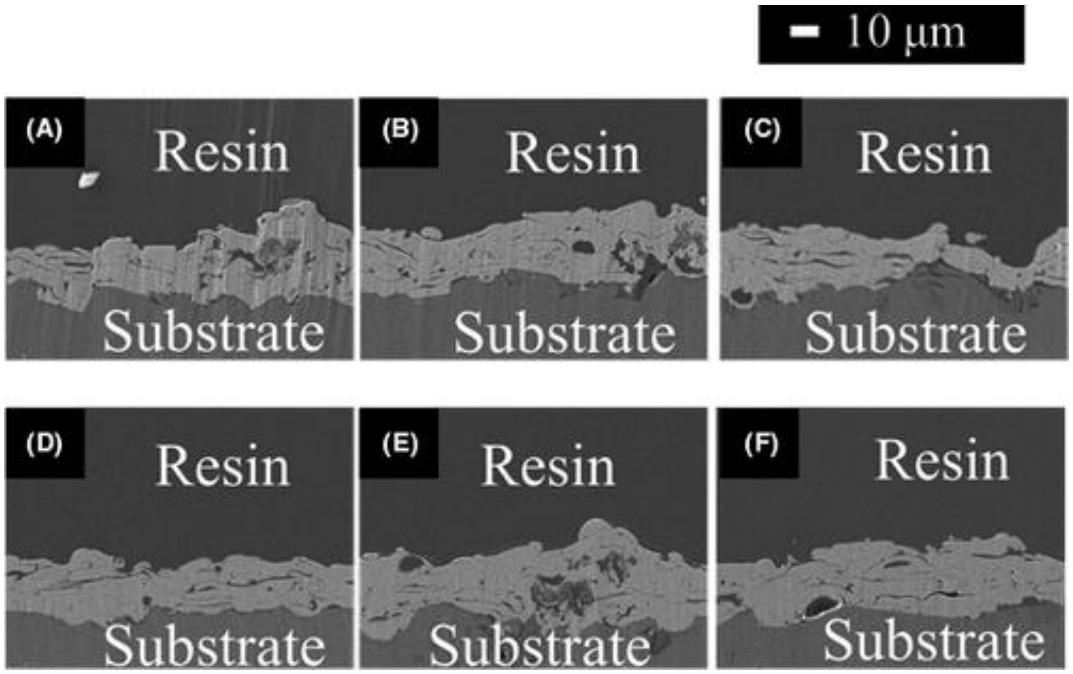

Figure 6-13 Cross-sectional SEM images of the films synthesized on the A5052 substrates at various blast pressures, (A, D) 0.2 MPa, (B, E) 0.6 MPa, and (C), (F) 0.8 MPa. (A-C) were taken before the thermal shock test, and (D-F) were taken after the test.

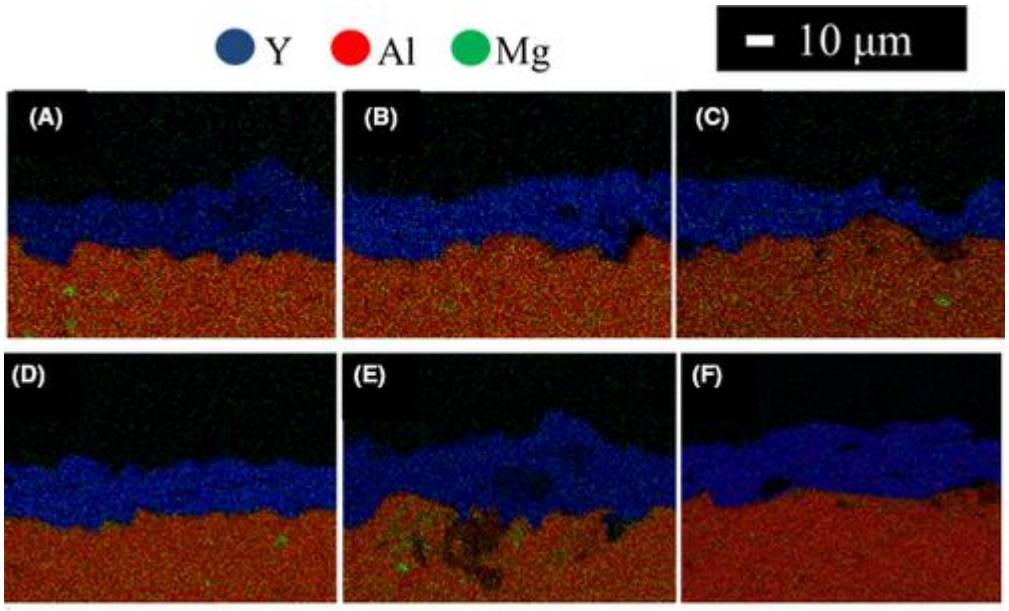

Figure 6-14 Cross-sectional EDX images of the films synthesized on the A5052 substrates at various blast pressures, (A, D) 0.2 MPa, (B, E)0.6 MPa, and (C), (F) 0.8 MPa. (A-C) were taken before the thermal shock test, and (D-F) were taken after the test.

Table 6-3 Values of estimated film thicknesses, cross-sectional porosities, estimated crack numbers, and number of cracks per unit area of films synthesized on the A5052 substrates. SD is standard deviation

Blast pressure (MPa)	Thickness (µm)		Number of cracks		Number of cracks per unit area $\times 10^{-4}$ (f/µm^{-2})		
	Average	SD	Average	SD	Average	SD	
Before cyclic thermal test	0.2	22.8	5.4	45	3.8	1.6	0.2
	0.6	20.6	4.7	43	3.2	1.7	0.1
	0.8	19.7	8.0	47	4.0	1.9	0.5
After cyclic thermal test	0.2	25.0	5.4	75	9.2	2.5	0.3
	0.6	25.6	4.5	86	21.5	2.8	0.3
	0.8	18.9	2.2	63	7.5	2.8	0.2

As described in the experimental section, the Y_2O_3 films with EDTA•Y•H complex were synthesized directly on the aluminum-alloy substrates with the assistance of an H_2-O_2 flame. The coefficient of thermal expansion for the A5052 substrate is 23.8×10^{-6} K^{-1} [20]. In contrast, the thermal expansion coefficient for Y_2O_3 crystals is 8.19×10^{-6} K^{-1} [21], the A5052 substrate coefficient is approximately four times that of the Y_2O_3 crystal. This large difference in the thermal expansion between the deposited films and the substrates introduces delamination, peeling, and deformation in deposited films. In the cyclic thermal tests, the samples were heated close to the melting point of the A5052 substrate (607-649°C) [15]. Hence, the Y_2O_3 films synthesized on A5052 form a ceramic-metal joining with strong adhesion and thermal shock properties. In the synthesis, the decomposition of the metal-EDTA complex occurred initially; the decomposition temperature for EDTA•Y•H was 365°C, from a previous study [22]. These complexes were then converted to metal oxides at temperatures of 2310-2380°C in the combustion flame. Finally, each metal oxide was deposited on the substrate, followed by a cooling and solidification processes. To explain the formation of a Y_2O_3

layer on the A5052 substrate, two effects could have happened during the deposition processes. First, a heat transfer effect due to the thermal conductivity of the A5052 substrate. The solidification is linked to the heat transfer between the splat bottom and the substrate [23]. The solidification affects the flattening behavior because splat cooling depends on the heat transfer rate through the initial solidification layer between the wetting range of both critical lines. However, the wetting at the splat/substrate interface seems to be the most dominant fac-tor with regard to the flattening of the thermally sprayed ceramic particles. The transition from a splashed to a disk-shaped splat occurs, and the temperature of which increases with droplet wetting at the interface. In this report, the wet-ting was not investigated. The other effect to consider is the heat dissipation effect on substrates, In other words, water produced by an H_2-O_2 flame with a high heat of evaporation (2250 kJ/kg) can rapidly absorb the heat on a substrate [24], allowing the joining to be synthesized without interlayers. In the synthesis, the Y_2O_3/A5052 substrate joining occurs through a mechanism combining physical and chemical joining processes. One prospective joining process is the chemical joining process between Y_2O_3 and MgO at a nanoscale. Thermodynamically, the below reaction is thought to occur in the aluminum-magnesium alloy,

$$3Mg + Al_2O_3 \rightleftharpoons 3MgO + 2Al$$

The existence of nano-MgO layers in the A5052 substrate would be responsible for strong adhesion of the Y_2O_3/A5052 joining. In previous studies, it was found that the MgO layer in A5052 plays an important role for joining in ceramic-aluminum alloys, revealed by focused ion beam and transmission electron microscopy (TEM)analysis [25,26]. The nanolayer of MgO would also have an important role in the Y_2O_3/aluminum alloy joining formed from the EDTA•Y•H complex. Aside from the mechanical bonding (the anchor effect) and Van der Waals interaction forces, chemical bonding was considered as a bonding mechanism of these materials. Hence, a Y_2O_3/aluminum alloy joining with strong adhesion and thermal shock properties was synthesized without interlayers.

6.4 Conclusions

Y_2O_3 films were synthesized from metal-EDTA complexes on aluminum alloy substrates directly using a flame-spray apparatus with an H_2-O_2 flame. Atmospheric annealing was performed to investigate the heat resistance and adhesion of the Y_2O_3 films. A cubic Y_2O_3 crystalline phase was observed after annealing, while $Y_4Al_2O_9$, $YAlO_3$, and Y_2O_3-MgO solid solutions were not observed. A joining of the Y_2O_3 and aluminum alloy with high thermal durability was obtained. In addition, the strong adhesion of the Y_2O_3/Al joining after annealing was con-firmed by scratch tests.

References

[1] Chang S, Li S, Shi R. Design and manufacturing technology of highspeed milling cutter for aluminum alloy, *Procedia Eng.*, **174**, 630–7 (2017).

[2] Dursun T, Soutis C. Recent developments in advanced aircraft aluminum alloys, *Mater. Des.*, **56**, 862–71 (2014).

[3] Zaraska L, Sulka GD, Szeremeta J, Jaskula M. Porous anodic alumina formed by anodization of aluminum alloy (AA1050) and high purity aluminum, *Electro. Chim. Acta.*, **55**, 4377–86 (2010).

[4] Jafari R, Farzaneh M. Fabrication of superhydrophobic nanostructured surface on aluminum alloy, *Appl Phys A.*, **102**, 195–9 (2011).

[5] Puchi-Cabrera ES, Staia MH, Lesage J, Gil L, VillalobosgutierrezC, Gutierrez JL, et al. EAO fatigue behavior of AA7075-T6 aluminum alloy coated with ZrN by PVD, *Int. J. Fatigue.*, 30, 1220–30 (2008).

[6] Murakami K, Hino M, Furukawa R, Kanadani T. Effects of alloying elements in aluminum alloys and activations on zincate treatment and electroless nickel-phosphorus plating, *Mater Trans.*, **51**, 78–84 (2010).

[7] Bolelli G, Lusvarghi L, Barletta M. HVOF-sprayed WC–CoCr coatings on Al alloy: effect of the coating thickness on the tribo-logical properties, *Wear.*, **267**, 944–53 (2009).

[8] Akasaka H, Ohto M, Hasebe Y, Nakamura A, Ohshio S, SaitohH. Yttria coating synthesized by reactive flame spray processing Y-EDTA complex, *Surf. Coat. Technol.*, **205**, 3877–80 (2012).

[9] Komatsu K, Sekiya T, Toyama A, Hasebe Y, Nakamura A, Noguchi M, et al. Deposition of metal oxide films from metal-EDTA complexes by flame spray technique, *J. Therm. Spray Tech.*, **23**, 833–8 (2014).

[10] Komatsu K, Shirai T, Toyama A, Iseki T, Xin DY, Costa T, et al. Densification of metal oxide films synthesized from metal complexes by flame spraying, *Surf. Coat. Tech.*, **325**, 89–97 (2017).

[11] Xin DY, Komatsu K, Keita K, Costa T, Ikeda Y, Nakamura A, et al. Heat-shock

properties in yttrium-oxide films synthesized from metal-ethylenediamine tetraacetic acid complex through flame-spray apparatus, *Appl Phys A.*, **123**, 194(7page) (2017).

[12] Komatsu K, Toyama A, Sekiya T, Shirai T, Nakamura A, Toda I, et al. Flame-spayed Y2O3films with metal-EDTA complex using various cooling agents, *J. Therm. Spray Tech.*, **26**, 195–202 (2017).

[13] Yasuda H, Ohnaka I, Mizutani Y, Waku Y. Selection of eutectic systems in Al2O3-Y_2O_3 ceramics, *Sci. Technol Adv Mater.*, **2**, 67–71 (2001).

[14] Lopato LM, Tresvyatskii SG. The phase diagram of the systemY_2O_3-MgO, *Powder Metall Met Ceram.*, **2**, 454–7 (1963).

[15] Yusof F, Muhamad MR, Moshwan R, Miyashita Y. Effect of surface states on joining mechanisms and mechanical properties of aluminum alloy (A5052) and polyethylene terephthalate (PET) by Dissimilar friction spot welding. Metal, **6**, 101(13page) (2016).

[16] Patel K, Doyle CS, Yonekawa D, James BJ. Effect of surface roughness parameters on thermally sprayed PEEK coatings, *Surf. Coat. Technol.*, **204**, 3567–72 (2010).

[17] Suga M, Kitamura Y.Kaenn-to-bakuhatu. Sankyo publishing Co., Ltd; 1972. http://www.sankyoshuppan.co.jp/abouts/

[18] Kagaku-Daijitenn-Henshyuu-iinnkai.Kagaku-Daijiten 3 (in Japanese). Kyoritsu Shuppan Co., Ltd. 1963. Available from http://www.kyoritsu-pub.co.jp/

[19] Bao Y, David T, Gao GJ, Cuenca BD, Alberdi A, Thermal-spray deposition of enamel on aluminum alloys, *Surf Coat Technol.*, **232**, 150–8 (2013).

[20] Kiuchi T, Todoroki A, Matsuzaki R, Mizutani Y, Fiber-waviness model in filament winding process, *J. Solid Mech. Mater. Eng.*, **4**, 63–74 (2010).

[21] Klein PH, Croft WJ. Thermal conductivity, diffusivity, and expansion of Y_2O_3, $Y_3Al_5O_{12}$, and LaF_3 in the range 77°–300°K, *J. Appl. Phys.*, **38**, 1603–7 (1967).

[22] Komatsu K, Tsuchiya T, Hasebe Y, Sekiya T, Toyama A, Nakamura A, et al. Synthesis of metal oxide particles using reaction route from rare-earth metal-EDTA complexes, *J. Therm. Spray Technol.*, **23**, 885–9 (2014).

[23] Fauchais P, Fukumoto M, Vardelle A, Fukumoto, M. Knowledge, concerning splat formation: an invited review, *J. Therm. Spray Technol.*, **13**, 337–60 (2004).

[24] Grissom WM, Wierum FA. Liquid spray cooling of a heated surface. *Int J Heat Mass Trans*, **24**, 261–71 (1981).

[25] Nagatsuka K, Bolyu A, Tsuchiya A, Tsukamoto M, Nakata K.Dissimilar materials joining of Al alloy/CFRP by friction lap Joining. *Trans JWRI.*, **44**, 9–14 (2015).

[26] Kotani K, Ikeuchi K, Matsuda F, Interfacial phases in diffusion-bonded joints of commercial Al alloys diffusion-bonding mechanism of aluminum alloys by transmission electron microscopy (Report 2), *J. Japan Soc.*, **14**, 382–8 (1996).

Chapter 7

Thermal insulation capability of Y_2O_3 and Er_2O_3 coatings on aluminum alloy substrate

Abstract

Nowadays, selection of a suitable spray method to design the coating microstructure such as porosity is a key to effectively improve properties of the base materials. In this study, microstructures and thermal insulation capability of chelate flame-sprayed (CFS) erbium oxide (Er_2O_3) and yttrium oxide (Y_2O_3) coatings were directly deposited on aluminum alloy (A5052) substrate have been investigated. A rotation apparatus and cooling agent (liquid nitrogen) were used during the synthesis to coolant substrate and control the deposition particles shape form during coatings deposition. The results show that the Y_2O_3 coatings had higher thermal insulation capability than the Er_2O_3 coatings. It is worth noting that the thermal insulation capacity of the Y_2O_3, Er_2O_3 coatings synthesized by the cooling substrate with liquid nitrogen method is improved. For the thicknesses of 90 – 128 μm and cross-sectional porosity of 12-33 % Y_2O_3 coatings, the temperature drop (ΔT_f =37 ℃) of the coarse-voids-structure Y_2O_3 coating at 440 ℃ and upgrade from 0.10 to 0.32 of ΔT_f per unit micron (℃/μm). It is mainly associated

with the coat having more undulated layer surface and more complicated microstructures. Therefore, it is a new idea with the chelate flame-spray method to synthesize the TBCs coating on the low-melting-point-metal material.

7.1 Introduction

Thermal barrier coatings (TBCs) have been widely used as high-temperature protective coatings in aeronautic, motor industry, and jet engines in vessels, etc., for their helpful performance like a thermal barrier and oxidation resistance**[1-3]**. TBCs often consist of a thermally resistant top-coat and an oxidation-resistant bond coat applied on a metal substrate**[4, 5]**. The TBCs are typically prepared by plasma-spray (PS) method, and especially in motor industry**[6, 7]**. Their lamellar structure with intersplat pores and intrasplat gaps contributes to excellent performance with respect to thermal insulation and strong adhesion with the substrate, the latter of which affects the lifetime of TBCs significantly**[8-11]**.

There is an urgent demand for designed film structure (such as porous, layer gap, etc.) to retard their erosion at high operating temperatures. As we all know, thermal spraying is a process in which a protective film is deposited on a substrate by spraying on its small size and high-velocity (above 100 m/s) molten (or decomposition and molten) of metals, alloys or ceramics which merge and solidify after impact producing dense or porous and thin layers or lamellae that conform and adhere to the substrate surface and form the protective coating. The thermal conductivity (k) empirical relationship (Eq.(q1)) can be used to describe the improvement in thermal insulation performance by increasing the porous in the coating**[12]**. The coating deposition and solidified shape

to increase the layer gap(or porosity) that are dependent on the material properties of the powder, impact conditions(such as velocity and temperature) and substrate conditions (such as temperature).

$$k \approx kc(1-\beta P) \quad (1)$$

where kc is thermal conductivity of bulk material, β is the factors of materials and material microstructure, p is the coating porosity. From the equation, it can be seen that the thermal conductivity decreases as the porosity increases.

Therefore, a new deposition technique using a metal-ethylenediaminetetraacetic acid(EDTA) complex has been developed**[13-15]** and called the chelate flame-spray(CFS) technique. In this spray technique, the raw materials of metal-EDTA complexes are placed into a feed unit and transported by flowing carrier gas (such as O_2 or N_2) to the spray gun. These complex powders decompose in the flame and reacted with oxygen to form metal oxide particles, which are subsequent deposited on the substrate. In a previous study, the metal oxide films with thickness of 10 - 20 μm and cross-sectional porosities of 3 – 24 % were deposited on stainless steel (SUS) substrates in several seconds**[16]**. In addition, the effect of the starting material state(mechanically mixed) and carrier gases ((N_2, air, and O_2) on the porosity of yttria-erbia (Y_2O_3-Er_2O_3), $(Y, Er)_2O_3$, Y_2O_3, and Er_2O_3**[17]** were discussed. After, it has been found that the carrier gas plays an important role in determining the porosity of the resulting films. The carrier gas of N_2 was noted to control the structure of the coat with porosity, in past reports**[15]**. In the follow-up study, we successfully synthesized Y_2O_3 coating on an aluminum alloy with low melting point, and the results showed strong adhesion without delamination

and elemental diffusion**[14]**. Thus, the chelate flame-spray method has the potential to be used as a new technology candidate on the special substrate (such an aluminum alloy) to synthetic TBCs. However, systematic research on its properties as TBC material has been rarely reported in literature.

Within the present study, the aim of this article was to investigate Er_2O_3 and Y_2O_3 films deposited on the aluminum alloy substrate by chelate flame-sprayed(CFS) with an H_2-O_2 flame and assess whether they benefits same the traditional TBCs in thermal insulation capability. And the films of microstructure, porosity evaluation, and control were investigated by changing the spray parameters such as flow rates of powder, carrier gas types, distance, substrate with coolant. In addition, the thermal insulation tests were conducted of the Er_2O_3 and Y_2O_3 coatings deposited on the aluminum alloy substrate.

7.2 Experimental

7.2.1 Raw materials

The complex of EDTA(ethylene-diamine-tetraacetic acid), EDTA·Er·H and EDTA·Y·H (Chubu Chelest Co., Ltd.), were synthesized of Er_2O_3 and Y_2O_3 porous thick coatings on materials with aluminum alloy (A5052, 50×50×10 mm^3 Fuji Manufacturing Co., Ltd.) substrate that had been previously blasted by #60 alumina grit (99.7% purity, 212-250 μm particle size, Fuji Manufacturing, Fujioka, Japan) to improve the adhesion between the substrates and the coatings in this research.

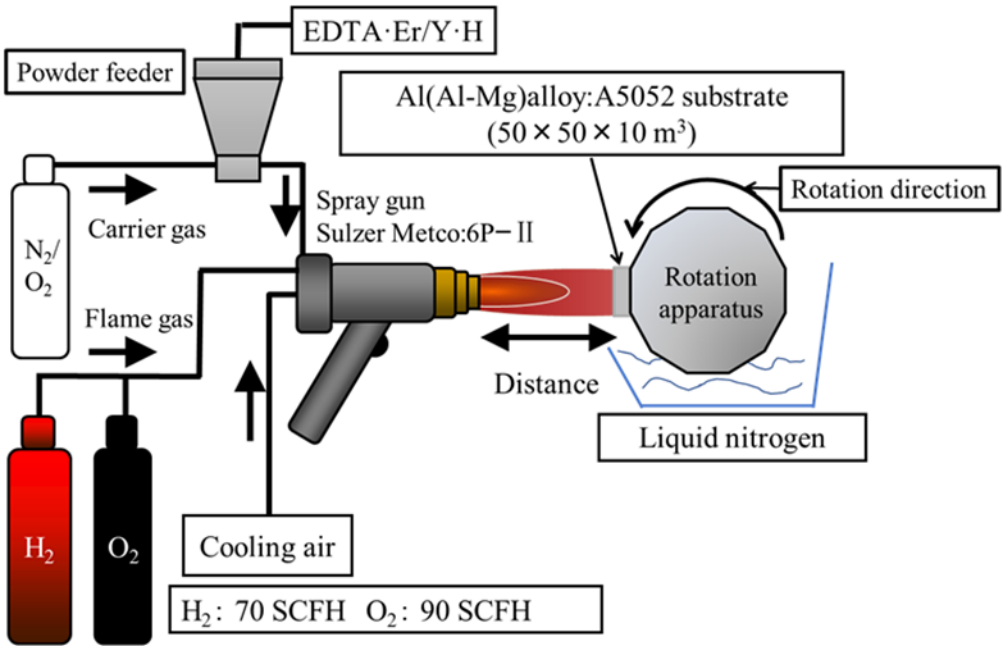

Figure 7-1. Schematic of the films deposited setup for Er_2O_3 and Y_2O_3 films.

7.2.2 Spray conditions

The **Fig.**7-1 shows the flame-spray equipment for film deposition on the aluminum alloy (A5052, 50×50×10 mm^3) substrate. A traditional hydrogen-oxygen fuel thermal spray system consisting of a feed unit (5MPE, Sulzer Metco, Westbury, NY) and flame-spray gun (6-P Ⅱ,Sulzer Metco) was used to execute splat spraying. A mixture of H_2 and O_2 was applied as the flame gas, with flow rates of 70 and 90 SCFH, respectively.

In addition, for the purpose of study the relationship between substrate temperature and particle morphology, we used the **Fig.**7-1 shows flame-spray apparatus and a 12-side rotation apparatus that substrate is fixed on it, and the substrate temperature is lowered by rotation. Then, we dig a groove on the reverse side of the substrate and inserted the K-type thermocouple to measure the temperature at different rotation speeds of the substrate during the experiment. The thermocouple was combined with a

data logger (EL-USB-TC-LCD, MK Scientific) to receive data of substrate temperature every second interval. Temperature profiles were obtained in each experiment using analysis software.

Table 7-1 Flame spraying parameters for Er_2O_3 coating deposition.

Sample	Materials (average diameter (μm))	Flow rates of powder (g/min)	Carrier gas types	Distance (mm)	Liquid nitrogen
(a)	EDTA · Er · H (60.3)	10	N_2	160	None
(b)		10	N_2	130	None
(c)		10	N_2	130	Yes
(d)		20	O_2	100	None
(e)		20	O_2	100	Yes

7.2.2.1 Thick oxide films synthesized (Preparation of Er_2O_3, Y_2O_3 TBCs)

The Er_2O_3 coatings with different porosity were manufactured by H_2-O_2-Flame-Spray and 12-side Rotation Unit (**Fig**.7-1) on blasted aluminum alloy (50×50×10 mm^3) substrate. Unscreened raw materials(EDTA·Er·H) were used to synthesized Er_2O_3 coatings of (a), (b), (c), (d), (e) conditions. For comparison, conditions (c), (e) used liquid nitrogen to lower the substrate temperature. The related thermal spraying parameters are shown in **Tabel** 7-1.

Table 7-2 Flame spraying parameters for Y_2O_3 coating deposition.

Sample	Materials (average diameter (μm))	Flow rates of powder (g/min)	Carrier gas types	Distance (mm)	Liquid nitrogen
(f)	EDTA・Y・H (36.2)	10	N_2	130	None
(g)		20	O_2	130	None
(h)		20	O_2	130	Yes
(i)		20	O_2	100	None
(j)		20	O_2	100	Yes

For comparison, we also synthesized the Y_2O_3 coatings on the blasted aluminum alloy (50×50×10 mm^3) substrate with the same as the Er_2O_3 coatings preparation method. Unscreened raw materials (EDTA·Y·H) were used to synthesized Y_2O_3 coatings of (f), (g), (h), (i), (j) conditions. Where (h) and (j), we used liquid nitrogen as a coolant to compare for not liquid nitrogen ((f), (g), (i)). The related thermal spraying parameters are shown in **Tabel** 7-2. In addition, in all conditions, Y_2O_3 and Er_2O_3 coatings with thickness are ~100 μm (the thickness was measured to 100 μm using a vernier caliper during spray process.).

7.2.3 Thermal insulation capability test

The thermal insulating tests of Er_2O_3, Y_2O_3 TBCs were performed in a k-type thermocouple**[18]**, hot-plate (CHPS-170AN, AS ONE), and data logger (midi LOGGER GL200, GRAPHTEC). A complete thermal insulating process consists of an

iso-thermal heat at 400℃ with the dwell time 30 min and the data logger recorded each temperature at intervals of 0.1 s. The average value (between 1500 and 1800 s) of the temperature difference in the quasi-stationary state of the temperature T_2 on the hot-plate side and the temperature T_1 on the back surface of the sample was taken as the temperature gradient ΔT for that sample ($\Delta T = T_2 - T_1$). The thermal insulation capability ΔT_f was calculated as the difference between the ΔT of each sample and the temperature gradient of the measured value ΔT_{al} of the aluminum alloy ($\Delta T_f = \Delta T - \Delta T_{al}$). The test model, as shown in **Fig.**7-2. From the above, steady-state method performing a measurement for thermal insulation performance when the sample has reached thermal equilibrium**[18]**.

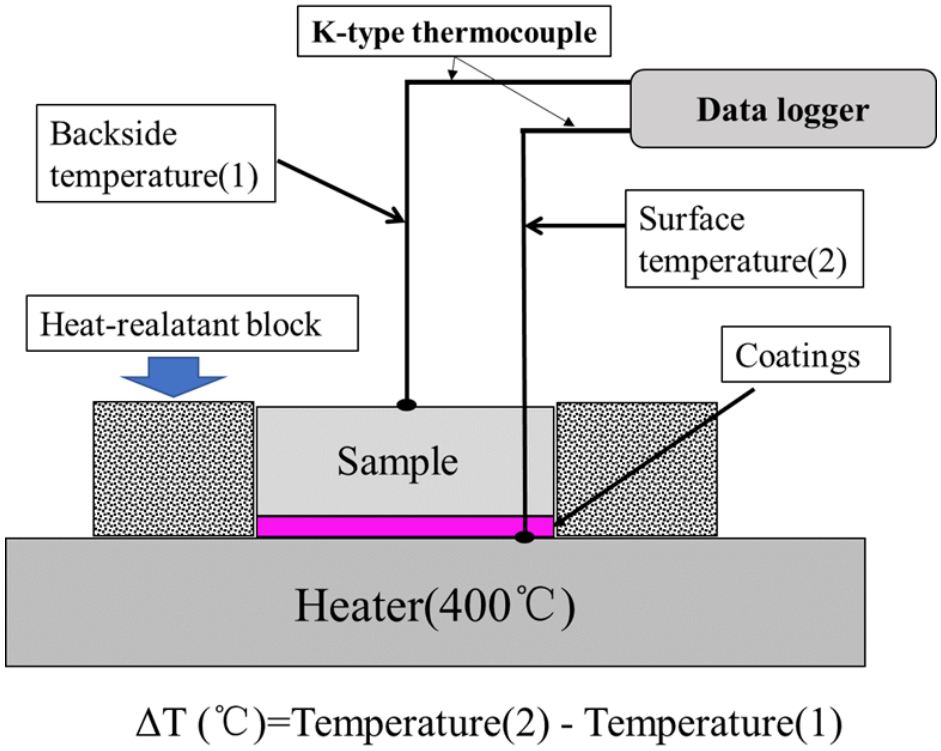

Figure 7-2 Schematic diagram of thermal insulation capability test.

7.2.4 Characteristics

The phase analysis of the synthesized various coatings was characterized by X-ray diffractometer (XRD, M03XHF22, Mac Science, Kanagawa, Japan) with Cu-Kα radiation, over 2θ values of 10˜90°. The splat morphology, microstructure, and composition of the films (deposited splat and thick metal oxide coatings) were observed using field-emission scanning electron microscopy (FE-SEM, JSM-6700F, JEOL, Japan) equipped with an energy dispersive X-ray spectroscopy (EDX, JED-2201-F, Japan). Secondary electron and backscattered electron(compositional) images of the synthesized thick coatings were acquired. All the synthesized thick coatings for cross-section analysis were firstly embedded in transparent epoxy resin and then polished with water-resistant abrasive paper. The coating thickness is the average thickness of 20 transverse section that was estimated by analyzing the whole SEM image with the commercial software SmileView, and the porosity of the coating was evaluated based on the analysis of the 2D images via ImageJ software. The average thicknesses and porosity of the coating were estimated by over 5 images randomly from the polished cross-sections.

7.3 Results and discussion

7.3.1 Bulk properties of deposited Er_2O_3 and Y_2O_3 thick coatings

7.3.1.1 Phase analysis

The XRD pattern of the synthesized Er_2O_3 thick coatings of various conditions is shown in **Fig.**7-3, which matches well with standard the International Centre for Diffraction Data(ICDD) cards as references. In **Fig.**7-3 (a), (b), (c), (d), (e), the all of

conditions Er_2O_3 thick coatings deposited on A5052 substrate exhibited cubic and monoclinic Er_2O_3 crystalline phases. Er_2O_3 exhibits three structural polymorphisms: cubic, monoclinic, and hexagonal, which are commonly known as C-, B-, and A-type structures, respectively**[17, 19]**. Hence, the distance and cold-treatment(liquid nitrogen) have no effect on the crystal structure of the deposited coatings. In addition, the deposited Y_2O_3 thick coatings by various conditions of the XRD pattern are shown in **Fig.**7-4, from all of the peaks contained only cubic Y_2O_3 crystalline phase was confirmed in the thick coatings formed by EDTA·Y·H powder. The results imply that Y_2O_3 coatings have no effect on the crystal phase before and after the cold-treatment.

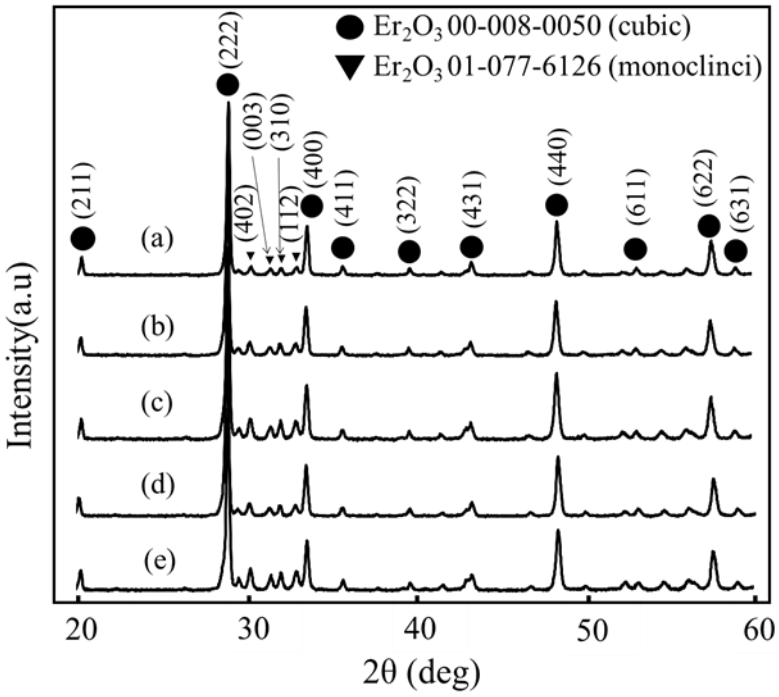

Figure 7-3 XRD patterns: (a)-(e) Er_2O_3 coatings of various conditions.

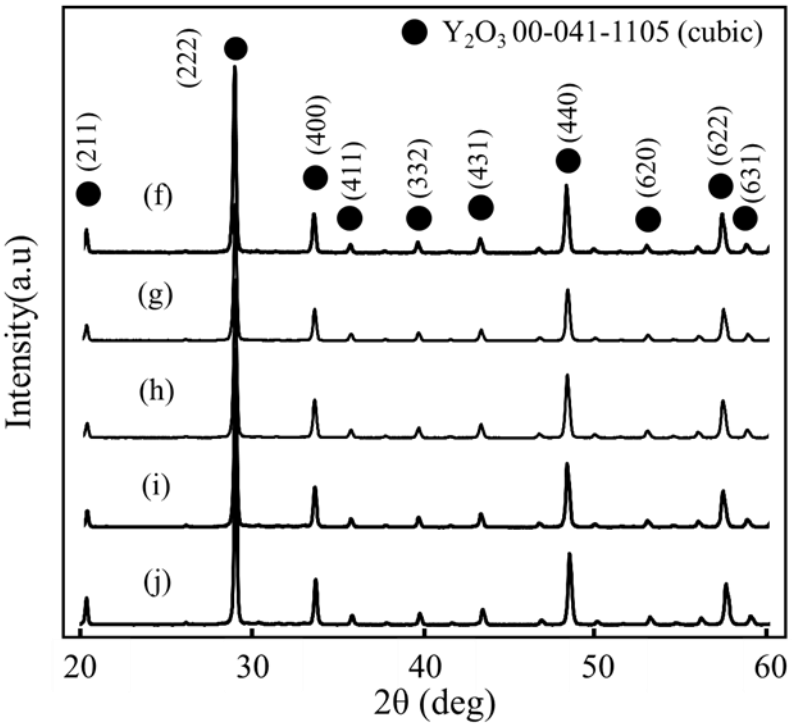

Figure 7-4 XRD patterns: (f)-(j) Y_2O_3 coatings of various conditions.

7.3.1.2 Microstructure of Er_2O_3, Y_2O_3 coatings

Table 7-3 gives the maximum substrate temperature per 30 scans of each rolling velocity during spraying. From the results, as the rolling velocity increases that the substrate temperature becomes lower. In addition, it is proved that the rotation apparatus is effective for cooling the substrate.

Fig.7-5 shows surface SEM images of the five Er_2O_3 coatings. When the flow rates of carrying gas with 10 SCFH, nozzle-distance was 160 mm, and not using liquid nitrogen, a number of spherical (i.e., not flattened) particles with sizes of approximately 1-11 μm was observed, and pores also can be seen in the surface, as shown in the **Fig.**7-5(a). The rest of the conditions are the same except for the use of liquid nitrogen of

samples (c) and (e), from those SEM images which were observed flatten particles. Further, pores were present, porous particles were also seen in the Er_2O_3 coating synthesized using liquid nitrogen, and the structure of gully gap has also been noticed, as shown in the **Fig.**7-5 (c). A stacked structure similar to the sample (b) was observed in the surface image of the sample (d), as shown in the **Fig.**7-5(d). Finally, in **Fig.**7-5(e), the particles with the highest degree of out-of-flatness (or raised) were observed in the Er_2O_3 coating deposited with using liquid nitrogen, for comparing to sample (d) (not liquid nitrogen).

Thus, the choice of using the liquid nitrogen caused differences in the surface morphologies of the deposited Er_2O_3 coating. As we all know, the microstructure of the films deposited by the PS coating technique varies with the rapid solidification and cooling of the particles**[20-22]**. The reason why are these parameters determine the flame's temperature and velocity of the in-flight particles in the reaction system**[23, 24]**. These, in turn, determine the particle's degree of melting on the substrate.

Table 7-3 Maximum substrate temperature at 30 scans per each revolution speed.

Rolling velocity (rpm)	Maximum substrate temperature/ SD (℃)
30	306 / 3.1
75	181 / 2.9
90	168 / 1.2

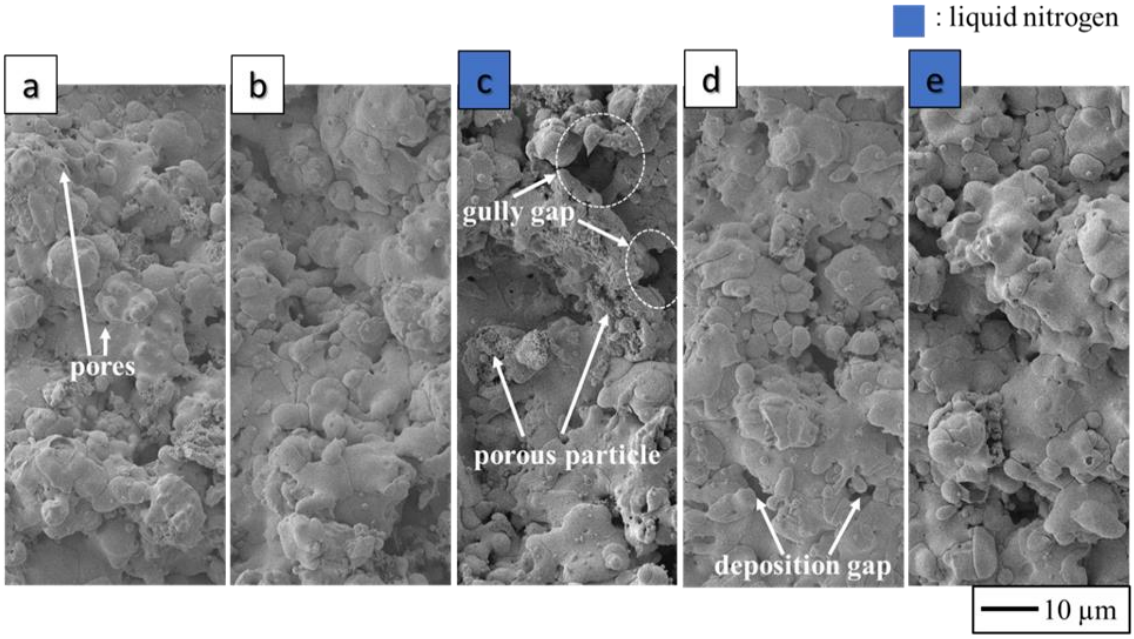

Figure 7-5 Surface SEM images: (a)-(e) Er_2O_3 coatings of various conditions.

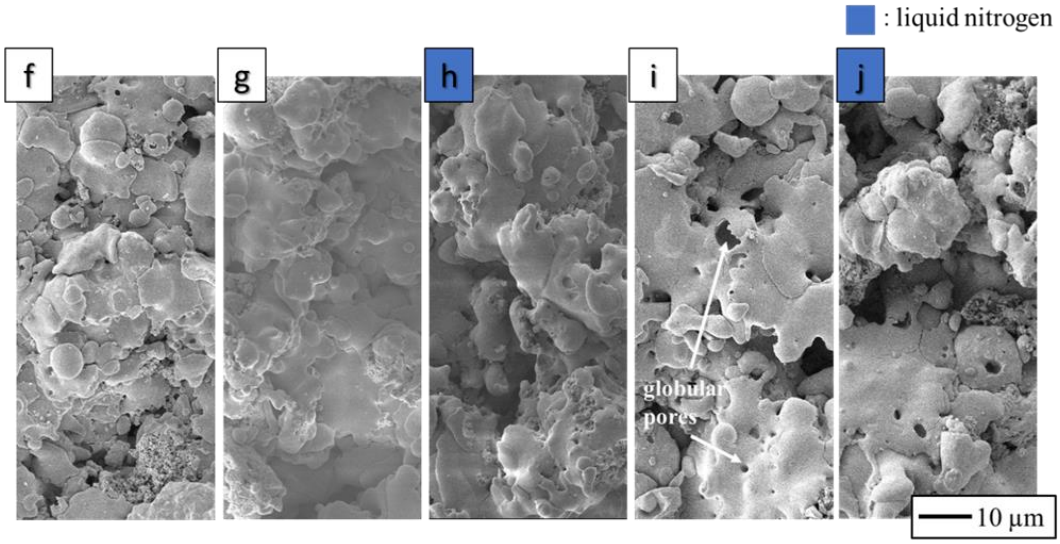

Figure 7-6 Surface SEM images: (f)-(j) Y_2O_3 coatings of various conditions.

Fig.7-6 shows surface SEM images of the five Y_2O_3 coatings (**Fig.**7-6 f-j). In the case of same conditions, sample (f) was not significantly different from sample (b) of the surface images. Next, when using liquid nitrogen (**Fig.**7-6 (h)), it can be observed

the outstanding particle stacking area and different from not using (**Fig.**7-6 (g)). Then, in the case of the spray distance was getting closer, it can be seen that a number of globular pores with sizes of approximately 1-3 μm was observed, and the degree of porous was higher than Er_2O_3 coatings (see **Fig.**7-5), as shown the **Fig.**7-6 (i) and (j). Thus, the particle stacking shapes of the molten oxide can be varied by changing the spray distance and the carrier gas, the liquid nitrogen used.

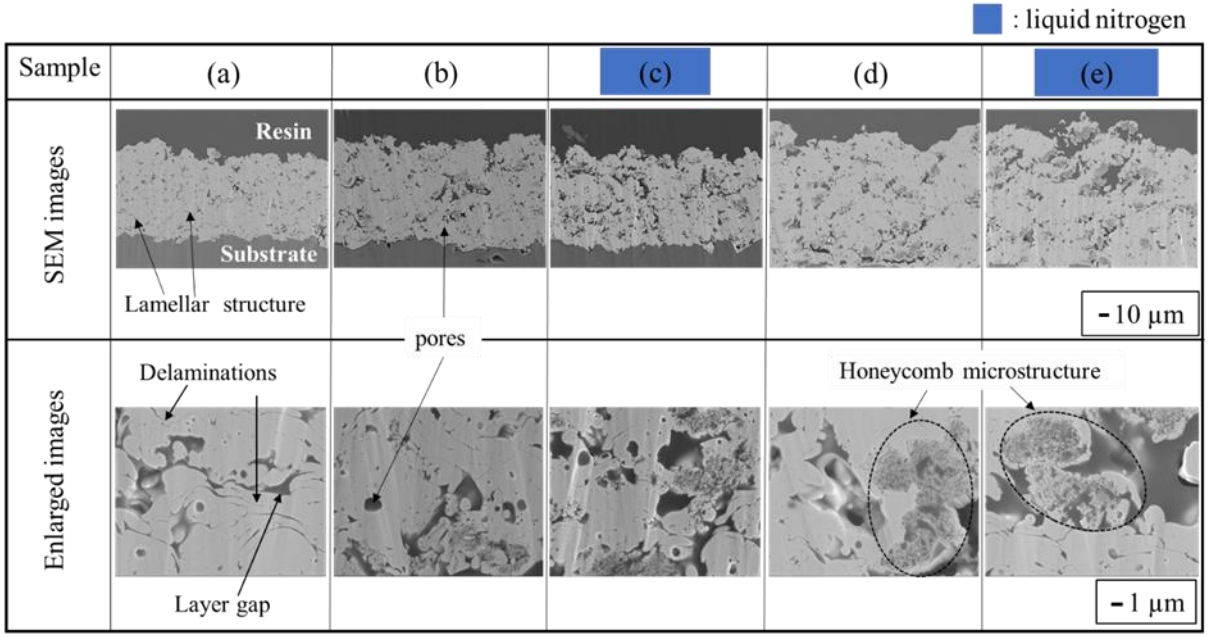

Figure 7-7 Cross-sectional SEM and enlarged images: (a)-(e) Er_2O_3 coatings of various conditions.

Thermal insulation capability depends on its form of solidified splats (microstructure), such as the pore-forming and spherical splats. the full cross-sectional morphologies of the Er_2O_3 coatings were determined using SEM, shown in **Fig.**7-7 (a)-(e) and enlarged images, respectively. A typical lamellar structure with flatted grains, micro-gap, and pores were observed in all coatings. Because the molten droplets successively impinged and spread on the substrate or the previous splats to form

continuous layers**[25]**. In the previous study, the carrier gas and distance affect the temperature and velocity of the in-flight particles with EDTA·Er·H**[16, 26]**. From the study, those were indicated that the different carrier gases(such as O_2 and N_2) used have an effect on the decomposition and oxidation of the complex. And compared to the traditional thermal spraying method(such as plasma spraying(PS) et al), as one of the highlight in this study is that the chemical reaction of EDTA·M·H (M: metal species) can be represented by equation(2) as :

$$2EDTA{\cdot}M(Er\ or\ Y){\cdot}H + 24\ O_2 \rightarrow M_2O_3 + 20CO_2\uparrow + 13H_2O\uparrow + NO_2\uparrow \qquad (2)$$

As described in Eq. (2), the H_2-O_2 flame reacts with various types of the carrier gas, thus, the structure of the metal oxide coatings can be formed by supplying higher or lower amounts of thermal energy to the inflight particles, which was determining the splat shape on the substrate, thus, it means that the carrier gases of O_2 and N_2 resulting in coatings with higher and lower porosities, respectively. Therefore, the particles were well-molten and decomposed in the flame as the spraying distance was long, and were orderly deposited on the substrate to reduce the pores in the coating (see **Fig.**7-7 (a)), on the contrary, the uneven melting time of the particles results in a shape of solidification on the substrate and makes up the unique structure with large layer gap and pores, as shown in the **Fig.** 7-7 (c) and (d). In addition, it can be clearly noted in the rolling structure at the outer layer, which we called the mountain pack structure. The reason is that the in-flight molten droplets successively impinged and deposited on the rotating substrate with the rotation apparatus. **Table** 7-4 gives the thicknesses and cross-sectional porosities of the Er_2O_3 coatings. The porosities were determined by

analyzing SEM images of the coatings. This analysis method can be used to determine the numbers of both open and closed pores**[27]**. First, Sample (a) had an average thickness of 101 μm and a cross-sectional porosity of 5 % when the nozzle-substrate distance was 160 mm. Next, when the distance becomes shorter at 130 mm, these(Sample (b)) values were 116 μm and 12 %, respectively. From the results, the main effect of standoff distance increase in sample(a) and (b) is a reduction in coating thickness, increase of porosity. In addition, it also changes in both the in-flight particle temperature and inflight particles velocity, resulting in the deposited single splats shape to change, such as the disk-like, splash, and semi-melting in the coating. Generally, when the EDTA • M • H complex is used, it would rapidly decompose and oxidizes in the flame**[28]**. It can be considered that an increase in particle dwell time is expected with an increase in standoff distance, as the result that a higher in-flight thermal transfer would also be obtained, and formed the denser coating. In the case of using the liquid nitrogen, the films(Sample (c)) obtained with an average thickness of 114 μm and porosity of 27 %, respectively. Sample (c) has almost the same thickness as Sample (b), the porosity of sample c(27%) is twice or more compared to sample b(12%) in the same spray condition only the coolant(shown in **Table** 7-4). When O_2 was the carrier gas, and nozzle-substrate distance was 100 mm, the resulting coating(Sample (d)) was the thickest, having an average thickness of 144 μm and porosity of 14 %. On the other hand, using coolant to synthesis coating(Sample (e)) that it the thickness of 149 μm and porosity of 22 %. From these results, in the case of N_2 as the carrier gas, the greatest increase of the porosity to be compared with O_2. Based on the Eq.(2), the reaction

process that takes place when the metal-EDTA complex is introduced into flame. First, the precursor melts and thermally decomposes, resulting in the production of the gases CO_2, H_2O, and NO_2. Next, metal ions are released from the chelating ligand. Finally, the metal oxide particles are formed and undergo rapid cooling. These cooled particles then solidify rapidly. Therefore, in the case of the O_2 as the carrier gas that the temperature of the in-flight particles was highest and easy to decomposition, oxide, and melt of the particles(Er_2O_3). In fact, we measured the inflight particles the temperature of 2400 ℃ in carrier gas O_2 and 2290 ℃ in carrier gas N_2, hence, it can be said that the precursor melting rate in H_2-O_2 flame would be higher in O_2 than that of in N_2. The same behavior was reported previously**[26]**, and further confirmed in this study. In addition, the porosity was increased after the use of liquid nitrogen under the same conditions(Sample (b)-(c) and (d)-(e)). The reasons why are, two-point effects could have happened during the deposition processes. First, this was attributed to the presence of absorbates and condensates on the substrate surface at lower temperatures that induce splashing during particle spreading**[29]**, and for high cooling rates, splat solidification could occur during spreading and induce splashing. Thence, when the particles impact the cooled substrate, these were affected by rapid cooling to form a layer gap. In other words, the solidification process of molten droplet was very fast, resulting in limited time for the fully spreading of the droplet, thus, the liquids solidified before forming a disk-like shape showed a complicated morphology due to the difference of the surface temperature of substrate, resulting in the irregular shape of the splat formed in the coating structure to be increased the porosity. Chen et al.**[30]** illustrated that the

deposition of the difference splat shape with the different preheated temperature of the substrate, thus, affecting the formation of pores(including inter-lamellar gap) in the coating. The other effect to consider is the nitrogen gas remaining in the gap between the top layer(each top layer of spray), in other words, micron-sized pores are mostly in the middle of the coatings, that could be resulted by the subsequent molten particles impact top layer and enclose the nitrogen gas (or air, water vapor) to form large-sized pores. Hence, the effective cooling of the substrate can affect the porosity of the coating. Therefore, it is expected that this micro-structure has well thermal insulation properties.

Table 7-4 Results of estimated film thickness, cross-sectional porosities of Er_2O_3 coatings synthesized on the aluminum alloy(A5052) substrate. coating with liquid nitrogen in content of the blue area (the same as below).

Samples	Coating materials	Thickness (μm)	Cross-sectional porosity(%)
substrate	-	-	-
(a)	Er_2O_3	101	5
(b)		116	12
(c)		114	27
(d)		144	14
(e)		149	22

Table 7-5 Results of estimated film thickness, cross-sectional porosities, of Y_2O_3 coatings synthesized on the aluminum alloy(A5052) substrate.

Samples	Coating materials	Thickness (μm)	Cross-sectional porosity(%)
substrate	-	-	-
(f)	Y_2O_3	105	12
(g)		96	14
(h)		90	27
(i)		113	15
(j)		128	33

Fig.7-8 shows cross-sectional SEM images for the Y_2O_3 coatings obtained using the various conditions (carrier gases, distance, liquid nitrogen), and shows cross-sectional SEM with enlarged images for various samples(Samples (f-j)). It can be clearly seen in **Fig.**7-8 that the microstructures of the using coolant and not are significantly different. The Y_2O_3 coatings reveal a lamellar structure showing that the coating was built-up by splats that impacted over each other and same as Er_2O_3 coatings. However, the presence of coarse voids with diameters of approximately 10-20 μm was observed in the deposited Y_2O_3 coatings under the conditions of using liquid nitrogen, as shown in **Fig.**8(h) and (g). Furthermore, a few characteristics also are noted such as the presence of pores between the substrate and the bond coat (bottom layer) in sample (h) and (g). **Table** 7-5 shows the thicknesses and cross-sectional porosities of the Y_2O_3 coatings. From **Tables** 7-4 and 7-5, the Er_2O_3 coatings were thicker than the Y_2O_3 ones. The Er_2O_3 coatings have a higher true density compared to Y_2O_3. In addition, the difference

in used powder size from sample (e)(average diameter: 60.3 μm as shown in **Table** 7-1) to sample(j)(average diameter: 36.2 μm as shown in Table 2) corresponds to a change in porosity 22% to 33%. In this respect, a change in powder size mainly affects the kinetic energy(E). Thus, the kinetic energy of the in-flight particles can be calculated as shown equation (3) as below:

$$E=1/2mv^2 \quad (3)$$

Where m is the mass of sample (kg), and v is the velocity of the inflight particle(m/s). And the density of Er_2O_3 and Y_2O_3 are 8.64 (g/cm^3) and 4.84 (g/cm^3). Then, the velocity of the inflight particles obtained through previous study**[16]**, we obtain $E(Er_2O_3) \approx 1.5$ or more $E(Y_2O_3)$, which predicts an easier formed the disk-like shape splat on the substrate for the Er_2O_3 splat compared to the Y_2O_3 splat, thereby the reduction of porosity in Er_2O_3 coating. Therefore, Er_2O_3 particle would be have higher adhesion efficiency compared to that of Y_2O_3, because higher collision energy of the in-flight particle, and it was reported in the previous study**[11]**. These results indicated that cooling of the substrate is important for depositing the porous metal oxide coatings. Such microstructure (including honeycomb microstructure) could improve the thermal insulation capability because semi-molten particles with loose distribution could form more pores (or globular pores) to lower thermal conductivity and more horizontal layer-gap might be beneficial to resist heat conduction**[31]**.

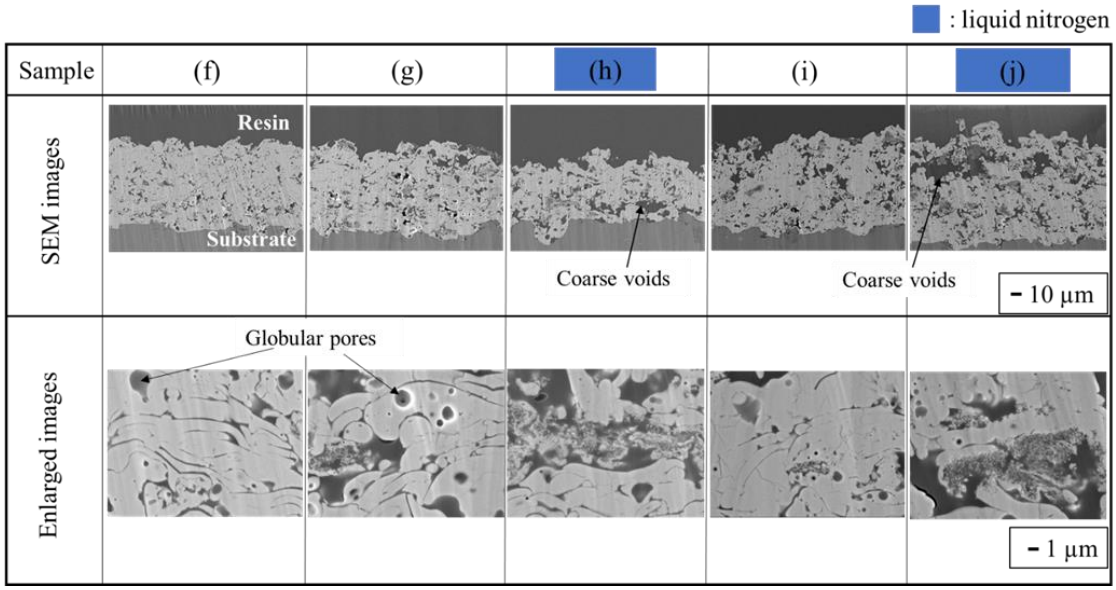

Figure 7-8 Cross-sectional SEM and enlarged images: (f)-(j) Er_2O_3 coatings of various conditions.

7.3.2 Thermal insulation capability

The fundamental function of TBCs is to protect the substrate materials from thermal flow transfer. Therefore, thermal insulation capability is considered as one of the most important factors to evaluate the performance of TBCs. In this study, the thermal insulation capability was evaluated by the temperature drop across TBCs ($\Delta T = T_2 - T_1$) in a self-made set-up. **Fig.**7-9 shows the recorded heating temperature curves of the heater (coating surface, T_0), the substrate (reference) specimen backside (T_1), the TBCs specimen backside (T_2), and coating with liquid nitrogen sample backside (T_3), respectively.

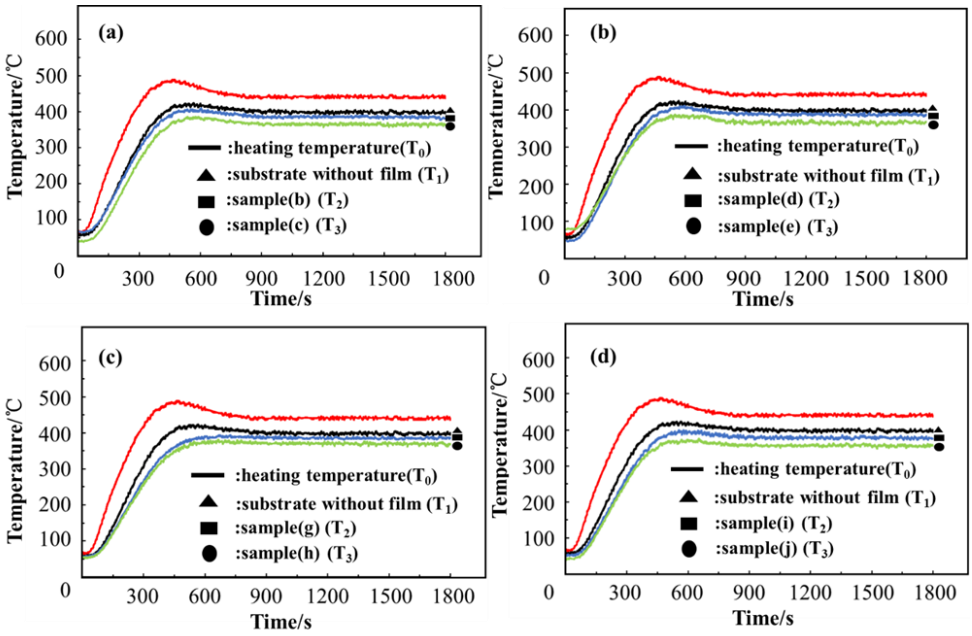

Figure 7-9 Heating temperature curves(T_0), substrate without coatings (T_1), TBCs sample backside(T_2), and coating with liquid nitrogen sample backside(T_3). (a) and (b) Er_2O_3 coatings, (c) and (d) Y_2O_3 coatings.

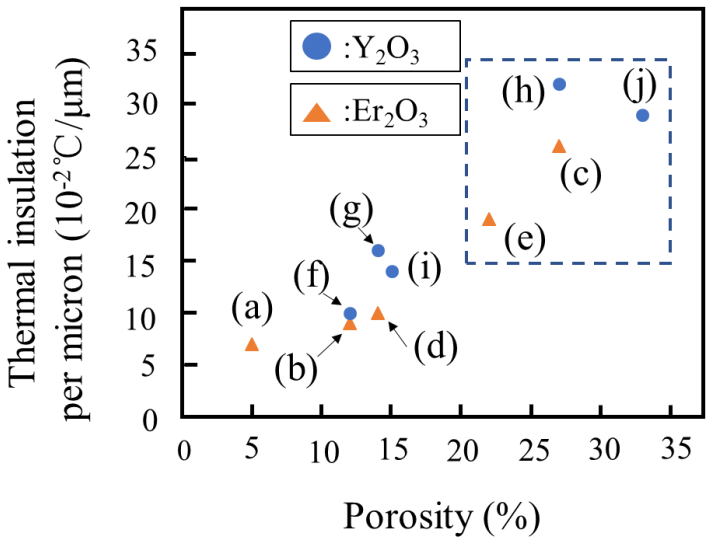

Figure 7-10 Evolution of thermal insulation per micron with total porosity for Er_2O_3 and Y_2O_3 coatings.

Fig.7-9, it can be seen that as heater temperature (T_0) increases, all T_1, T_2, and T_3 increase. The results of temperature data indicated that T_1, T_2, and T_3 became stable

when the holding time at T_0 of 440 ℃ was longer than 10 min. And there was an obvious distinction between normal-coating and coating with liquid nitrogen on temperature increase. It means that TBCs contributes to decrease the temperature of the metal substrate. Furthermore, the temperature drops across TBCs became larger in all coatings as heater temperature stable. Apparently, TBCs plays a more important role in higher temperature environment. In addition, reduce the temperature (or T_3) effect is better by coating with liquid nitrogen. The temperature drops across samples (Er_2O_3 and Y_2O_3 coatings; ΔT) measured at 440 ℃ for stable values with from 25 min to 30 min are listed in **Tables** 7-6 and 7-7 apparently, TBCs plays a more important role in higher temperature environment. In addition, tables also have given the values of TBCs (ΔT_f) and ΔT_f per unit micron. As can be seen, ΔT_f values depend on the melt-ceramic coating porosity and materials. The ΔT_f values increased with increasing the Er_2O_3 and Y_2O_3 coatings porosity from 5 % to 27 % and from 12 % to 33 %, respectively. The Y_2O_3 coatings exhibited higher ΔT_f values than the Er_2O_3 coatings. For the spray parameters of the flow rates of powder and distance are 10 g/ min and 130 mm, using the carrier gas of N_2, the Er_2O_3 coatings with porosity approximately of 12 % and 27 % (samples b and c), the coating with coolant and not, the ΔT_f values of 11 ℃ and 30 ℃, respectively. When the flow rates of powder, and distance of 20 g/ min and 100 mm, respectively, as using the carrier gas of O_2, the coatings with the porosity 14 % and 22% (samples d and e), the ΔT_f values of 14 ℃ and 28 ℃, respectively. The spray condition with coolant exhibits higher ΔT_f values than spray with not, as shown in **Table** 7-6. The T_0 value at 440 ℃ of the Er_2O_3 coating with coolant increased more

than 2 times compared with that of the conventional Er_2O_3 coating. In addition, it can be noted that it is also compatible with the Y_2O_3 coating by the same as the Er_2O_3 coating. For the results of thermal insulation test with Y_2O_3 coatings, when the spray parameters of the flow rates of powder and distance are 20 g/ min and 130 mm, using the carrier gas of O_2, the coatings with porosity approximately of 14 % and 27 % (samples g and h), the coating with coolant and not, the ΔT_f values of 15 ℃ and 29 ℃, respectively. With same the flow rates of powder of 20 g/ min, standoff the distance from130 to 100 mm, and using the carrier gas of O_2, deposited the coatings with the porosity of 15 % and 33 % (samples i and j), the ΔT_f values of 16 ℃ and 37 ℃, respectively, as shown in **Table** 7-7. From the above, the spray distance(or standoff distance) could effect on porosity with improved in the coatings. It means that the spray conditions could affect the formation of the microstructure in the coatings, which is beneficial to improve the thermal insulation performance. However, ΔT_f per unit micron value of the thinnest sample (h) exhibits higher than other coating. It could be due to the larger undulating in the outer layer, in which the pores are mostly distributed in the bottom and the inner layer. In addition, the evolution of thermal insulation per micron with total porosity for Er_2O_3 and Y_2O_3 coatings that it could be seen more clearly by shown in **Fig.**7-10. It means that the Y_2O_3 coatings have higher thermal insulation capability than the Er_2O_3 coatings. This result can have several reasons, as mentioned above the Y_2O_3 coatings had a higher porosity, but also the material itself has a lower thermal conductivity as compared to Er_2O_3 material**[32, 33]**. The different types(such as shape, size, et al.) of the pores in the two coatings, it is clearly evidenced

that, for those cross-sectional SEM images(**Fig.** 7 and 8), there is an angle between the direction of the pores(or gaps) and the substrate, in the Er_2O_3 coatings. From the Y_2O_3 SEM images, the large size pores and the number of honeycomb splats have been formed and oriented along the axis parallel to the coating substrate interface, which was improving the thermal insulation capacity due to coatings surface perpendicular to the heat flow in this test. Furthermore, the microstructural characteristic of the pore-structure Y_2O_3 coatings also has a contribution for the improved thermal insulation capability because increased grain boundaries hinder the transportation of phonons and decrease the thermal conductivity. In contrast, although the Er_2O_3 coatings(Sample (d) and (e)) are thick which the continuous dense microstructure is resulting in the easy to the thermal transportation. Generally, in the TBCs, the ΔT values depend on the coating thickness, materials, and pores-microstructure. However, it was found that the effect of pores-structure on thermal insulation performance is greater than the thickness in this study. The reason is that the increase in the thickness compared with the pores(or gaps) of the coating was not significant to the thermal insulation performance**[34]**. From the above results, it is clear that thermal insulation capability can be correlated to the total porosity if the macro-porosity dominates the porous structure of the coatings**[34]**. Furthermore, compared to the conventional spraying method such as atmospheric plasma spray, using the chelate flame spraying method results showed that the thermal insulation capability close or more than these, as shown in **Table** 7-8 **[25, 35, 36]**. By depositing on aluminum alloy(A5052) substrate, and through the various spray conditions to design the TBCs with good thermal insulation capability could be

obtained without bond coating. It could greatly reduce the weight of the hot components.

Table 7-6 Results of the temperature of the test(ΔT) and thermal insulation temperature(ΔT_f) of Er_2O_3 coatings synthesized on the aluminum alloy(A5052) substrate.

Samples	Coating materials	**ΔT (℃)**	**ΔT_f (℃)**	**ΔT_f** per unit micron (℃/μm)
substrate	-	41		-
(a)		48	7	0.07
(b)		55	11	0.09
(c)	Er_2O_3	71	30	0.26
(d)		52	14	0.10
(e)		69	28	0.19

Table 7-7 Results of temperature of test(ΔT) and thermal insulation temperature(ΔT_f) of Y_2O_3 coatings synthesized on the aluminum alloy(A5052) substrate.

Samples	Coating materials	**ΔT (℃)**	**ΔT_f (℃)**	**ΔT_f** per unit micron (℃/μm)
substrate	-	41		-
(f)		51	10	0.10
(g)		56	15	0.16
(h)	Y_2O_3	70	29	0.32
(i)		57	16	0.14
(j)		78	37	0.29

Table 7-8 Results of thermal insulation capability with APS and CFS.

Method	Coatings/ bonding layer	Thickness (μm)/ porosity(%)	ΔT (℃)	Thermal insulation per micron ΔT_f(℃/μm)
APS	7-8 wt%YSZ/ NiCrAlY	430/20.37	133	0.31
APS	8 wt%YSZ/ NiCrAlY	320/13.0	71	0.22
APS	8 wt%YSZ	150/6.83	65	0.43
CFS	**Er_2O_3 / without**	**114/27**	**30**	**0.26**
CFS	**Y_2O_3 / without**	**128/33**	**37**	**0.29**

APS: Atmospheric Plasma Spray

CFS: Chelate Flame Spray

4. Conclusions

In this work, Er_2O_3, Y_2O_3 thick coatings were synthesized from metal-EDTA complexes on aluminum alloy(A5052) substrates directly using the flame-spray and the rotation apparatus with H_2-O_2 flame. In addition, an experimental study was carried out two types of TBC coatings structure by four kinds of spraying parameters(carrier gas, flow rates of powder, distance, coolant-substrate) to assess their properties(porosity, thermal insulation capacity) and functional performances as protective layers deposited in metal substrate.

The results showed that:

- In all samples, the Y_2O_3 coatings(12-33 %) showed high porosity than the Er_2O_3 coatings(5-27 %).
- The thermal insulation test results were revealed by the Y_2O_3, Er_2O_3 coatings indicate it as a promising coating material for low melting point metal(aluminum alloy), especially the Y_2O_3 coatings. These results could be due to the honeycomb microstructure, the layer gap, and the closed porosity that are characteristics of the CFS-sprayed coatings. In addition, the correlation between thermal insulation capability and coating thickness was not found in this study.
- There are microstructural differences between the deposited on the aluminum alloy substrate by Y_2O_3 coatings and Er_2O_3 coatings. These differences are due to the different density.

The sample properties combined with the thermal insulation test results indicate that it can be expected to have a better thermal insulation effect with the use of ceramic coatings applied on the car-body material and piston crown (aluminum alloy). This idea will be expanded and deepened in further studies.

ORCID
Yan Xin Dan ID: http://orcid.org/0000-0003-0178-8795

References

[1] S. Chen, X. Zhou, W.J. Song, J.B. Sun, H. Zhang, J.N.Jiang, L.H. Deng, S.J. Dong, and X.Q. Cao, *J. Eur. Ceram. Soc.,* **39**, 2397-2408 (2019).

[2] N.P. Padture, M. Gell, E.H. Jordan, *Science*, **296**(5566), 280–284 (2002).

[3] A.G. Evans, D.R. Clarke, C.G. Levi, *J. Eur. Ceram. Soc.,* **28**(7), 1405–1419 (2008).

[4] J. Ilavsky, G.G. Long, A.J. Allen, and C.C. Berndt, *Mat. Sci. Eng. A-Struct.,* **272**(1), 215–221 (1999).

[5] J.T. Demasimarcin, D.K. Gupta, *Surf. Coat. Tech.,* **68**, 1–9 (1994).

[6] R. Dhiman, A.G. McDonald, S. Chandra, *Surf. Coat. Technol.,* **201**(18), 7789–7801 (2007).

[7] J.A. Thompson, T.W. Clyne, *Acta. Mater.,* **49**(9), 1565–1575 (2001).

[8] H. Xie, Y.C. Xie, G.J. Yang, C.X. Li, and C.J. Li, *J. Therm. Spray Technol.,* **22**(8),1328–1336 (2013).

[9] I.O. Golosnoy, A. Cipitria, T.W. Clyne, *J. Therm. Spray Technol.,* **18**(5–6), 809–821 (2009).

[10] G.R. Li, B.W. Lv, G.J. Yang, W.X. Zhang, C.X. Li, and C.J. Li, *J. Therm. Spray Technol.,* **24**(8), 1355–1367 (2015).

[11] Y. Tan, A. Shyam, W.B. Choi, E. Lara-Curzio, and S. Sampath, *Acta. Mater.,* **58**(16), 5305–5315 (2010).

[12] S. Sivakumar, K. Prvaveen, G. Shanmugavelayutham, S. Yugeswaran, and J. Mostaghimi, *Surf. Coat. Technol.,* **326**, 173-182 (2017).

[13] H. Akasaka, M. Ohto, Y. Hasebe, A. Nakamura, S. Ohshio, and H. Saitoh. *Surf. Coat. Technol.,* **205**, 3877–80 (2012).

[14] K. Komatsu, T. Costa, Y. Ikeda, K. Abe, Y.X. Dan, T. Kimura, A. Nakamura, T. Shirai, and H. Saitoh, *Int. J. Appl. Ceram. Tech.,* **00**, 1-10 (2018).

[15] D.Y. Xin, K. Komatsu, K. Keita, T. Costa, Y. Ikeda, A. Nakamura, S. Ohshio, and H. Saitoh, *Appl. Phys. A.,* **123**, 194(7) (2017).

[16] K. Komatsu, T. Shirai, A. Toyama, T. Iseki, D.Y. Xin, T. Costa, A. Nakamura, Y. Li, S. Ohshio, H. Muramatsu, and H. Saitoh, *Surf. Coat. Tech.,* **325**, 89–97 (2017).

[17] K. Komatsu, T. Sekiya, A. Toyama, T. Shirai, A. Nakamura, S. Oshio, and H. Saitoh, *Mater. Trans.,* **57**(1), 70–74 (2016).

[18] M. Sekine, K. Sonoya, M. Nakamura, *Surf. Coat. Technol.,* **65**(6), 276-282 (2014).

[19] K. Komatsu, T. Sekiya, A. Toyama, Y. Hasebe, A. Nakamura, M. Noguchi, Y. Li, S. Ohshio, H. Akasaka, H. Muramatsu, and H. Saitoh, *J. Therm. Spray Technol.,* **23**, 833(8) (2014).

[20] M. Rezvani rad, G.h. Farrahi, M. Azadi, and M. Ghodrati, *Ceram. Int.,* **40**, 15925-15940 (2014).

[21] C.J. Li, A. Ohmori, *J. Therm. Spray Technol.,* **11**(3), 365–374 (2002).

[22] G.J. Yang, C.X. Li, S. Hao, Y.Z. Xing, E.J. Yang, and C.J. Li, *Surf. Coat. Technol.* **235**, 841–847 (2013).

[23] A. Cipitria, I.O. Golosnoy, T.W. Clyne, *Acta Mater.,* **57**(4), 980–992 (2009).

[24] M. Markus, M. Georg, M. Robert, G. Olivier, and V. Robert, *Surf. Coat. Technol.,* **318**, 157-169 (2017).

[25] D. Chen, F. Luo, X. Lou, Y.H. Qing, W.C. Zhou, and D.M. Zhu, *Ceram. Int.,* **43**, 4324-4329 (2017).

[26] K. Komatsu, T. Tsuchiya, Y. Hasebe, T. Sekiya, A. Toyama, A. Nakamura, H. Akasaka, and H. Saitoh, *J. Therm. Spray Technol.,* **23**, 885(9) (2014).

[27] S. Deshpande, A. Kulkarni, S. Sampath, and H. Heraman, *Surf. Coat. Technol.,* **187**, 6-16 (2004).

[28] Y. Tanaka, M. Nakashima, M. Fukumoto, *Quarterly Journal of the Japan Welding Society*, **20** (2), 317-321 (2002).

[29] S. Sampath, X. Jiang, *Mater. Sci. Eng. A*, **304–306**(0), 144–150 (2001).

30) S.Y. Chen, G.Z. M, H.D. Wang, P.F. He, M. Liu, H.J. Wang, B.S. Xu, *Appl. Surf. Sci.*, **409**, 277–284 (2017).

[31] R.S. Lima, B.R. Marple, *J. Therm. Spray Technol.,* **17**, 846–852 (2008).

[32] Kevin M. Hubbard, Brent F. Espinoza, *Thin Solid Films,* **366**(1-2), 175-180 (2000)

[33] Y. Tsukuda, *Japan Sci. and Tech. Agency*, **8**, 1106-1108 (1979).

[34] G. Bertrand, P. Bertrand, P. Roy, C. Rio, and R. Mevrel, *Surf. Coat. Technol.,* **202**, 1994-2001 (2008).

[35] R. Ghasemi, H. Vakilifard, *Ceramics International*, **43**, 8556-8563 (2017).

[36] W.B. Gong C.K. Sha, D.Q. Sun, W.Q. Wang, *Surf. Coat. Technol.*, **201**, 3109-3115 (2006).

Chapter 8

New method development for thermal analysis of metal-oxide coating

Abstract

In order to cope with heavy energy efficiency and reduced the temperature of the engines have been the driving force for mechanical industry in the past decades and the new thermal barrier coatings are being investigated. Er_2O_3 coatings were directly deposited on an aluminum alloy substrate without bond coating by chelate flame spraying(CFS). The thermal insulation capability, thermal conductivity, microstructure, porosity, and splats of these two kinds of coatings with thickness were studied. For the coating with a thickness of 300 μm, exhibits higher ΔT value, which increases by 43.1 % compared with that of the thickness of the 100 μm coating with the same spray conditions. It exhibited low thermal conductivity, decreasing from 4.56 $Wm^{-1}K^{-1}$ to 2.57 $Wm^{-1}K^{-1}$ at the stable phase(500 ℃ and 600 ℃), which is mainly due to its special microstructure with more mesh-splats, higher porosity(28.3 %). This study provides a new idea of test method, which can be measured that thermal conductivity and thermal insulation capability.

8.1 Introduction

Thermal barrier coatings (TBCs) are widely used in the hottest sections protection with thermal, corrosion, and erosion of aero and land based gas turbines in order to significantly enhance the durability of components or allow the increase in working temperatures for better engine performance and efficiency [1-6]. A typical TBCs are double-layer coatings applied to protect components consisting of a metallic bond coat and a ceramic top coat [7,8]. The main function of the bond coat is to protect the substrates from oxidation and corrosion with thermal [9]. As we all know, the ceramic coat has a relativity low thermal conductivity that can reduce the requirements for the cooling system [10]. Generally, the ceramic surface coat is usually deposited using the plasma spraying technique [11,12]. The traditional plasma-sprayed ceramic coating exhibit a lamellar structure with large connected gaps and high porosity, which is the reason to enhance the insulation and lower the thermal conductivity [13]. However, high energy consumption and large-scale installation requirements limit the further application of these methods [14]. Therefore, searching for a new flame spraying system to synthesis the TBCs with high thermal insulation capability and good high-temperature stability is still of both scientific significance and technological importance.

Recently, a new deposition technique using a metal-ethylenediaminetetraacetic acid (EDTA) complex has been researched [15,16]. In this technique, the metal-EDTA complex powders are introduced using the flame spraying method that we called this method for chelate flame spray (CFS). These complex powder decompose and oxide in the flame, forming metal oxide particles, which are subsequently deposited on the substrate. In this method, the metal oxide coatings were synthesized with thickness:9.7-13.5 μm and cross-sectional porosity:1.6 – 33% on the stainless steel and aluminum alloy substrate [17,18]. The metal oxide films were deposited on the metal substrate from EDTA complexes through the flame of H_2-O_2. Furthermore, it has been found that the carrier gas types, powder feed ratio, and substrate temperature play an important role in determining the microstructure such as shape and size of pore and gaps size between the splats of the sprayed coating. Based on the above, the thermal conductivity of a porous ceramic coating depends on the intrinsic thermal conductivity of the

material related to the composition and structure as well as on the architecture of the porous network, while the enhanced thermal insulation capability. In addition, it has been reported that the deposited the metal-oxide coating exhibits a strong adhesion and good thermal shock performance on the aluminum alloy and stainless steel substrate [15,19]. Up to now, the series studies have been based on comparisons between coatings produced from different spray conditions with substrate temperature, carrier gas types and powder feed ratio which did allow to demonstrate that a relationship exists between the size and shape of the pore, as well as the nature porosity, and the thermophysical properties, but there is still a need to establish quantitative microstructure thermal conductivity correlations for the optimal design.

Within the present study, TBC coating with different porous and thickness was synthesized on an aluminum alloy substrate by appropriate manipulation of the variables controlling the CFS processes. The microstructures features and thermal insulation capability of the deposited coatings were investigated, and to provide some foundation for improving the properties of TBC. In addition, the thermal response (Laser flash method) tests were conducted on various porosity of TBCs, which were calculated the thermal conductivity.

8.2 Experimental

8.2.1 Chelate flame spraying process

We first prepared EDTA· Er· H (Chubu Chelest Co., Ltd.) for the deposition of Er_2O_3 thick coatings. **Fig**.8-1 shows the experimental setup for TBC deposition from the EDTA· Er· H complex onto the aluminum alloy(aluminum-magnesium alloy, A5052) substrate with the thermal insulation capability test. A conventional flame-spray apparatus consisting of a feed unit(5MPE, Sulzer Metco, Westbury, NY) and spray gun (6P-II, Sulzer Metco) was used to perform reactive spraying. This apparatus is used commercially for the deposition of TBCs with H_2-O_2 flame. And the rotation apparatus with the capability of depositing 12-samples(dodecahedron) at a time was fabricated inhouse. The rotation velocity of the apparatus was kept to the 90 rpm. As has been stated above, we employed different carrier gases and standoff distance with the

substrate to determine the effects on the microstructure of the coatings. Five different types of samples were sprayed in this work, as shown in **Table** 8-1. One type of sample was sprayed by carrier gas O_2, and it was aim of the coating (sample (a)) with thickness and porosity of 100 μm and 10 %, respectively. The second (sample (b)) and the third (sample (c)) were sprayed by carrier gas N_2, and both conditions are the same, only the one of the coating which in order to improve the porosity, liquid nitrogen was used as a substrate coolant. Those samples were prepared to synthesis with porosity of 20 and 30%, respectively. Finally, the two samples (sample (d) and (e)) were sprayed with same spray parameters with sample (b) and (c), only the thickness was varied.

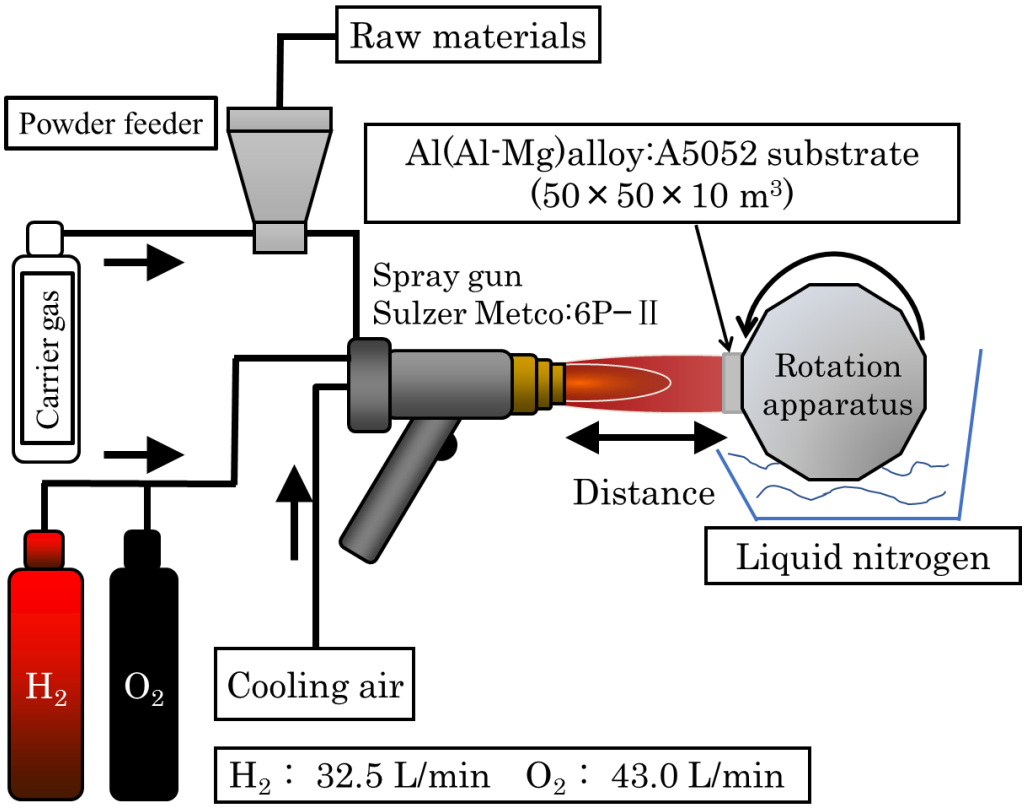

Figure 8-1 Schematic of the films deposited setup for splat morphologies and porous film.

Table 8-1 Flame spraying parameters.

Sample	materious	Flow rates of powder (g/min)	Carrier gas types	Flow rates of carrying gas (SCFH)	Distance (mm)	Rolling velocity (rpm)	Liquid nitrogen
(a)		20	O_2		100		None
(b)		10	N_2		130		None
(c)	EDTA · Er · H	10	N_2	10	130	90	Yes
(d)		10	N_2		130		None
(e)		10	N_2		130		Yes

8.2.2 Characteristics

The cross-sectional morphology and microstructure of the coatings were observed using field-emission scanning electron microscopy(FE-SEM)(JSM-6700F, JEOL). At least 6 SEM images with magnification 200 and 400 respectively are randomly acquired and used for each sample. The coating thickness is the average thickness of 20 transverse section that was estimated by analyzing the whole SEM image with the commercial software SmileView, and the porosity of the coating was evaluated based on the analysis of the 2D images via ImageJ software. The average thicknesses and porosity of the coating were estimated by over 5 images randomly from the polished cross-sections.

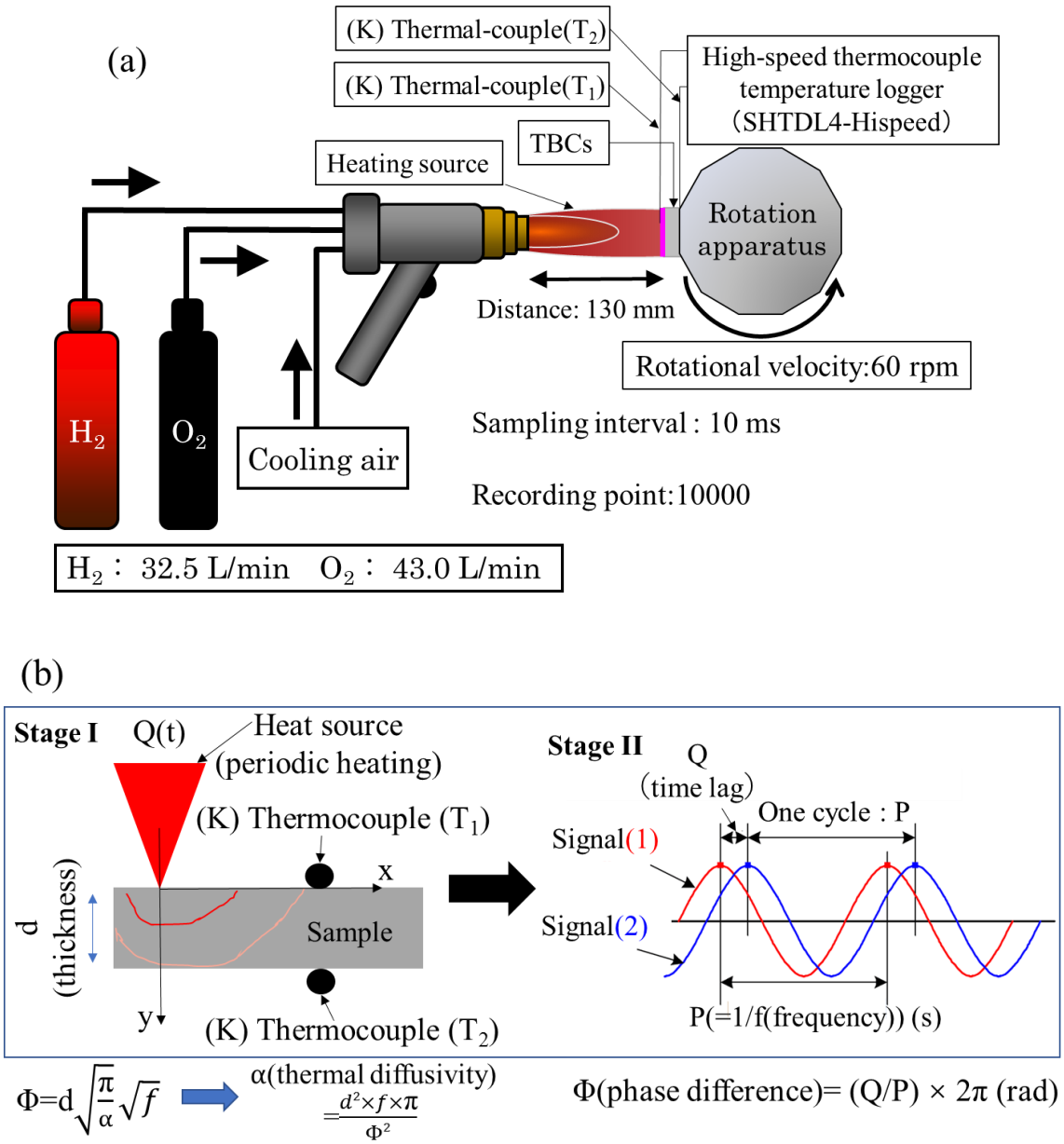

Figure 8-2 (a) Schematic diagram of thermal conductivity test, and (b) schematic diagram of the principle of measurement by the AC calorimetric method.

8.2.3 Thermal conductivity measurement

The schematic diagram of the thermal insulation capability test is shown in **Fig.**8-2. The parameters of the heating source are the same as previously described(Fig.8-1) with H_2-O_2 flame. The TBCs samples or the substrate samples were fixed in the rotation

apparatus, and the rotation velocity was kept the 60 rpm. The surfaces of the TBCs sample or the substrate sample were heated by the H_2-O_2 flame, and the sample backsides were in the rotation apparatus. Two K-types thermocouples were used as sensors, one was located in the sample surface to measure the surface temperatures(coating surface temperatures, T_1=T_{1s}(substrate)=T_{1c}(coatings)) and another one was fixed on sample backside to collect the Temperatures(T_2=T_{2s}(substrate)=T_{2c}(coatings)) of the sample backside. The K-types thermocouples were linked to the wireless high-speed thermocouple temperature function logger (SHTDL4-Hispeed) respectively to record the heating temperature curves (T_1, T_2) in real-time with 60 s. For scientific, it is recorded that the change curve of surface temperature 100 points (times) at 1 rpm(1s). The temperature data were analyzed and stored by a computer. In this study, the two temperature stages will be analyzed respectively as the rising curve, and the stable curve, the temperature drops across the sample and substrate (T_1-T_2 = ΔT_s, ΔT_c), across the TBCs (ΔT_s - ΔT_c) were calculated. In addition, the thermal conductivity of the coatings would be measured by AC calorimetric method [20]. In this study, **Fig.**8-2 (b) shows a schematic diagram of the principle of measurement by the AC calorimetric method with stages I and II. The phase difference(Φ) is calculated by time lag (Q) and one cycle (P). In a simplified approach, when the coating thickness more than to 10 μm, the thermal diffusivity(α) can be calculated as Eqs. (1),(2) [21]:

$$\Phi = \sqrt{\frac{\pi f}{\alpha_s}}x \quad (1)$$

$$\Phi = \mathrm{d}\sqrt{\frac{\pi}{\alpha_c}}\sqrt{f} \quad (2)$$

where θ is the phase difference in both of the curves(T_1 and T_2), d is the thickness of the coating, f is the frequency in the thermal cycle, α_s and x are the thermal diffusivity and thickness of the substrate, respectively, α_s is the thermal diffusivity of the coating. Eq.(1) states that phase difference(Φ) is measured by the substrate thickness(x) and frequency(f) obtained in the thermal cycling, and then, the substrate thermal diffusivity(α_s) is obtained from the gradient of the relationship between the phase difference(θ) and the substrate thickness(x). In addition, the phase difference(θ)

at the coating thickness(d) is measure by changing the frequency(f). Therefore, the substrate thermal diffusivity(α_c) is obtained from the gradient of the relationship between the phase difference(θ) and frequency($\sqrt{f}$) in Eq.(2). Hence, the thermal conductivity(k) can be described using the following equation(3) [22]:

$$k = \alpha \times \rho \times C \quad (3)$$

where α is the thermal diffusivity, ρ is the density of the material, c is the specific heat capacity of the coating or substrate. Based on the above, the thermal conductivity(k) is calculated by Eq.(1) from the thermal diffusivity(α), density(ρ), and specific heat capacity(C) on the real test.

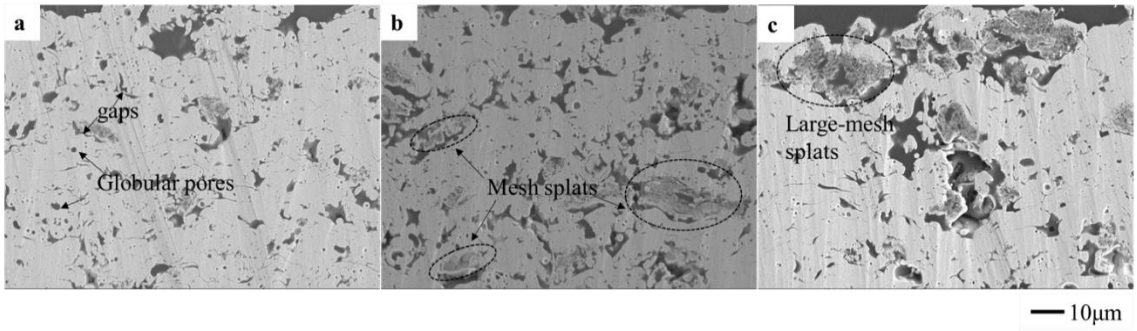

Figure 8-3 SEM cross-section images of Er_2O_3 coating with a thickness of approximately 100 μm: (a) and (b) sprayed with no coolant, (c) sprayed with liquid nitrogen.

Table 8-2 Results of estimated film thickness, cross-sectional porosities of Er_2O_3 coatings synthesized on the aluminum alloy(A5052) substrate. coating with liquid nitrogen in content of the blue area.

Samples	Coating materials	Thickness (μm)	Cross-sectional porosity(%)
(a)	Er_2O_3	106	7.7
(b)		108	15.6
(c)		108	28.3

: liquid nitrogen

8.3 Results and discussion

8.3.1 Microstructure coatings

As we all know, Thermal insulation capability depends on its microstructure, especially is related to the porosity and semi-molten particles.

Fig.8-3 shows the cross-section morphologies of the three types with the different porosity of coatings. It shows that coating (sample (a)) is uniform and dense except a few pores with top layers (Fig.8-3(a)). For coating(sample(b)), a typical porosity structure with special mesh splats, the splats are the special microstructure that is different form the un-melted splat, and we called it that honeycomb microstructure. The number of pores and mesh splats inclusions exist in both coatings, which are obviously raised in coating sample (c) sprayed with coolant (liquid nitrogen) additions (Fig.8-3(b) and (c)). **Table** 8-2 shows the thicknesses and cross-sectional porosities of the Er_2O_3 coatings. The porosities were determined by analyzing SEM images of the coatings. Firstly, the thickness of the three coatings reached the expected target of closing to 100 μm (106, 108, and 108 μm, respectively). Moreover, the Er_2O_3 coating obtained using O_2 as the carrier gas had a cross-sectional porosity of 7.7 %. In the case of the N_2 as the carrier gas, the sample (b), and sample (c), these were sprayed with the same conditions, only one using the coolant, resulting in the porosity of 15.6 % and 28.3 %, respectively. In the previous study, these were reported that the change carrier types for temperature and velocity of the in-flight particles are useful for determining their impact behavior and affect the morphology with the porosity of the sprayed coatings. Furthermore, in order to compare the microstructure and the thermal insulation properties, increase the number of spraying to obtain the coating thickness with 300 μm(calculated thickness: sample(d) 334 μm and sample (e) 312 μm). It can be clearly seen in **Fig.**8-4 that the microstructures of the using and not with coolant are significantly different. **Table** 8-3 shows the thicknesses and cross-sectional porosities of the Er_2O_3 coating with thicker. From **Tables** 8-2 and 8-3, as they were sprayed with the same spray parameters, the porosity was close to each other, thus, it can be said that these spray conditions significantly control the pores in the coatings, and the thickness has no effect on it. In

addition, the interesting phenomenon was observed that some of the inside the splats with formed the mesh microstructure in all samples. However, in the case of the sprayed with liquid nitrogen, the splat with mesh microstructure not only produced the formations to raise, but also the size of the internal voids became larger. Therefore, it has a reasonable assumption that using the coolant to lower the substrate temperature and can control the number of the pores in the coating, as well as benefit to increase the size of the voids inside the splats.

Moreover, the phenomenon was found that the layer connected to the substrate is denser than the top layer in all of the coatings. It would be explained as follow, in this study, flame spraying with the chelate complex was used as a thermal spray technique in which the jet is a flame formed by the combustion of H_2 with O_2 and the injected feedstock is EDTA· Er· H powder. The in-flight EDTA· Er· H particles decomposition, oxide and melt in the flame, spread into disk-shaped or splashing-shaped impact with the substrate surface, transfer heat to the underlying substrate and solidify rapidly. The coating is thus built up from an agglomeration of solidified Er_2O_3 splats. During this process, the aluminum alloy substrate receives heat from the solidifying splats, and it is also heated by the tail-end of the flame, as its hot gas jet escapes from the impact area by flowing out sideways over the substrate [23,24]. These two sources of heat can raise the temperature of the substrate significantly, and so may affect the porosity of the splat layers close to the aluminum alloy substrate with temperature-sensitive [25]. It is expected to provide favorable thermal insulation performance.

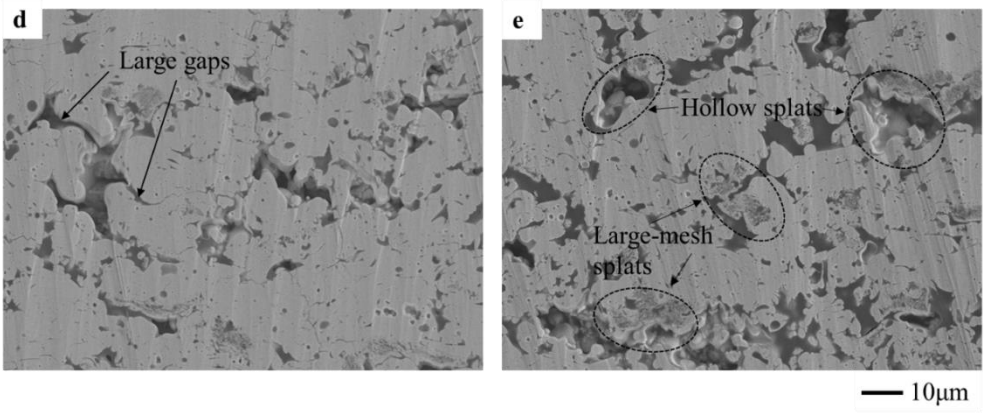

Figure 8-4 SEM cross-section images of Er_2O_3 coating with the thickness of approximately 300 μm: (d) sprayed with no coolant, (e) sprayed with liquid nitrogen.

Table 8-3 Results of estimated film thickness, cross-sectional porosities of Er_2O_3 coatings synthesized on the aluminum alloy(A5052) substrate. coating with liquid nitrogen in content of the blue area.

Samples	Coating materials	Thickness (μm)	Cross-sectional porosity(%)
(d)	Er_2O_3	334	16.9
(e)		312	25.5

: liquid nitrogen

8.3.2 Thermal conductivity

The fundamental function of TBCs is to protect thermal flow from transferring into substrate materials insulation performance. Therefore, thermal insulation capability is considered as one of the most important factors to evaluate the performance of TBCs, in this investigation, the thermal insulation capability of TBCs was evaluated by the temperature drop across TBCs($\Delta T= T_1-T_2$), in addition, from the heating temperature curve, using the Eq (1)-(3) to calculate the thermal conductivity with various thickness and porosity of coating(sample (a)-(e)). In this study, in order to calculate the phase difference(θ) of the sample, all-temperature values in the figure below are the lowest inflection point of the curve peak, and ten values around each reference temperature point were selected.

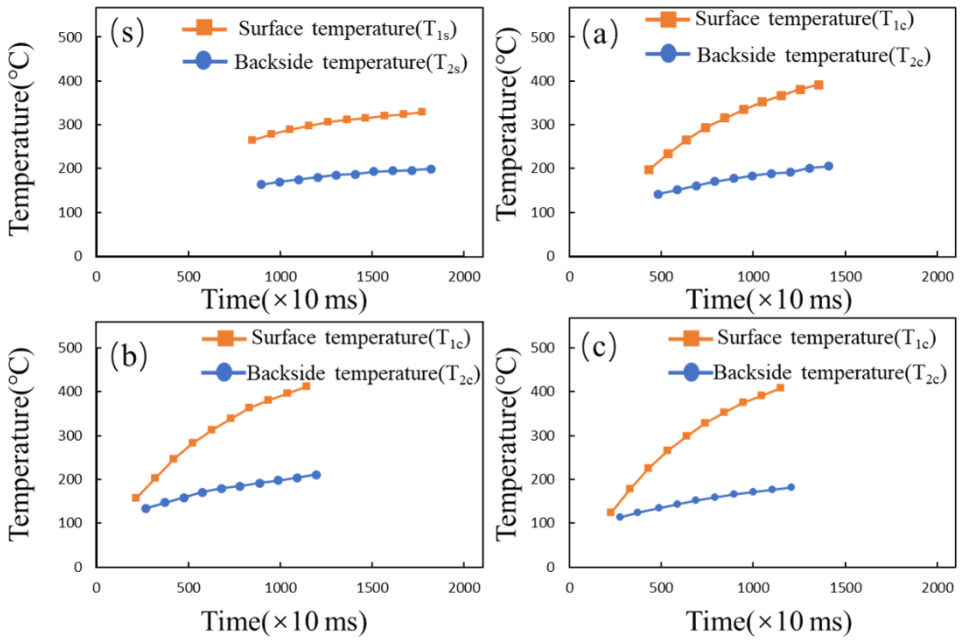

Figure 8-5 Heating temperature curves of surface temperature with substrate(T_{1s}) and TBCs sample (T_{1c}), substrate sample backside(T_{2s}) and TBCs sample backside(T_{2c}) (the same as below).(a) substrate, (b) porosity of 7 %, (c) porosity of 16 % (d) porosity of 28 % Er_2O_3 coating at temperature of 300℃.

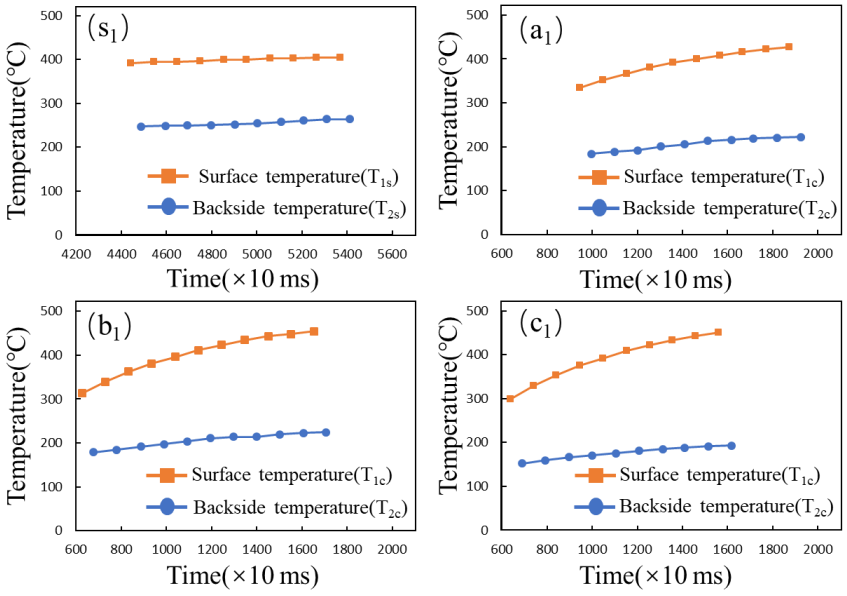

Figure 8-6 Heating temperature curves. (s_1) substrate, (a_1) porosity of 7 %, (b_1) porosity of 16 % (c_1) porosity of 28 % Er_2O_3 coating at temperature of 400℃.

Table 8-4 the temperature values of the surface(T_1) and backside (T_2) at reference temperature of 300 and 400℃.

	Reference temperature 300 ℃			Reference temperature 400 ℃		
Sample	Time (× 10 ms)	Surface temperature (T_1/°C)	Backside temperature (T_2/°C)	Time (× 10 ms)	Surface temperature (T_1/°C)	Backside temperature (T_2/°C)
substrate	1159	300.9	182.5	4957	400.0	258.1
(a)	746	300.3	170.7	1459	400.4	217.5
(b)	532	301.0	172.3	1043	401.7	206.6
(c)	639	300.8	154.2	1052	400.0	178.2

Figs. 8-5 and 8-6 illustrates the recorded heating temperature curves(warming trend) of the substrate sample surface(T_{1s}), the TBCs sample surface(T_{1c}), and the substrate sample backside(T_{2s}), the TBCs sample backside (T_{2c}) at temperature range 300 – 400 ℃. From **Figs.** 8-5 and 8-6, it can be seen that with enhancing spray flame time, T_1 and T_2 increase. And the surface temperature of the TBCs is faster than that of the substrate. In addition, the surface temperature of the substrate tends to be stable, at the reference temperature of 400 ℃. Furthermore, when the temperature of the TBCs and substrate was raised to 300 and 400 degrees, the temperature value of the backside of each sample with the result was listed in **Table** 8-4. In this result, the ΔT_c values of each sample are 182 ℃, 195 ℃, and 221℃, respectively, as the substrate surface temperature tends to be stable with about 400 ℃. It means that TBCs contribute to a decrease in the temperature of the metal substrate. Moreover, the temperature drops across TBCs became larger in different porosity coatings as spray flame time, and temperature increased. In addition, the surface temperature of the TBCs with the spray

flame time tends to stable of the range from the 500 ℃, the temperature selection point, as shown in **Fig.**8-7. From the results, it can be clearly seen that all of the TBCs both side temperature curves to become stable, and as the porosity increases, the difference between the curves on both sides becomes significantly larger, especially the porosity of 28.3%. In addition, from the **Figs.**8-5 and 8-7, an interesting phenomenon was discovered that the TBCs are higher than the temperature of the substrate, which is because the formed the pore and voids in the coatings, especially on the top layers spread, it can be explained that the thermal radiation crosses the pores, voids and mesh-splats become slower while the coating is heated, resulting in a reduction in the surface heat transfer rate, thereby increasing the surface temperature. Furthermore, the thermal conductivity of Er_2O_3 coating with various types of porosity was calculated by the previously described equation. The density(ρ) was measured according to Archimedes Principle. The phase difference(θ) was measured according to the temperature curves with AC calorimetric method. The deviation of thermal conductivity was estimated to be ± 6 % due to the deviation for ρ, α, and C, and the results are listed in **Table** 8-5. From these results, at the temperature of 500 ℃, thermal conductivity is varying between 1.56 $Wm^{-1}K^{-1}$ and 0.90 $Wm^{-1}K^{-1}$, depending on the porosity. For the thickness of the coating becomes thicker with 300 μm(real thickness as shown in Table 8-3), the heating temperature curves with rising phase(sample (d) and sample (e)) and stable phase(sample (d_1) and sample (e_1)) as shown in **Fig.**8-8. In the rising phase, it can be clearly seen that with enhancing spray flame time, T_1, and T_2 increase. In addition, the rising ratio of T_2 is much lower than that of T_1, and it is shown the flat curve with raise

the temperature of the backside. For a reason, thermal insulation capability depends on its microstructure, especially is related to the porosity and splat gaps or formed voids, thus, looking back shown in **Fig.**8-4, not only described above with the microstructure but also the orientations of the newly formed hollow splats(the splats are hollow inside, and the splats wall is significant) are slope to the heat flus direction, which are beneficial to the enhancement of thermal insulation capability, in other words, the decrease of thermal conductivity. On the other hand, which is responsible for the easy flow of the heat into the surface with the pore of the coating and top layer as a thermal storage layer proved to be better for the heat blocking. **Table** 8-6 shows the rising phase of each sample with the backside temperature at the reference temperature of 400 ℃ and 500 ℃(only the sample(e)). As can be seen, the sample (d) with ΔT_d of 244 ℃ at the reference temperature 400 ℃, and the sample (e) with ΔT_e of 260℃ and 347, respectively, at the reference temperature 400 ℃ and 500 ℃. Furthermore, in the stable phase, the temperature curves on both sides tend to be flat range at 500 ℃ and 600 ℃, respectively, as shown in **Fig.**8-8 (d_1) and (e_1). Moreover, it can be calculated that the thermal conductivity of the 4.56 $Wm^{-1}K^{-1}$ and 2.57 $Wm^{-1}K^{-1}$, respectively, And the details shown in **Table** 8-7. The thermal conductivity difference values depending on the spraying conditions, thereby to improve the porosity in the coatings.

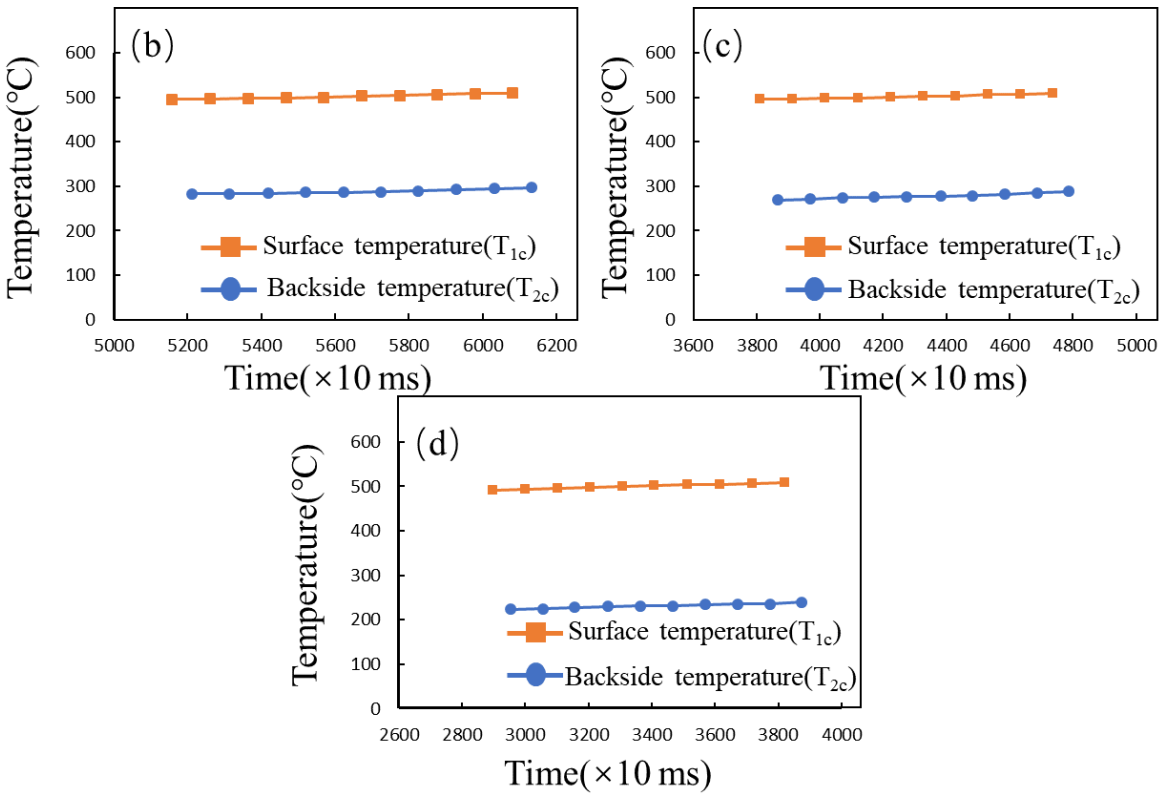

Figure 8-7 Heating temperature curves with each sample (b)-(c). (b) porosity of 7 %, (c) porosity of 16 % (d) porosity of 28 % Er_2O_3 coating at temperature of 500℃.

Table 8-5 The results of each sample at the stable phase.

Sample	Time (× 10 ms)	Surface temperature (T1/°C)	Backside temperature (T2/°C)	ΔT(°C)	Thermal conductivity (W/(mK))
(a)	5571	500.5	291.5	209	1.56
(b)	4225	500.1	281.7	218	1.25
(c)	3308	500.1	235.5	264	0.90

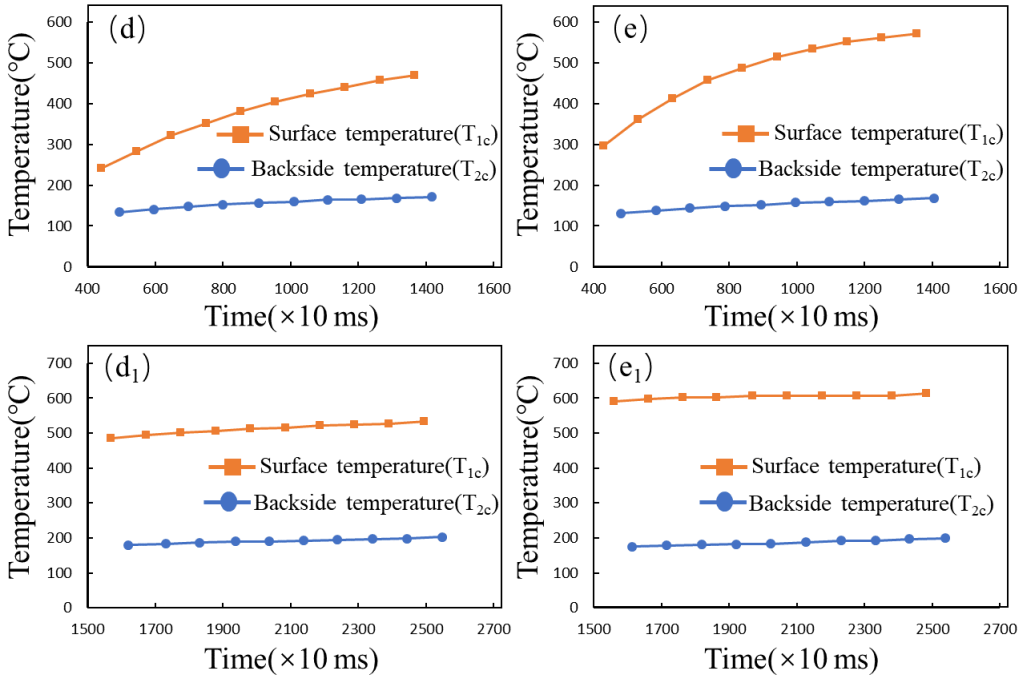

Figure 8-8 Heating temperature curves with each sample (d), (e). (d) porosity of 16 %, 300 μm thick Er_2O_3 coating, (e) porosity of 25 % 300 μm thick Er_2O_3 coating at temperature of 400 - 500℃, and (d_1) porosity of 16 %, 300 μm thick Er_2O_3 coating, (e_1) porosity of 28 %, 300 μm thick Er_2O_3 coating at temperature of 500 - 600℃.

Thermal insulation capability was reported versus porosity, thickness. Mesh-splats and hollow splats for each coating. Two groups of coating with thickness 100 μm and 300 μm have been identified that show different behaviors (in Fig.8-7 and Fig.8-8 (d_1),(e_1)). Firstly, It can be clearly seen that ΔT values depend on the coating thickness and porosity or microstructure. The ΔT values increased with increasing the coating thickness from 100 μm to 300 μm. Using the carrier gas N_2 and coolant as the conditions which are sprayed coatings exhibited higher ΔT values than the conventional coatings(e.g., O_2 as the carrier gas). For 300 μm thick coatings, the ΔT value at the

stable phase of the Er_2O_3 coating increased by 43.1 % compared with that of the thickness of the 100 μm coating with the same spray conditions(sample (b) and (d)). It means that the thickness as the factor, which can be affected the thermal insulation capability in this study. From **table** 8-5 and 8-7, the thermal conductivity values of 300 μm coatings are larger than the thickness of the 100 μm coating in all of the samples. Generally, the factors affect coating thermal conductivity are mainly determined firstly by the spray conditions such as types of coating, sprayed with raw materials size and heat flow direction, and secondly by the coating microstructure such as pore characteristics and moisture ratio. Based on the above, two groups, the sample (b), (c), and sample (d), (e) were sprayed with the same conditions, hence, it can be considered that the coating microstructure affects the thermal conductivity values. To explain the phenomenon, two effects could have happened during the thermal insulation test. First, the spray flame with H_2-O_2, result in the moisture generated during the spraying, thus, when there is moisture(including water vapor) in the pores of the coating, the diffusion of steam in the pores or gaps and the movement of water molecules will play a major role in heat transfer, which is responsible a significant increase in its effective thermal conductivity. The other effect to consider is the thick coating with more pores or gaps, thus, during the deposition processes with the chemical reaction of EDTA· Er· H, and it can be represented by Eq.(4), as shown in follow.

$$2EDTA{\cdot}Er{\cdot}H + 24O_2 \rightarrow Er_2O_3 + 20CO_2 \uparrow + 13H_2O \uparrow + 4NO_2 \uparrow \quad (4)$$

Hence, as the deposited with each layer or splats which the generated water vapor might be entering the pores formed in the layer or between the layers, which further

increases the thermal conductivity values. In other words, it is provided that a new kind of thermal insulation capability and thermal conductivity test method is feasible in this study. By depositing on aluminum alloy substrate, successfully synthesized the TBCs with the thickness of 108-334 μm, and have a good thermal insulation capability could be obtained without bond coating. It could greatly reduce the weight of the hot components.

Table 8-6 The temperature values of the surface(T_1) and backside (T_2) at reference temperature of 400 and 500℃ at the rising phase.

Sample	Time (× 10 ms)	Surface temperature (T1/°C)	Backside temperature (T2/°C)	Time (× 10 ms)	Surface temperature (T1/°C)	Backside temperature (T2/°C)
(d)	858	404.1	159.6	-	-	-
(e)	539	400.3	139.5	845	502.0	154.6

Table 8-7 The results of each sample at the stable phase.

Sample	Time (× 10 ms)	Surface temperature (T1/°C)	Backside temperature (T2/°C)	ΔT(°C)	Thermal conductivity (W/(mK))
(d)	1676	500.0	187.7	312	4.56
(e)	1764	601.1	182.4	418	2.57

8.4 Conclusions

A variety of types thick Er_2O_3 coatings were synthesized from a metal-EDTA complex using a flame-spraying system. By varying the spray conditions, the cross-sectional porosity of the deposited TBCs could be varied from 7.7 % to 28.3 % and

16.9 % to 25.5 % in thickness of 100 μm and 300 μm, respectively. As a new TBC material, Er_2O_3 exhibits a better thermal insulation capability. For the coating with a thickness of 300 μm, exhibits higher ΔT value, which increases by 43.1 % compared with that of the thickness of the 100 μm coating with the same spray conditions. In addition, it exhibited low thermal conductivity, decreasing from 4.56 $Wm^{-1}K^{-1}$ with the porosity of 16.9 % to 2.57 $Wm^{-1}K^{-1}$ with the porosity of 25.5 % at the stable phase(500 ℃ and 600 ℃) have been systematically investigated. This study provides a new idea of the test method, which can be measured that thermal conductivity and thermal insulation capability have been discussed. Therefore, it is expected that the expanded and deepened in further studies with deposited TBC on the lightweight metal.

References

[1] R. Vaßen, M. Ophelia-Jarligo, T. Steinke, D. Emil-Mack, D. Stöver, Overview on advanced thermal barrier coatings, *Surf. Coat. Technol.*, **205**, 938–942 (2010).

[2] S. Sampath, U. Schulz, M.O. Jarligo, S. Kuroda, Processing science of advanced thermal-barrier systems, *MRS Bull.*, **37** (10), 903-10 (2012).

[3] N.P. Padture, M. Gell, E.H. Jordan, Thermal barrier coatings for gas-turbine engine applications, *Science*, **296** (5566), 280-84 (2012).

[4] X.Q. Cao, D. Stöver, R. Vaßen, F. Tietz, W. Jungen, E.V. Fischer, Lanthanum cerium oxide as thermal barrier coating material for high temperature applications, *Adv. Mater.,* **15**, 1438–1442 (2003).

[5] A.G. Evans, D.R. Clarke, C.G. Levi, The influence of oxides on the performance of advanced gas turbines, *J. Eur. Ceram. Soc.*, **28** (7), 1405-419 (2008).

[6] K. Kokini, J. Dejonge, S. Rangaraj, B. Beardsley, Thermal shock of functionally graded thermal barrier coatings with similar thermal resistance, *Surf. Coat. Technol.,* **154** (2–3), 223–231 (2002).

[7] N.P. Padture, M. Gell, E.H. Jordan, Thermal barrier coatings for gas-turbine engine applications, *Science*, **296**, 280–284 (2002).

[8] B. Li, X.L. Fan, K. Zhou, T.J. Wang, Effect of oxide growth on the stress development in double-ceramic-layer thermal barrier coatings, *Ceram. Int.*, **43**, 14763–14774 (2017).

[9] R. Vaßen, M.O. Jarligo, T. Steinke, D.E. Mack, Overview on advanced thermal barrier coatings, *Surf. Coat. Technol.*, **205**, 938–942 (2010).

[10] D.R. Clarke, M. Oechsner, N.P. Padture, Thermal-barrier coatings for more efficient gas-turbine engines, *MRS Bull.*, **37**, 891–898 (2012).

[11] J. Wang, J. Sun, Q. Jing, B. Liu, H. Zhang, Y. Yongsheng, J. Yuan, S. Dong, X. Zhou, X. Cao, Phase stability and thermo-physical properties of ZrO_2-CeO_2-TiO_2 ceramics for thermal barrier coatings, *J. Eur. Ceram. Soc.*, **38**, 2841-2850 (2018).

[12] B. Lv, R. Mücke, X. Fan, T.J. Wang, O. Guillon, R. Vaßen, Sintering resistance of advanced plasma-sprayed thermal barrier coatings with strain-tolerant microstructures,

J. Eur. Ceram. Soc., **38**, 5092-5100 (2018).

[13] A. Cipitria, I.O. Golosnoy, T.W. Clyne, A sintering model for plasma-sprayed zirconia TBCs. Part I: free-standing coatings, *Acta Mater.*, **57**, 980-992 (2009).

[14] M.P. Planche, H. Liao, B. Normand, C. Codde, Relationships between NiCrBSi particle characteristics and corresponding coating properties using different thermal spraying processes, *Surf. Coat. Technol.*, **200**, 2465–2473 (2005).

[15] D.Y. Xin, K. Komatsu, K. Keita, T. Costa, Y. Ikeda, A. Nakamura, S. Ohshio, H. Saitoh, Heat-shock properties in yttrium-oxide films synthesized from metal-ethylenediamine tetraacetic acid complex through flame-spray apparatus, *Appl. Phys. A.*, **123**, 194(7) (2017).

[16] K. Komatsu, T. Sekiya, A. Toyama, Y. Hasebe, A. Nakamura, M. Noguchi, Y. Li, S. Ohshio, H. Akasaka, H. Muramatsu, H. Saitoh, Deposition of metal oxide films from metal-EDTA complexes by flame spray technique, *J. Therm. Spray Technol.*, **23**, 833(8) (2014).

[17] Y.X. Dan, X.L. Zhou, A. Nakamura, K. Komatsu, H. Saitoh, Splat morphology and microstructure of chelate flame sprayed Er_2O_3 films, *J. Ceramic Society of Japan*, submitting.

[18] Y.X. Dan, T. Costa, Z.Y. Guo, A. Nakamura1, K. Komatsu, H. Saitoh, Thermal barrier coatings formed by flame spray with metal-EDTA, *Japanese Journal of Applied Physics*, DOI: https://doi.org/10.35848/1347-4065/ab9ef6.

[19] K. Komatsu, T. Costa, Y. Ikeda, K. Abe, Y.X. Dan, T. Kimura, A. Nakamura, T. Shirai, H. Saitoh, Synthesis of Y_2O_3 films on an aluminum alloy substrate using flame-spray apparatus with a H_2-O_2 flame, *Int. J. Appl. Ceram. Tech.*, **00**, 1-10 (2018).

[20] W. J. Parker, R. J. Jenkins, C. P. Butler, and G. L. Abbott, Flash Method of Determining Thermal Diffusivity, Heat Capacity, and Thermal Conductivity, *J. Appl. Phys.*, **32**, 1679-1684 (1961).

[21] Kazuya Okamoto and Hiroaki Anno, Fabrication of Anisotropic Thermal Diffusivity Measurement System for Thin Films by an AC Calorimetric Method, Tokyo University of Science, 61-65 (2018).

[22] Z.Y. Shen, L.M. He, Z.H. Xu, R.D. Mu, G.H. Huang, Rare earth oxides stabilized

La2Zr2O7 TBCs: EB-PVD, thermal conductivity and thermal cycling life, *Surf. Coat. Technol.*, **357**, 427-432 (2019).

[23] Y. Bao, T. Zhang, D. T. Gawne, *Surf. Coat. Technol.*, **194**, 82 (2005).

[24] T. Zhang, Y. Bao, D.T. Gawne, P. Mason, *Prog. Org. Coat.*, **70**, 45 (2011).

[25] S.K. Panigrahi, R, Jayaganthan, *J. Mater. Sci.*, **45**, 5624 (2010).

Chapter 9

General conclusions

In this study, metal oxides were synthesized from metal-ethylenediaminetetraacetic acid (EDTA) complex using the flame spraying method. From this method, two types of coating such as Er_2O_3 and Y_2O_3 were deposited on the different materials, among them are optical materials (quartz glass), and another one of metal materials with high-temperature sensitivity such as aluminum alloy which was selected as the substrate. And through the studies have been based on comparisons between coatings produced from different spray conditions with substrate temperature, types of carrier gas and powder feed ratio which did allow to demonstrate that a relationship exists between the size and shape of the pore, as well as the nature porosity, and the thermophysical properties, the estimation of the amount of the formed pores in the coating relationship with the thermal insulation capability as well as the thermal conductivity is the focus of the thesis. The most important conclusions obtained in this study were summarized as below:

In Chapter 2, the two types of metal-oxide coatings of Y_2O_3 and Er_2O_3 were deposited on stainless steel substrates using various gases such as nitrogen, commercial air (nitrogen and oxygen), and oxygen as the carrier gas and a mixture of H_2-O_2 as the combustion gas. By varying the carrier gas, the microstructure with cross-sectional

porosity of the deposited metal-oxide coatings which could be different from 3% to 23.4%. It was found that O_2 was the better carrier gas for fabricating dense metal oxide coatings at low costs by the synthesis. On the other hand, in the case of N_2 as the carrier gas to synthesis the coating shows the high porosity with 23.4%, therefore, the temperature of the inflight particles can be affected the microstructure with coating. Based on the study, it provides a new idea for the design of coating structures for the subsequent study.

In Chapter 3, two series of experiments were performed to study the cross-sectional structure of Er_2O_3 coatings deposited by the chelate-flame spraying method. First, Er_2O_3 coatings were sprayed on substrates with different materials, i.e., quartz glass, stainless steel (304), and aluminum alloy (A5052). From microstructure and obtained the images were analyzed by image analysis software, the result shows that more density Er_2O_3 coatings with the porosity of 1.6% on the quartz glass, and a typical lamella structure was observed in Er_2O_3 coating with the aluminum alloy as the substrate. And second, deposited the Er_2O_3 coating with the various sizes on the three types substrate, and then characterizing the coating thickness, microstructure, the results suggested that the solidification speed of the molten particles deposited on the substrate may be related to the physical properties of the substrate material itself. From this study, the chelate thermal spraying method has been found and exhibited great advantages in depositing ceramic coatings on optical materials and low melting metals.

In Chapter 4, flame sprayed Er_2O_3 splats directly deposited on mirror polished aluminum alloy substrate with different spraying conditions and deals with the quantitative characterization of spreading, morphologies of the splats. And using the rotation apparatus with 12-hedron, combine the rotation speed to reduce the substrate temperature. The results suggested that the influence of in-flight particle temperature and velocity, substrate temperature, carrier gas types, and carrier gas ratio on the solidification mechanism of molten droplets. In particular, A spraying method combined with multi-dimensional modes is proposed to control the morphology of splats.

In Chapter 5, the yttrium-oxide(Y_2O_3) coatings synthesized using the various size

raw materials with the metal-EDTA complex by flam-spraying method. The heat-shock properties of deposited Y_2O_3 coatings on the stainless-steel substrate were investigated. From the characterizing, the coating thickness, crystal structure, and microstructure (surface and cross-sectional) exhibit a high plasma resistance by the cyclic thermal shock test. The Y_2O_3 coatings have great potential in thermal properties with the application.

In Chapter 6, Y_2O_3 coatings were synthesized on an aluminum alloy substrate directly using a flame-spray method with an H_2-O_2 flame. The crystalline structure and element diffusion analysis of the coating was performed by using a combination of FE-SEM, TEM, EDX, and XRD as well as annealing tests. The results suggested that the nanolayer of MgO would have a role in the Y_2O_3/ aluminum alloy joining formed from the EDTA·Y·H complex and exhibit strong adhesion and thermal shock properties. It is provided that a new spraying method for the application of aluminum alloy in high temperature resistance.

In Chapter 7, microstructures and thermal insulation capability of chelate flame-sprayed erbium oxide (Er_2O_3) and yttrium oxide (Y_2O_3) coatings were directly deposited with the suitable controlling spray conditions on aluminum alloy (A5052) substrate have been investigated. The results show that the Y_2O_3 coatings had higher thermal insulation capability than the Er_2O_3 coatings by the steady-state test. It is worth noting that the thermal insulation capacity of the Y_2O_3, Er_2O_3 coatings synthesized by the cooling substrate with liquid nitrogen method is improved. For the thicknesses of 90 – 128 μm and cross-sectional porosity of 12-33 % Y_2O_3 coatings, the temperature drop (ΔT_f =37 ℃) of the coarse-voids-structure Y_2O_3 coating at 440 ℃ and upgrade from 0.10 to 0.32 of ΔT_f per unit micron (℃/μm).

In Chapter 8, The thermal insulation capability, thermal conductivity, microstructure, porosity, and splats of these two kinds of coatings with thickness were investigated. The coating with thickness of 300 μm, exhibits higher ΔT value, which increases by 43.1 % compared with that of the thickness of the 100 μm coating with the same spray conditions. It exhibited low thermal conductivity, decreasing from 4.56 $Wm^{-1}K^{-1}$ to 2.57

$Wm^{-1}K^{-1}$ at the stable phase(500℃ and 600℃), which is mainly due to its special microstructure with more mesh-splats, higher porosity(28.3%). It can be provided a new idea of test method, which can be measured that thermal conductivity and thermal insulation capability.

In conclusion, we are using the chelate flame spray method to synthesis various types of structure of metal-oxide coatings such as thick, densification, and porous. Hence, this method can be suitable for coating structure design with multiple requirements. Moreover, the chelate flame spray method provides that not only the synthesized the metal-oxide coating exhibit the excellent performance in thermal insulation but also is possible to obtain the thermal conductivity of the coating at different temperature with can simulate engine working environment.